1998

Technical

Digest Series

Volume 3

Laser Applications to Chemical and Environmental Analysis

Technical Digest

March 9–11, 1998

Sheraton World Resort Orlando
Orlando, Florida

Postconference Edition

OSA
Optical Society of America

Sponsored by the **Optical Society of America**

In cooperation with the **Laser Institute of America**

REPORT DOCUMENTATION PAGE

Form Approved
OMB No. 0704-0188

1. AGENCY USE ONLY *(Leave blank)*	2. REPORT DATE	3. REPORT TYPE AND DATES COVERED
	March 23, 1999	Final Sept. 25, 1997 - March 24, 1999

4. TITLE AND SUBTITLE

Organization of the 1998 Laser Applications to Chemical Environmental Analysis Topical Meeting

5. FUNDING NUMBERS

DAAG55-97-1-0405

6. AUTHOR(S)

Stephen D. Fantone

7. PERFORMING ORGANIZATION NAMES(S) AND ADDRESS(ES)

Optical Society of America
2010 Massachusetts Ave., NW
Washington, DC 20036

8. PERFORMING ORGANIZATION REPORT NUMBER

9. SPONSORING / MONITORING AGENCY NAMES(S) AND ADDRESS(ES)

US Army Research Office
P.O. Box 12211
Research Triangle Park, NC 27709-2211

10. SPONSORING / MONITORING AGENCY REPORT NUMBER

ARO 37855.1-EV-CF

11. SUPPLEMENTARY NOTES

The views, opinions, and/or findings contained in this report are those of the author(s) and should not be construed as an official Department of the Army position, or decision, unless so designated by other documentation.

a. DISTRIBUTION / AVAILABILITY STATEMENT

Approved for public Release
Distribution unlimited

12. DISTRIBUTION CODE

13. ABSTRACT ***(Maximum 200 words)***

The topical meeting on Lasers and Applications to Chemical and Environmental Analysis provided an informal atmosphere that fostered communication between researchers and practitioners in the field. In this 1998 meeting, the technical focused on surface spectroscopies, advances in single frequency diode laser for gas sensing, environmental monitoring and remediation, applications to micro- analytical systems, combustion diagnostics, ultra-sensitive biomedical spectroscopy, and advances in laser applications to large-scale chemical analysis.

14. SUBJECT TERMS

15. NUMBER OF PAGES

16. PRICE CODE

17. SECURITY CLASSIFICATION OF REPORT	18. SECURITY CLASSIFICATION OF THIS PAGE	19. SECURITY CLASSIFICATION OF ABSTRACT	20. LIMITATION OF ABSTRACT
unclassified	unclassified	unclassified	UL

Standard Form 298 (Rev. 2-89)
Prescribed by ANISE Sad Z39-18
298-102

Laser Applications to Chemical and Environmental Analysis

Conference Edition

Technical Digest

March 9–11, 1998

Sheraton World Resort Orlando
Orlando, Florida

1998 OSA Technical Digest Series
Volume 3

Sponsored by
Optical Society of America
2010 Massachusetts Avenue, NW
Washington, DC 20036-1023

In cooperation with the **Laser Institute of America**

Partial support provided by
U.S. Air Force Office of Scientific Research
Lambda Physik
New Focus

OSA®
Optical Society of America

Articles in this publication may be cited in other publications. To facilitate access to the original publication source, the following form for the citation is suggested:

Name of Author(s), "Title of Paper," in Laser Applications to Chemical and Environmental Analysis, Technical Digest (Optical Society of America, Washington DC, 1998), pp. xx-xx.

Optical Society of America

ISBN

Conference Edition	1-55752-533-1
Postconference Edition	1-55752-534-X
1998 Technical Digest Series	1-55752-521-8

Library of Congress Catalogue Card Number

Conference Edition	97-81333
Postconference Edition	97-81334

Printed in the U.S.A.

Contents

Technical Program Committee

Robert P. Lucht, *University of Illinois, General Chair*

Kay Niemax, *Institute of Spectrochemistry and Applied Spectroscopy, Germany, General Chair*

Mark G. Allen, *Physical Sciences Inc., Program Chair*

Robert W. Shaw, *Oak Ridge National Laboratory, Program Chair*

Volker Sick, *University of Michigan, Program Chair*

Dieter Brueggemann, *University of Stuttgart, Germany*

Ernest Cespedes, *U.S. Army Waterways Experiment Station*

Jay B. Jeffries, *SRI International Inc., OSA Technical Council Representative*

Kevin McNesby, *U.S. Army Research Laboratory*

David J. Rakestraw, *Sandia National Laboratories*

Markus Sauer, *University of Heidelberg, Germany*

Alan C. Stanton, *Southwest Sciences Inc.*

Nicholas Winograd, *Pennsylvania State University*

Edward S. Yeung, *Iowa State University*

Agenda

■ Sunday
■ March 8, 1998

Main Lobby
7:00am–8:00pm
Registration

■ Monday
■ March 9, 1998

Main Lobby
7:00am–5:30pm
Registration/Speaker Check-in

Coral Room

7:50am–8:00am
Opening Remarks

8:00am–10:00am
LMA ■ Ultrasensitive Detection for Biochemical Applications
Edward S. Yeung, *Iowa State University*
Markus Sauer, *University of Heidelberg, Germany, Presiders*

8:00am (Invited)
LMA1 ■ Large-scale chemical analysis by laser-induced fluorescence detection and multiple capillary electrophoresis separation, Norman J. Dovichi, Jian Zhong Zhang, Sue Bay, John Crabtree, Pieter Roos, *Univ. Alberta, Canada.* We have developed a number of 5, 16, 32, and 96 capillary electrophoresis instruments with laser-induced fluorescence detection. A 576 capillary device has been designed. **(p. 2)**

8:30am
LMA2 ■ Cell imaging by laser-induced native fluorescence microscopy, Edward Yeung, Wei Tong, *Iowa State Univ.;* Sheri Lillard, *Stanford Univ.* Direct visualization of the secretion process of individual bovine adrenal chromaffin cells was achieved with laser-induced native fluorescence excited at 275 nm and detected with an intensified CCD camera. **(p. 5)**

8:45am
LMA3 ■ Detection of single molecules in microcavities, N. Lermer, M.D. Barnes, C.-Y. Kung, W.B. Whitten, J.M. Ramsey, *Oak Ridge National Laboratory.* Detection of single fluorescent dye molecules in streams of glycerol microdroplets, and investigation of single-molecular microcavity effects and stimulated emission, are discussed. **(p. 8)**

9:00am
LMA4 ■ Confinement, detection, and manipulation of individual molecules in attoliter volumes, C.-Y. Kung, M.D. Barnes, N. Lermer, W.B. Whitten, J.M. Ramsey, *Oak Ridge National Laboratory.* Streams of submicron water droplets were used to confine and efficiently probe single rhodamine 6G molecules in attoliter volumes. **(p. 11)**

9:15am
LMA5 ■ How many labeled mononucleotide molecules can be identified in water on the single-molecule level, M. Sauer, F. Göbel, U. Lieberwirth, J. Wolfrum, *Univ. Heidelberg, Germany;* J. Arden-Jacob, K.H. Drexhage, *Univ.-Gesamthochschule Siegen, Germany;* C. Zander, *Univ. Heidelberg and Univ.-Gesamthochschule Siegen, Germany.* We demonstrate that at least three differently labeled analyte molecules can be identified by time-resolved fluorescence spectroscopy in pure water on the single-molecule level, even in a mixture. **(p. 14)**

9:30am (Invited)
LMA6 ■ Dual-molecule fluorescence spectroscopy: kinetic observation of single molecule reactions, Shimon Weiss, *Lawrence Berkeley National Laboratory.* Single-pair fluorescence resonance energy transfer (spFRET) and single molecule fluorescence polarization anisotropy (smFPA) are used to study protein dynamics. **(p. 17)**

Atlantic/Pacific Room
10:00am–10:30am
Coffee Break/Exhibits

Coral Room

10:30am–11:45am

LMB ■ Laser Applications in Micro-Analytical Systems

David J. Rakestraw, *Sandia National Laboratory, Presider*

10:30am (Invited)

LMB1 ■ Lab-on-a-chip devices: thinking small about chemical and biochemical measurements, J. Michael Ramsey, *Oak Ridge National Laboratory.* Microfabricated devices (lab-on-a-chip) which accomplish chemical and biochemical analysis procedures will be discussed. **(p. 20)**

11:00am

LMB2 ■ Environmental monitoring with fiber-optic immunosensors and compact optoelectronics, J.T. Ives, B.J. Sullivan, J. Thamer, L. Diruscio, J. Bechtel, *TACAN Corp.;* T.C. Thomas, *Armstrong Laboratory.* A continuous environmental monitor based on fiber-optic immunosensors and circuit board optoelectronics is being developed. BTEX compounds and pesticides are detected at sub-ppm levels. **(p. 23)**

11:15am

LMB3 ■ High-speed microchip electrophoresis, Stephen C. Jacobson, Christopher T. Culbertson, J. Michael Ramsey, *Oak Ridge National Laboratory.* Using a planar microchip format, binary mixtures were resolved by free solution electrophoresis in less than 1 msec by optimizing the separation conditions. **(p. 26)**

11:30am

LMB4 ■ Progress toward a chip-based detector for explosives, Christopher G. Bailey, Don W. Arnold, David J. Rakestraw, *Sandia National Laboratories.* As a prelude to chip-based detection, a mixture of explosive has been separated using microcapillary chromatography and detected using a semiconductor laser and photodiode. **(p. 29)**

Patio

6:00pm–7:30pm

Conference Reception

Atlantic/Pacific Room

7:00pm–9:00pm

LMC ■ Poster Session

LMC1 ■ Interferometrically decoded fiber-optic vibration sensor using low-power laser diode, Tarun Kumar Gangopadhyay, Philip James Henderson, *Univ. Sydney, Australia.* A laser-based interferometric fiber sensor for measuring vibration amplitudes up to 2.72 μm has been demonstrated. It uses a monotonically varying fringe contrast function to identify fringe order. **(p. 34)**

LMC2 ■ Laser diode refractive index detection in capillary, V.L. Kasyutich, *National Academy of Sciences, Belarus.* A model based on ray-tracing and Huygens principles is discussed to optimize an interference refractive index detector with laser diode for analytical techniques using a capillary. **(p. 37)**

LMC3 ■ A laser and fiber-optics-based, passive, differential system to measure the optical properties of liquids and gases, Jennifer Harrolle, Michael Bass, *Univ. Central Florida;* Madhu Acharekar, *Schwartz Electro Optics.* A passive device is demonstrated that enables remote detection of the optical properties of liquids and gases. By use of laser sources and fiber optics, the properties of liquids have been measured at distances of ~300 m. Performance, design, and applications are discussed. **(p. 40)**

LMC4 ■ Velocity, temperature, and density measurements in reacting flows using laser-induced gratings, Michael S. Brown, *MetroLaser Inc.;* William L. Roberts, *North Carolina State Univ.* Progress in the use of laser-induced grating techniques for simultaneous single-point measurement of velocity, temperature, and density in pressurized reacting flows is presented. **(p. 43)**

LMC5 ■ A phase-based metrology system for measuring trace-gas concentration, J.H. Rentz, J.A. Gargas, C.R. Schwarze, *Optra Inc.* A phase-based metrology system is presented by use of the slope of the anomalous dispersion around a resonance to measure trace gas concentration. **(p. 46)**

LMC6 ■ Laser probe of surfaces of bacteriorhodopsin Langmuir–Blodgett films by the method of second harmonic generation, A.V. Kir'yanov, I.A. Maslyanitsyn, V.V. Savranskii, V.D. Shigorin, *General Physics Institute, Russia.* The method of second harmonic generation in Langmuir–Blodgett films (LBF) under the action of powerful IR radiation is suggested to evaluate their surface quality on the example of multilayer LBF of bacteriorhodopsin. **(p. 49)**

LMC7 ■ Laser-induced fluorescence of aromatic hydrocarbons in diesel oil laminar premixed flames, F. Cignoli, S. Benecchi, S. De Iuliis, G. Zizak, *CNR-TeMPE, Italy.* Classes of aromatic hydrocarbons and soot volume fraction have been detected and correlated in laminar premixed rich flames of different diesel oils. **(p. 52)**

LMC8 ■ Optical pulse propagation via whispering gallery modes in glass spheres, W.B. Whitten, R.W. Shaw, M.D. Barnes, J.M. Ramsey, *Oak Ridge National Laboratory.* Picosecond optical pulses were coupled into whispering gallery propagation modes of glass spheres. Applications of this technique to absorption spectroscopy are discussed. **(p. 55)**

LMC9 ■ Sodium concentration measurements with resonant holographic interferometry for gas and multi-phase environments, Ramon Dimalanta, Jr., Derek Dunn-Rankin, *Univ. California–Irvine;* Neal J. Brock, Peter A. DeBarber, Mike S. Brown, Jeff Segall, James E. Millerd, *Metrolaser Inc.* Using resonant holographic interferometry, a nonintrusive, laser-based diagnostic, concentrations of sodium vapor were measured in a static cell of varying pathlength and near a sodium seeded droplet stream. **(p. 58)**

LMC10 ■ Diode-laser-difference frequency spectrometer for carbon monoxide detection, Torsten Blanke, Ulrike Willer, Dietmar Kracht, Wolfgang Schade, *Univ. Kiel, Germany.* Mid-infrared difference frequency generation by two single-mode diode lasers and absorption spectroscopy is applied to detect carbon monoxide in cigarette smoke. **(p. 61)**

LMC11 ■ Remote radiation sensing using a fiber-coupled, optically stimulated luminescence dosimeter, Alan L. Huston, Brian L. Justus, *Naval Research Laboratory.* We describe a remote radiation sensor that uses a diode laser to stimulate visible luminescence from an optically transparent phosphor fused to an optical fiber. **(p. 64)**

LMC12 ■ Paper withdrawn.

LMC13 ■ Near-infrared frequency modulated detection of transient species, Andrew J. Marr, Gregory E. Hall, Trevor J. Sears, *Brookhaven National Laboratory;* Bor-Chen Chang, *National Central Univ., Taiwan.* Highly sensitive absorption spectrometers working at near-infrared wavelengths incorporating frequency modulation detection and a multi-pass Herriott-type cell have been developed. Method and results are described. **(p. 68)**

LMC14 ■ Following the dynamics of single oligonucleotide molecules in water, M. Sauer, K.-T. Han, S. Nord, C. Zander, *Univ. Heidelberg, Germany;* K.H. Drexhage, *Univ.-Gesamthochschule Siegen, Germany.* The dynamical behavior of conformational transitions between various states with different electron transfer efficiency between oligonucleotides and an attached oxazine dye is monitored on the single-molecule level in water. **(p. 71)**

LMC15 ■ Laser-induced fluorescence in inhibited counterflow diffusion flames, Robert G. Daniel, Kevin L. McNesby, R. Reed Skaggs, Andrzej W. Miziolek, Barrie E. Homan, *U.S. Army Research Laboratory.* We are studying counterflow diffusion flames inhibited with several agents via modeling and laser-induced fluorescence of H, O, and OH to understand the fundamental suppression mechanism of iron pentacarbonyl. **(p. 75)**

LMC16 ■ CW diode-pumped tunable Nd^{3+}:KY_3F_{10} laser for environmental sensing, M.A. Dubinskii, K.L. Schepler, *USAF Research Laboratory;* A.K. Naumov, V.V. Semashko, R. Yu. Abdulsabirov, S.L. Korableva, *Kazan State Univ., Russia.* A Nd^{3+}:KY_3F_{10}-based laser is characterized under cw diode end-pumping. Tunability of 1053.6–1059.1 nm aimed at laser applications for HBr contamination tracing as well as satellite-based H_2O and ground-based CO_2 detection was demonstrated. **(p. 78)**

LMC17 ■ Influence of the nonlinear characteristic of the laser source on detected signals in derivative spectroscopy for gas analysis, Miguel A. Morante, José M. López-Higuera, *Univ. Cantabria, Spain;* George Stewart, Brian Culshaw, *Univ. Strathclyde, U.K.* The baseline in signals from derivative spectroscopy caused by nonlinearity of the laser characteristic is derived, and a simple method is presented to extract it in real time. **(p. 81)**

LMC18 ■ Dual-wavelength temperature measurements in an IC engine using 3-pentanone laser-induced fluorescence, S. Einecke, C. Schulz, *Univ. Heidelberg, Germany;* V. Sick, *Univ. Michigan.* The application of a laser-induced fluorescence technique for temperature measurements under high-pressure conditions, i.e., in IC engines, with imaging capabilities is described. **(p. 84)**

LMC19 ■ Instantaneous velocity field measurements of air flows by ozone tagging velocimetry, Lubomir A. Ribarov, Joseph A. Wehrmeyer, Robert W. Pitz, *Vanderbilt Univ.;* Peter A. DeBarber, *MetroLaser Inc.* A narrowband ArF excimer laser creates lines of ozone in an air flow. The displaced ozone lines are detected by a sheet of narrowband KrF excimer light. **(p. 87)**

LMC20 ■ High-resolution hole burning spectroscopy of aluminum phthalocyanine tetrasulfonate in MCF-10F human breast epithelial cells, N. Milanovich, T. Reinot, G.J. Small, John Hayes, *Iowa State Univ.* Hole burning of the photodynamic therapeutic dye, aluminum phthalocyanine tetrasulfonate in human breast cells is reported. Pressure shifts allow measurement of the compressibility in lysosmes. **(p. 90)**

LMC21 ■ Diode-laser absorption measurements of CO_2, H_2O, and N_2O near 2 μm, Douglas Baer, Radu M. Mihalcea, Ronald K. Hanson, *Stanford Univ.* An external-cavity diode laser was used to record absorption measurements of CO_2, H_2O, and N_2O near 2.0 μm. Measured spectroscopic parameters are compared with published values. **(p. 92)**

LMC22 ■ Raman measurements of supersonic hydrogen/air mixing, Dieter Brüggemann, Peter Kasal, Joachim Boltz, Peter Gerlinger, *Univ. Stuttgart, Germany.* Raman spectroscopy was employed to simultaneously determine the distributions of hydrogen, oxygen, nitrogen, and temperature on a line in a supersonic mixing channel. **(p. 95)**

LMC23 ■ High sensitivity detection of molecular oxygen using cavity-enhanced frequency modulation spectroscopy, Livio Gianfrani, R.W. Fox, L. Hollberg, *National Institute of Standards and Technology.* Spectroscopy at 763 nm in a Fabry–Perot cavity is demonstrated by use of frequency modulation techniques. Weak magnetic dipole transitions have been detected in isotopic oxygen (^{16}O–^{18}O) molecules. **(p. 98)**

LMC24 ■ Degenerate four-wave-mixing spectroscopy: multistate resonances and multimode laser effects, Thomas A. Reichardt, William C. Giancola, Robert P. Lucht, *Univ. Illinois.* We investigate theoretically degenerate-level (multistate) resonances and multi-axial-mode laser effects in degenerate four-wave-mixing spectroscopy. **(p. 101)**

LMC25 ■ Polarization spectroscopy: calculation of lineshapes and saturation effects, Thomas A. Reichardt, Robert P. Lucht, *Univ. Illinois.* We analyze saturation, collisional, and Doppler effects in polarization spectroscopy by numerical integration of the time-dependent density matrix equations for a multi-Zeeman-state system. **(p. 104)**

Tuesday
March 10, 1998

Main Lobby
7:00am–6:00pm
Registration/Speaker Check-in

Coral Room

8:00am–10:00am
LTuA ■ Advances in Diode Laser Sources
Alan C. Stanton, *Southwest Sciences Inc., Presider*

8:00am (Invited)
LTuA1 ■ Single-frequency semiconductor diode lasers for gas sensing, Ramon Martinelli, *Sarnoff Corp.* Sarnoff has developed single-frequency, distributed-feedback (DFB) semiconductor diode lasers with emission wavelengths from 760 to 2000 nm. These devices are ideal sources for trace-gas monitoring systems employing laser absorption spectroscopy. After a brief description of DFB laser operating principles, the salient features of these devices are presented. **(p. 108)**

8:30am
LTuA2 ■ Mid-infrared interband cascade lasers with external and internal quantum efficiencies >200%, B.H. Yang, D. Zhang, Rui Q. Yang, C.-H. Lin, Shin-Shem Pei, *Univ. Houston.* External and internal quantum efficiencies exceeding 200% and an average output power >16 mW at 4 μm have been achieved. **(p. 111)**

8:45am
LTuA3 ■ Mid-IR vertical-cavity surface-emitting lasers for chemical sensing, W.W. Bewley, C.L. Felix, I. Vurgaftman, E.H. Aifer, J.R. Meyer, L. Goldberg, *Naval Research Laboratory;* D.H. Chow, E. Selvig, *Hughes Research Laboratory.* The first mid-IR VCSEL ($\lambda = 2.9$ μm) shows promising characteristics for chemical detection applications: narrow linewidth, low cw optical-pumping threshold (4 mW at 80 K), high-efficiency, pulsed operation up to 280 K, and cw operation up to 160 K. **(p. 114)**

9:00am
LTuA4 ■ Mid-infrared laser source for gas sensing based on frequency-converted diode lasers, Douglas J. Bamford, Konstantin Petrov, Andrew T. Ryan, Thomas L. Patterson, Lee Huang, David Hui, Simon J. Field, *Gemfire Corp.* Tunable mid-infrared radiation, produced by difference frequency generation in periodically poled lithium niobate, has been used to detect water vapor, carbon dioxide, and methane. **(p. 117)**

9:15am
LTuA5 ■ Trace gas monitoring with antimonide diode lasers, Daniel B. Oh, Alan C. Stanton, *Southwest Sciences Inc.;* Jean-Christophe Nicolas, *Univ. Montpellier II, France.* Application of antimonide diode lasers operating near room temperature to high sensitivity absorption detection of carbon monoxide, formaldehyde, and methane is described. **(p. 120)**

9:30am
LTuA6 ■ Continuously tunable, single mode, external cavity diode lasers at 2 μm, G.S. Feller, I-Fan Wu, T. Day, *Focused Research Inc.;* R.J. Menna, R.U. Martinelli, J.C. Connolly, *Sarnoff Corp.;* R.M. Mihalcea, D.S. Baer, R.K. Hanson, *Stanford Univ.* We demonstrate tunable, room-temperature, single-longitudinal-mode operation of external cavity diode lasers from 1.870 to 2.060 μm. Laser characteristics and spectroscopic measurements on CO_2 are presented. **(p. 122)**

9:45am
LTuA7 ■ Laser-based absorption sensor for trace gas monitoring in a spacecraft environment, D.G. Lancaster, R.F. Curl, F.K. Tittel, *Rice Univ.;* D. Richter, *Fachhochschule Ostfriesland, Germany;* J.C. Graf, *Lyndon B. Johnson Space Center.* Real-time detection and measurement of sub-ppm levels of trace gases in ambient spacecraft air using a compact, laser-based difference frequency sensor are reported. Using continuous flow sampling, a minimum detectable H_2CO concentration of 30 ppb was measured. **(p. 125)**

Atlantic/Pacific Room
10:00am–10:30am
Coffee Break/Exhibits

Coral Room

10:30am–12:00m
LTuB ■ Surface Spectroscopy and Analysis
Nicholas Winograd, *Pennsylvania State University, Presider*

10:30am (Invited)
LTuB1 ■ Applications of surface nonlinear optical spectroscopy, Y.R. Shen, *Univ. California–Berkeley.* Second-order nonlinear optical spectroscopy provides unique opportunities for studies of surfaces, interfaces, and films. **(p. 130)**

11:00am
LTuB2 ■ Spectroscopic characterization of semiconductor surface impurities by near-field scanning optical microscopy, Wolfgang Schade, David L. Osborn, Jan Preusser, Stephen R. Leone, *Univ. Colorado* and *NIST.* Ultraviolet and infrared near-field photoconductivity is used to study surface impurity sites on a GaAsP photodiode with a spatial resolution of about 200 nm. **(p. 131)**

11:15am
LTuB3 ■ A laser desorption mass spectrometer microprobe for surface mapping of lithium, Grant A. Bickel, Harry M. Adams, *AECL, Canada.* A laser desorption mass spectrometer microprobe has been utilized to map Li distributions in CANDU® nuclear reactor components. Lithium is present in the heat transport system of the reactor and can be used as a tracer of HTS leakage. **(p. 134)**

11:30am
LTuB4 ■ Molecular photoionization and chemical imaging, Kenneth F. Willey, Vasil Vorsa, Nicholas Winograd, *Penn State Univ.* Molecules desorbed from a 100-nm area with a focused ion beam are photoionized using a high-repetition-rate femtosecond laser pulse. **(p. 137)**

11:45am
LTuB5 ■ Laser probe of surface reaction dynamics, Xiaoyang Zhu, *Univ. Minnesota.* State-resolved laser spectroscopy and laser-induced surface reactions are employed to address the multidimensional nature of surface reaction dynamics, e.g., the role of internal motions. **(p. 140)**

12:00m–2:00pm
Lunch Break

Coral Room

2:00pm–3:30pm
LTuC ■ Environmental Applications: 1
Robert P. Lucht, *University of Illinois–Urbana, Presider*

2:00pm (Invited)
LTuC1 ■ Use of a fiber optic-based, laser-induced breakdown spectroscopy (LIBS) probe for *in-situ* determination of metals in soils, Gregory A. Theriault, Stephen H. Lieberman, *Space and Naval Warfare Systems Center;* Scott Bodensteiner, Richard Tripoli, *San Diego State Univ. Foundation.* A Cone Penetrometer-deployed fiber optic probe for the *in-situ* assessment of metal contamination of soil is described. In this talk both system design features and field-testing results will be discussed. **(p. 144)**

2:30pm
LTuC2 ■ Microanalysis of solids by laser ablation with one shot, H.E. Bauer, *Univ. Hohenheim, Germany;* K. Niemax, *Institute of Spectrochemistry and Applied Spectroscopy, Germany.* Complete element analysis of ng-samples ablated by a pulsed laser have been performed applying optical emission spectrometry with an Echelle spectrograph and a gated intensified CCD camera. **(p. 145)**

2:45pm
LTuC3 ■ Single-shot laser-induced breakdown spectroscopy of energetic materials, Edwin D. Lancaster, Robert G. Daniel, Kevin L. McNesby, Andrzej W. Miziolek, *U.S. Army Research Laboratory.* Each LIBS microplasma produces spectrally rich atomic, ionic, and molecular fragment emissions characteristic of the chemical composition of the irradiated sample. This information is evaluated to determine the presence of energetic/explosive materials. **(p. 148)**

3:00pm
LTuC4 ■ A diode-laser-based resonance ionization mass spectrometer for selective ultratrace analysis, K. Wendt, K. Blaum, C. Geppert, P. Müller, W. Nörtershäuser, A. Schmitt, N. Trautmann, B. Wiche, *Univ. Mainz, Germany;* B.A. Bushaw, *Battelle Pacific Northwest Laboratories.* A compact diode-laser-based resonance ionization mass spectrometer for isotope-selective ultratrace determination is presented; measurements include spectroscopy and ^{41}Ca-determination for radiodating, cosmochemistry, and medical investigations. **(p. 151)**

3:15pm
LTuC5 ■ Isotope-selective analysis by diode laser spectrometry, Hans-Dieter Wizemann, *Univ. Hohenheim, Germany;* Kay Niemax, *Institute of Spectrochemistry and Applied Spectroscopy, Germany.* Single-mode laser diodes are used for isotope-selective Doppler-limited and Doppler-free element analysis using a low pressure graphite furnace atomizer. **(p. 154)**

Atlantic/Pacific Room
3:30pm–4:00pm
Refreshment Break/Exhibits

Coral Room

4:00pm–5:30pm

LTuD ■ Environmental Applications: 2

Jay B. Jeffries, *SRI International Inc., Presider*

4:00pm

LTuD1 ■ Feasibility study of on-line detection of sulphuric acid aerosols in the atmosphere by laser photofragmentation and plasma spectroscopy, M. Hidalgo Nuñez, P. Cavalli, G.A. Petrucci, N. Omenetto, *Joint Research Centre, Italy.* Sulphuric acid aerosols are measured on-line in air indirectly by laser photofragmentation of sodium hydroxide aerosols and directly by laser spark emission of atomic sulphur. **(p. 158)**

4:15pm

LTuD2 ■ Application of LIBS to monitor compositions for plant control, Yoshihiro Deguchi, Seiji Iwasaki, Naohiko Ishibashi, *Mitsubishi Heavy Industries Ltd., Japan.* LIBS has been applied to fly ash, alkali metals, and cement raw material composition measurements. The automated LIBS unit was tested in the cement plant field. **(p. 161)**

4:30pm

LTuD3 ■ Toxic multi-metal continuous emission monitoring by laser-induced breakdown spectroscopy, Hansheng Zhang, Fang-Yu Yueh, Jagdish P. Singh, *Mississippi State Univ.* Laser-induced breakdown spectroscopy has been used to monitor the concentration of toxic metals in the off-gas emission of an USEPA test facility at Raleigh, North Carolina, during a performance test of multi-metal continuous emissions monitors. **(p. 164)**

4:45pm

LTuD4 ■ Real-time, *in situ* measurement of aerosol light absorption with a new photoacoustic instrument: quantification of black and elemental carbon aerosol, Hans Moosmüller, W. Patrick Arnott, C. Fred Rogers, *Desert Research Institute.* A novel photoacoustic instrument with a light absorption detection limit of 0.4 Mm^{-1} is described. Field intercomparisons with black and elemental carbon measurements are discussed. **(p. 167)**

5:00pm

LTuD5 ■ *In situ* sensing of atmospheric trace gases using airborne near-IR diode laser sensors, David M. Sonnenfroh, William J. Kessler, Mark G. Allen, *Physical Sciences Inc.;* John Barrick, *NASA Langley Research Center.* Diode laser sensors are being designed and tested for *in-situ* measurements of atmospheric species such as H_2O, CO_2, and CH_4 from aircraft using external probes. **(p. 170)**

5:15pm

LTuD6 ■ Intracavity laser spectral analysis of trace elements in environmental samples, V.S. Burakov, P.Ya. Misakov, S.N. Raikov, *National Academy of Sciences of Belarus.* An intracavity laser spectrometer equipped with appropriate atomizers and samplers for direct trace element analyses of liquid, gaseous, and solid samples is proposed and described in detail. **(p. 173)**

■ Wednesday
■ March 11, 1998

Main Lobby
7:30am–6:00pm
Registration/Speaker Check-in

Coral Room

8:00am–10:00am
LWA ■ Laser Diagnostics for Combustion Analysis
Dieter Brüeggemann, *University of Stuttgart, Germany, Presider*

8:00am (Invited)
LWA1 ■ Diagnostics and sensors for turbine engines, J.M. Seitzman, R.T. Wainner, R. Tamma, *Georgia Institute of Technology.* We describe laser-induced incandescence measurements of soot for combustors and engine exhausts, and development of absorption sensors for monitoring temperatures in high pressure combustor exhausts. **(p. 178)**

8:30am
LWA2 ■ Cavity ringdown calibration of laser-induced incandescence, Randy L. Vander Wal, *Nyma, Inc.;* Thomas M. Ticich, *Centenary College of Louisiana.* Using cavity-ringdown, quantification of laser-induced incandescence for parts-per-billion soot volume fraction levels is demonstrated in a laminar methane/air diffusion flame. **(p. 181)**

8:45am
LWA3 ■ Vapor/liquid mass fraction measurements by linear Raman spectroscopy, Dieter Brüggemann, Bernd Mewes, Gerd Bauer, *Univ. Stuttgart, Germany.* Linear Raman spectroscopy has been used to discriminate between the vapor and liquid phase of methanol. Mass fractions across an evaporating droplet stream are measured. **(p. 184)**

9:00am
LWA4 ■ Simultaneous laser-induced fluorescence and Rayleigh scattering measurements for precise determination of flame structure, Jay B. Jeffries, Norbert Heberle, Gregory P. Smith, David R. Crosley, *SRI International.* The spatial locations of CH and OH radicals are precisely determined with respect to the temperature gradients in a partially premixed flame by simultaneous LIF and Rayleigh scattering. **(p. 187)**

9:15am
LWA5 ■ Evaluation of 2-line laser-induced atomic fluorescence for two-dimensional thermometry in practical combustion applications, C.F. Kaminski, J. Engström, *Lund Institute of Technology, Sweden.* Two-line planar laser-induced fluorescence thermometry using atomic indium is demonstrated in flames, and the first application of the technique in automotive engines is reported. **(p. 190)**

9:30am
LWA6 ■ Measurement of fluorescence of formaldehyde in atmospheric pressure flame, Susumu Yamagishi, *Ship Research Institute, Ministry of Transport, Japan.* The quantum efficiency of the fluorescence of formaldehyde excited by YAG(THG) laser under atmospheric pressure was measured and the noise level was evaluated by statistical method. **(p. 193)**

9:45am
LWA7 ■ Theoretical investigation of phase matching schemes for degenerate four-wave mixing spectroscopy, Thomas A. Reichardt, Robert P. Lucht, *Univ. Illinois.* We compare the phase-conjugate geometry and forward phase-matched geometry in degenerate four-wave-mixing spectroscopy by numerical integration of the density matrix equations. **(p. 196)**

Atlantic/Pacific Room
10:00am–10:30am
Coffee Break

Coral Room

10:30am–11:30am
LWB ■ Diode-Laser Sensors for Combustion Monitoring
Kay Niemax, *Institute of Spectrochemistry and Applied Spectroscopy, Germany, Presider*

10:30am
LWB1 ■ Diode-laser sensor system for combustion monitoring, Douglas Baer, Radu M. Mihalcea, Ronald K. Hanson, *Stanford Univ.* A 2.0-μm diode-laser sensor system was applied for real-time measurements of gas temperature and concentrations of CO_2 and H_2O in a methane/air combustion system. **(p. 200)**

10:45am

LWB2 ■ Near-infrared tunable diode laser diagnostics in laboratory and real-scale inhibited flames, Kevin L. McNesby, R. Reed Skaggs, Andrzej W. Miziolek, Robert G. Daniel, *U.S. Army Research Laboratory;* Craig S. Miser, *U.S. Army Aberdeen Test Center.* Near-infrared tunable diode lasers are used to measure fuels, oxidizers, and combustion products during suppression of laboratory and real-scale flames by Halon 1301 (CF_3Br) and FM-200 (C_3F_7H). **(p. 203)**

11:00am

LWB3 ■ *In situ* oxygen-monitoring using near-infrared diode lasers and wavelength modulation spectroscopy, V. Ebert, K.-U. Pleban, J. Wolfrum, *Univ. Heidelberg, Germany.* We describe a new approach to the use of wavelength modulation spectroscopy for *in situ* applications by utilizing the 1f signal for a transmission correction of the 2f signal. **(p. 206)**

11:15am

LWB4 ■ *In situ* measurements of combustion species using near-IR diode laser sensors, Mark G. Allen, Bernard L. Upschulte, David M. Sonnenfroh, *Physical Sciences Inc.* Novel diode laser architectures are used to make *in situ* measurements of combustion species such as CO, CO_2, OH, NO, H_2O, as well as temperature in laboratory flames. **(p. 209)**

11:30am–11:45am

Closing Remarks

Laser Applications to Chemical and Environmental Analysis

Ultrasensitive Detection for Biochemical Applications

Monday, March 9, 1998

Edward S. Yeung, Iowa State University
Markus Sauer, University of Heidelberg, Germany
Presiders

LMA
8:00am–10:00am
Coral Room

Large-scale chemical analysis by laser-induced fluorescence detection and multiple capillary electrophoresis separation

Norman J. Dovichi, JianZhong Zhang, Sue Bay, John Crabtree, and Pieter Roos
Department of Chemistry, University of Alberta, Edmonton Alberta CANADA T6G 2G2
Voice - 403-492-2845
FAX - 403-492-8231
e-mail norm.dovichi@ualberta.ca

Capillary electrophoresis provides rapid separation of long DNA sequencing fragments. However, it is necessary to operate many capillaries in parallel to compete with slab-gel electrophoresis systems. A number of capillary array instruments have been reported based on a scanning optical detector; these systems suffer from a low detection duty cycle.

To eliminate the severe duty cycle penalty paid by the use of a scanning detector system, several systems have been built with detector arrays. In these systems, one detector, or detector element in a camera, continuously monitors fluorescence from each capillary. Because each capillary is continuously monitored, there is no penalty in duty cycle. In our smaller-scale systems, a laser beam illuminates analyte migrating from a linear array of capillaries in a sheath flow cuvette. Two laser beams are used to excite fluorescence from DNA sequencing fragments prepared with Applied Biosystem's dye labeled primers or dye-labeled dideoxynucleotides. Fluorescence is collected at right angles with a microscope objective, which provides a high efficiency image of the fluorescent analyte. In this system, fluorescence is imaged onto a set of fiber optics, with one fiber per capillary. The image size from the capillary is about 1-mm in diameter, which is larger than the core of the optical fiber. A 1-mm diameter GRIN lens is used to collect the fluorescence and couple it with the optical fibers. A filter wheel is used to resolve fluorescence into four spectral bands. The filter wheel is synchronized with a sector wheel so that fluorescence is monitored in the appropriate spectral band for each laser wavelength. Fluorescence is detected with avalanche photodiodes. These solid state devices, from EG&G Canada, have high quantum efficiency and are extremely rugged.

The heart of our technology is an advanced sheath-flow cuvette. The capillaries fit as a linear array within a rectangular glass chamber. The depth of the flow chamber matches the outer diameter of the capillaries while the width matches the width of the array of capillaries. Sheath fluid is pumped through the interstitial space between the capillaries. As DNA fragments migrate from the capillary tips, they are entrained within the sheath fluid, forming distinct streams within the cuvette. The laser beam passes through the cuvette, below the capillary tips. Because the beam passes through the sheath fluid, rather than the capillaries, its passage is unimpeded by any curved glass surface, which would act to deflect or defocus the beam. Because the DNA concentration is very small and the stream diameter is very narrow, there is very little loss in the beam intensity while traversing each sample stream.

The total number of capillaries that can be used a linear array is limited by two optical properties of the system. First, width of the array should not be larger than the size of the photodetector. It is a fundamental law of optics that a demagnifying optical system

can not efficiently collect fluorescence. If the capillary array is larger than the photodetector array, then the collection optics inherently are inefficient. For example, a 1-cm^2 CCD camera can be used with at most 67 capillaries of 150-μm outer diameter in a unit magnification optical system before significant optical losses are generated in the system.

Of course, discrete photodetectors can be used over a larger area. A second optical property limits the number of capillaries that can be used efficiently. In general, the laser beam spot-size should be relatively uniform across the array. If the beam is much larger or smaller than the size of the same stream, then analyte molecules will be inefficiently excited. Unfortunately, diffraction prevents collimation of a laser beam over a large distance. At best, the beam will remain roughly collimated over a distance given by twice the Rayleigh length about the beam focus. The more tightly focused the beam, the shorter the Rayleigh distance. If the beam size at the focus is matched to the sample stream radius (~25-μm), then the Rayleigh length for an argon ion laser beam is about 4-mm. The beam will remain collimated over about 50 capillaries before diffraction causes the beam to become significantly larger than the sample stream.

In any event, optics limit the efficient excitation and collection of light from an array of 50 to 75 capillaries, and only if the capillaries are closely packed and 150-μm outer diameter. Linear arrays of this size are useful instruments for medium-scale sequencing projects that require a sample throughput that is a few times larger than current commercial slab-gel instruments. A completely different optical design is required for larger scale sequencing.

We have developed several designs for very large scale capillary arrays. In one instrument, a two-dimensional array of capillaries is inserted into a square flow chamber. In this instrument, the sheath flow is directed upwards to efficiently sweep bubbles from the chamber. Several rows of capillaries are inserted into the flow chamber and these rows are offset to form a staircase. Sheath fluid is pumped in the interstitial space between capillaries, drawing the DNA fragments as discreet streams, one stream from each capillary.

To ensure that each row of capillaries is illuminated, an elliptically-shaped laser beam forms a line-focus slightly downstream from the capillary tips. The laser beam generates a two-dimensional set of fluorescent spots, one spot down-stream from each capillary. Fluorescence is collected from the side by a high efficiency optical condenser that generates a unit magnification image on a CCD camera. To avoid overlap of the spots, the rows of capillaries are offset, so that the last row of capillaries is furthest down-stream. When imaged from the side, each illuminated sample stream forms a discreet spot at the image plane. However, the first row of capillaries is imaged through a very small thickness of sheath fluid, while the last row is imaged through the entire thickness of the fluid. To equalize the optical paths, an aberration-correction prism can be inserted in the optical train so that the optical distance is equal for all rows of capillaries.

A 32 X 32 array of capillaries terminates in a 4.8 X 4.8 mm array. This array of 1,024 capillaries may be imaged efficiently onto a 1-cm^2 CCD camera. Fluorescence is spectrally resolved by use of a rotating filter wheel. If necessary, the system could be expanded to a 64 X 64 array of capillaries for the simultaneous determination of sequence from 4,096 clones.

We have constructed 25 and 96 capillary instruments, a 576 capillary device is under construction and a 1,024 capillary system is in design. The 576 capillary instrument mates with 6 microtiter plates. The instruments have an interesting property: after the system is designed for a single capillary, the incremental cost of an additional capillary is simply the cost of the capillary itself. A 1,024 capillary instrument costs about $2,000 more to construct than a single capillary device. A 30-cm long capillary draws 2-μA of current when operated at an electric field of 200 V cm^{-1} (V = 6 kV). An array of 1,024 capillaries draws 2 mA of current; 10 W of power will be dissipated in the capillaries. A single 30-W power supply easily can operate all the capillaries simultaneously. Our major limitation in the design and construction of the largest scale systems is simply the cost of DNA fragments to evaluate the system!

The throughput of these large scale systems is much larger than that of the present generation of sequencers. We have demonstrated 1,000 base separations in 135 minutes with our current generation sequencers. If we are conservative and anticipate 600 bases of raw sequence per capillary in a two hour separation, then one run of the 576 capillary instrument will generate 345,000 bases of raw sequence. Assuming a one-hour period is required to replace the separation medium and prepare the capillary for a subsequent run, then eight runs can be performed per day, generating 2.7 Mbase of raw sequence. At 7-fold redundancy, this throughput corresponds to 400,000 bases of finished sequence per day per instrument. Throughput for a 1,024 or 4,096 capillary device is proportionally higher. Of course, sample preparation technology will be severely stressed to support the largest-scale instruments.

Cell Imaging by Laser-Induced Native Fluorescence Microscopy

Edward S. Yeung*, Wei Tong and Sheri Lillard†

Ames Laboratory-USDOE and Department of Chemistry
Iowa State University, Ames, IA 50011
Phone 515-294-8062, FAX 515-294-0266

†Department of Chemistry
Stanford University, Stanford, CA 94305-5080

The high degree of heterogeneity of the nervous and endocrine systems makes it extremely important for real-time monitoring of dynamic chemical changes at the single-cell level to gain a better understanding of the interaction of cells with their environment. Secretion mediated by exocytosis is one of the fundamental phenomena whose mechanism mimics the release of neurotransmitters at synaptic sites. Although the regulation of the secretory pathway has been studied extensively, its molecular mechanism is still not clear. It is important to develop methods that can follow real-time secretory processes with both high temporal and high spatial resolution. The native fluorescence of some proteins and neurotransmitters excited by a deep-UV laser has been shown to be a powerful probe for single-cell analysis. The advantages of direct native fluorescence detection include: (1) no chemical derivatization with fluorescent dyes is needed so no contamination or additional background will be introduced; (2) uncertainties about the efficiencies of the derivatization reaction are eliminated to ensure fast and quantitative response, without influences from slow reaction kinetics or incomplete equilibrium; and (3) the biological integrity of the cells will not be unnecessarily disturbed by having additional reagents or from exposure to artificial environments. We report the coupling of laser-induced native fluorescence detection with capillary electrophoresis (CE) to quantitatively monitor the secretion of insulin, serotonin and catecholamines from single cells. The uptake of serotonin by single living astrocytes was also recorded by native fluorescence imaging microscopy. The catecholamine (mainly epinephrine and norepinephrine) secreting adrenal chromaffin cells have been used as "model nerve terminals" to elucidate the molecular mechanism of neurotransmitter secretion at the nerve terminal. The *in vitro* dynamics of catecholamine release from bovine adrenal chromaffin cells was monitored with both high spatial and high temporal resolution.

A conventional upright laboratory microscope was used for imaging. To facilitate transmission of the deep-UV fluorescence, the original glass tube lens of the microscope was replaced with a quartz lens and the extra glass optics inside the microscope was removed. An intensified CCD (ICCD) camera was mounted on the top port of the microscope with a home-made adapter. The power of the 275-nm line actually irradiating the cell was only about 1 mW. The angle of incidence was approximately 30°. The native fluorescence was collected through a 40× quartz microscope objective (N.A. = 0.65) and passed through a WG-305 filter and a UG-1 filter before hitting the ICCD camera.

2 μL of cell suspension was placed on the cover slide and the cells were allowed to adhere. The other cover slide was then mounted and the flow cell was filled with physiological buffer solution (PBS) through one of the inlets. The flow cell was flipped over carefully and taped onto the

sample stage of the microscope to avoid movement during the experiment. Acetylcholine (ACh) (5×10^{-4} M in PBS) was then pumped through the other inlet to stimulate cell secretion. The secretory process of the chromaffin cells was monitored by taking a sequence of "movies" with the ICCD camera. The exposure time for each frame was 150 ms. This allowed us to determine the release of catecholamine as a function of time based on the change in fluorescence intensity. Background variations due to the changes in laser intensity and light collection for each cell sample were normalized by dividing each data set by the background intensity (non-cell region) in the corresponding images.

It is known that the adrenal chromaffin granules contain several proteins. Both the catecholamines and the SDS lysates of adrenal chromaffin cells in PBS exhibit fluorescence maxima at about 310 nm. No substantial amount of fluorescence is observed in the vicinity of 350 nm for the cell lysate. This indicates that the proteins in chromaffin cells either do not fluoresce substantially or the amounts of proteins are so low that their fluorescence (at least by tryptopan residuals) is negligible. In addition, here we are looking at a time-dependent fluorescence change. Contributions from stray light and fluorescence from the background matrix, cell membrane, and cell nuclei are canceled out in the process. For these reasons, we can interpret the decrease of the fluorescence intensities as being due to the release of catecholamines and the co-release of some granular proteins. However, since the fluorescence spectra of NE and E are so similar (data not shown), it is not possible to distinguish between the release of NE vs. E.

Figure 1 shows some selected images for adrenal chromaffin cells when stimulated with ACh. The first image is the normal transmission optical image before stimulation and the sixth image is the transmission optical image after the experiment. The location, size and shape of each cell did not change dramatically. After the laser experiment, the cells were still viable and were not stained by trypan blue. The second to fourth images correspond to the first, 24th, 48th and 72nd frame after stimulation with ACh. The frame rate of the image sequence is 8.8 s/frame. The interval could have been much shorter, but the release process under study was relatively slow.

Quantitative profiles of the release process could be obtained by integrating the background-corrected fluorescence intensities of each cell in each frame, and then plotting these against time. The slope of the profiles reflect the rate of release at that particular time. As expected, there are large variations in the catecholamine content as well as the secretion kinetics among different cells. Generally, the rate of release is faster at the early stages of stimulation and slows down or even stops later on. This is in agreement with our results from dynamic release experiments in CE. Bulk release experiments with many cells have shown the same trend with time. A plot of the average of 31 cells also shows the same trend. This can be explained by desensitization of receptors and channels and the rapid termination of the intracellular Ca^{2+} signal. The large error bars are not due to experimental errors. They reflect actual variations among individual cells. There are also relatively large variations during the first minute, reflecting the large asynchronous release behavior at the early stages of stimulation. Amperometric detection with small diameter microelectrodes have revealed that release sites with different activities are spatially localized on endocrine cells in culture. We also observed similar phenomena for mast cells.

To further prove the decrease of the UV fluorescence intensities of the cells is not due to the bleaching of catecholamines by laser exposure, we also did control experiments with catecholamine solutions and chromaffin cells without ACh stimulation. Neither the catecholamine solution (1.25×10^{-3} M, NE/E = 1/4) nor the cells were bleached during laser exposure at the levels used in this study. It is interesting to note that release here and in astrocytes is reflected by a *decrease* in fluorescence intensity, while release in mast cells causes an *increase* in fluorescence intensity. This

is because serotonin in mast cell granules is so densely packed that fluorescence quenching is the dominant relaxation process. Only when the granules are dissolved in the surrounding fluid will the native fluorescence of serotonin be observable.

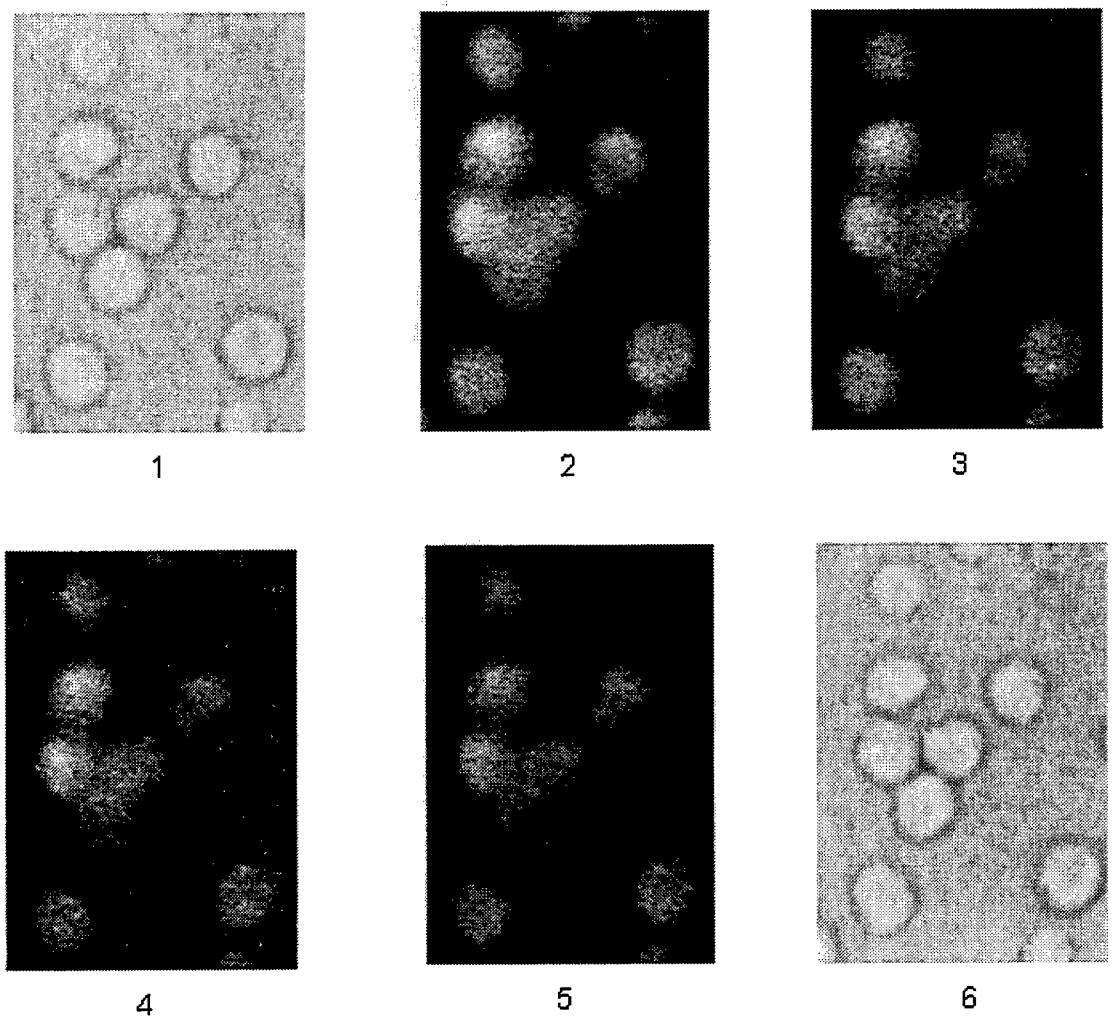

Figure 1. Images of bovine adrenal chromaffin cells at different stages after stimulation. (1) transmission optical image of the cells before stimulation; (2) UV fluorescence image of the cells at the point of stimulation (0 s); (3)-(5) UV fluorescence images of the cells at 211.2, 422.4 and 633.6 s after stimulation (i.e., the 24th, 48th and 72nd frames); and (6) transmission optical image of the cells after release and laser exposure.

Detection of Single Molecules in Microcavities

N. Lermer, M. D. Barnes, C-Y. Kung , W. B. Whitten, J. M. Ramsey

Chemical and Analytical Sciences Division, Oak Ridge National Laboratory

Oak Ridge, Tennessee 37831-614

Phone: 423-576-1870

Fax: 423-574-8363

e-mail:Q24@ornl.gov

A significant limitation in the detection and spectroscopy of individual dye molecules in liquid room temperature samples is the loss of fluorescence signal through chromophore photobleaching. Although often considered a fundamental restriction on sensitivity, it has been shown that the probability per excitation cycle of photobleaching may be reduced by enhancing the spontaneous emission rate of the chromophore located inside a microdroplet, which acts as a optical cavity. Studies of glycerol microdroplets containing R6G dye molecules, and levitated in a three-dimensional electrodynamic trap, have demonstrated a significant enhancement of both the fluorescence decay rate [1] and the total fluorescence yield [2] of the chromophore. Modification of the emission rate is greatest for molecules located near the surface of small (< 10 μm) microdroplets, where the influence of the droplet cavity modes of the droplet is most significant. To exploit this surface sensitivity, surfactant forms of rhodamine dyes were recently studied [3]. Fluorescence emission of the dye molecules, constrained to the droplet surface and with fixed transition moments perpendicular to the surface normal, were shown to be significantly enhanced at small droplet sizes. Additionally, at larger droplet sizes corresponding to higher droplet Q's, preferential emission into the cavity modes was observed, however the detection of fluorescence photons was delayed by the storage time of the cavity, which may be on the same order as the fluorescence lifetime. These measurements, performed on relatively concentrated dye solutions, suggest that microcavity effects may be exploited to greatly

enhance single molecule detection sensitivity in glycerol microdroplets. Furthermore, the large cavity storage time of the high-Q droplets opens the possibility for re-excitation of the molecule following emission into the droplet resonance, and subsequent stimulated emission, that is, single-molecule lasing.

The onset of single-molecule lasing in microdroplets may be identified by a change in the photocount distribution (ie. an increase in the average number of emitted photons) as a function of incident laser power. As the precise determination of photocount statistics for ultradilute solutions requires measurements of many thousands of droplets (with many droplets containing no dye molecules), the inherently low droplet throughput rate of the levitated microdroplet approach is problematic. This shortcoming has been resolved with the recent development of a linear quadrupole system that provides single-molecule measurement sensitivity for falling streams of microdroplets at throughput rates approximately three orders of magnitude greater than the levitated approach [4]. Shown in figure 1 are the photocounts for a 500-droplet subset of measurements obtained with the linear quadrupole systems at a throughput rate of approximately 1 Hz. The droplets were generated from a 1.6 fM Rhodamine B solution, and were ~8.5 microns at the point of interrogation. A histogram of the photocount distribution is shown in figure 2, exhibiting a Gaussian distribution corresponding to blank droplets, and approximately exponential distribution of Rb photocounts. The high-sensitivity and high throughput of the linear-quadrupole microdroplet system is particularly well suited for the investigation of cavity enhancement and single molecule stimulated emission in microdroplets [5]. Studies of these phenomena are in progress.

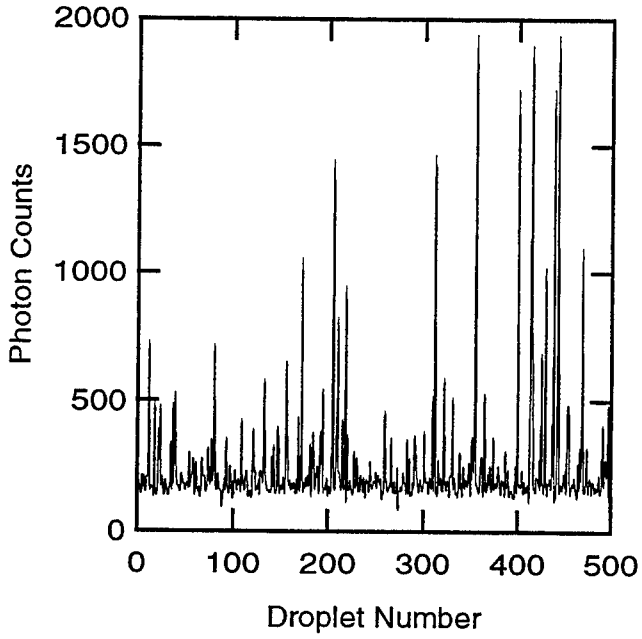

Figure 1: Photocounts for 500 droplets of a 1.6 fM Rb solution

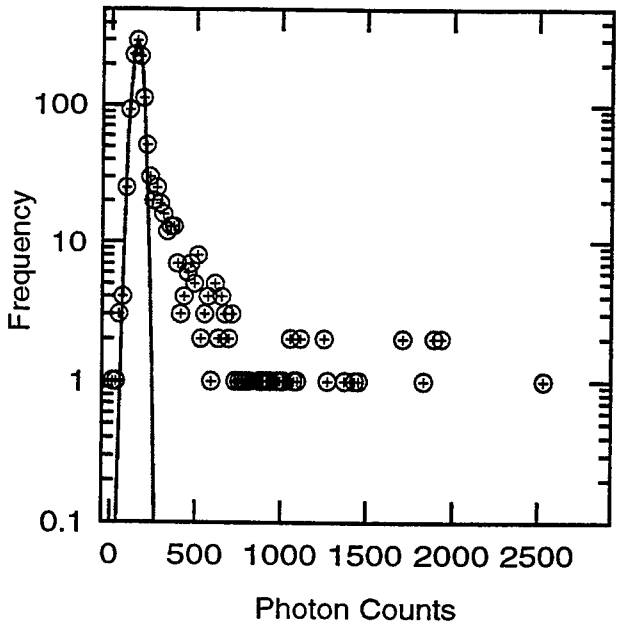

Figure 2: Histogram of photocounts for 1.6 fM Rb solution. The solid line is a Gaussian fit approximating the blank background distribution.

[1] M. D. Barnes, W. B. Whitten, S. Arnold, J. M. Ramsey, J. Chem. Phys. **97**, 7842 (1992).
[2] M. D. Barnes, W. B. Whitten, J. M. Ramsey, J. Opt. Soc. Am. B **11**, 1297 (1994)
[3] M. D. Barnes, C.-Y. Kung, W. B. Whitten, J. M. Ramsey, S. Arnold, S. Holler, Phys. Rev. Lett. **76**, 3931 (1996).
[4] N. Lermer, M. D. Barnes, C.-Y. Kung, W. B. Whitten, J. M. Ramsey, Anal. Chem. **69**, 2115 (1997)
[5] M. D. Barnes, N. Lermer, C.-Y. Kung, W. B. Whitten, J. M. Ramsey, S. C. Hill, Opt. Lett. **22**, 1265 (1997)

Confinement, Detection, and Manipulation of Individual Molecules in Attoliter Volumes

C-Y. Kung, M. D. Barnes, N. Lermer,
W. B. Whitten, and J. M. Ramsey

Chemical and Analytical Sciences Division
Oak Ridge National Laboratory
P. O. Box 2008,
Oak Ridge, Tennessee 37831-6142
Phone (423)576-1870
Fax (423)574-8363
Email kungc@ornl.gov

We report observation of fluorescence from individual rhodamine 6G molecules in streams of charged 1-μm diameter water droplets. With this approach, probe volumes comparable to diffraction-limited fluorescence microscopy[1] techniques (≤ 500 attoliters) are achieved, resulting in similarly high contrast between single molecule fluorescence signals and nonfluorescent background. However, since the fluorescent molecules are confined to electrically charged droplets, *in situ* electrodynamic manipulation can be accomplished in a straightforward manner, allowing experimental control over both the delivery of molecules of interest to the observation region and the laser-molecule interaction time.

While our previous work emphasized on single-molecule fluorescence detection in glycerol droplets levitated in an electrodynamic trap,[2,3] or focused in a linear quadrupole,[4] many applications of single-molecule probes relevant to the biotechnology community demand the ability to detect fluorescent molecules in aqueous solution. However, the nearly two-order of magnitude reduction in photostability of rhodamine dyes in water relative to ethanolic solvents places much more stringent demands on droplet production and single-molecule detection.

In the experiments illustrated in Figure 1, streams of water droplets were produced with a piezoelectric droplet generator specifically designed and built in our laboratory for on-demand production of small (< 5 μm diameter) droplets. Solvent evaporation rapidly (≈ 50 msec) reduced the droplet diameter to less than 1 μm. Droplets were illuminated 2 - 3 mm below the tip orifice, using a needle with a small DC bias (≈ 0.5 Volts) to guide the slightly charged droplets through the waist of a focused low power cw Ar^+ laser (150 mW, 25 μm waist diameter). Fluorescence from each droplet was detected with a cooled GaAs photomultiplier tube and gated photon counter.

We show that droplets of solution containing individual molecules can be actively delivered to a desired target. Moreover, the fluorescent molecules being probed cannot diffuse out of the droplet volume.[5] Detection of individual rhodamine 6G molecules in extremely diluted (< 30 fM) aqueous solution has been achieved in real-time, as shown in Figure 2.

Further work of employing orthogonal electrostatic, aerodynamic and photophoretic forces to manipulate droplet trajectory is currently being carried out. Preliminary experimental results and potential applications of fluorescence-triggered single-molecule sorting will be discussed.

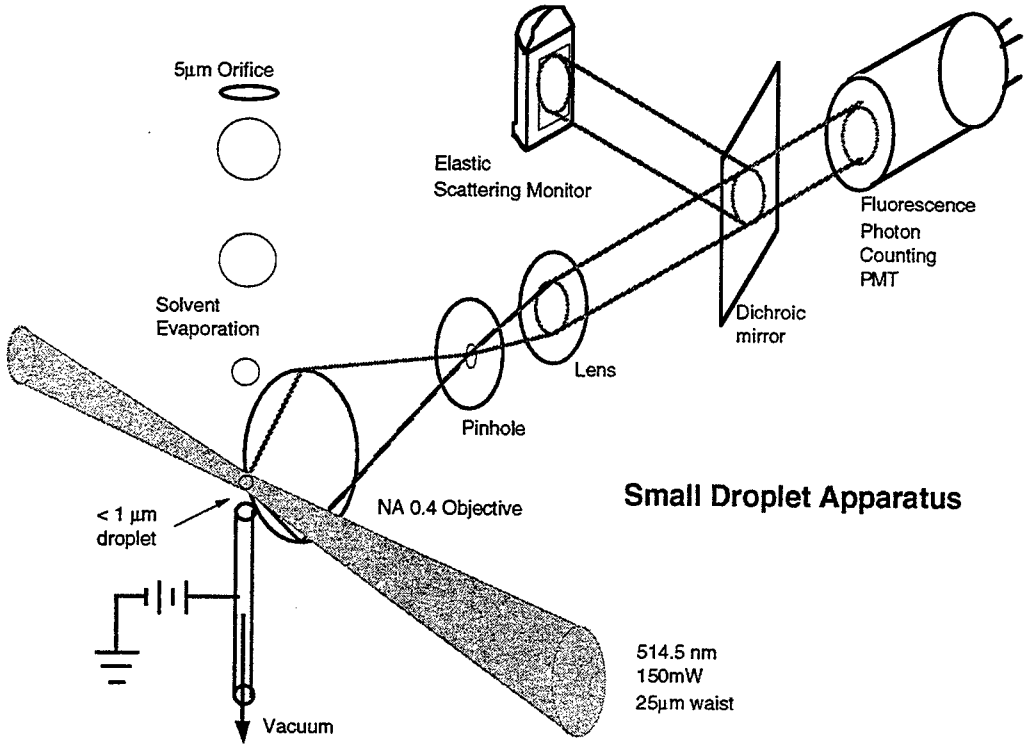

Figure 1. Schematics of small-droplet single-molecule fluorescence detection experiment.

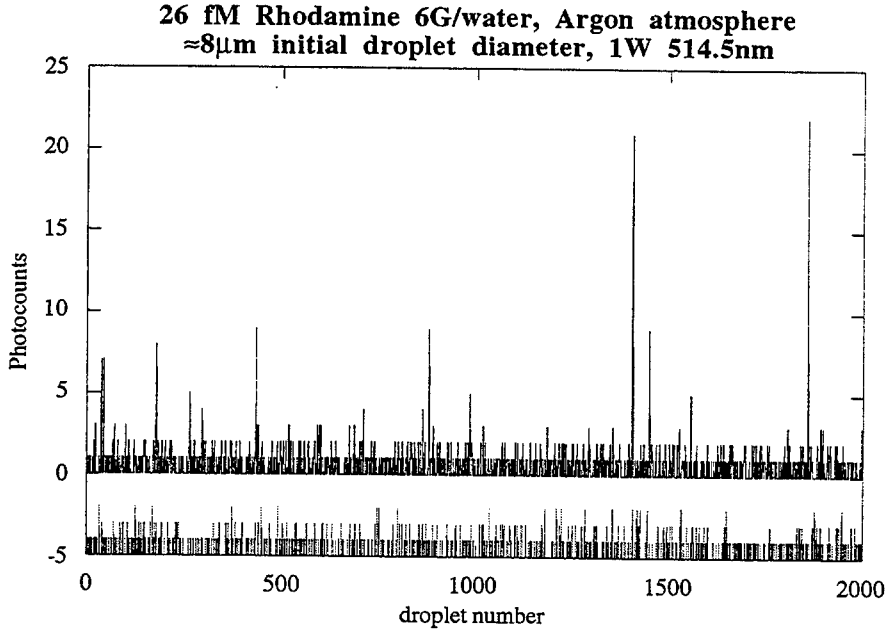

Figure 2. Raw real-time fluorescence photon bursts from rhodamine 6G.

[1] D. T. Chiu, and R. N. Zare, J. Am. Chem. Soc. **118**, 6512 (1996).

[2] M. D. Barnes, K. C. Ng, W. B. Whitten, and J. M. Ramsey, *Anal. Chem.*, **65**, 2360 (1993).

[3] M. D. Barnes, C-Y. Kung, W. B. Whitten, J. M. Ramsey, S. Arnold, and S. Holler, *Phys. Rev. Lett.*, **76**, 3931 (1996).

[4] N. Lermer, M. D. Barnes, C-Y. Kung, W. B. Whitten, and J. M. Ramsey, *Anal. Chem.* **69**, 2115 (1997).

[5] C-Y. Kung, M. D. Barnes, N. Lermer, W. B. Whitten, and J. M. Ramsey, submitted *to Analytical chemistry*, October 1997.

How many labeled mononucleotide molecules can be identified in water on the single-molecule level

M. Sauer[1*], J. Arden-Jacob[2], K. H. Drexhage[2], F. Göbel[1],
U. Lieberwirth[1], C. Zander[1,2], J. Wolfrum[1]

[1]Physikalisch-Chemisches Institut, Universität Heidelberg, Im Neuenheimer Feld 253, 69120 Heidelberg, Germany

[2]Institut für Physikalische Chemie, Universität-Gesamthochschule Siegen, Adolf-Reichwein-Straße 3, 57068 Siegen, Germany

[*]corresponding author (e-mail: sauer@sun0.urz.uni-heidelberg.de; Phone: 49-6221-548460; Fax: 49-6221-544255)

1. Introduction

One of the most popular application of the single-molecule detection (SMD) technique is fast DNA sequencing on the single-molecule level as proposed by Keller and coworkers.[1,2] The principle idea of this very elegant method involves the incorporation of fluorescently labeled mononucleotides in a growing DNA strand, attachment of a single labeled DNA to a support (generally latex beads), movement of the supported DNA into a flowing sample stream, microchannel or microcapillary[3] and detection of the analyte molecules as they are cleaved from the DNA strand by an exonuclease. The DNA sequence is determined by the order in which differently labeled nucleotides are detected and identified. Although a lot of problems are associated with the enzymatic incorporation of labeled mononucleotides and the selective handling of a single DNA strand different detection and identification strategies have been developed. However, up to now, only two different dyes have been successfully identified on the single-molecule level in aqueous solution due to their different fluorescence lifetimes.[4,5] Hence, the critical question in DNA sequencing on the single strand is how many labels can be identified on the single-molecule level in aqueous solvent systems.

2. Experimental

The fluorescent mononucleotides Cy5-dCTP (carbocyanine dye), MR121-dUTP (oxazine dye), Bodipy-dUTP (bodipy dye), and JA53-dUTP (rhodamine dye) were synthesized from Boehringer Mannheim GmbH (Werk Penzberg, Germany). Reversed-phase HPLC with a gradient of 0-75% acetonitrile in 0.1 M aqueous triethyl ammonium acetate (TEAA) was used for the purification of the labeled mononucleotides. All measurements were carried out in pure water. Details of the experimental setup are described elsewhere.[3,5] A pulsed diode laser (640 nm) served as the excitation source. The pulsing of the diode was performed by a self-matched tunable pulse generator. The system provided pulses of less than 400 ps (FWHM) duration with a repetition rate of 56 MHz. Measurements were done with an average excitation power of 630 µW at the sample. An avalanche photodiode served as the detector behind a 100 µm pinhole. For time-resolved measurements we used a TCSPC PC-interface card (SPC-330). With this card the signal was collected in 100 histograms with an integration time of 625 µs. The instrument response function of the entire system was measured to be 420 ps (FWHM). Measurements were performed in microscope slides with a small depression covered by a cover glass. The fluorescence lifetime determination of single-molecule events was realized by a maximum likelihood estimator (MLE).[6]

3. Results and discussion

Table 1 shows the spectroscopic characteristics of the labeled mononucleotide molecules Cy5-dCTP, MR121-dUTP, Bodipy-dUTP, and JA53-dUTP in water. Due to their similar absorption and emission maxima but unequivocal fluorescence lifetimes they are ideally suited for time-resolved single-molecule identification using pulsed diode laser excitation at 640 nm.

	λ_{abs} [nm]	λ_{em} [nm]	τ_{bulk} [ns]	τ_{MLE} [ns]	σ_{exp} [ns]
Cy5-dCTP	651	670	1.04	1.05	0.22
MR121-dUTP	668	682	2.10	2.07	0.37
Bodipy-dUTP	633	650	3.87	3.88	1.25
JA53-dUTP	652	673	2.21	2.24	0.43

Table 1. Spectroscopic characteristics of the conjugates in water. The fluorescence lifetime τ_{bulk} of bulk solutions (10^{-6} M) were measured with the SMD apparatus. The lifetimes τ_{MLE} for single-molecule events were calculated with the MLE. The standard deviation σ_{exp} is derived from the distribution of the lifetimes τ_{MLE}. Only those single-molecule events with a minimum of 30 collected photons were used for the calculation of the fluorescence lifetimes τ_{MLE}.

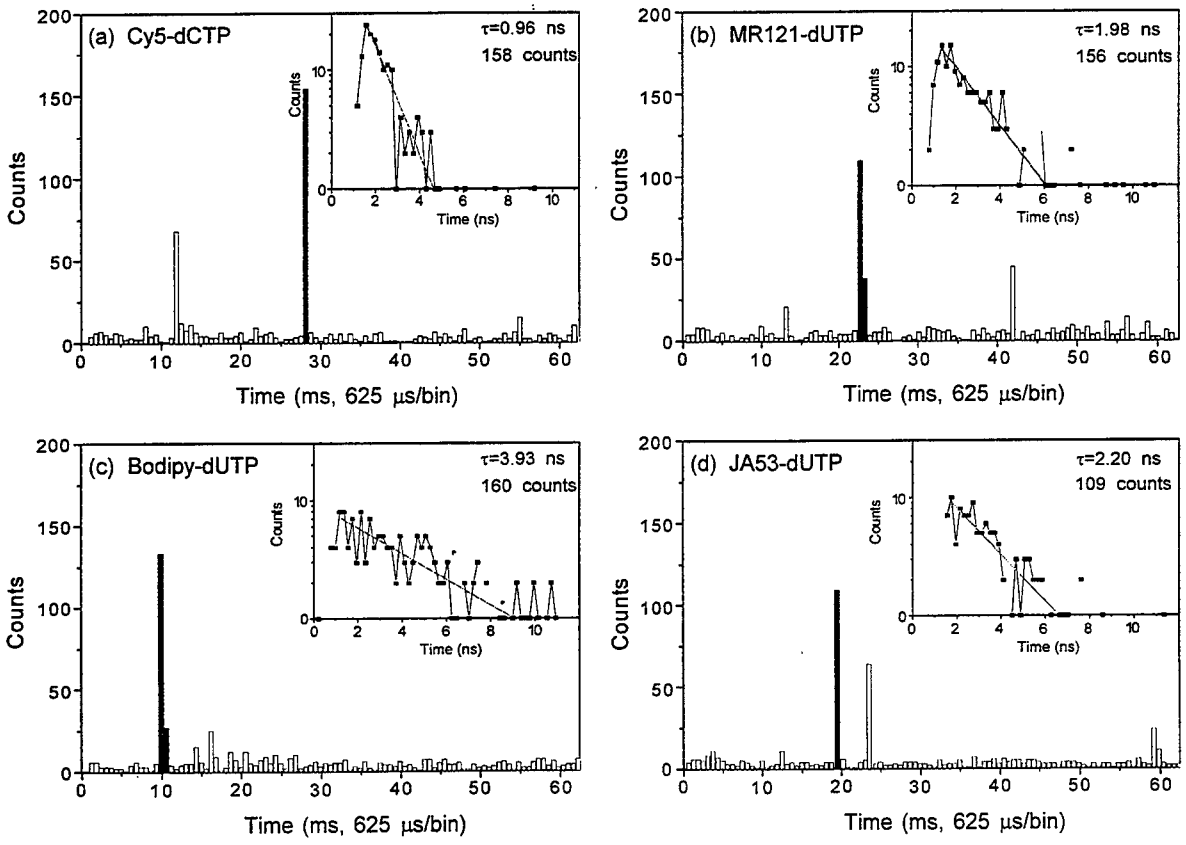

Figure 1. Fluorescence signals observed from aqueous solutions (10^{-11} M) of labeled mononucleotides recorded with the SMD apparatus.

In Figure 1 the time-dependent fluorescence signals (625 µs/bin) observed from 10^{-11} M aqueous solutions of differently labeled mononucleotide molecules with burst rates of up to 150

photons in 625 µs (240 kHz) are shown. With our experimental setup an average background level of 1.1 kHz was obtained in pure water. On the basis of this background we calculate signal-to-background ratios of more than 200 for the most intense peaks in our time-resolved experiments. We measured more than 250 time-resolved decays for individual Cy5-dCTP, MR121-dUTP, Bodipy-dUTP, and JA53-dUTP molecules and calculated the fluorescence lifetimes τ_{MLE}. Figure 2a demonstrates that three differently labeled mononucleotide molecules can be identified in water on the single-molecule level with a missclassification probability of approximately 10% due to their characteristic fluorescence lifetimes of 1.05±0.22 ns (Cy5-dCTP), 2.07±0.37 ns (MR121-dUTP), and 3.88±1.25 ns (Bodipy-dUTP). The histogram in Figure 2b was obtained from a 1:1:1 mixture of the mononucleotide molecules in water. As can be judged from the intersection points of the corresponding Gaussian fits in Fig. 2 at 1.4 ns and 2.7 ns, respectively, an identification is possible, even in a mixture of three different analyte molecules.

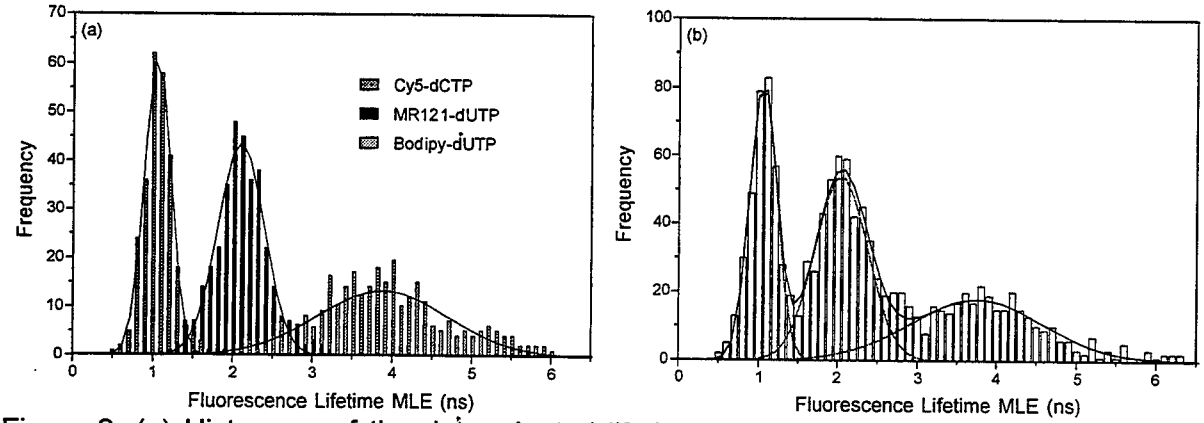

Figure 2. (a) Histogram of the determinated lifetimes of single Cy5-dCTP, MR121-dUTP, and Bodipy-dUTP molecules in water and corresponding Gaussian fits. The fluorescence lifetimes measured on the single-molecule level are in good agreement with the fluorescence lifetimes measured in bulk solutions (Table 1). (b) Histogram of more than 1000 measured fluorescence lifetimes of a 1:1:1 mixture of the same mononucleotide molecules 10^{-11} M in water with a minimum of 30 collected photons per single-molecule event.

References

1) P. M. Goodwin, W. P. Ambrose, R. A. Keller *Acc. Chem. Res.* **29**, 607 (1996).
2) P. M. Goodwin, H. Cai, H. J. Jett, S. L. Ishaug-Riley, N. P. Machara, D. J. Semin, A. Van Orden, R. A. Keller *Nucleosides&Nucleotides* **16**, 543 (1997).
3) C. Zander, K. H. Drexhage, K.-T. Han, J. Wolfrum, M. Sauer, submitted to Chem. Phys. Lett. (1997).
4) C. Zander, M. Sauer, K. H. Drexhage, D.-S. Ko, A. Schulz, J. Wolfrum, L. Brand, C. Eggeling, C. A. M. Seidel *Appl. Phys.* B **63**, 517 (1996).
5) M. Sauer, C. Zander, R. Müller, F. Göbel, A. Schulz, S. Siebert, K. H. Drexhage, J. Wolfrum *SPIE Proc.* **2985**, 61 (1997).
6) S. A. Soper, B. L. Legendre, Jr., D. C. Williams *Anal. Chem.* **67**, 4358 (1995).

Dual-molecule fluorescence spectroscopy: kinetic observation of single molecule reactions

Shimon Weiss
Molecular Design Institute, Materials Sciences Division, Lawrence Berkeley National Laboratory, 1 Cyclotron Road, Berkeley, CA 94720}

Summary

Traditional structural biology ensemble techniques such as x-ray crystallography, electron cryomicroscopy with angular reconstruction, electron microscopy, nuclear magnetic resonance (NMR) and electron paramagnetic resonance (EPR) provide detailed information on the structure of biological macromolecules. In cases where the crystal form of the macromolecule is available, the structure is known with the ultimate atomic resolution. The knowledge of the static structure can provide some insight to the macromolecule function, especially if it is coupled with other biochemical measurements, but in general the structure-function relationship is to a large extent unknown. With the aid of recently developed techniques such as patch clamp, atomic force microscopy (AFM) and optical tweezers, ionic current fluctuations in individual ion channels and forces and/or displacements generated during single molecular motor reaction were measured. Such measurements furnish information about function, but do not provide local, dynamical structural information.

Ensemble NMR and EPR measurements can provide information on conformational changes of biological macromolecules in solution. However, because of the background-free nature of fluorescence spectroscopy, the sensitivity of fluorescence detection is far superior to that of NMR and EPR, enabling the detection of single molecules. More importantly, in contrast to ensemble measurements, the time trajectory of conformational changes can be directly observed when individual molecules are probed one at a time, eliminating the need for synchronizing the reaction over the whole ensemble.

The advances in room temperature single molecule detection (SMD) and single molecule spectroscopy (SMS) by laser induced fluorescence (LIF) provide new tools for the study of individual biological macromolecules under physiological conditions. Two properties of a single fluorescent probe attached to a macromolecule can be exploited to provide local structural information. The first is the very high sensitivity of the fluorophore to its immediate local environment, including the sensitivity to the presence of other fluorophores and quenchers near-by. The second is its unique absorption and emission transition dipoles, which can be interrogated by polarized excitation light and/or by analyzing the emission polarization. Conformational changes can be detected by measuring distance and orientation changes on the macromolecule. Distance changes between two sites on the macromolecule can be measured via single-pair fluorescence resonance energy transfer (spFRET)[1]. Orientation changes can be detected by measuring the changes in the dipole orientation of a rigidly attached probe or changes in the rotational diffusion parameters of a tethered probe via single molecule fluorescence polarization anisotropy (smFPA)[2,3].

Various chemistries are available for site specific labeling of macromolecules. For instance, fluorophores can be covalently bound to termini of peptides and

oligonucleotides and to nucleotide analogs on oligos. They can also be bound to cysteines and/or artificial amino-acids which are inserted to a specific position along the peptide by site-directed mutagenesis. It is therefore possible to choose one or two points of interest, usually from the known static structure, on a single macromolecule or between two interacting molecules and label them with two different dye molecules which fluoresce at two different colors.

spFRET and smFPA experiments done on model systems as well as initial measurements done on working and unfolding enzymes will be described.

This work was supported by the Laboratory Directed Research and Development Program of Lawrence Berkeley National Laboratory under U.S. Department of Energy, contract No. DE-AC03-76SF00098.

References

1 T. Ha, T. Enderle, D. F. Ogletree, D. S. Chemla, P. R. Selvin, and S. Weiss, *Proceedings Of the National Academy Of Sciences Of the United States Of America* **93,** 6264-6268 (1996).

2 T. Ha, T. Enderle, D. S. Chemla, P. R. Selvin, and S. Weiss, *Physical Review Letters* **77,** 3979-3982 (1996).

3 T. Ha, J. Glass, D. S. Chemla, and S. Weiss, *submitted for publication in Phys. Rev. Lett.* (1997).

Laser Applications to Chemical and Environmental Analysis

Laser Applications in Micro-Analytical Systems

Monday, March 9, 1998

David J. Rakestraw, Sandia National Laboratory
Presiders

LMB
10:30am–11:45am
Coral Room

Lab-on-a-Chip Devices: Thinking Small About Chemical and Biochemical Measurements

J. Michael Ramsey
Oak Ridge National Laboratory
P.O. Box 2008, Oak Ridge, TN 37831-6142
423-574-5662 (voice), 423-574-8363 (fax)
mail: ramseyjm@ornl.gov

Demonstrations of microfabricated chemical instrumentation initially focused on chemical separations, first in the gas phase and later in condensed phase using capillary electrophoresis. It soon became clear that microfabrication could be extended to include a much larger portion of the chemical measurement problem and the concept of the Lab-on-a-Chip resulted[1,2,3]. The realization of the Lab-on-a-Chip requires the development of a number of functional elements or unit processes that can eventually be integrated to solve chemical and biochemical measurement problems. As the field of micromachined chemical instrumentation continues to grow, more sophisticated devices with increased functionality are being fabricated and tested. Functional elements that have been demonstrated for chemical and biochemical analysis include free solution electrophoresis [4,5,6,7,8,9], electrophoretic sizing of DNA fragments [11,12], and methods for isolation of neutral species [13,14,15]. In addition, initial levels of monolithic integration have been demonstrated by coupling chemical separations with chemical and enzymatic reactions [16,17,18,19,20]. Quantification tools used for detection of materials on or from microchips have primarily included fluorescence which is particularly applicable due to its extreme sensitivity[21] and electrospray ionization for off-chip analysis using mass spectrometry [22]. In addition to these more conventional chemical analysis methods, electrokinetically driven fluidics have been used to perform electrokinetically focused flow cytometry [23] and homogeneous enzyme reaction kinetics [24]. These latter two capabilities are described in greater detail below.

A microchip based version of flow cytometry has a two-dimensional focusing chamber that uses electrokinetic forces for sample transport and spatial confinement. The sample and focusing streams can be electrokinetically manipulated with sufficient dexterity that stream widths as narrow as 3.3 μm in a 18 μm long by 18 μm wide chamber are observed. The electrodynamic focusing characteristics were tested using cationic, neutral, and anionic samples to evaluate the influence of electric fields on the sample stream. Focusing is achieved using electrophoresis, electroosmosis, or a combination of the two. In addition, concentration enhancement is achieved in the focusing chamber by employing sample stacking. Also, the focusing chamber is multiplexed to confine spatially more than one sample stream simultaneously (Figure 1).

Enzyme kinetics were determined by performing homogeneous enzyme assays within the channel network fabricated on a glass substrate. Reagent mixing and fluid manipulations of the enzyme, substrate, and inhibitor within the channel network were computer-controlled using electrokinetic transport. Applied voltages were derived from an equivalent circuit model of the microchip, and precise fluid control was demonstrated using fluorophore-doped buffer. The enzyme ß-galactosidase (ß-Gal) was studied using a fluorogenic substrate, resorufin-ß-D-galactopyranoside (RBG) and a competitive inhibitor, phenylethyl-ß-D-thiogalactoside (PETG, Figure 2). Kinetics of the reaction were determined by monitoring the hydrolysis product, resorufin, using laser-induced fluorescence. An on-chip enzyme assay required only 120 pg of enzyme and 7.5 ng of substrate, reducing the amount of reagent consumed by at least four orders of magnitude over a conventional absorbance based assay. The relative inhibition of lactose, *p*-hydroxy-mercuribenzoic acid and PETG, was determined by varying the inhibitor concentration with constant enzyme and RBG concentration.

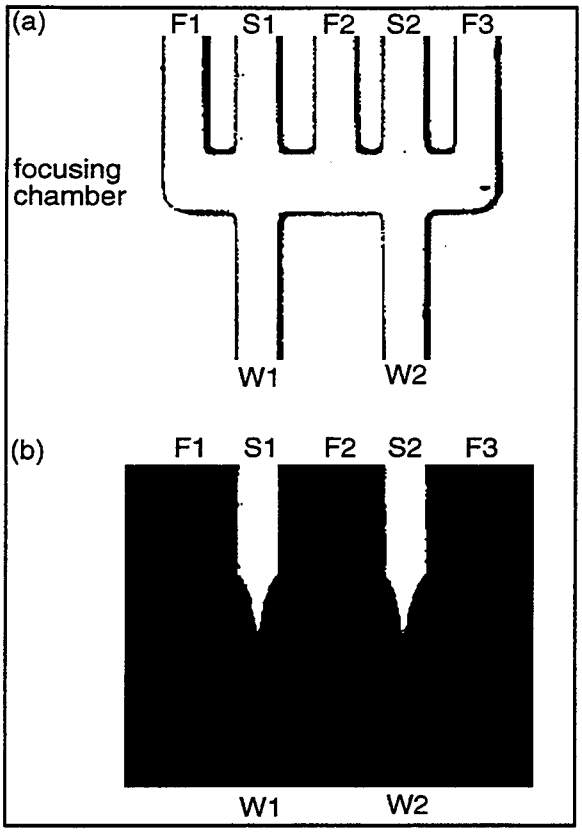

Figure 1. (a) CCD image of focusing chamber with two sample channels (S1 and S2) and three focusing channels (F1, F2, and F3). (b) CCD fluorescence image of focusing for two rhodamine 6G streams with a field strength of 40 V/cm in S1 and S2, 400 V/cm in F1 and F3, and 750 V/cm in F2.

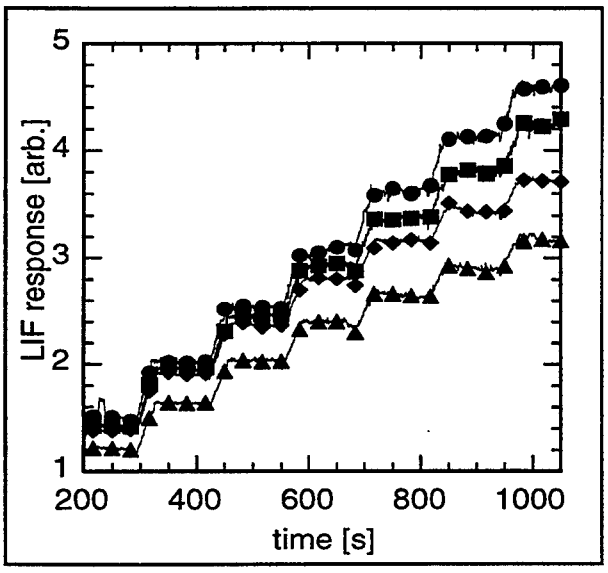

Figure 2. Plot of the fluorescence signal of resorufin produced in the PETG inhibited hydrolysis of RBG and ß-Gal. Each plateau represents increments of 14 µM RBG from 28 to 115 µM mixed with (●) buffer, (■) 0.60 µM PETG, (◆) 2.25 µM PETG and (▲) 4.50 µM PETG. Lines are labeled with every tenth data point. Conditions: 570 µg/L ß-Gal for each reaction in 100 mM TRIS, 2.0 mM KCl, and 100 µM $MgCl_2$ pH 7.8 buffer at 21 °C.

References:

1. J. M. Ramsey, S. C. Jacobson, and M. R. Knapp, "Microfabricated Chemical Measurement Systems," Nature Medicine, 1, 1093 (1995).
2. Stephen C. Jacobson and J. Michael Ramsey, "Microfabricated Devices for Performing Capillary Electrophoresis," in Handbook of Capillary Electrophoresis, CRC Press, James Landers, ed., Ch. 29, pg. 827 (1997).
3. Stephen C. Jacobson and J. Michael Ramsey, "Electrokinetic Separations on Microchips," book chapter in High Performance Capillary Electrophoresis, John Wiley & Sons, Morteza G. Khaledi, ed., (in press).
4. Harrison, D. J., Manz, A., Fan, Z., Ludi, H., Widmer, H.M., Anal. Chem. 64,1926 (1992).
5. Seiler, K., Harrison, D. J., Manz, A., Anal. Chem., 65, 1481 (1993).
6. Effenhauser, C. S., Manz, A., Widmer, H. M., Anal. Chem., 65, 2637 (1993).
7. Jacobson, S. C., Hergenröder, R., Koutny, L. B., Warmack, R. J., Ramsey, J. M., Anal. Chem., 66, 1107 (1994).
8. Jacobson, S. C., Hergenröder, R., Koutny, L. B., Ramsey, J.M., Anal. Chem., 66, 1114 (1994).
9. S. C. Jacobson, A. W. Moore, Jr., and J. M. Ramsey, "Fused Quartz Substrates for Microchip Electrophoresis," Anal. Chem., 67, 2059 (1995).
10. Woolley, A.T., Mathies, R.A. Proc. Natl. Acad. Sci. 91, 11348 (1994).
11. Effenhauser, C.S., Paulus, A., Manz, A., Widmer, H.M. Anal. Chem. 66, 2949 (1994).
12. Jacobson, S.C., Ramsey, J.M. Anal. Chem. 68, 720 (1996).
13. Jacobson, S. C., Hergenröder, R., Koutny, L. B., Ramsey, J. M., Anal. Chem., 66, 2369 (1994).
14. Moore, A.W., Jacobson, S.C., Ramsey, J.M., Anal. Chem. 67, 4184 (1995).
15. J. P. Kutter, S. C. Jacobson, and J. M. Ramsey, "Electrokinetic Solvent Mixing for Isocratic and Gradient Elution in MEKC on Microfabricated Devices," Anal. Chem. (in press).
16. S. C. Jacobson, L. B. Koutny, R. Hergenröder, A. W. Moore, Jr., and J. M. Ramsey, "Microchip Capillary Electrophoresis with an Integrated Postcolumn Reactor," Anal. Chem., 66, 3472 (1994).
17. S. C. Jacobson, R. Hergenröder, A. W. Moore, Jr., and J. M. Ramsey, "Pre-Column Reactions with Electrophoretic Analysis Integrated on a Microchip," Anal. Chem., 66, 4127 (1994).
18. Stephen C. Jacobson and J. Michael Ramsey, "Integrated Micro-Device for DNA Restriction Fragment Analysis," Anal. Chem., 68, 720 (1996).
19. L. C. Waters, S. C. Jacobson, N. Kroutchinina, Y. Khandurina, R. S. Foote, and J. M. Ramsey, "Microchip Device for Cell Lysis, Multiplex PCR Amplification and Electrophoretic Sizing," Anal. Chem. (in press).
20. J. P. Kutter, R. S. Ramsey, S. C. Jacobson, and J. M. Ramsey, "Determination of Metal Cations in Microchip Electrophoresis using On-Chip Complexation and Sample Stacking," J. Microcolumn Separations (in press).
21. J. C. Fister, S. C. Jacobson, L. M. Davis, and J. M. Ramsey, "Counting Single Chromophore Molecules for Ultrasensitive Analysis and Separations on Microchip Devices," Anal. Chem. (in press).
22. R. S. Ramsey and J. M. Ramsey, "Generating Electrospray from Planar Glass Chips Using Electroosmotic Pumping," Anal. Chem., 69, 1174 (1997).
23. Stephen C. Jacobson and J. Michael Ramsey, "Electrokinetic Focusing in Microfabricated Channel Structures," Anal. Chem., 69, 3212 (1997).
24. A. G. Hadd, D. E. Raymond, J. W. Halliwell, S. C. Jacobson, and J. M. Ramsey, "Microchip Device for Performing Enzyme Assays," Anal. Chem., 69, 3407 (1997).

Environmental Monitoring with Fiber Optic Immunosensors and Compact Optoelectronics

J.T. Ives, B.J. Sullivan, J. Thamer, and J.H. Bechtel, TACAN Corporation, 2330 Faraday Avenue, Carlsbad, CA 92008, phone: (760) 438-1010, Fax: 760-438-2412, and
T.C. Thomas, Armstrong Laboratory, AL/OE-1, 2402 E Drive, Brooks Air Force Base, TX 78235, phone: (210) 536-2001

Summary

Environmental hazards are often detected by gas chromatography, mass spectroscopy, or high performance liquid chromatography. These methods are well characterized, but they are expensive and usually not performed on-line. Antibody-based technologies are increasingly being applied due to the specificity of the antibodies, and the low cost of the detection kits. With the immunoassay kits, personnel collect samples, mix them with the kit components, and observe the results on-site.

An advance over the kits is obtained by combining the antibodies with compact instrumentation to make sensors for automated detection. A variety of electrochemical, acoustic wave, and optical (light scattering, surface plasmon, fluorescence) methods have been used for these immunosensors [1]. Among the optical methods, optical fibers with fluorescence detection provide good sensitivity, and monitoring at locations distant from the operator and optoelectronics. Several fiber optic immunosensors using fluorescence detection have been reported [2,3].

At TACAN Corporation, we are developing a fiber optic immunosensor to continuously monitor environmental hazards in groundwater or other aqueous locations. This immunosensor is based on evanescent excitation and collection of fluorescence from fluor-labeled analyte molecules bound to surface immobilized antibodies. Figure 1 illustrates the design of the sensor tip.

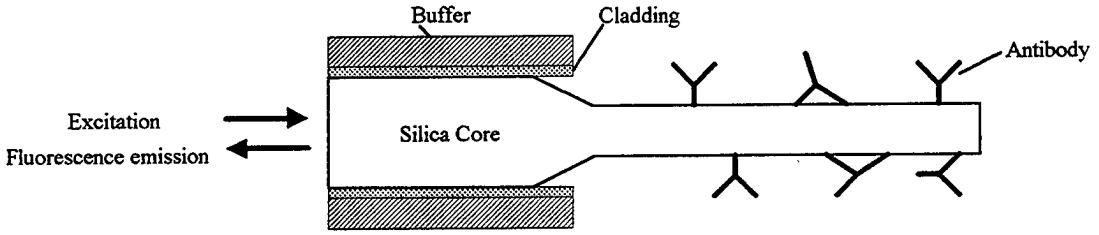

Figure 1. Schematic illustration of antibody-bound fiber optic tip.

The exposed fiber core has a smaller diameter than the clad region of fiber to compensate for their different numerical apertures and therefore, mismatched mode propagation. Evanescently back-coupled fluorescence in the higher order bound modes of the tip (surrounded by the relatively low refractive index aqueous solution) radiate when reaching the clad region, particularly when the diameters are equal. Reducing the diameter of the exposed tip results in fluorescent signals that are 1-2 orders of magnitude larger than those obtained with a constant diameter fiber. Other researchers have also investigated reduced diameter fibers for evanescent detection [4,5].

Another important feature of the fiber optic sensor is the use of a displacement assay and a porous membrane (Figure 2). The BTEX compounds (benzene, toluene, ethylbenzene, and xylene), pesticides, and most other environmental analytes are low molecular weight molecules. These molecules are not inherently fluorescent, at least not with large yields and at visible wavelengths, so fluorescent labels are used. The small size of these analytes usually prevent detection by multiple antibody, sandwich immunoassays. Therefore, competition for antibody-binding sites is set up between analyte and fluor-labeled analyte molecules. To apply this approach to continuous monitoring, we are designing probes that surround the antibody-coated fiber tip with a size-selective membrane (Figure 2). The volume around the fiber tip and within the membrane is

filled with a solution containing fluor-labeled analyte. When placed in groundwater or other aqueous environments, analyte molecules pass through the membrane and displace labeled analyte molecules, resulting in a change in detected signal. The larger, fluor-labeled analyte molecules provide a self-regulating source of signal that cannot pass through the membrane.

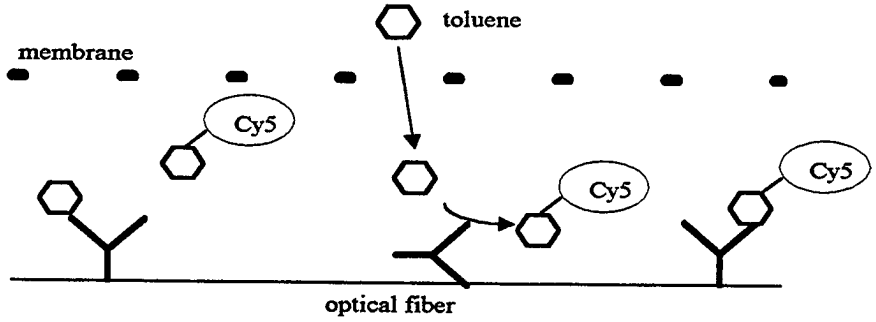

Figure 2. Schematic illustration of displacement reaction for toluene detection. Toluene, indicated by the hexagon, passes through a size-selective membrane. Some of the toluene displaces Cy5™-labeled toluene from antibodies, thereby changing the fluorescence signal.

Our work has used 600 μm core, plastic clad fibers. Approximately 4cm long ends of the fibers are stripped, and immersed in hydrofluoric acid (HF) to reduce the diameter. With different tapering conditions, constant diameter or gradually tapered fibers can be prepared. Antibodies are bound with aminosilane and carbodiimide crosslinking chemistries.

Analyte molecules are labeled in-house with Cy5™ succinimidyl esters (Amersham) [6] using chemistries specific to each analyte. For example, toluene derivatives have been labeled. Cy5™ labeling chemistries for the insecticides, parathion and malathion, have also been designed.

Fibers are connected to a handheld terminal containing the optoelectronics and software. The most notable components are a 635nm laser diode, compact filter block, photodetector, and a 20-bit A/D. The system is designed for optional battery operation.

Figure 3 shows results obtained with Cy5™-labeled toluene binding to a fiber coated with anti-toluene antibodies. Results with a control fiber coated with anti-mouse IgG antibodies are also shown. In contrast to the control, the toluene/anti-toluene antibody signals gradually increase with time, and significant signal remains after washing with phosphate buffered saline (PBS).

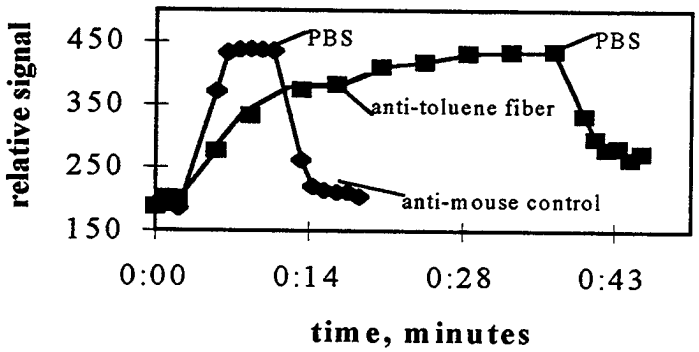

Figure 3. Toluene antibody binding. Two fibers were exposed to an 800 part per trillion solution of Cy5™-toluene followed by a PBS wash. One fiber (diamonds) had a coating of anti-mouse IgG antibody as a control, and the other fiber was coated with anti-toluene antibodies.

An example of a reversible assay for toluene is shown in Figure 4. This experiment used a flow cell because the membrane was not yet incorporated. In this experiment, a series of steps to: 1) bind Cy5™-toluene on the fiber, 2) wash off non-bound Cy5™-toluene, and 3) displace Cy5™-toluene with a toluene solution at a concentration of 1 part per million (ppm), was performed three times. Cy5™-toluene binds and is displaced from the fiber in 5 minutes or less. Toluene solution concentrations of 1 part per million (ppm) are easily observed to displace labeled toluene. Further investigations of displacement are being performed.

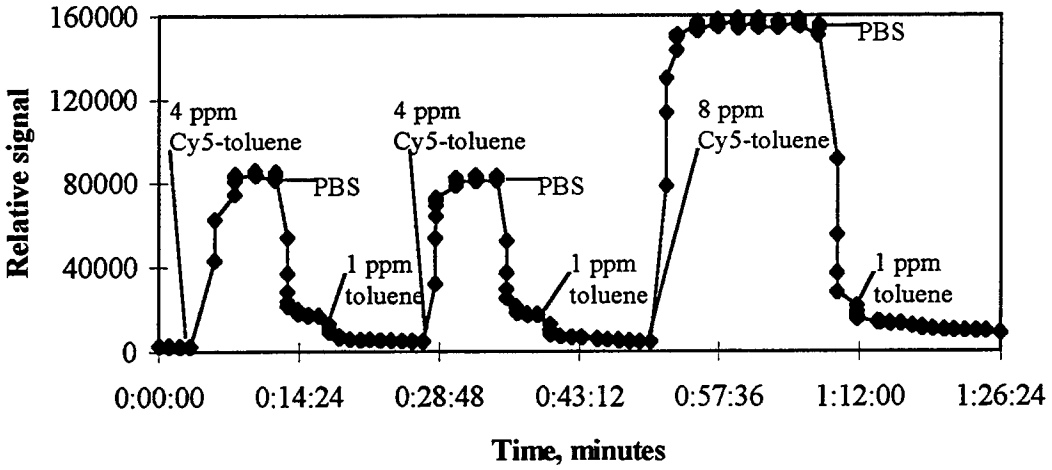

Figure 4. Toluene Assay. Cy5™-labeled toluene is injected at 4 ppm concentration twice, then at 8 ppm. Each dye label solution is flushed with PBS, followed by a solution of 1ppm toluene in PBS. The lines indicate when the respective solutions were injected into the flow cell.

In conclusion, the described work is progressing toward a continuous monitor of environmental hazards. The surface-bound antibodies provide high selectivity, and, in combination with the fluorescence system, allow measurements with good sensitivity. To support the sensing probe, compact and fieldable instrumentation is being developed. Field applications will require further development on probe design, multi-fiber instrumentation, and assay verification.

References

1. Morgan, C.L., Newman, D.J., and Price, C.P. Clin. Chem. **42**, 193 (1996).
2. Golden, J.P., Saaski, E.W., Shriver-Lake, L.C., Anderson, G.P., and Ligler, F.S. Opt. Eng. **36**, 1008 (1997).
3. Astles, J.R. and Miller, W.G. Sens. Actuators B **11**, 73 (1993).
4. Gao, H.H., Chen, Z., Kumar, J., Tripathy, and Kaplan, D.L. Opt. Eng. **34**, 3465 (1995).
5. Golden, J.P., Anderson, G.P., Rabbany, S.Y., and Ligler, F.S. IEEE Trans. Biomed. Eng. **41**, 585 (1994).
6. The wavelengths of maximum absorption and emission for Cy5™ are 649nm and 670nm, respectively.

High Speed Microchip Electrophoresis

Stephen C. Jacobson, Christopher T. Culbertson, and J. Michael Ramsey

Oak Ridge National Laboratory, P.O. Box 2008

Oak Ridge, TN 37831-6142

Phone: 423-574-8002, Fax: 423-574-8363

email: jacobsonsc@ornl.gov

Introduction

Open tubular separations in the liquid phase including capillary electrophoresis are conventionally practiced in capillary tubes with diameters of tens of micrometers and lengths of tens of centimeters. Structures having similar dimensions can be fabricated on planar substrates using micromachining techniques. Microfabricated separation devices have been demonstrated for capillary electrophoresis,[1 2] synchronized cyclic electrophoresis,[3] and free-flow electrophoresis.[4] The separation performance hinges upon minimizing the spatial extent of the injection plug and detector observation region, and optimizing the separation field strength. The injection plug width can be minimized by fabricating narrow channel dimensions for the injection valve, and the detector observation region can be minimized by having a small excitation volume or tight spatial filtering for fluorescence detection. For high speed separations, the separation column does not have to be long, e.g., < 1 mm long. Unfortunately, the footprint of these microfluidic devices is usually > 200 mm^2, but the channel manifold can be designed such that the potential drop is small in areas not contributing to the separation. This results in a maximum field strength in the separation column. Because the resistance in the channel is proportional to the length and inversely proportional to the cross-sectional area, thin channels are fabricated for the injection valve and separation column, and wide channels for all other sections of the channel manifold.

With these criteria, the microchips were fabricated using standard photolithographic, wet chemical etching and bonding techniques as described previously.[5] Figure 1 shows a picture of the photomask used to generate the microchips. The pattern was written using a CAD/CAM laser machining system (Ar+ laser, 457 nm). The fabricated microchips had dimensions for the wide channel of 440 μm wide at half-depth and 6.2 μm deep, and for the narrow channel 25 μm wide at half-depth and 6.2 μm deep. These dimensions give a relative resistance between the two channels widths of 17.6, and, therefore, for comparable lengths the separation field strength is 17.6 times greater for the narrow channel. This design allowed an electric field strength of 5 kV/cm in the separation column for 1 kV applied to the microchip. The microchip in Figure 1 has a the separation column that is 500 μm long.

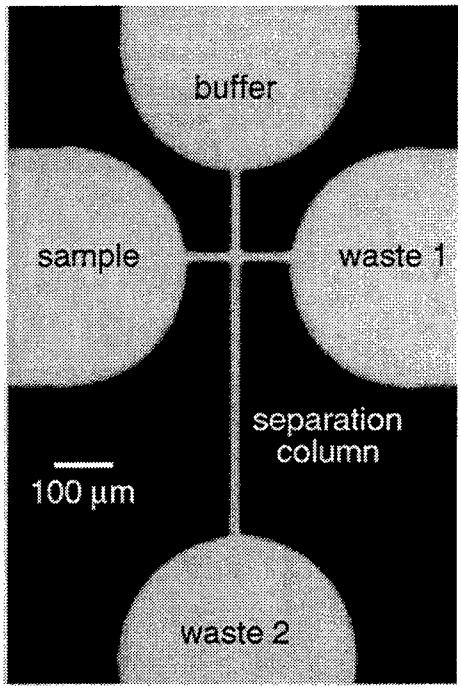

Figure 1: Photomask of microchip generated using a direct write laser system.

In Figure 2, a binary mixture of rhodamine B and dichlorofluorescein is resolved in 1 ms using this microchip. The separation was monitored 200 μm downstream from the injection valve, and a separation field strength of 35 kV/cm was used. These separations are two orders of magnitude faster than what has been previously reported. To minimize Joule heating in the channels with the high electric fields applied, a zwitterionic organic buffer, (HEPES; 5 mM) was used in addition to borate buffer (1 mM). Such microchips can provide high speed separations for the second dimension to 2-dimensional separation or to monitor kinetics.

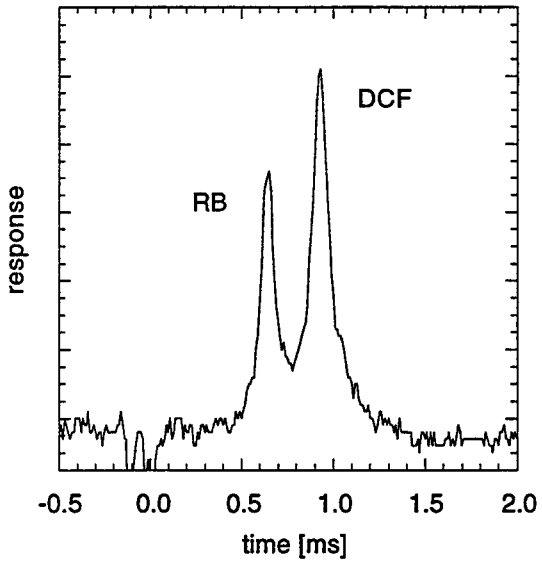

Figure 2: Electropherogram of rhodamine B (RB) and dichlorofluorescein (DCF) using a separation field strength of 35 kV/cm and a separation distance of 200 μm.

References

[1] D. J. Harrison, A. Manz, Z. Fan, H. Lüdi, H.M. Widmer, *Anal. Chem.* ***64***, 1926 (1992).

[2] S.C. Jacobson, R. Hergenröder, L.B. Koutny, J.M. Ramsey, *Anal. Chem.* ***66***, 1114 (1994).

[3] N. Burggraf, A. Manz, C.S. Effenhauser, E. Verpoorte, N.F. de Rooij, H.M. Widmer, *J. High Res. Chromatogr.* ***16***, 594 (1993).

[4] D.E. Raymond, A. Manz, H.M. Widmer, *Anal. Chem.* ***66***, 2858 (1994).

[5] S.C. Jacobson, R. Hergenröder, L.B. Koutny, J.M. Ramsey, *Anal. Chem.* ***66*** 1107 (1994).

Progress towards a Chip Based Detector for Explosives

Christopher G. Bailey, Don W. Arnold, and David J. Rakestraw
Sandia National Laboratories
P.O. Box 969
Mail Stop 9671
Livermore, CA 94551-0969
(510) 294-1351, Fax (510) 294-1489

I. Introduction

The need for rapid, accurate detection of chemical species in the environment has prompted much interest in the development of chemical detectors. A number of considerations must be taken into account in the design of a successful sensor such as low false alarm rates, low levels of detection, ease of use and reliability. Moreover, the ideal device would be compact and have low power requirements. Recent progress in chip based chemical analysis offers great promise toward the development of such a detector.[1] Chip based devices offer a number of advantages such as speed, reproducibility, and the need for low sample volume. An example of a class of compounds that demands rapid and accurate detection are the nitroaromatic and nitramine explosives. Prompt, reliable detection of explosives amidst a complex background is important in a number applications such as mine detection, anti-terrorism measures, environmental remediation, forensics, and health and safety concerns. Here we present results on the separation of explosive compounds using microcapillary electrokinetic chromatography and their detection using indirect laser-induced fluorescence. These techniques are readily amenable toward miniaturization and integration into a single chip based device.

II. Results and Discussion

In electrokinetic chromatography the mobile phase is driven through a stationary phase[2] (capillary electrochromatography or CEC) or pseudostationary phase[3] (micellar electrokinetic chromatography or MEKC) by electro-osmotic flow which offers certain advantages over pressure driven chromatographic separations. The plug like flow profile of electro-osmotic flow results in narrower elution bands and higher separation efficiency over the parabolic profile of pressure driven flow. Moreover, in electro-osmotic flow, there is no pressure drop over the column enabling the use of smaller particles in the stationary phase than those generally used in pressure driven chromatography.[4]

Figure 1 shows separations of a mixture of 14 explosives and their degradation products using microcapillary electrokinetic chromatography. Figure 1a is a CEC separation using a 16 cm x 75μm id capillary packed with 1.5 μm C18 coated nonporous particles run at 14 kV. The mobile phase was 15% methanol and 85% 10mM MES. The injection of the sample (12mg/L each component in the above mobile phase) was done electrokinetically at 4 kV for 0.5 seconds. Each peak thus corresponds to a mass loading of approximately 15 fg of each component. The height equivalent to a theoretical plate in Figure 1a is <2 μm. Figure 1b shows a MEKC based separation using a 70 cm x 50 μm id capillary. The psuedostationary phase was 50mM SDS in a 25 mM phosphate buffer adjusted to pH 7.[5] This separation was run at 20 kV following a 4 second injection of 50 mg/L sample at 5 kV. The theoretical plate height obtained in this

separation is 2-3 μm.

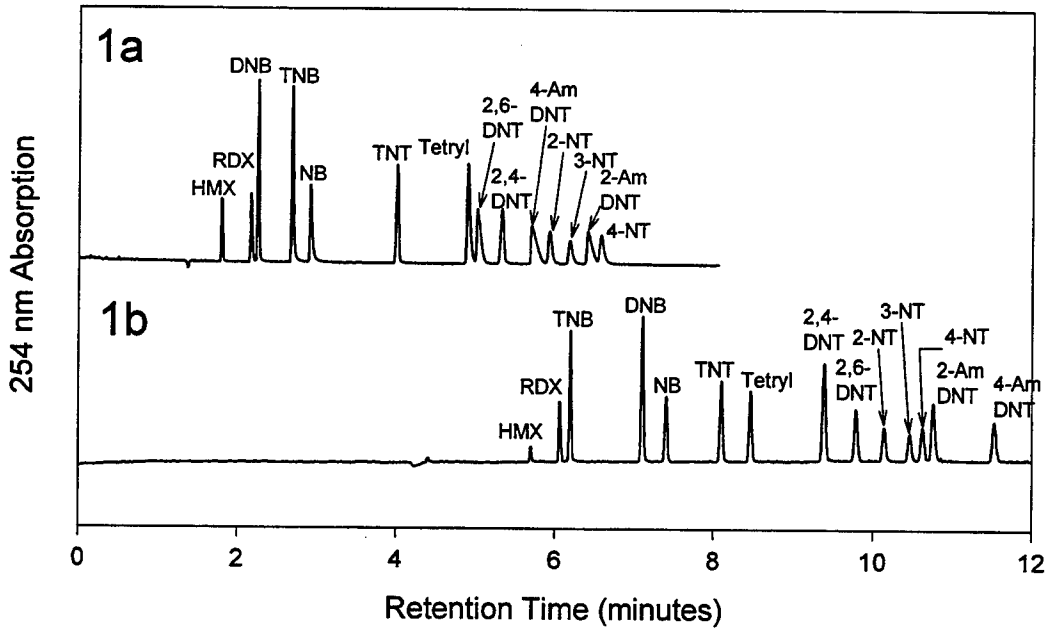

Figure 1. Electrokinetic separations of explosives, a) CEC, b) MEKC.

The separations of the 14 explosives shown in Figure 1 demonstrate the extraordinary efficiencies attainable in electrokinetic chromatography. Theoretical plate heights obtained in pressure driven separations are typically 10 times higher. The fact that two separate electrokinetic chromatographic techniques were able to successfully resolve a complex mixture of explosives is promising toward a parallel channel detection scheme. The different retention times and elution order switching exhibited by the compounds in the two separations could lead to development of a detector with a very low false alarm rate.

The detection method used in the separations of Figure 1 is UV absorption. The ease and generality of this technique has led to its becoming one of the most commonly used methods in laboratory analyses. However, due to the unavailability of appropriate compact light sources, UV absorption does not readily lend itself to miniaturization. The current generation of diode lasers is limited to wavelengths greater than 635 nm. An optical based detection method that can exploit the currently available semiconductor light sources is indirect fluorescence detection.[6] In this a tag which fluoresces at the excitation wavelength is added to the mobile phase, yielding a constant fluorescent background. As a band of analyte moves through the detection region there is a dip in the fluorescence background due to the displacement of the fluorophores. Often, the simple displacement effect is enhanced by other factors, such as quenching of the fluorescence by the analyte.

Figure 2 demonstrates the detection of 2 ppm of four nitroaromatic compounds using indirect fluorescence. The separation conditions are the same as those used in figure 1b (MEKC) except for the addition of 10^{-5} M of the near ir dye Cy-5 to the mobile phase. The addition of the dye had no effect on the separation of the explosives. The measurements were made using a home built epifluorescence system with a 635 nm diode laser excitation source and a commercial photodiode detector. The fluorescence background shown in figure 2 varied by less than 1% despite the fact that the laser was not stabilized. Further, the fluorescence background was not normalized to fluctuations in the laser power. Both of these improvements could be easily incorporated into the system leading to an improvement in the limit of detection.[7]

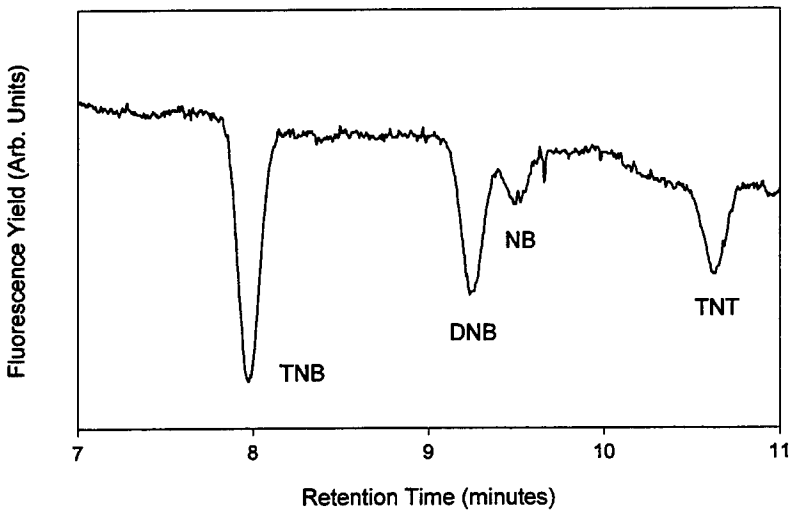

Figure 2. Indirect fluorescence detection of explosives.

III. Conclusion

The results presented here demonstrate the ability to separate and detect explosive compounds at the part per million level using micro capillaries and semiconductor excitation and detection. The integration of these onto a single substrate using silica etching techniques, including the use of VCSELs and diffractive optics will be addressed in more detail during the presentation.

References

1) R. S. Ramsey and J. M. Ramsey, *Anal. Chem.* **69**, 1174 (1997) and references therein.
2) V. Pretorious *et al, J. Chromatogr.* **99**, 23 (1974).
3) S. Terabe *et al, Anal. Chem.* **56**, 111 (1984).
4) L. A. Colon *et al, Anal. Chem.* **69**, 461A (1997).
5) S. A. Oehrle, *Electrophoresis*, **18**, 300 (1997).
6) E. S. Yeung, *Acct. Chem. Res.* **22**, 125 (1989).
7) X. Yongjun and E. S. Yeung, *Anal Chem.* **65**, 2923 (1993).

Laser Applications to Chemical and Environmental Analysis

Poster Session

Monday, March 9, 1998

LMC
7:00pm–9:00pm
Atlantic/Pacific Room

Interferometrically-decoded fibre-optic vibration sensor using low-power laser diode

Tarun Kumar Gangopadhyay and Philip James Henderson

University of Sydney
Department of Electrical Engineering, NSW 2006, Australia
Tel: +61-2-9351-2010, Fax: +61-2-9351-3847

Summary

Laser-based sensors have a number of significant advantages over other sensors for monitoring of vibration. Proper control of vibration may prevent deformation of components, failure of machineries and also unwanted vibrational sound hazard (as an environmental remediation). Applications of laser with fibre-optic technologies are providing a new approach to vibration monitoring in electromechanical equipment. Evolution of vibration signature is a recognised hallmark of equipment degradation [1,2]. Optical fibre sensors using laser interferometry are particularly suited to this application because of their inherent electrical isolation, superb dielectric properties and immunity to electromagnetic interference.

In this paper, a fibre-optic interferometric vibration sensor is presented which combines the high sensitivity of Michelson interferometry with a practical sensing arrangement (Figure 1). The sensor uses a movable reflective surface as the transducing device, a 0.25 pitch GRIN lens for efficient light-guiding, and two adjacent 50/125μm step-index fibres for transmitting the input and output signals. The sensor signal was supplied by 680nm light from a low-power laser diode.

In order to identify a practical engineering design, the reflected intensity was calibrated against displacement from the fibre-ends using both plane mirror and polished steel reflectors (Figure 2). Monotonicity and high sensitivity were maintained between 1 to 5.5mm, indicating a practical working range of some 4.5mm.

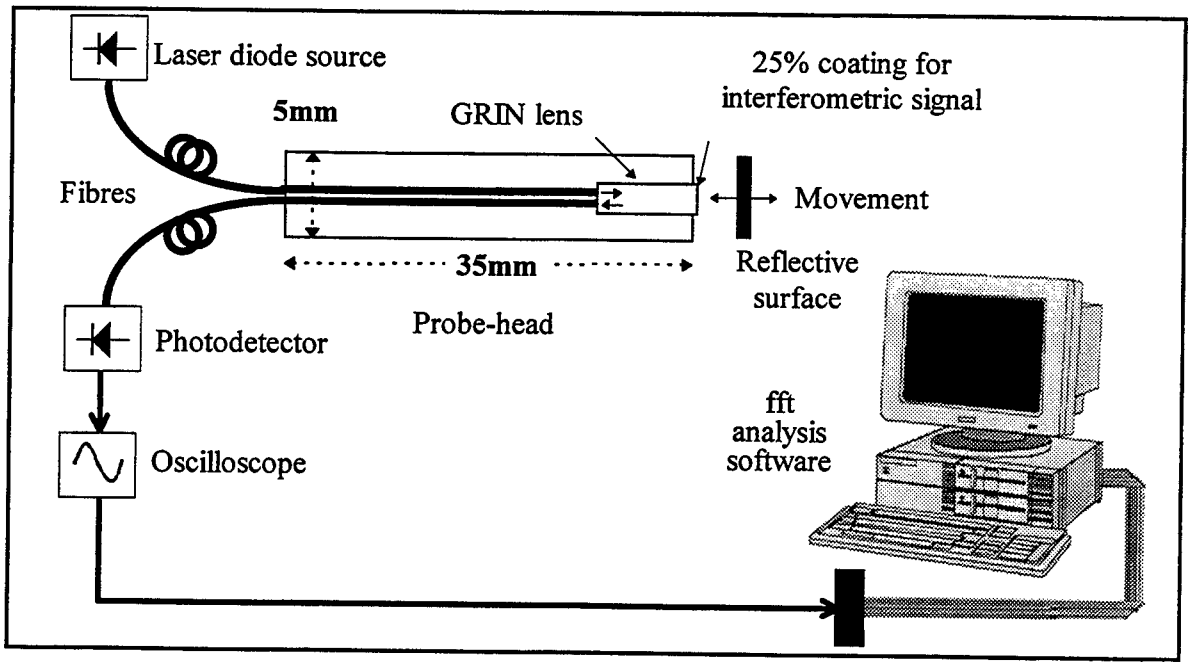

Figure 1 Schematic of the sensor system

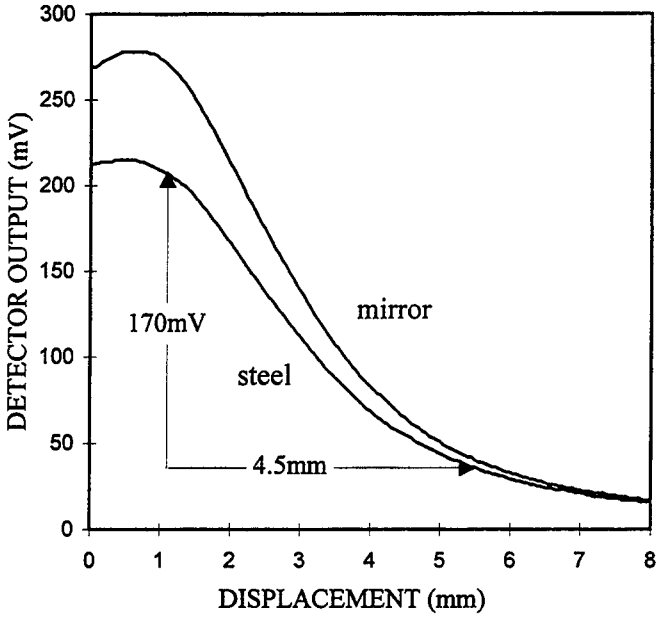

Figure 2 Calibration of the intensity-modulating sensor, comparing the plane-mirror and polished-steel reflectors

The steel surfaces, however, were found to be just 23% less reflective and are more-practical engineering components. A system with a steel surface had an output change of 170mV and a noise level of 0.5mV p/p. Its resolution was thus 13μm over the 4.5mm working range.

For interferometric measurements, a 25% reflective coating was deposited on the free end of the GRIN lens. Light from the coating combined with phase-modulated light from the displacing steel surface to produce interference fringes.

Fringes were obtained by displacing the steel surface with a piezoelectrically controlled displacement stage. Thirty fringes of monotonically decreasing contrast were obtained (Figure 3), equivalent to a displacement of about 10.2μm (30×0.68/2). The ability to identify fringe order and thus displacement direction over multiple orders is an important feature of using physically distinct launch and receive fibres.

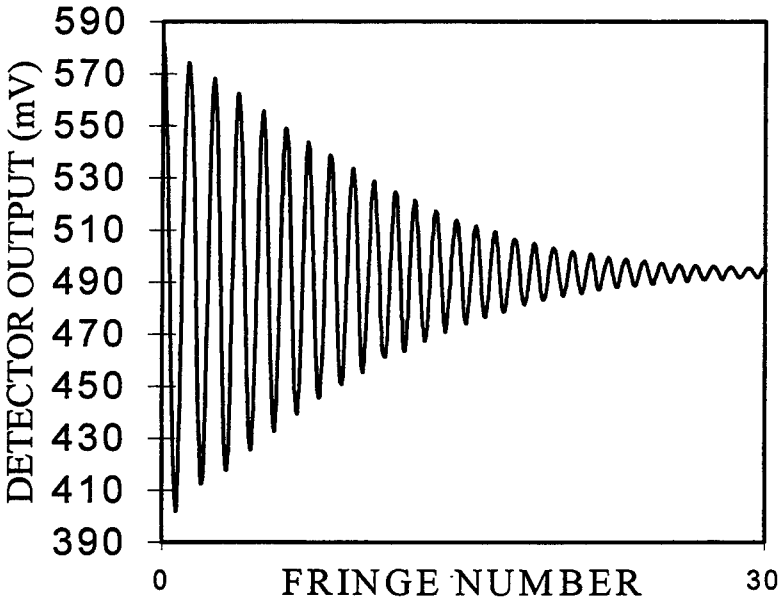

Figure 3 Calibration of the phase-modulating sensor over 30 fringes

The fringe contrast is maximum at zero displacement, where the geometry for the signal and reference beams is identical, and decreases elsewhere. The fringes can be resolved to at least 1 part in 10, giving a measurement resolution of better than 0.034μm over the 10.2μm range.

Dynamic testing involved applying a 2kHz vibration to the steel surface with a piezoelectrically controlled vibrator. Figure 4 shows the dynamic response of the sensor. At low vibration amplitude, the detector output varies repetitively with unique values between the zero and 1/2 fringe position. Here the vibration amplitude is λ/4 (680nm/4 = 0.17μm). At high amplitude, the output has a more complex structure, with a repetitive unit consisting of eight fringes of unique amplitude extending from the zero position. An optical path difference of eight fringes is equivalent to a displacement of 8λ/2 (8×680nm/2 = 2.72μm). Dynamic measurement of large vibrations is thus possible through identification of fringe order for coarse resolution, together with interpolation between fringes for high resolution.

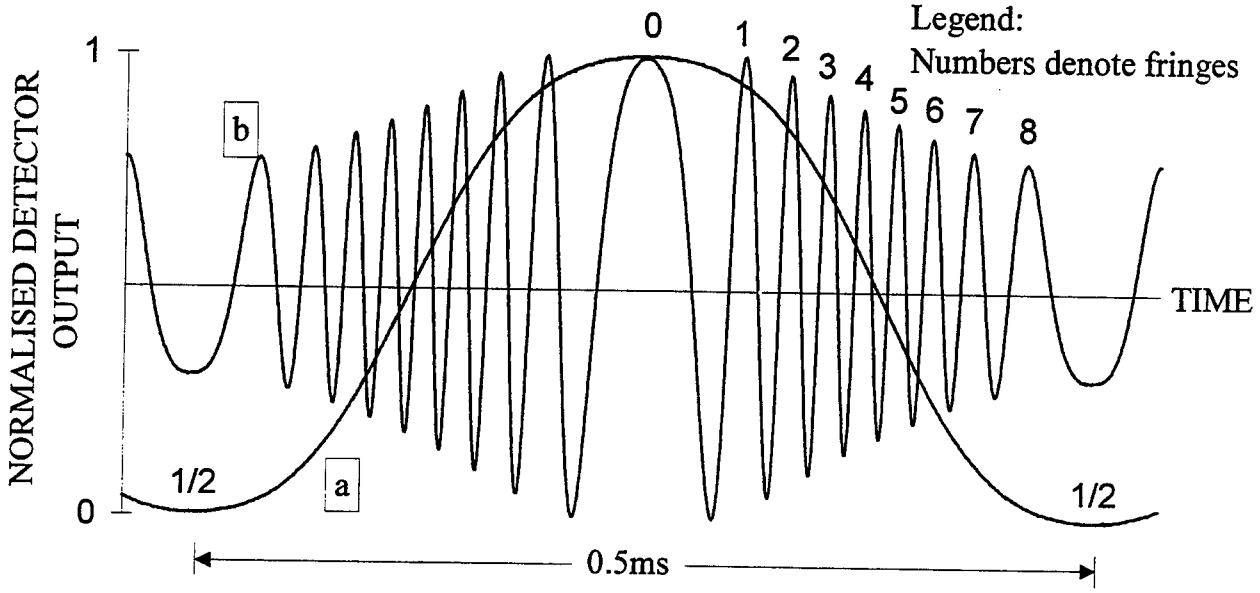

Figure 4 Dynamic response of the phase-modulating sensor to 2kHz excitation
(a) at low amplitude: 0.17μm (≡ 1/2 fringe or λ/4 displacement)
(b) at increased amplitude: 2.72μm (≡ 8 fringes or 8λ/2 displacement)

In conclusion, a laser-based interferometrically-decoded fibre-optic vibration sensor has been demonstrated. It is suitable for measuring both vibration amplitudes and displacements up to several microns (directly), while an intensity-based version can measure displacements over several millimetres. Notable example areas for these low-cost devices include micro-displacement measurements in mechanised areas, and use in high-voltage and explosive environments. Although laser interferometry is a well established technique but in practical and industrial situation of controlling vibration needs different design principles. Presented here is the sensor technique by which dynamic measurement of large vibrations is possible. It is particularly suited to monitoring equipment, whose operation is marked by occasional highly-energetic vibrations of sub-second duration, interspersed by long quiescent periods.

References

[1] M.Serridge, "What makes vibration condition monitoring reliable?", Noise & Vibration Worldwide, September 1991, pp.17-24.

[2] J.Q.Lang & A.D.Stokes, "Vibration Monitoring of High-Voltage Switchgear", CIGRE Australian 13 Symposium, 31 May 1995.

Laser diode refractive index detection in capillary.

Kasyutich V.L.
Institute of Molecular and Atomic Physics, National Academy of Sciences,
70, ave. F. Scorina, Minsk, 220072, Belarus
Phone: (375)(172)685763; Fax: (375)(172)393064; E-mail: lldp@imaph.bas-net.by

1.Introduction

A cylindrical sample cell (capillary) is used widely in photothermal lens spectroscopy [1-4], refractive index (RI) detectors for microbore liquid chromatography [5,6] and capillary electrophoresis [7-9], in analysis of fluids [10,11]. An inner diameter of the capillary can be varied from hundreds down to tens microns and laser sources are appreciable for probing of the samples in the capillary.

Theoretical models are known to describe a scattering of the laser beam by glass fiber [12], a beam deflection by capillary in air on base of the geometric optics [6] and an interference of the beams probing the capillary immersed in the matching fluid [8,11]. Usually, interference pictures observed in the far field are a lot of the fringes and an adjustment of the laser beam relative to the capillary was found to be tedious [11] for most mentioned above RI detectors. RI detector with an automatic adjustment of the laser beam and photoreceiver was proposed for the capillary electrophoresis device and based on laser diode [9,13].

A ray-tracing theory of the laser beam propagation through the capillary and a formation of the interference fringe pattern on base of the Huygens principle can be applied to optimize the laser diode RI detector for capillary electrophoresis and other analytical techniques using a capillary. A good coincidence is observed for numerically simulated and experimental fringe patterns for the different capillaries. Factors that cause and limit RI sensitivity are estimated for the laser diode RI detector.

2.Experimental

RI detector used in the experiment and an algorithm of the automatic adjustment were described elsewhere [9,13]. A laser diode (780 nm, 5 mW, single frequency regime, power stabilization about 0.01%) with a ball lens (focus 14 mm) was employed for probing the borosilicate glass capillary with the inner diameter (i.d.) 100 μm and the outer diameter (o.d.) 200 μm and n=1.511. A polarization plane of the laser beam is perpendicular to the capillary axis. The laser spot was an ellipse with 26μm×80μm diameters in the probed zone and a confocal distance was about 680 μm near the capillary position. Detection of the beam profile after passing through the capillary filled by sample was accomplished by the displacement of the silicon diode with the split diaphragm (width 100 μm) on the arc. The arc center coincided with the capillary axis and had a radius 80 mm.

As a distance between the laser beam and the capillary axes increases, a beam profile in the photodiode plane transforms from the Gaussian type to a set of the fringes with different intensities. A position of the high intensity fringe deflected on maximal angle was observed to change higher with RI change of the sample. The photodiode was located near the point of the half maximum of this peak. If the temperature stabilization of surrounding air was less 0.01 ^{0}C, RI sensitivity (S/N=2, time constant=1 sec) was measured about 2×10^{-6} RIU (0.0016% of 87% glycerol solution) and the dynamic range was observed about 10^3. The intersection of the 80 μm diameter elliptical laser beam with 100 μm diameter capillary tube is approximately 0.6 nl. There is only about 0.8 pg of glycerol present at the detection limit.

3.Theory

A capillary cross section and a propagation of the ray are shown in Fig.1. From Bougner formula angles of the ray refraction are known as

$$u = \arcsin\left(\frac{d}{r_2}\right); v = \arcsin\left(\frac{n_1 \cdot d}{n_2 \cdot r_2}\right); s = \arcsin\left(\frac{n_1 \cdot d}{n_2 \cdot r_1}\right); t = \arcsin\left(\frac{n_1 \cdot d}{n_3 \cdot r_1}\right) \quad (1)$$

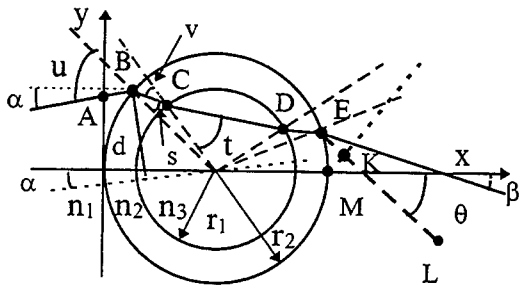

Fig.1. Capillary cross section.

where $d = \sqrt{r_2^2 - y_B^2} \cdot \sin(\alpha) + y_B \cdot \cos(\alpha)$, $n_1 < n_3 < n_2$. The deflection angle β is derived as

$$\beta = 2 \cdot (u - v + s - t) - \alpha \quad . \quad (2)$$

On base of the Huygens principle let consider a complex phase amplitude of a wave at the point L under the angle θ as a result of a superposition of the Huygens wavelets emanating from all points on the capillary surface with coordinates (x_E,y_E) and this amplitude of the wave may be written as

$$A(\theta) = k \cdot \int_l \frac{E_E}{L_4 + L_5} \cdot \exp\left\{-\left[\frac{2 \cdot \pi i}{\lambda} \cdot (n_1 L_1 + 2 n_2 L_2 + n_3 L_3 + n_1 L_4 + n_1 L_5)\right]\right\} \cdot (1 + \cos(\theta - \beta)) \cdot dl_E \quad (3)$$

where k-coefficient, E_E is an amplitude of the wave in the point E on the capillary surface, and L_1=|AB|, L_4=|EK|, L_5=|KL| - paths in the air, L_2=|BC|=|DE| - path in the capillary wall, L_3=|CD| - path in the sample. To simplify calculations an effect of the rays passing out of the fluid was neglected in the equation (3). Due to the large waist length the laser beam can be approximated as a parallel beam falling on the capillary surface (a≅0). In result, the optical path of the wavelet and the quantity $dl(y_E)$ can be expressed through the coordinate x_A ,y_A of the point A by geometric calculations of the ray tracing and the amplitude E_E can be calculated by applying Fresnel formulae to the amplitude E_A of the beam at the point A.

4.Discussion and conclusion

Theoretical and experimental (after the automatic adjustment) fringe patterns are represented in Fig.2 for the capillary filled by a distillate water (n=1.329) and an ethyl alcohol (n=1.356). A good coincidence of the numerically simulated and experimental interference pictures was observed for other capillaries (i.d.=100 μm, o.d.=170, n_2=1.454 and i.d.=75 μm, o.d.=310, n_2=1.454) also.

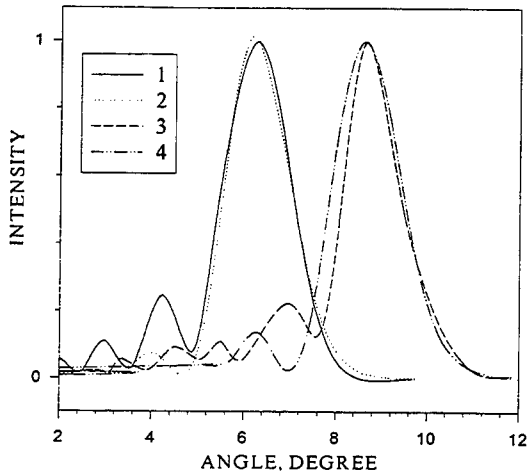

Fig.2. Experimental and calculated interference fringe patterns: 1,3-water and alcohol, experiment; 2,4-water and alcohol, theory.

Results of calculation of the relative signal change caused by the water RI increment 10^{-6} are shown in Fig.3 for the different capillary versus position y_0 of the Gaussian beam center relative to the capillary axis. For each case there is an optimal distance between the beam and capillary axes for which a maximal increment of the signal can be observed, and this distance is not equal zero.

One can see that the RI sensitivity increases with rise of the ratio r_1/r_2 (curves 1, 2). For the same capillaries the RI sensitivity increases with growth of the n_3/n_2 ratio (curve 1, 3). Moreover, from Fig.3 one can conclude that relative fluctuations of

the laser diode power are sufficient and limit RI sensitivity on level of the 10^{-6} RI units for the capillary and the laser diode used in the experiment.

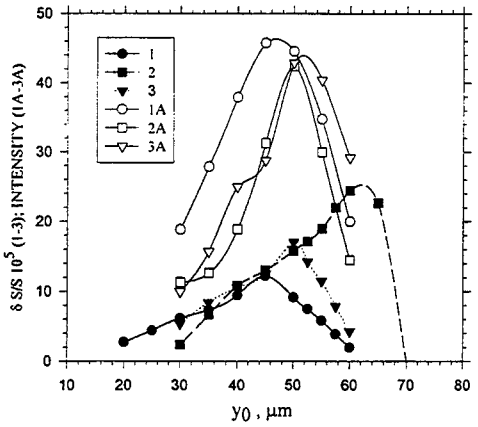

Fig.3. Relative change of the signal caused by sample RI increment 10^{-6} (1-3) and intensity of maximal peak (1A-3A) versus the beam center position y_0:
1-n_1=1.0; n_2 = 1.511; n_3=1.329; r_1=50μm; r_2=100μm;
2-as 1 except r_2=85μm; 3-as 1 except n_3=1.356.

Fig.3 shows also that an amplitude of the maximal peak depends on the distance y_0. For some capillary (curve 2A) the best signal/noise ratio can be reached for the lower values of the RI sensitivity (curve 2). So, an adjustment of the RI detector is expected correct if the main fringe deflected maximally has a maximal intensity.

Thus, to achieve high RI sensitivity of the detection it's important to reduce not only the temperature fluctuations of the probed sample, but to decrease the laser power noise and to select the position of the laser beam also. This proposed model can be applied for the optimization of the RI detectors in various areas of the analytical chemistry and physics where the cylindrical cell is used.

References

1. A.Chartier, S.E. Bialkovski, "Opt. Eng. **36**(2)1997,303-311.
2. A.E. Bruno, A. Paulus, D.J. Bornhop, Appl. Spectrosc. **45**,1991,3,462-467.
3. D.J. Bornhop, N.J. Dovichi, Anal.Chem. **59**,1987, 1632-1636.
4. B. Kratigger, A. Bruno, H.M. Widmer, R. Dändliker, Anal. Chem. **67**, 1995, 124-130.
5. D.J. Bornhop, N.J. Dovichi, Anal.Chem. **58**, 1986, 504-505.
6. R.E. Synovec, Anal.Chem. **59**,1987,2877-2884.
7. A.E. Bruno, B. Krattiger, F. Maystre and H.M. Widmer, Anal. Chem. **63**, 1991, 2689-2697.
8. B.E. Krattiger, A.E. Bruno, H.M. Widmer, M. Geiser, R. Danliker, Appl. Opt. **32**, 1993, 956-965.
9. V.L. Kasyutich, I.I. Mahnach, Proc. SPIE **2208**, 1995, 94-102.
10. D.J. Bornhop, J. Hankins, Anal. Chem. **68**, 1996, 1667-1684.
11. H.J. Tarigan, P.Neil, C. K. Kenmore and D.J. Bornhop, Anal. Chem. **68**, 1996, 1762-1770.
12. L.S. Watkins, J. of the Opt. Soc. of Am. **64**, 1974, 6, 767-772.
13. Kasyutich V.L., Burakov V.S., accepted to "Instruments and Experimental Techniques"17th April 1997.

A Laser and Fiber Optics Based, Passive, Differential System to Measure the Optical Properties of Liquids and Gases

Jennifer Harrolle and Michael Bass
Center for Research and Education in Optics and Lasers (CREOL)
University of Central Florida
Orlando, FL 32801
Tel: (407) 823-6977 FAX: (407) 823-6880
E-mail:bass@creol.ucf.edu
and
Madhu Acharekar
Schwartz Electro Optics
3404 N. Orange Blossom Trail
Orlando, FL 32804

Summary

It is often desirable or necessary to measure the optical properties of liquids and gases in remote locations. Examples include measurement of the absorption and scattering of ocean water or the monitoring of liquid quality during manufacturing large volumes of product. In such cases it may be inconvenient or dangerous or both to retrieve samples for off line measurement and it may be too risky or expensive to submerse the appropriate conventional instruments. In this paper a device is described in which laser light is delivered to a remote sample of liquid by a fiber optic and collected through another fiber optic enabling measurement of optical absorption, scattering and also, if fluorescing materials are present, their emissions. The device is shown schematically in Fig. 1. In a safe location, in a console, are all the operator controls, laser light sources, beam handling and control optics and electronics to generate the light, deliver it to the send fiber and sense light returned by the appropriate collector lens - return fiber combination. At the distal end of the send fiber a lens collimates the beam for transmission through the medium. A second lens collects the transmitted or scattered light and focuses it into a return fiber. Detectors and electronics in the console record and process this data.

By viewing the light directly transmitted through the liquid optical absorption is measured. In fact, by including two send fibers and two return fibers which probe different lengths of the liquid in the cell a differential measurement of absorption is obtained and the liquid's absorptivity can be calculated. By viewing off axis light scattering can be determined and changes monitored. Should it be required to sense fluorescence, an exciting wavelength can be sent to the remote cell and appropriate filters can be placed before the detectors to limit the sensed signal to just the emitted light.

Initial experiments to determine the absorption of water through fibers as long as 300 m have already been carried out. The results of these measurements at three wavelengths derived from HeNe lasers are shown in Fig. 2 where they are also compared to results obtained from a conventional spectrophotometer. These data were taken in the

visible since that is the optical pass band of water. It is likely that the difference in the measured values is a result of scattering in the water. Off-axis scattered light is not refocused by the transmitted light collecting lens into the return fiber and so will result in a large apparent absorption coefficient. Measurements at other wavelengths or with a tunable laser source rather than three different wavelength lasers are easily implemented. The present results demonstrate the feasibility of the concept.

Measurements of scattering and fluorescence from remote samples will also be presented. Applications and design questions will be discussed.

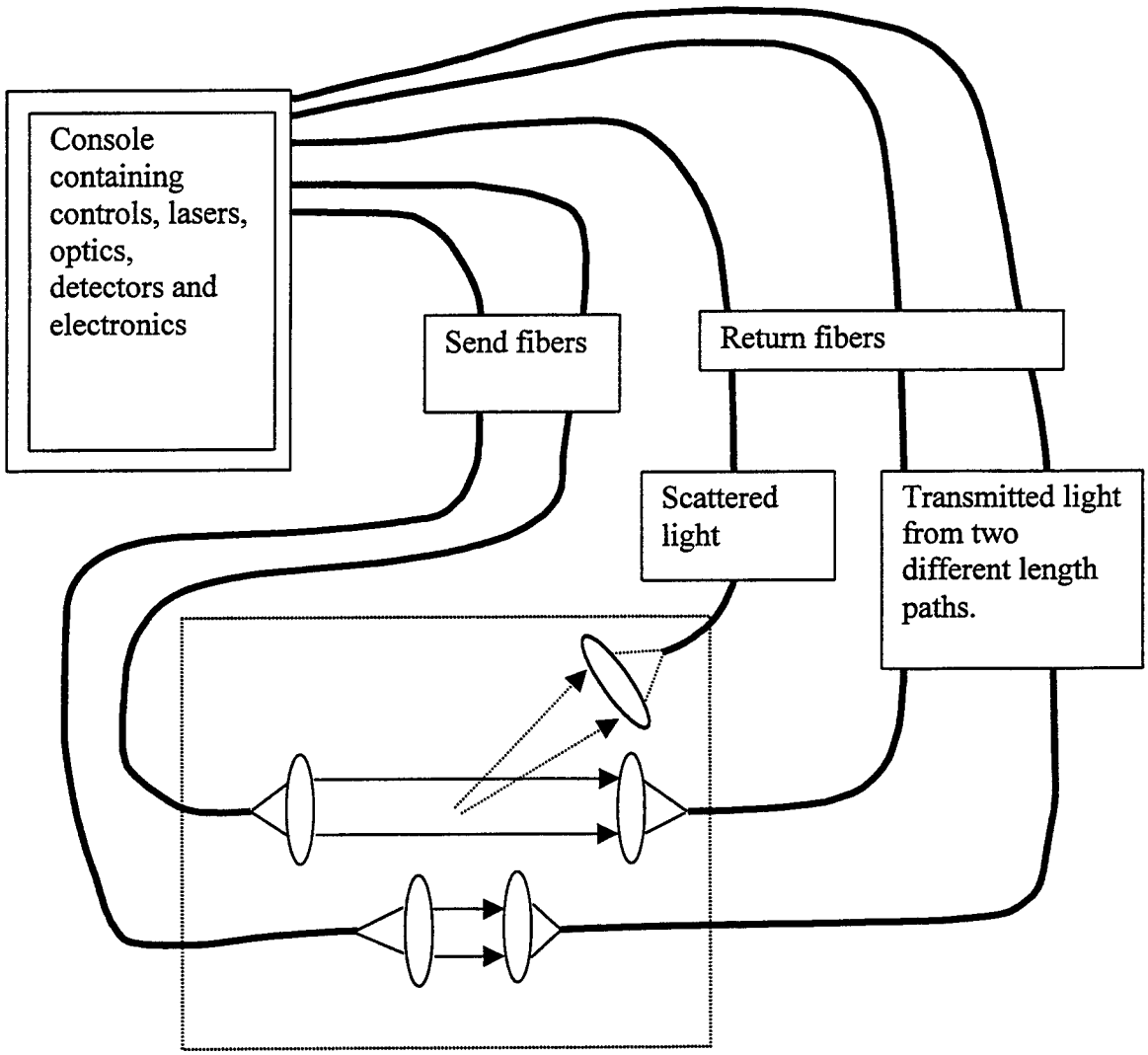

Liquid or gas filled cell containing only passive components such as lenses, fiber ends and filters. The send and collect lenses may serve as windows on the cell to keep liquid away from the fiber ends.

Figure 1. Sketch of remote sensing system concept.

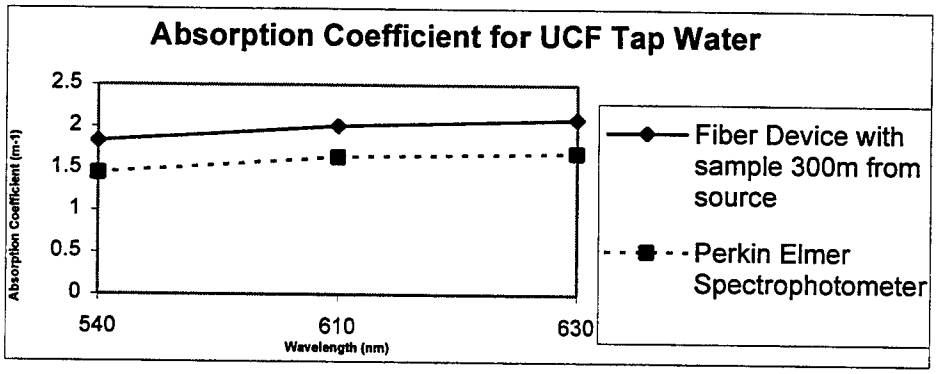

Fig. 2. Absorption coefficient measured for tap water using the reported system and a conventional spectrophotometer.

Velocity, Temperature and Density Measurements in Reacting Flows Using Laser-Induced Gratings

Michael S. Brown
Applied Spectroscopy Group
MetroLaser, Inc.
18010 Skypark Circle, Suite 100
Irvine, CA 92614
Ph (714) 553-0688, Fax (714) 553-0495, e-mail mbrown@metrolaserinc.com

William L. Roberts
Dept. of Mechanical and Aerospace Engineering
P.O. Box 7910
North Carolina State University
Raleigh, NC 27695
Ph (919) 515-5294, Fax (919) 515-7968, e-mail roberts@mae.ncsu.edu

The development of future commercial combustors, as well as the refinement of current models, relies heavily on diagnostic information collected on operating combustors. Key diagnostic information includes spatially resolved maps of the local velocity, temperature, and density fields. Optical diagnostics in commercial combustors are hampered by complications due to high pressure and the presence of particulates, such as soot, which greatly increases the flame luminosity. To meet these challenges we are pursuing laser-induced grating techniques. Recent work has shown that these techniques perform well at high pressure (Brown *et al* 1995) and in the presence of soot (Brown and Roberts 1997). To date successful speciation and thermometry have been demonstrated, and the first report of velocity measurements has recently been communicated by Paul Ewart's group.

We are currently engaged in work to demonstrate the multiplex capabilities of laser-induced grating techniques by measuring the local velocity, temperature and density simultaneously using non-resonant pump beams. This work requires heterodyne detection of the time-resolved signal. Careful analysis of the corresponding power spectrum permits extraction of the local velocity, temperature and density. The response of the probed medium includes the generation of two counter-propagating acoustic modes that behave as dictated by the local velocity, temperature and density. Hence, monitoring the dynamics of the acoustic modes permits diagnostic measurement of these three physical parameters. To date, nearly all transient grating measurements have been made using homodyne detection. We note that with the addition of a third pump beam, two-dimensional velocity measurements will be possible.

Typically, transient grating signals are acquired with the grating planes oriented parallel to the flow direction. In this geometry, net molecular motion is perpendicular to the propagation direction of the acoustic waves. By re-orienting the grating planes normal to the net flow, the net molecular motion parallels that of the induced sound waves. Herein lies the essence of transient grating velocimetry. For the parallel grating orientation, the scattered signal beam bears the Doppler shifts of the acoustic waves only. In the perpendicular configuration, however, the signal beam bears the Doppler shifts of both the sound waves and the net molecular motion. By analyzing the laser-induced grating signal in the frequency domain, these Doppler shifts can be measured. This analysis is performed using the power spectrum of the acquired signal. It is important to note that the local speed of sound is a strong function of the local temperature but a weak function of the local mixture fraction.

In **Figure 1**, we show a typical non-resonant transient grating signal taken at ambient conditions along with a theoretical best fit to the data. The power spectrum of the fit plotted in **Figure 1** is shown in

Figures 2-3 below for both homodyne and heterodyne detection. **Figure 2** represents the no-flow condition while **Figure 3** represents flow fields with a velocity equal to 1/10 that of the sound speed. For both cases, the homodyne spectrum consists of two features: one near zero frequency, representing the entropy fluctuations (Rayleigh feature) induced in the gas, and the other at a shifted frequency, representing the acoustic fluctuations (Brillouin feature). The Brillouin spectral feature is frequency shifted by an amount determined by the local sound speed and the grating wavelength. The halfwidth is determined by the acoustic damping coefficient making it proportional to the inverse of the density. The Brillouin feature in the homodyne spectrum lies at a frequency shift corresponding to twice the speed of sound. This is due to the fact that the counter-propagating acoustic modes produce a modulation at twice the acoustic Doppler frequency shift, $2f_B$. For no net flow, the heterodyne spectrum shows three spectral features, the $0f_B$ and $2f_B$ features of the homodyne spectrum along with a feature at $1f_B$. This third feature gives the Doppler beat between either of the acoustic modes and the non-propagating entropy wave. For non-zero flow, this third feature splits into two features. In **Figure 3**, we show an example of this splitting for the case of $V/C_s = 0.1$. The new feature components are split by the Doppler shift between the net fluid flow and the acoustic modes, $f_B \pm f_V$. So, in a heterodyne transient grating power spectrum, the temperature is given by the half the shift of the $2f_B$ feature while the component of the velocity is given half the frequency separation of the split component at $1f_B$. We note that by definition a power spectrum has only positive frequency components. The left most split feature will continue to move toward lower frequencies as the fluid velocity increases until the fluid velocity equals that of the sound speed. At this point, the feature will begin shifting to higher frequencies.

In summary then, simultaneous velocity, temperature and density information can be extracted from a transient grating signal when heterodyne detection is employed. The frequency shifts of the Brillouin features in the corresponding power spectrum are determined by the local temperature and fluid velocity. The widths of these features are determined inversely by the density. Our current laboratory work centers on determining the accuracy of these types of measurements for reacting-flow applications.

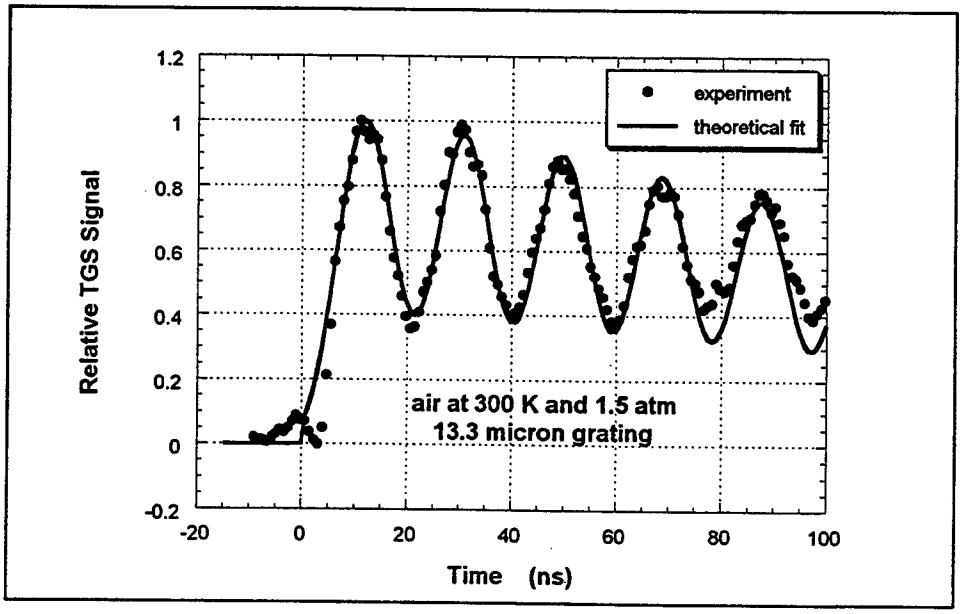

Figure 1. Nonresonant laser-induced grating signal with the accompanying theoretical fit. (Homodyne detection was used.)

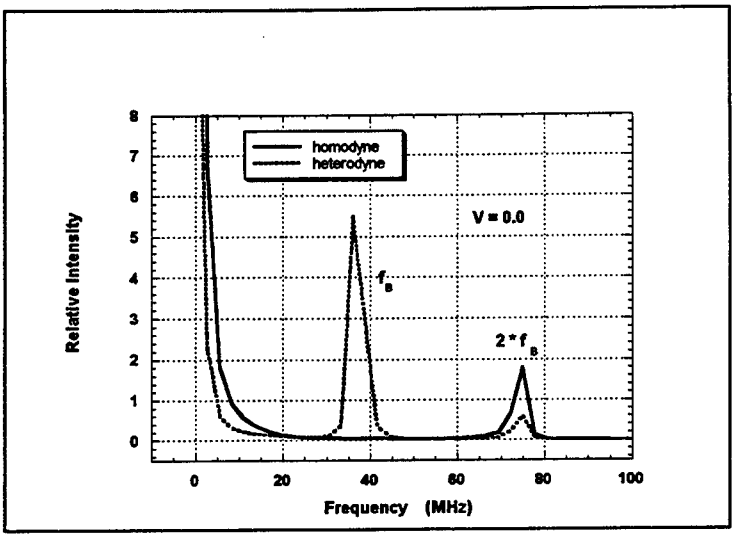

Figure 2. Heterodyne and homodyne power spectra for the transient grating signal shown in Figure 1 (zero velocity case).

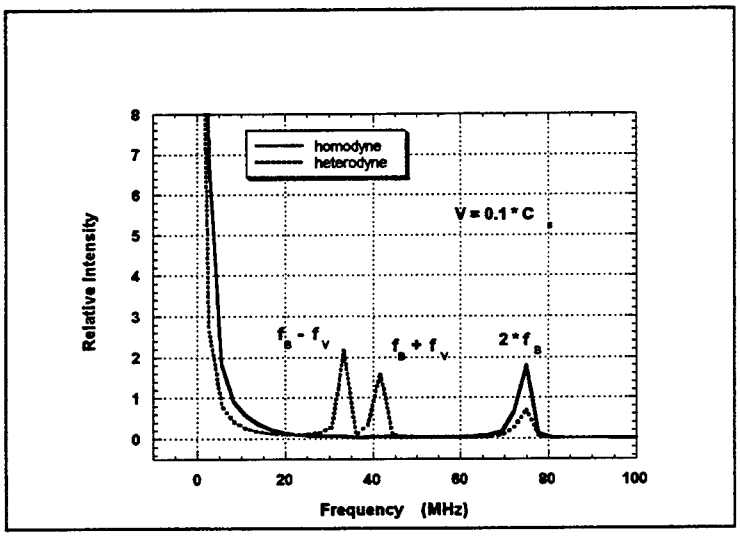

Figure 3. Power spectra for the conditions of Figure 1 assuming a net fluid velocity equal to one-tenth that of the speed of sound, $V/C_s = 0.1$.

M.S. Brown, P.A. DeBarber, E.B. Cummings and H.G. Hornung, "*Trace Species Concentration and Temperature Measurements at High Pressure Using Laser-Induced Grating Spectroscopy*," paper # 2546-72, SPIE, Optical Science, Engineering and Instrumentation, San Diego, CA (1995).

M.S. Brown, W.L. Roberts, "*Single Point Thermometry in High Pressure, Sooting, Combustion Environments,*" submitted to (AIAA) Journal of Propulsion and Power (Sept. 1997).

A Phase-Based Metrology System for Measuring Trace-Gas Concentration

J.H. Rentz, J.A. Gargas, and C.R. Schwarze

Optra, Inc.
461 Boston St.
Topsfield, MA 01983-1290
phone: (978) 887-6600 fax: (978) 887-0022

Project Summary

I. Introduction

Recent advances in tunable laser diodes and their availability at multiple wavelengths in the near-IR has opened a new era of spectroscopic gas concentration measurement techniques. By adjusting temperature and injection current, the laser diode can be tuned to the wavelength of a molecular resonance of interest, and the absorption can be measured and used to obtain concentration. The injection current can also be modulated, allowing for synchronous detection schemes such as wavelength and frequency modulated spectroscopy (WMS and FMS) which effectively bypass the large 1/f noise component of the laser diode.[1-4] In this paper, a new WMS technique is presented which measures phase due to the anomalous dispersion around a resonance for trace gas detection.

II. Theory

This technique uses a polarization sensitive Mach-Zhender interferometer to measure a phase signal which is proportional to the slope of the anomolous dispersion profile. One arm of the interferometer contains a sample cell filled with the gas under study and the other arm a vacuum reference cell as shown in Figure 1.

Figure 1.

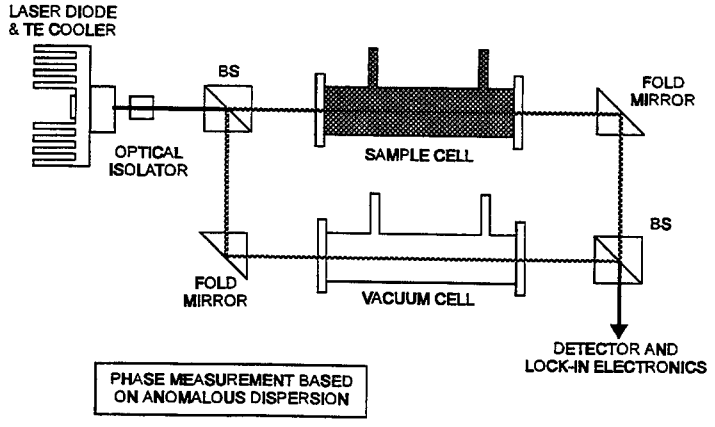

The laser is dithered about the line center with an amplitude equal to the full-width at half-max (FWHM) of the transition. Light which traverses the sample gas cell develops a phase shift relative to the vacuum reference cell due to the anomolous dispersion in the gas; the resulting optical signals at the detectors are given by

$$P_{A,B} = \frac{P_0}{2}(1 \pm Sin(2\pi\sigma L(\Delta n)) \quad (1)$$

where P_o is the laser diode power, σ is the wavenumber, L is the path length, and Δn is the refractive index difference due to the anomolous dispersion. The phase is extracted by normalizing the difference signal by the sum signal,

$$V_\phi = \frac{V_{A-B}}{V_{A+B}} = Sin(2\pi\sigma L(\Delta n)). \quad (2)$$

Equation 2 also shows that this technique eliminates laser relative intensity noise (RIN). The refractive index difference, Δn, for an input frequency modulation equal to the FWHM is

$$\Delta n = \frac{\alpha_o}{4\pi\sigma_o}. \quad (3)$$

For ppm and ppb concentrations, the magnitude of the phase becomes

$$V\phi = \frac{\alpha_o L}{2}. \quad (4)$$

Equation 4 demonstrates the direct dependence of phase on absorption and, thus, concentration.

Figure 2 depicts the relationship between slope of the anomalous dispersion and phase modulation amplitude. The input frequency modulation, $\Delta\omega$, generates an output phase modulation, V_ϕ, which is proportional to the slope of the anomalous dispersion. It is also clear from Figure 2 that this phase-based method produces a significantly larger signal than absorption techniques for small modulation amplitudes. This difference is because the slope of the absorption profile goes to zero near line center while the slope of the anomalous dispersion profile is at its maximum at line center.

Figure 2.

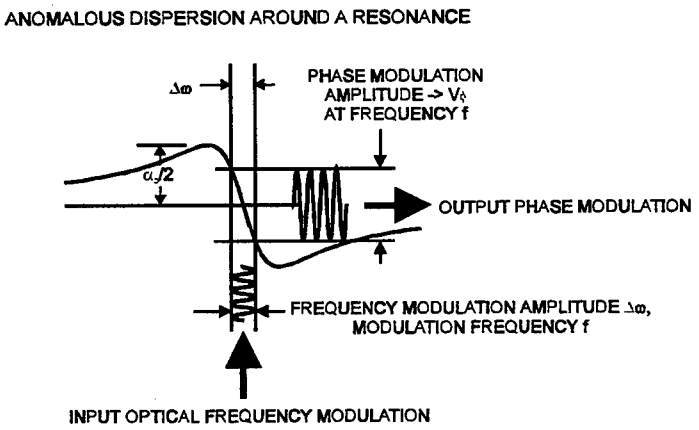

III. *Experimental Results*

Measurements have been made using this technique for water vapor at 1392.5 nm. Water vapor cells were made containing two different known concentrations. A low concentration cell was filled with dry nitrogen of a known water quantity and pumped down to the Doppler region. A high concentration cell was filled with 100% RH air and pumped down to the same pressure. A computer model was used to overlay the data and extract a concentration measurement. Figure 3 shows the profile obtained at the first harmonic of the input modulation frequency for the high concentration cell. The profile generated is actually the first derivative of the anomalous dispersion curve as dictated by the Kramers-Kronig relations; the profile seen at the second harmonic is the second derivative, which also resembles the original anomalous dispersion curve.[5] The measured concentration was $3.25*10^{15}$ molecules/cm^3 with a theoretical concentration of $9.8*10^{14}$ molecules/cm^3. The discrepancy can be attributed to the sealing process of the cells extracting excess water from the cell walls. The low concentration profile is shown in Figure 4. The measured concentration was $6.5*10^{14}$ molecules/cm^3 with a theoretical concentration of

$2.4*10^{13}$ molecules/cm^3. Again, uncertainty in the control measurement can be attributed to the sealing process. The asymmetry in the low concentration profile is the result of a slight path difference in the two arms of the interferometer which exhibits itself as a bias away from the resonance. This bias was small, however, in comparison to the measurement signal.

Further work demonstrating this measurement technique is in progress utilizing variable pressure cells with a hygrometer, a pressure transducer, and a vacuum pump. The goal is to eliminate the uncertainty due to the sealing process through real time monitoring of the cell's humidity and pressure. This work will allow for multiple measurement at various concentrations in the Doppler-, Voigt-, and Pressure-broadened regimes.

Figure 3.

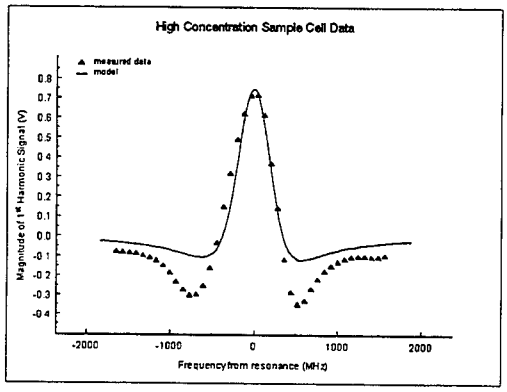

Figure 4.

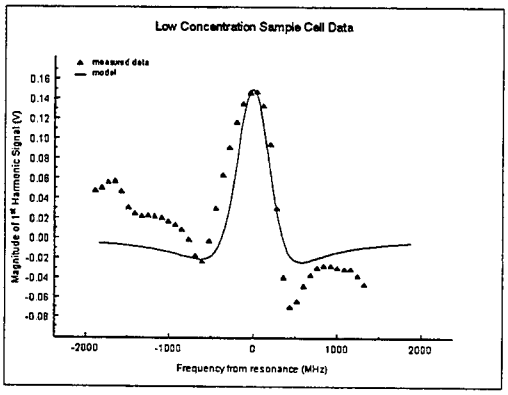

IV. Summary

A new and innovative method for trace gas detection has been presented using the slope of the anomalous dispersion curve around a resonance to determine concentration. This method has proven to be superior to straight absorption techniques in that the measurement signal is independent of laser relative intensity noise as well as intensity modulation. This phase-based technique also results in a significantly larger signal than absorption-based methods for small modulation amplitudes.

References

[1] Reid, J. and Labrie, D., "Second-Harmonic Detection with Tunable Diode Lasers - Comparison of Experiment and Theory", Appl. Phys. B, 26, pp 203-10 (1981).

[2] Carlisle, C. and Cooper, D., "Tunable-Diode-Laser Frequency-Modulation Spectroscopy Using Balanced Homodyne Detection", Opt. Lett., Vol 14, No 23, pp. 1306-08 (1989).

[3] Goldstein, N. and Adler-Golden, S., "Long-Atmospheric-Path Measurements of Near-Visible Absorption Lines of O_2 Isotopes and H_2O with a Prototype AlGaAs Laser Transceiver System", Appl. Opt., Vol 32, No 30, pp. 5849-55 (1993).

[4] Hovde, D. and Parsons, C., "Wavelength Modulation Detection of Water Vapor with a Vertical Cavity Surface-Emitting Laser", Appl. Opt., Vol 36, No 6, pp. 1135-38 (1997).

[5] Yariv, A., Quantum Electronics, 3rd Edition, John Wiley & Sons, NY. (1989).

Laser Probe of Surfaces of Bacteriorhodopsin Langmuir-Blodgett Films by the Method of Second Harmonic Generation

A.V.Kir'yanov, I.A.Maslyanitsyn, V.V.Savranskii, and V.D.Shigorin
General Physics Institute, Vavilov St.,38, Moscow 117942, Russia.
Phone: (095) 135-0327, fax: (095) 135-2055

Among the numerous methods of laser probing surfaces of Langmuir-Blodgett films (LBF), the method of Second Harmonic Generation (SHG) seems to be one of the most powerful ones. This method followed the discovery of SHG phenomenon in LBF [1]. So far, SHG was observed in LBF of various organic compounds. Recently, a few papers appeared dealing with studies of LBF surfaces by the SHG method (see, for example, [2]). It is characteristic that one can use this method to conclude about such properties of the films as degree of their homogeneity, orientation of the component molecules, etc. A strong dispersion-induced increase in the nonlinearities in combination with weak absorption in thin LBF can result in the generation of quite strong SH even if the molecules do not have the specific structural criteria [3] of high hiperpolarisability. Among such molecules, bacteriorhodopsin (bR, pygment of purple membranes of bacterium *Halobacterium Halobium*) is selected in this paper to demonstrate possibilities of the method.

The bR LBF samples were manufactured using KSV-5000 deposition system and the deposition technique described in [4]. The LBF were multilayer films of both Y- and Z-configurations, which are deposited from the surface of water (ph=6.6, T=20.5°C) subphase on fused silica wafers. It is worth noting that bR LBF of Z-type of up to 40 layers were manufactured at first (see [5]) and that namely LBF of such type can be used for SHG experiments.

The nonlinear optical properties of the films were investigated with the modified apparatus described in [6]. Its schematic diagram is shown in Fig.1. It should be noted that the filters pass band and the quadratic dependence of the observed signal on the pump radiation (λ=1.06 μm) power provided evidence that the SH was actually generated. A plane-parallel qurtz plate, oriented at angle of incidence corresponding to the maximum of the Maker fringes, was used as a reference. We concluded about the homogeneity of a LBF sample and its potential use for further experiments and usage by scanning its surface with the pump laser beam (in steps of 1 mm) and recording the SH signal. The angle of incidence of p-polarised pump radiation on a sample was 45° and a p-polarised SH was recorded. The charts of the spatial distribution $I_{2\omega}$ (X,Y) obtained by such a way made it possible to determine "quality" of the surface composed of multilayer LBF

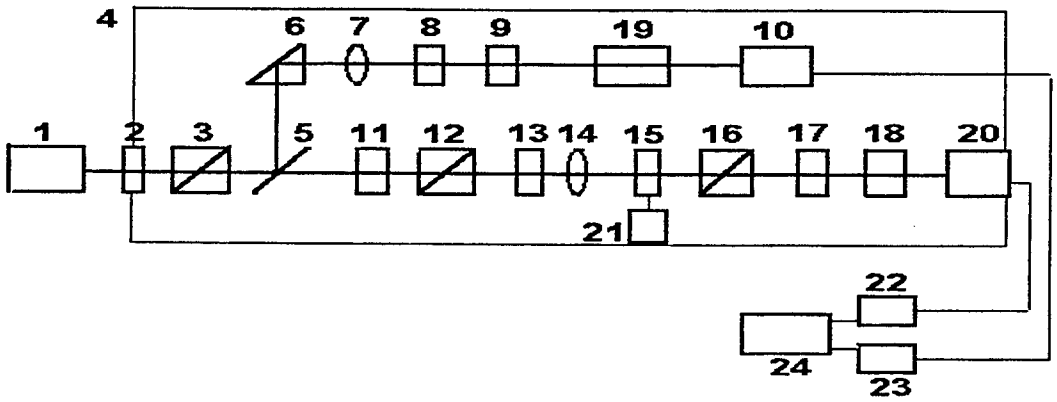

Fig.1. Schematic diagram for testing surfcaes of LB films by the method of SHG.

1 - pulsed Nd-YAG laser (1.06 mkm, 1 mJ, 18 ns); 2, 13 - IR filters; 3, 12, 16 - Glan prisms; 4 - "black box"; 5 - beam splitter; 6 - prism; 7, 14 - lenses; 8 - reference crystal; 9, 17 - neutral filters; 10, 20 - photodetectors; 11 - polarization rotator; 18, 19 - SH (0.53 mkm) intereference filters; 21 - scanning engine; 22, 23 - Analog-to-digital converters; 24 - personal computer.

structure on the wafer. (Our setup also allows to rotate the sample, with step of 1°, and to study the nonlinear properties of surfaces by analysis of well-known Maker's oscillation. Such experiments permit to conclude on second-order susceptibility tensor elements of LBF quasycristalline structure for a variety of organic compounds.)

One of the "SHG maps" $I_{2\omega}$ (X,Y) of bR LBF of Z-type is shown in Fig.2. It is important that the suggested technique makes it possible to control quality of deposited LB layers step-by-step during the deposition, that, equally with a control of transfer coefficient provided by the automatical KSV-5000 system, is fruitful method to manufacture organic LBF of high quality. The last is especially crucial for their use for phase conjugating, optical data storage, etc.

References

[1] O.A.Aktsipetrov, et al. JETP Lett., **37** (1983), p.207.

[2] L.V.Belovolova, et al. Sov. J. Quantum Electrn., **26** (1996), p.538.

[3] D.S.Chemla and J.Zyss (Eds.) Nonlinear Optical Properties of Organic Molecules and Crystals (N.-Y.: Academic Press, 1987).

[4] M.Ikonen, et al. Thin Solid Films, **213** (1992), p.277.

[5] A.V.Kir'yanov, et al. Technical Digest of "Thin Organic Films'97 Topical Meeting" (Long beach, California, 1997), Poster Session (in press).

[6] A.A.Kaminskii, et al. Phys. Stat. Solidi A, **125** (1991), p.671.

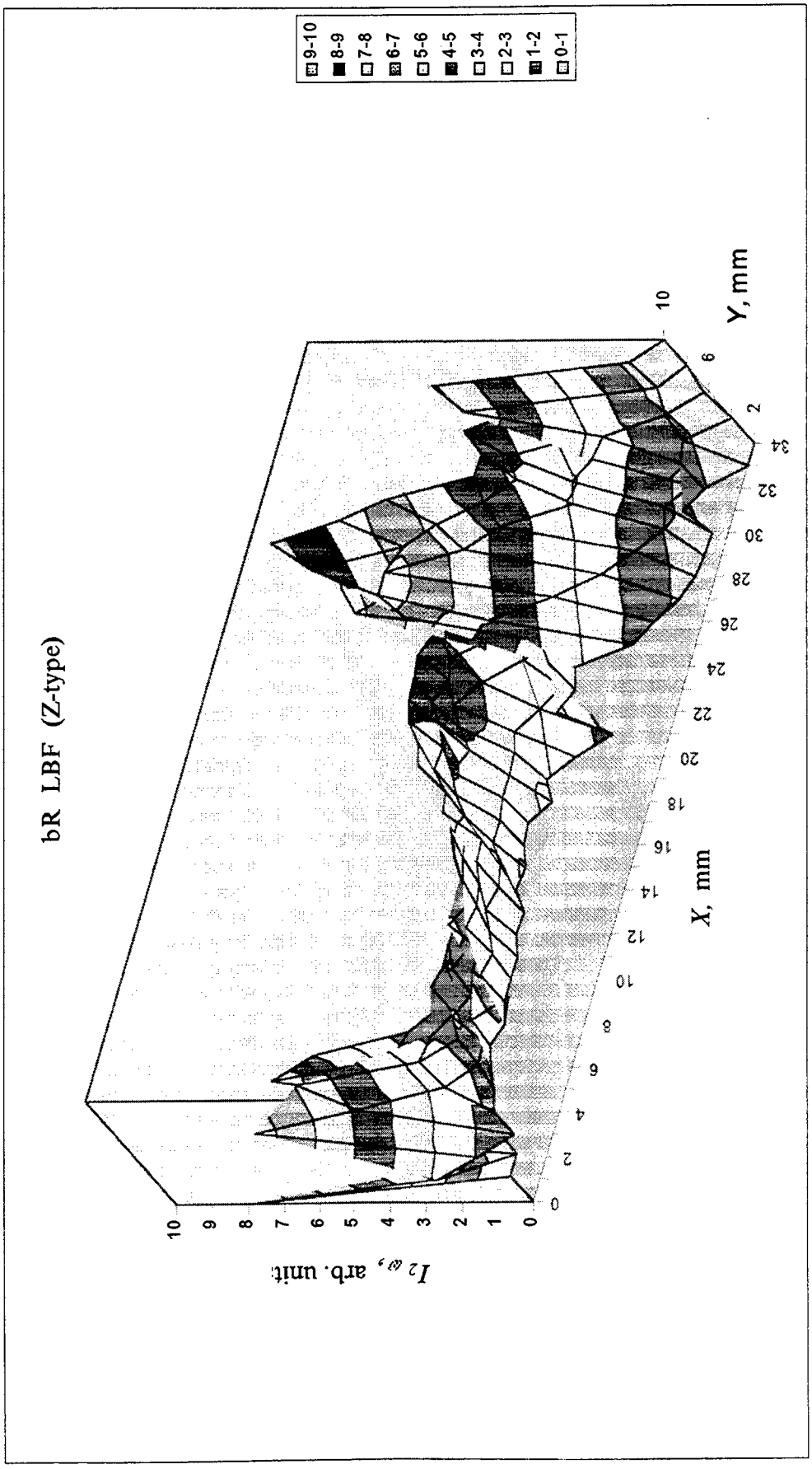

Fig.2. "SHG map": Distribution of SH intensity, $I_{2\omega}$, (in units of 10^{-6} of SH intensity from a reference sample, α-SiO_2) emitted by multilayer bR LBF (Z-type, number of layers - 35).

X, Y - coordinates along the length and width of the sample. Both the waves of incident fundamental radiation (pumping) and SH are p-polarized. Angle between IR pumping wave and bR LBF surface is 45°.

Laser Induced Fluorescence of Aromatic Hydrocarbons in diesel oil laminar premixed flames

F. Cignoli, S. Benecchi, S. De Iuliis and G. Zizak
CNR-TeMPE Istituto per la Tecnologia dei Materiali e dei Processi Energetici
via Cozzi, 53 - 20125 Milano – ITALY
tel: +39-2-66173.304, fax: +39-2-66173.321

Introduction. Because of the planned limitations on pollutants it is becoming more and more stringent to reduce IC engines emissions. In particular, for diesel oil engines, the reduction of soot emission is mandatory. It is well known that aromatic compounds play an important role in the mechanisms of soot production. It is possible that the different classes of aromatics naturally present in the Diesel fuel lead to the formation of different amounts of soot. For this work a set of seven fuels with calibrated composition of different blend of mono-, di- and tri-aromatics but with total aromatic content of about 27% was made available by ELF (Solaize, France). Soot and aromatic hydrocarbons profiles have been detected on the axis of rich premixed flames in order to find possible correlations.

Experimental. To produce rich premixed diesel oil flames, we have developed a special burner assembly in which the inner air flow sucks and nebulizes the fuel in a heated chamber. To obtain stable fuel consumption a special reservoir was developed keeping the free surface at constant level with a peristaltic pump. The diesel oil droplets evaporate and mix with an external pre-heated air flow. A double air feed allowed the achievement of a wide range of equivalence ratios. By means of a cable heater with thermocouple feed-back, the whole body of the burner was kept at about 200°C, which turned out to be the best compromise for flame stability and good vaporization without self-ignition. The mixing tube was 30 cm long thus allowing homogeneous mixing without recondensation of the fuel components. At the 9 mm burner mouth a Bunsen type flame was obtained and a multi-hole ring produced a surronding annular flame for anchoring the main flame and reducing air entrainment. The burner was fixed on a motorized two-axis table allowing maximum displacements of 100 mm with 0.1 mm resolution. Some scattering tests have been carried out to select the most suitable flame structure for the application pursued. A good trade off between flame stability and soot scattering signal was found to be around $\phi = 2.3$. In these conditions, flames of total visible height of 130-140 mm were obtained with soot starting at a height of 45-50 mm.

SOOT MEASUREMENTS BY LASER EXTINCTION/SCATTERING. For soot measurements, the extinction/scattering technique was used in order to determine the soot volume fraction, optical diameter and number density of soot particles. The measurements were carried out by focussing the beam of a He-Ne laser (25 mW at 632.8 nm) in the flame and measuring the extinction by a photodiode placed beyond the flame. A further photodiode was used in order to monitor the laser intensity. For scattering measurements, the scattered light was collected at 90° with respect to the incident beam by a monochromator equipped with a photomultiplier. Signals were processed by a lock-in amplifier after mechanical chopping of the laser beam. The output voltage was measured by means of a digital voltmeter and stored in a PC. In order to reduce the effect of flame instability axial and radial profiles were obtained tipically averaging 100 measurements . With this system good sensitivity was achieved with a detection limit of 10^{-3}.

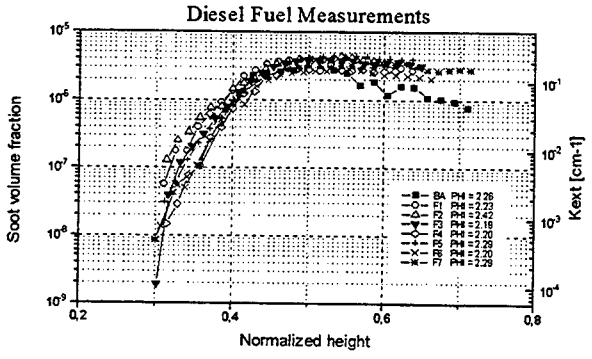

Fig. 1:Soot volume fraction and Kext

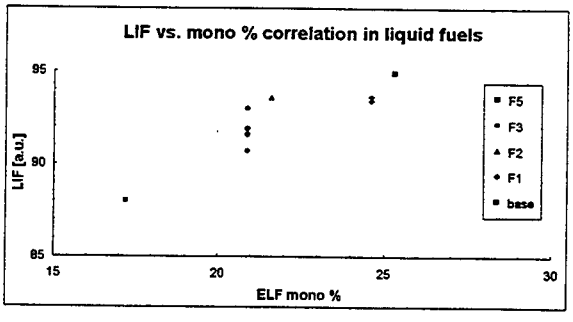

Fig. 2: Correlation between LIF and mono- content

Due to the line-of-sight nature of the extinction measurements a mathematical Abel inversion procedure [1] was employed to obtain the local profiles of the extinction coefficient, k_{ext}, from the chordal measurements. Thorough application of the scattering/extinction technique has resulted in a significant amount of data concerning soot

production in premixed flames of all fuels. These data are summarized in fig. 1 where the axial profile of soot volume fraction for all fuels is shown. The use of the logarithmic scale highlights that the soot formation dynamics is rather similar for all flames. A steep growth (in the region corresponding to 0.3-0.45 of the total flame height) is observed followed by a flattening at about the mid-point of the flame, while further upwards soot consumption takes place. The maximum soot volume fraction is obtained for fuels F5 and F2, while the minimum is for fuels F4, F6 and Base. Nevertheless differences are small (about 25% from the average). More information concerning the optical diameter and the number concentration of soot particles have been obtained. In general particles are visible starting from around 5-10 nm and then continuously grow up to 35-50 nm depending on the fuel. After the mid-point of the flame the optical diameter reduces due to oxidation. As for the number density, a rather rapid growth is detected, peaking around 40% of the total flame height. Then a smooth decrease follows, mainly due to aggregation.

Overall, the test fuels do not display appreciable differencies as far as maximum soot yield is concerned. Although some differences were observed in particular associated with viscosity and tri-aromatic content, such differences are too small to draw definite conclusions. This is also due to the uncertainties and noise of the measurements, basically due to flame instabilities. Nonetheless, this is an indirect confirmation of the weakness of the effect under investigation. Provided that, as clearly illustrated by the figure 1, no outstanding differences are visible among the test fuels, the detection of classes of aromatic hydrocarbons (hereafter called for simplicity PAHs) was useful to elucidate the reason.

PAHs measurements by LIF. The highly efficient fluorescence of aromatic molecules under UV excitation was exploited for the detection of such compounds in diesel flames. The experimental apparatus is rather simple and employes a Nd:YAG laser. The UV output at 266 nm is mildly focussed in the probe volume (roughly 200 μm in diameter) from which the fluorescence signal was measured with an optical multichannel detector. Spectra were stored and elaborated in a PC. In order to interpret the data, spectra were deconvoluted by means of a previously implemented software and data bank. This last consists of about 150 fluorescence spectra of individual pure aromatic compounds, taken from different sources. The deconvolution procedure is based on a least square routine with positive solution and was previously validated on sample mixtures of known composition [2].. As a further test, we have taken the spectra from the fuels in liquid phase (either pure or in cyclohexane solution). The results of the deconvolution were compared with the composition data made available by ELF. This is illustrated in fig. 2 for the content of monoaromatics where a good correlation between the LIF and the chemical analysis is shown. Similar plots were obtained for di- and triaromatics but the results are not reported here.

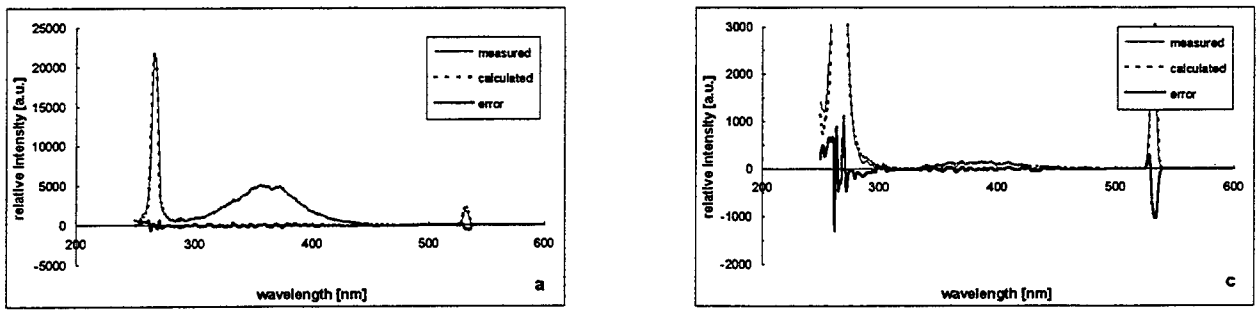

Fig. 3: Typical spectra along the flame axis.

Typical fluorescence spectra obtained in the inner core of the flame before the soot inception zone are reported in fig 3a and 3c. Fig. 3a was taken just above the burner mouth, where the spectral signature partly reflects the characteristics of the liquid fuel, while fig. 3b refers to a position higher in the flame just before the soot inception. Here the fluorescence signal drops to zero. Altough these spectra are related to fuel F3, the same behaviour is found for all fuels. In general three main zones are evident within the flame. At the burner exit a strong fluorescence signal is detected (fig. 3a) which is confined within 280-450 nm. Moving upwards the fluorescence intensity constantly decreases and the second zone is found where the fluorescence signal becomes very small (fig. 3c). This zone is about 10 mm long on the flame axis, and falls at about 30% of the total flame height. Above this, the third zone is entered, which is characterized by the presence of soot. Due to this, the spectrum changes significantly, with a strong resonant scattering and a non-flourescence broad band component as shown in fig. 4. This last originates from the laser induced soot incandescence and is structured as a black body emission [3,4]. This component can be evaluated by means of a time-delayed measurement, having a decay time much longer then the ones of resonant scattering and fluorescence [5]. The incandescence spectrum will be later subtracted from the complete spectrum to obtain the fluorescence contribution which in this zone grows again.

The deconvolution of the spectra allows the behaviour of PAH's families and soot to be followed along the flame. Fig. 5 for Base fuels gives an example of the general behaviour of all the fuels. The heights are normalized to the center of the "dark zone", which always falls, as already stated, around 30% of the flame height. From the analysis of the profiles for all fuels it is possible to see that whatever the initial conditions (fuel composition and/.or structure of the left side of the graphs), a zone is reached where all fluorescence signals are lost and exactly above it soot starts to be detected. Here some fluorescence from PAH's appears again, indicating that these compounds are newly formed in some amount. From the whole set of results given above it is apparent that at some distance (about 20 mm) from the burner mouth, no significant differences in the spectral shape of the fluorescence signal could be observed for the different fuels. Moreover, the fluorescence spectra at the exit of the burner, although showing some distinctive features according to the fuel, largely differ from the spectrum of the fuel in liquid phase. This suggests that some significant changes can take place in the mixing tube in spite of the relatively low bulk temperature

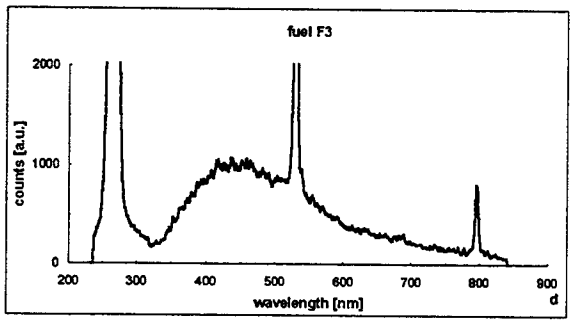

Fig. 4 Spectrum in the soot region

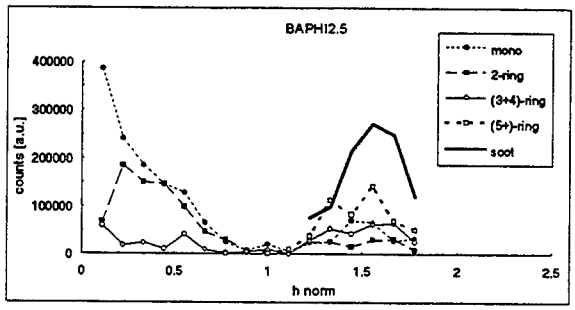

Fig. 5: Axial profiles of PAH's and soot for Base fuel.

Conclusions. A major conclusion of this work is that the formulation of the fuel composition (in the range examined, that is different percentages of mono-, di-, tri-aromatics but with constant total amount of about 27%) has little effect on soot production. This is consistent with some engine tests carried out by an other group within the frame of the same research programme. Some weak trends have been observed (with tri-aromatics and viscosity) but these are difficult to interpret because of the superimposition of flame instability effects. A tentative explanation of this behaviour is suggested by the observation of PAH's profiles. In particular, our data indicate that about 10 mm above the burner the same spectral signature (and therefore the same content in aromatics) is obtained for all fuels. Furthermore a zone exists in the flame where no fluorescence is detectable, again for all fuels. This leads to the conclusion that some important process occurs through which all aromatics are changed in other non-aromatics and non fluorescing species. If this is true, it become understandable that the production of soot would depends on the total amount of aromatics rather than on some specific classes of compounds.

References

[1] C.J.Dasch, Appl. Opt. **31**, 1146-1152 (1992).

[2] G.Zizak, F.Cignoli, G. Montas, S. Benecchi, R. Dondé, Recent Res.Devel. in Applied Spectro. **1**, 17-24 (1996).

[3] L.A.Melton, Appl. Opt. **23**, 2201-2208 (1984).

[4] B.Quay, T.W.Lee, T.Ni, R.J.Santoro, Comb.Flame **97**, 384-392 (1994).

[5] F.Cignoli, S.Benecchi, G. Zizak, Appl. Opt.**33**, 5778-5782 (1994).

Optical Pulse Propagation via Whispering Gallery Modes in Glass Spheres

W. B. Whitten, R. W. Shaw, M. D. Barnes, and J. M. Ramsey
Chemical and Analytical Sciences Division
Oak Ridge National Laboratory
P.O. Box 2008 MS-6142
Oak Ridge, TN 37831-6142
Phn: 423/574-4882 Fax: 423/574-8363

Introduction

Early in this century, Rayleigh[1] showed that waves could propagate close to the wall of a spherical cavity with very little loss as long as the wavelength was small compared to the cavity circumference. The treatment was primarily for acoustic waves, modeling the whispering gallery effect, but he pointed out that electromagnetic waves should behave similarly. Study of the optical properties of dielectric spheres has received new interest with improvements in optical instrumentation and the emergence of new applications for high-Q resonators. It has recently been shown that optical pulses propagating in whispering gallery modes can be treated analogously to pulses in a fiber optic waveguide. Since the optical fields extend beyond the surface of the sphere, the sphere's environment could alter propagation properties such as cavity ringdown time. We describe here some time and frequency-domain measurements of picosecond pulses in glass spheres of millimeter dimension and discuss potential analytical applications.

Experimental

Two-picosecond duration pulses near 920 nm were generated using a Kerr lens mode-locked titanium:sapphire laser. The pulse train repetition frequency was 76 MHz, and the average power was 1 watt. The pulses were focussed into a 30-mm equilateral prism (SF-18, n=1.722) at near normal incidence such that the beam waist was positioned near the second prism face, where evanescent wave coupling to a glass sphere (BK-7, n=1.51) occurred. The spheres were loosely mounted on an XYZ translation stage by seating them on the rim of a drill hole in the mount. This arrangement allowed the sphere to be brought into contact with the prism without the possibility for excessive forces. The majority of the laser pulse intensity did not couple into the sphere and continued through the prism, exiting as a specular beam. The portion of the beam that did couple travelled around the sphere equator, and subsequent to each round trip reentered the prism and traveled to the prism exit face. The image beyond the prism was the specular spot plus a horizontal streak of light, that exhibited low vertical divergence. A portion of the light streak was collected using a short focal length lens and imaged onto a fast photodiode (17 ps risetime). The photodiode signal was processed using a digital oscilloscope (6 GHz bandwidth) or a 10 KHz-21 GHz RF spectrum analyzer. Oscilloscope data were refined using a fast Fourier transform.

Glass spheres with 8, 10, and 26.25 mm diameters were examined. The 8 and 10 mm spheres were from Edmund Scientific (Barrington, NJ), and the 26 mm sphere was obtained from Applied Image, Inc. (Glasstec Division, Buffalo, NY).

The sphere diameter tolerance was ± 0.5 μm, and the sphericity was specified to be λ/2.

Results and Discussion

In the near normal incidence geometry described above, the incidence angle at the prism/sphere coupling face resulted in total internal reflection. Only weak sphere coupling was observed until it was discovered that a film of glycerin at the coupling point facilitated transfer between the media. A drop of glycerin was applied, and the excess was removed using a lens tissue, leaving a thin film of fluid. When acceptable coupling was achieved a bright and distinct equatorial ring of light was observed at the sphere equator, and the time profile of the collected light assumed an oscillatory character.

Figure 1 shows a time trace of the photodiode signal for the 26.25 mm sphere. The oscillation period is 416 ps, corresponding to travel around the sphere circumference at the speed of light in BK-7. When the sphere was backed away slightly from the prism face, this oscillatory signal disappeared. The signal decays with a characteristic time of about 5 ns, corresponding to a $1x10^6$ resonance quality factor (Q). The optical pulse undergoes approximately 32 trips around the sphere circumference within the 13 ns time period between the laser pulses; this corresponds to a pathlength of 2.6 m for potential interaction with a surrounding medium or adsorbed material. Fourier transformation of this data results in the spectrum of Figure 2 that exhibits only the 2.40 GHZ resonance and weak contributions from the second and third harmonics.

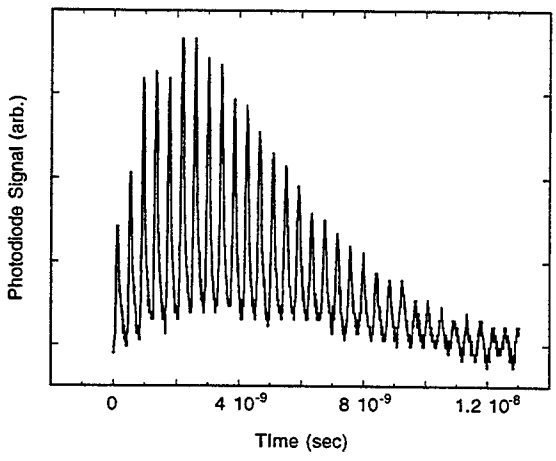

Figure 1. Time domain waveform.

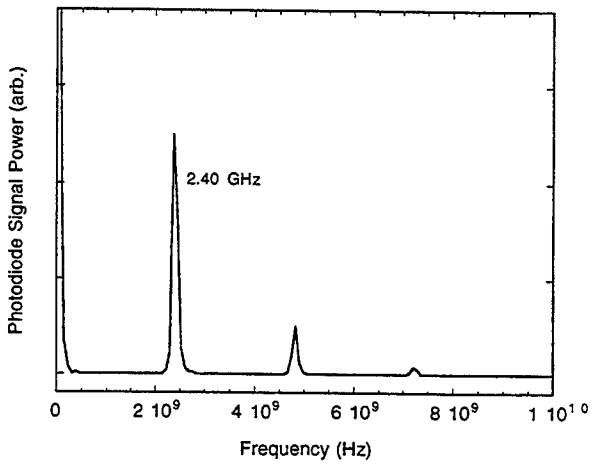

Figure 2. FFT spectrum.

Similar data were gathered for each of the sphere sizes. The frequencies observed were 7.92 (8 mm, 7.91 GHz calculated), 6.30 (10 mm, 6.33 GHz) and 2.40 GHz (26.25 mm, 2.41 GHz). Signal processing using the spectrum analyzer resulted in spectra similar to those calculated using the FFT.

The propagation modes excited here in any particular experiment are not singular. Higher time resolution traces can show multiple, near-degenerate modes. In some cases these mode combinations result in envelope modulation of the overall waveform, i.e., beating. Care must be exercised to avoid collection of the specular beam exiting from the coupling prism; the primary frequency dominates its time signature, but strong envelope modulation occurs. The character of the oscillating waveform can be slightly dependent upon the operating wavelength.

Conclusions and Future

Picosecond optical pulses were coupled into whispering gallery propagation modes of macroscopic glass spheres. The effects of coupling geometry, sphere diameter, laser wavelength, and laser repetition rate were examined. The detailed selection of particular sphere modes is presently beyond our control. Fiber optic, as opposed to prism, sphere coupling is currently under investigation. We are investigating the use of these spherical resonators as media for absorption spectroscopy via cavity ringdown methods[2]; optical absorption by species at the sphere surface will create loss during each round trip, yielding a shorter cavity decay time (lower Q), indicative of the absorption. Absorbing gases and adsorbed materials are sample candidates. A robust, sensitive detector would result from this approach in that the spherical cavity geometry is immune to misalignment.

Acknowledgement

This research was sponsored by the Division of Chemical Sciences, Office of Energy Research, U.S. Department of Energy, under Contract DE-AC05-96OR22464 with Oak Ridge National Laboratory, managed by Lockheed Martin Energy Research Corporation.

References

1. Lord Rayleigh, Phil. Mag. **20**, 1001 (1910); **27**, 100 (1914).

2. J. B. Paul and R. J. Saykally, Anal. Chem. **69**, 287A (1997).

Sodium concentration measurements with resonant holographic interferometry for gas and multi-phase environments

Ramon Dimalanta, Jr. and **Derek Dunn-Rankin**
Department of Mechanical and Aerospace Engineering
University of California at Irvine
Irvine, CA 92697-3975
Phone: (714) 824-8745 FAX: (714) 824-6518
ramon@eng.uci.edu
ddunnran@uci.edu

Neal J. Brock, Peter A. DeBarber,
Mike S. Brown, Jeff Segall and **James E. Millerd**
Metrolaser Incorporated
18010 Skypark Circle, Suite 100
Irvine, CA 92614-6428
Phone: (714) 553-0688 FAX: (714) 553-0495
nbrock@metrolaserinc.com
pdebarber@metrolaserinc.com

Summary

Resonant holographic interferometry (RHI) is a non-intrusive, laser-based diagnostic that has the potential to quantify species concentrations in both gas-phase and multi-phase (liquid and gas) environments. The technique exploits the rapid change in refractive index of a probed medium near absorption features. The change in refractive index is significant enough to change the effective pathlength or create a phase change in the light tuned to the absorption line. These phase changes can be resolved interferometrically during reconstruction. The interferogram's contours can then be analyzed for species concentration levels. One significant feature of RHI is its ability to uniquely create interferograms using species specific phase changes. Phase changes resulting from optical aberrations, thermal or pressure instabilities, or background species are subtracted out from the interferogram during reconstruction.

There are several advantages in RHI over other optical and non-optical techniques when obtaining species concentrations in a variety of experimental environments. In particular, RHI has the capability to provide gas phase information even when condensed phase objects are present. Although no spectroscopic information can be obtained from condensed phases, the benefit is that condensed phases within the probe volume do not interfere with the measurements in the gas. This is important in combustion or spray environments where particles or droplets may cause such an interference. Difficulties have occured when examining vapor very close to acetone droplet streams using laser induced fluorescence ([2]).

Figure 1 displays the schematic of the experimental setup. Details of the technique and its gas-phase applications can be found in the references ([1]). RHI is demonstrated on both gas-phase only and multi-phase environment experiments in the current work.

To record an RHI interferogram, two holograms are simultaneously recorded with beams tuned at two different wavelengths (Figure 2(a)); one near the absorption line (λ_2) and the other away from it (λ_1). Both beams are split into separate object and reference beams. The two object beams are later recombined and travel the same path coaxially through the probed volume. The resonant object beam alone experiences a species dependent phase change as it propagates through the medium (b). Each object beam creates a hologram with its respective reference beam. Upon reconstruction (c), an interferogram created by the

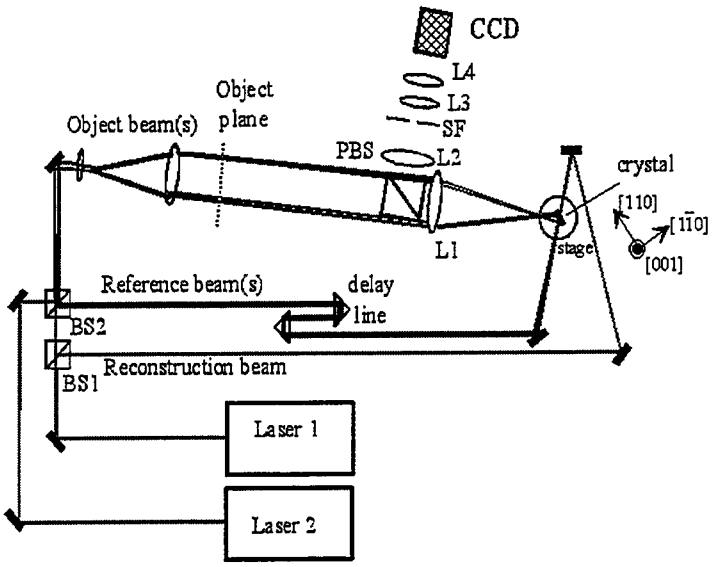

Figure 1: Experimental setup

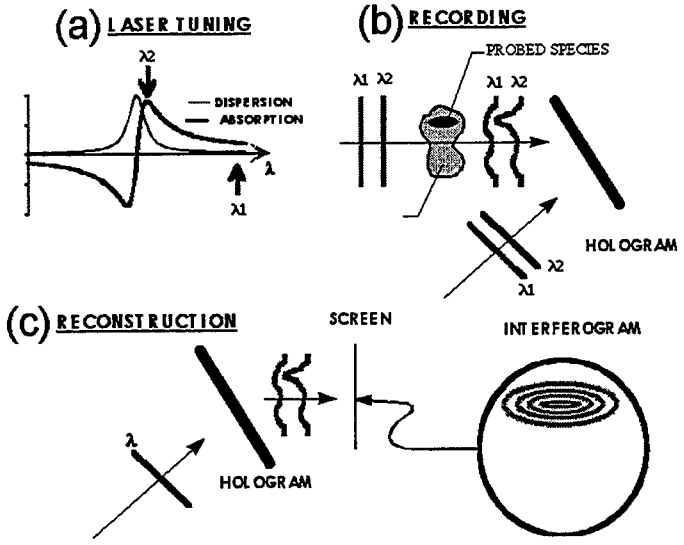

Figure 2: RHI phenomenology

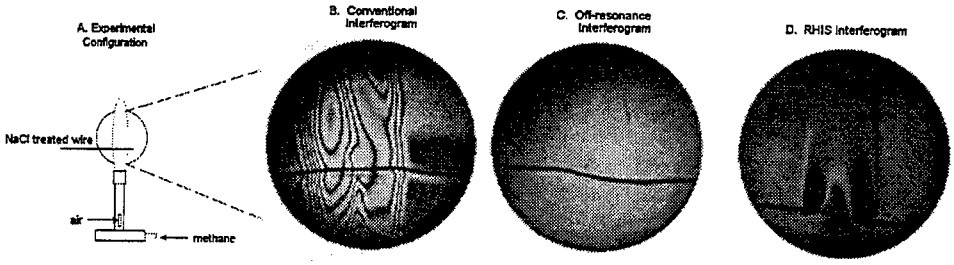

Figure 3: Sodium resonance

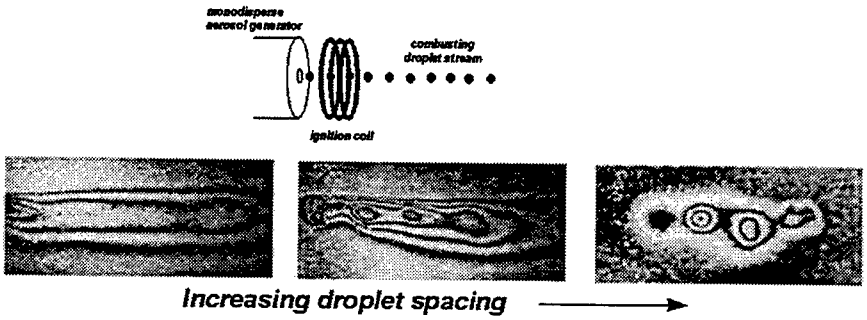

Figure 4: Potassium seeded methanol droplet stream flames

relative phase change between the two holograms is conveyed. These contours can then be converted to species number densities.

Figure 3 demonstrates the background subtraction capability of RHI. Figure 3(A) shows the probed volume: a wire dipped in a sodium chloride solution is suspended over a bunsen burner. A conventional interferogram (B) was taken by one laser tuned off-resonance at two different times; one time with and one time without the flame present. The result is evidence of bulk refractive index gradients due to the flame. Speciation is difficult to resolve here. In (C), two lasers tuned off-resonance were shot simultaneously with the flame present. Notice the removal of the interference fringes since both object beams experience the exact same phase change. Changing one laser's frequency to sodium's D_2 absorption line, the RHI interferogram (D) reveals phase changes due solely to species related refractive index changes in the medium.

As preliminary evidence of its usefulness in multi-phase environments, an example of an interferogram from an earlier experiment observing potassium vapor near a burning methanol droplet stream seeded with potassium is shown in Figure 4. The figure shows progressively larger droplet spacings.

In these current experiments, we attempt to quantify concentrations of sodium in a static cell with varying pathlengths and near a sodium seeded droplet stream.

References

[1] Brock, N.J., Brown, M.S., DeBarber, P.A., Millard, M.W., Millerd, J.E., and Trolinger, J.D., (1995), "Real-time resonant holographic interferometry for combustion and plasma environments," *Paper for AIAA Meeting, Reno, NV, Jan. 9-12,* paper no. 95-0643.

[2] Connon, C.S., Choi, C., Dimalanta, Jr., R., and Dunn-Rankin, D., (1996), "LIF Measurements of Fuel Vapor in an Acetone Droplet Stream," *Combustion Science and Technology,* in press.

Diode-Laser-Difference Frequency Spectrometer for Carbon Monoxide Detection

Torsten Blanke, Ulrike Willer, Dietmar Kracht, and Wolfgang Schade

Institut fur Experimentaplhysik, Universitat Kiel, Olshausenstrasse 40, D-24098 Kiel, Germany
Blanke@physik.uni-kiel.de

The application of laser absorption spectroscopy for remote sensing of environmental pollutants in the mid-infrared spectral range (MIR) is of fundamental interest, because most of the relevant molecules have strong vibrational transitions in this spectral region that can be used as "fingerprint" for a sensitive detection in complex environments, as air, water or soil. However, there is still a lack in simple, compact, portable and rugged MIR laser sources. In this context, diode-lasers and difference frequency generation recently have drawn considerable interest [1-3]. New and efficient non-linear crystals, as e.g. $AgGaS_2$ or GaAsSe, and recent progress in the fabrication of fiber optics for the MIR make it possible to set up compact MIR laser spectrometers with the option of evanescent field spectroscopy. The latter one is of essential advantage when a detection of pollutants in optical thick media, e.g. soil, is required.

In the present paper difference frequency generation (DFG) of two continous wave single mode diode-lasers with powers of 30 and 50 mW and an $AgGaS_2$ crystal with a cut for type I non-critical phase matching are used to set up a very compact and tunable diode-laser system for the MIR which operates at room temperature. For sensitive recording of absorption spectra a thermoelectrically cooled IR-detector, 2f-

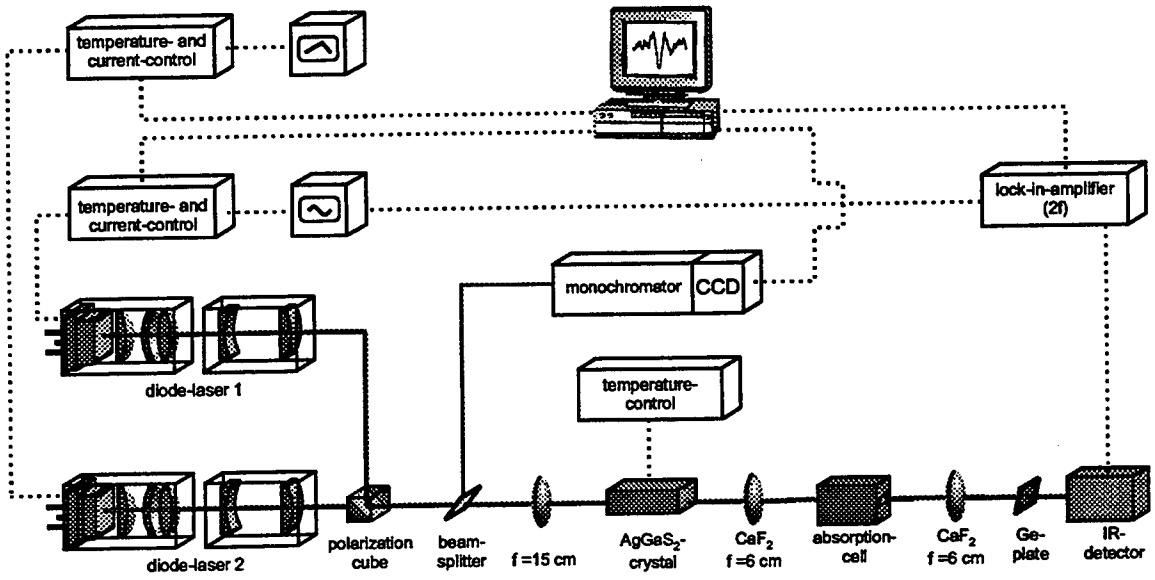

Figure 1: Experimental set-up for the MIR-diode laser spectrometer and 2f modulation spectroscopy

modulation spectroscopy and lock-in techniques are applied. The total MIR-spectrometer has a geometrical size of 30×90 cm^2 . In Fig. 1 a schematic diagram of the present experimental set-up is shown.

A disadvantage of diode-lasers for spectroscopic applications is, that single mode operation can not be achieved over the whole gain profile. This is only possible

for specific temperature ranges and they are different for each diode-laser. This is shown in fig. 2a. The black dots indicate the wavelength ranges for single mode operation of a standard laser-diode (Hitachi HL 6720G) and different temperatures. The signal and pump waves for the DFG process in the $AgGaS_2$ are generated by standard diode-lasers (Hitachi HL 7851G and Toschiba TOLD 9150) and the output wavelengths are centered at λ_s=791 nm and λ_p=682 nm. This gives a tuning range in the MIR from 4.9 to 5.1 μm by proper setting the temperature of the diode-lasers and the one of the non-linear crystal. The MIR laser power is typically P_{DFG}=0.2 μW. Details of the laser system are described in [2].

There are wavelengths within the gain profile for which a single mode operation is not possible. Unfortunately, this characteristic mode jump behavior limits the tunability of MIR wavelengths significantly when diode-lasers are used for the difference frequency generation. However, the tuning characteristics of diode-lasers can be improved very easily by building an external short cavity around the laser [4]. Therefore, a glas plate is mounted on a piezo and is fixed close to the diode-laser (d<100 μm) to form an external cavity. When changing the reflectivity of the glas plate and changing the external cavity length by applying different piezo voltages the mode structure of the diode-laser is modified. Results of such measurements are shown in fig. 2a (squares). In that case all wavelengths in the spectral range between 672 and 677 nm are coverd by single mode operation. In fig. 2b the mode behavior of the diode-laser with an external short cavity is shown for different piezo voltages. The same mode structures can be reproduced very accurately for different piezo voltages.

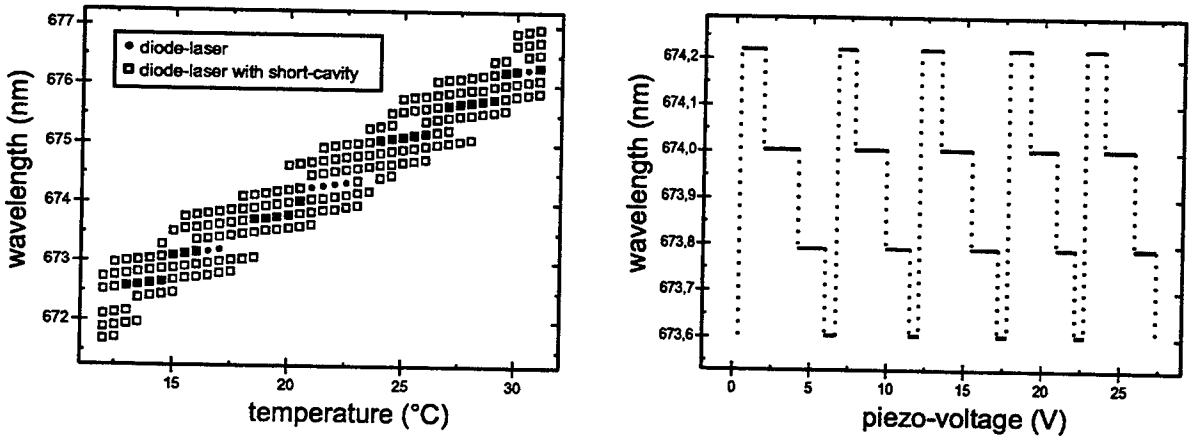

Figure 2: (a) Mode behavior of a single mode diode-laser (Hitachi HL 6720G) as a function of the temperature for a standard laser (•) and an external short cavity laser (□). (b) Dependency of the laser modes on the applied piezo voltage for the external short cavity diode-laser.

The performance of this MIR diode-laser spectrometer for detecting environmental pollutants is demonstrated as a single rotational state in the 1-0 band of the carbon monoxide molecule is probed in the smoke of a cigarette. The amount of CO in cigarette smoke is 3-5%. An absorption spectrum of CO for the P(28) rotational state is shown in fig. 3, as one diode-laser wavelength is fixed at λ_s=791.02 nm while the other one is tuned around λ_p=681.9 nm. During these measurements cigarette smoke was pumped into an absorption cell with a length of l=10 cm.

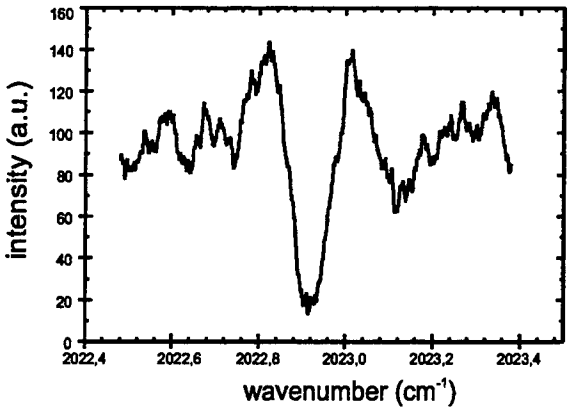

Figure 3: Absorption spectrum of the P (28) rotational state of carbon monoxide in cigarette smoke, which is measured by the MIR diode-laser spektrometer.

Recent progress in optical fiber technology suggests that evanescent field spectroscopy in the mid-infrared spectral range will be interesting for future sensor developments [5]. Several optical fibers with sufficient transmission in the spectral range between 2 and 16 μm exist, as there are sapphire fibers (<3.8 μm), infrared "SG" fibers (<5 μm), chalcogenide fibers (<11 μm), and silver halide fibers (<16 μm). However, there are still some problems with these fibers because of their toxicity and difficulties in the handling. First results of measuring carbon monoxide by evanescent field spectroscopy and the new MIR diode-laser spectrometer will be reported during the conference.

This research is supported by the Technologiestiftung Schleswig-Holstein (contract 94-35i) and the BMBF (contract 13N6883).

References

1. U, Simon, C.E. Miller, C.C. Bradley, R.G. Hulet, R.F. Curl, F.K. Tittel, Opt. Lett. **18**, 1062 (1993).
2. W. Schade, T. Blanke, U. Willer, C. Rempel, Appl. Phys. B **63**, 99 (1996).
3. H.-D. Kronfeld, G. Basar, B. Sumpf, J. Opt. Soc. Am B**13**, 1859 (1996).
4. G.P. Barwood, P. Gill, W.R.C. Rowley, Meas. Sci. Technol. 3, 406 (1992).
5. E.V. Skpanov, A.I. Konznetsov, P.V. Zyrianov, V.G. Plotnichenko, Yu.G. Selivamov, V.G. Artjushenko, Infrared Phys. and Technol. **37**, 149 (1996).

Remote Radiation Sensing Using a Fiber-Coupled, Optically Stimulated Luminescence Dosimeter

by

Alan L. Huston and Brian L. Justus
Optical Sciences Division, Code 5611
Naval Research Laboratory
Washington, D.C. 20375
Voice: (202)767-9470
FAX: (202)404-8114
e-mail: alan.huston@nrl.navy.mil

Fiberoptic-based, radiation measurement methods provide a convenient approach for remotely monitoring hazardous or difficult-to-access areas such as nuclear waste sites or sampling wells for in situ ground water monitoring. Fiberoptic systems are attractive for these applications because of their small size, mechanical flexibility and optical, as opposed to electrical, signal transmission. In this paper, we describe a new, optically stimulated luminescent (OSL) glass dosimeter that can be attached directly to commercial optical fibers for remote radiation sensing applications. The OSL glass is optically transparent and can be manufactured to any desired length to provide the necessary sensitivity required for a specific application.

The OSL glass used in this work is a composite material that contains Cu^{1+} ions in a SiO_2 matrix. Glass rods, 6mm in diameter, were hand-drawn into ~200 - 400 μm diameter fibers using a hydrogen torch. Dosimeter fibers ranging in length from 1 mm to 3 cm were joined to commercial, 200 μm core diameter, multimode optical fibers.

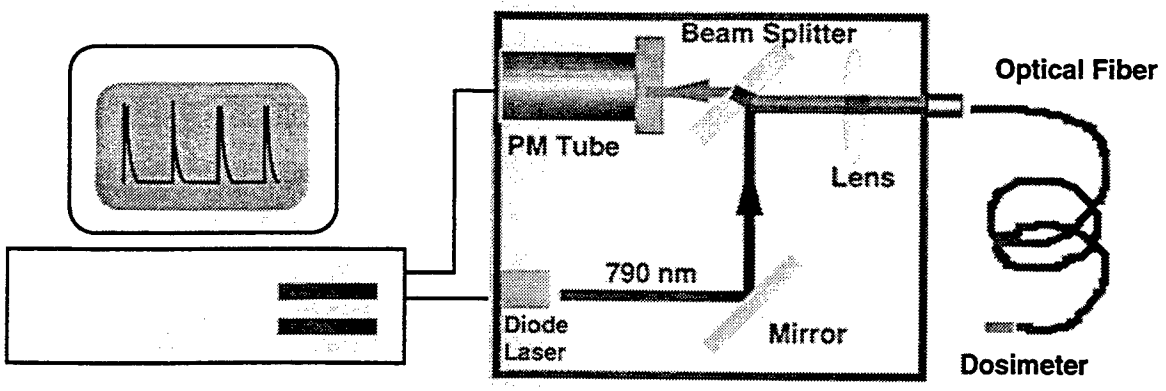

Figure 1. Schematic diagram of the optically stimulated luminescence, fiberoptic-coupled dosimeter.

A schematic of the fiberoptic-coupled, OSL dosimeter is shown in Fig. 1. The 790 nm output of a 1 watt, fiberoptic coupled diode laser was filtered with a Schott RGN9 color glass filter to remove short wavelength light due to

spontaneous emission. The laser light was reflected using a dichroic beamsplitter and injected into a 200 - 400 μm core diameter multimode optical fibers. The dichroic mirror was selected to reflect 780 nm - 830 nm light and transmit blue-green OSL signal light. The laser light was used to stimulate luminescence from the Cu^{+1}-doped glass fiber sensor that had been previously exposed to ionizing radiation. A fraction of the 500 nm, OSL emission was trapped by total internal reflection and directed back through the multimode fiber. The signal light was detected with a photomultiplier tube (PMT). A HOYA CM500 color glass filter was used to selectively block scattered diode laser light while passing the OSL signal. The PMT was operated in the photon counting mode (Hamamatsu HC135) to provide the highest sensitivity possible.

The fiber-coupled sensor was exposed to a variety of radiation sources including ^{60}Co γ-rays, broadband x-rays and ultraviolet lamps. The doses were controlled by irradiating the sensor for specific time intervals. Dose measurements were performed by exposing the fiber sensor to a preset cw laser power of about 100 mW and monitoring the signal decay for a period of 10 to 20 seconds. The traps emptied by laser illumination were reset, allowing repeated use of the sensor.

Several OSL signals obtained from the fiber dosimeter, exposed to a range of x-ray doses from a linear accelerator, are presented in Fig. 2.

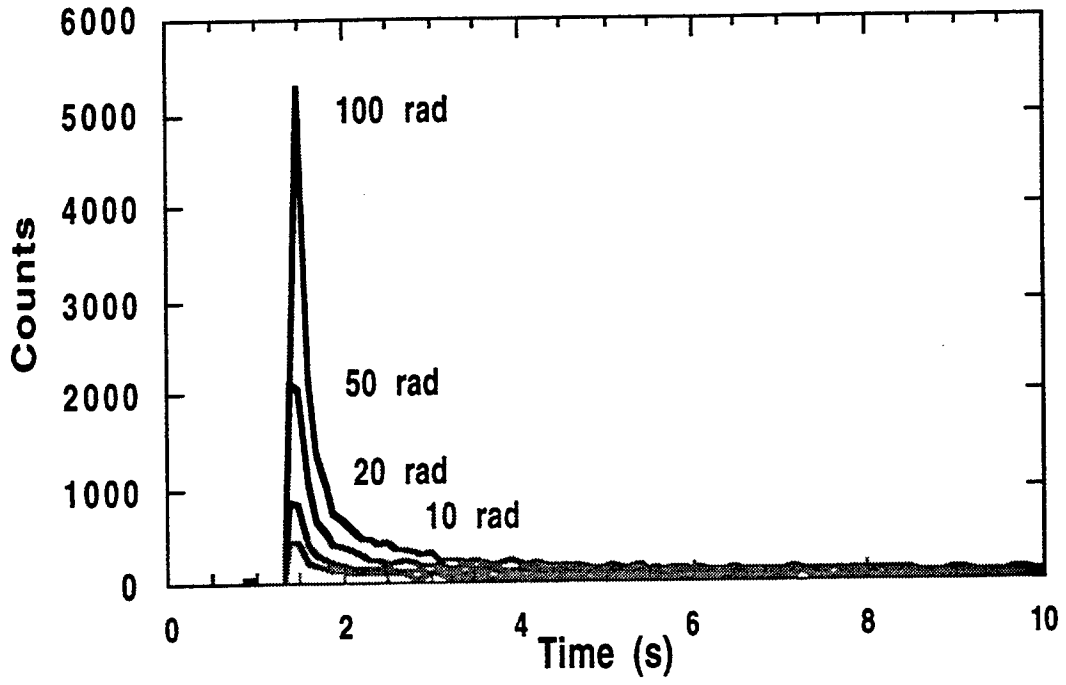

Figure 2. OSL signals obtained from a 1 mm long by 0.4 mm diameter Cu+1-doped glass dosimeter exposed to an x-ray source. Readout was accomplished using 100 mW cw power at 790 nm.

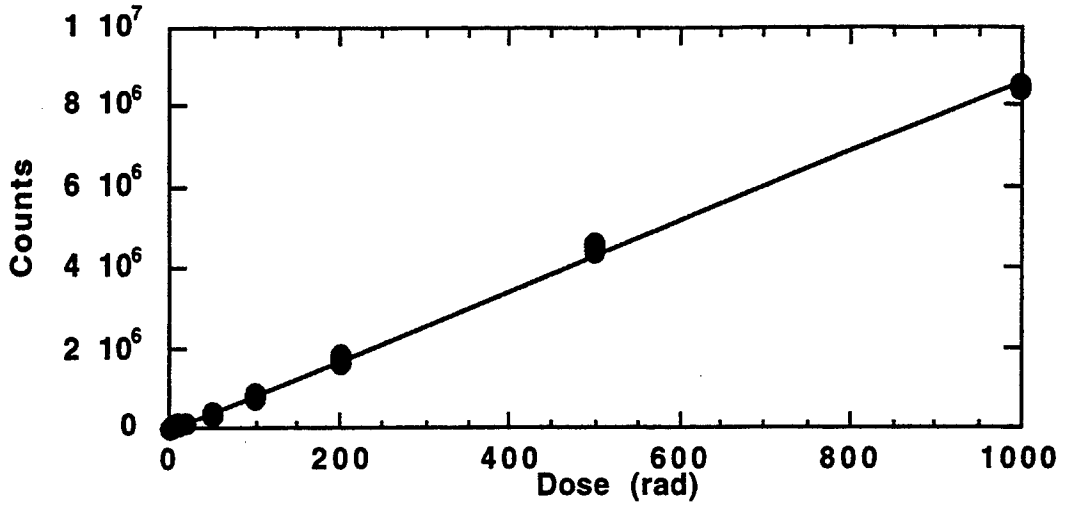

Figure 3. Calibration of the fiber-coupled dosimeter for a 1 mm long, 0.4 mm diameter sensor.

Figure 3. shows a calibration plot obtained for a 1 mm long, 0.4 mm diameter sensor exposed to x-radiation from a linear accelerator in a clinical setting. As a result of the optical transparency of the OSL material, the sensors can be manufactured to any length desired, thereby increasing the sensitivity of the sensor.

In summary, we have developed an all optical, fiberoptic-coupled radiation dosimeter that has excellent performance characteristics for remote radiation sensing applications. The enabling feature of the dosimeter is an optically transparent, OSL glass. The sensor utilizes relatively low cost components such as a diode laser array, a commercial multimode optical fiber, simple optical elements and direct photodetection. Dose information is correlated with the signal amplitude or the total integrated count, and requires minimal signal processing. Optical annealing of the dosimeter prepares the sensor for repeat use. The monitoring of radiation levels in ground water supplies around nuclear waste sites could utilize sensor arrays consisting of hundreds of fiber-coupled dosimeters, all interrogated from a central control center, using a single diode laser and photodetector. The small size and the high sensitivity of this fiberoptic radiation dosimeter should be ideal for medical applications such as near-real-time, in vivo, dose monitoring in patients undergoing radiation therapy

This work was supported by the United States Office of Naval Research.

Paper Withdrawn

Near-Infrared Frequency Modulated Detection of Transient Species

Andrew J. Marr[†], Bor-Chen Chang[‡], Gregory E. Hall[†] and Trevor J. Sears[†]

[†] Department of Chemistry, Brookhaven National Laboratory, Upton, NY 11973-5000;

phone :(516) 344-4375; fax: (516) 344-5815; e-mail: ajmarr@dynamics.chm.bnl.gov

[‡]Department of Chemistry, National Central University, Chunmg-Li, Taiwan 32054.

Presentation Summary

Recently, a frequency modulated Ti:sapphire laser was used as a highly sensitive means for detection of transient species (1). In particular it was used to measure spectra of methylene and its halo-derivatives (2,3) and in addition very high signal-to-noise Doppler lineshapes were recorded from which significant dynamical analyses have derived (4). Within the last year we have incorporated the frequency modulation (FM) method into a near-infrared diode laser system which works at wavelengths around 1 μm and this has produced an order of magnitude improvment in signal-to-noise of that system. A further improvement in sensitivity has been achieved by extending the interaction region of the probing laser and the gas sample using a Herriott-type cell. Systems based upon this diode laser spectrometer which is cheap, simple to use and maintain, and relatively compact may provide a sensitive monitor of important gaseous molecules that absorb at similar wavelengths.

A diagram of the experimental setup is shown in figure 1.

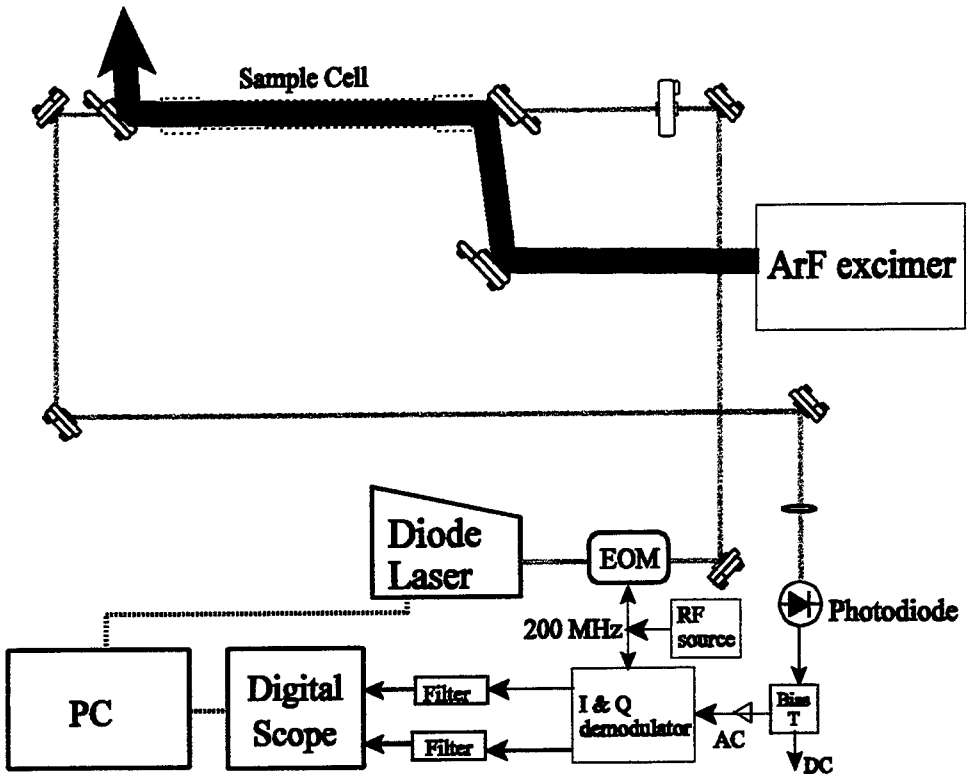

Figure 1. Near-infrared frequency modulated (200 MHz) transient absorption spectrometer

The diode laser radiation passes through an electro-optic-modulator (EOM) which adds radio-frequency sidebands at approximately ±200 Mhz. The power in each first order sideband is adjusted to about 20% of the carrier. In our experiments the transient molecules we examine are produced by flash photolysis using an excimer laser. The Herriott-type cell (see figure 2), based upon a previous design (5), is constructed such that the multi-pass probe laser beam, reflecting from mirrors at each end, and molecule forming pump laser, which passes through holes cut in the mirrors, overlap as much as possible.

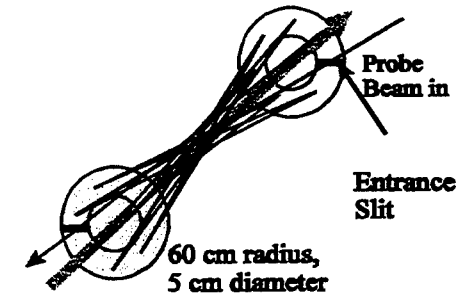

Figure 2. Herriot Cell with overlapping pump and probe beams

After exiting the cell the frequency-modulated beam is focused on to a fast silicon PIN diode. After filtering and amplification the signal is demodulated in a double balanced mixer. The mixer output was then filtered to eliminate frequencies above 75 Mhz and averaged using a digital scope controlled by a personal computer.

Figure 3 compares the spectra obtained with and without the incorporation of frequency modulation, in this case for a single pass absorption cell. The improvement in signal is clear and with the addition of the Herriott-cell further improvement has been achieved.

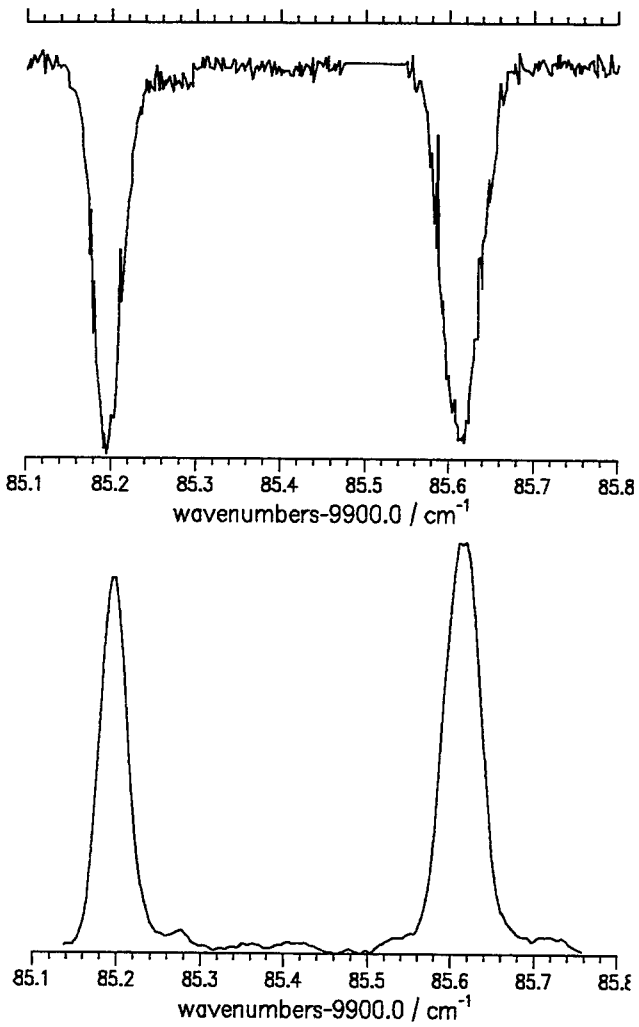

Figure 4. A portion of the CH_2 spectrum; upper panel without FM, lower panel with FM.

References

1. J. C. Bloch, R. W. Field, G.E. Hall and T. J. Sears, J. Chem. Phys. *101*, 1717 (1994).
2. B.-C. Chang and T. J. Sears, J. Chem. Phys. *102*, 6347 (1995).
3. B.-C. Chang, M. Wu, G. E. Hall and T. J. Sears, J. Chem. Phys. *101*, 9236 (1994).
4. S. W. North and G. E. Hall J. Chem. Phys. *106*, 60 (1997).
5. J. S. Pilgrim, R. T. Jennings and C. A. Taatjes, Rev. Sci. Inst. *in press*.

Acknowledgement

This work was performed under Contract No. DE-AC02-76CH00016 with the U.S. Department of Energy and supported by its Division of Chemical Sciences, Office of Basic Energy Sciences.

Following the Dynamics of Single Oligonucleotide Molecules in Water

M. Sauer[1*], K. H. Drexhage[2], K.-T. Han[1], S. Nord[1], C. Zander[1,2]

[1]Physikalisch-Chemisches Institut, Universität Heidelberg, Im Neuenheimer Feld 253, 69120 Heidelberg, Germany

[2]Institut für Physikalische Chemie, Universität-Gesamthochschule Siegen, Adolf-Reichwein-Straße 3, 57068 Siegen, Germany

[*]corresponding author (e-mail: sauer@sun0.urz.uni-heidelberg.de; Phone: 49-6221-548460; Fax: 49-6221-544255)

1. Introduction

The dynamic fluorescence characteristics of individual dye molecules in specific local environment are of particular interest for many biological applications.[1,2] Furthermore, dye molecules that are influenced by the environment can act as molecular probes, i. e. they exhibit information about neighbouring groups and changes in the microenvironment. They also allow the direct observation of individual dynamic events such as conformational changes of a biological macromolecule if they are monitored on the single-molecule level. In addition, measurements on individual molecules are well suited for the study of complex systems in which it is not known whether all molecules exhibit the same characteristics or each molecule contributes with its individual characteristics to the observed behaviour.

Previously, we found that rhodamine and oxazine dyes are more or less efficiently quenched by the DNA nucleoside guanosine.[3] Upon covalent linking of these dyes to oligonucleotides containing guanosine residues the fluorescence quantum yield and lifetime decreases due to an electron transfer reaction from ground-state guanosine residues to the excited chromophore. Due to the flexibility of the linker chain the dye can adopt different conformations with respect to the oligonucleotide sequence. Hence, the dynamical characteristics of these conformational changes can be monitored directly by measuring the changes in the fluorescence kinetics of individual labeled oligonucleotide molecules.

2. Experimental

All experiments were performed with the oxazine dye MR121 (Figure 1). The 18-mer oligonucleotides were custom-synthesized and modified at their 5'-terminus using C_6 amino-modifier. For single-molecule experiments we used confocal fluorescence microscopy. Details of the experimental setup are described elsewhere.[4]

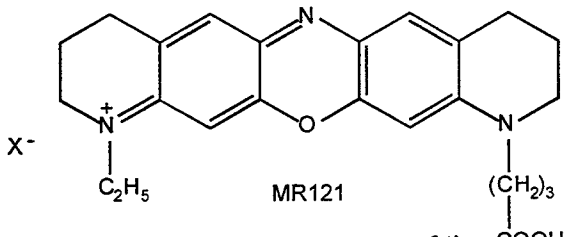

MR121

Figure 1. Molecular structure of the oxazine dye MR121.

A pulsed diode laser served as the excitation source (60 nm, 56 MHz, pulse length 400 ps). The pulsing of the diode was performed by a self-matched

tunable pulse generator. The fluorescence signal was imaged onto a 100 µm pinhole directly in front of an avalanche photodiode. The signal was amplified and splitted for a MCS-card and a time-correlated single-photon counting (TCSPC) PC-interface card (SPC-330) to acquire time-resolved data. The time-resolved signal was collected in up to 128 histograms with a minimal integration time of 625 µs each. Measurements were performed in microscope slides with a small depression covered by a cover glass. Fluorescence lifetime determination of single-molecule events was realized by a maximum likelihood estimator (MLE).[5]

3. Results and discussion

Table 1 presents the spectroscopic characteristics of the free dye MR121 and two oligonucleotide conjugates in water.

	λ_{abs} (nm)	λ_{em} (nm)	τ_1 (ns)	a_1	τ_2 (ns)	a_2
MR121	661	675	1.85	1.00	---	---
MR121-5'-TTTAAAACTACTTCCATT-3' (G-0)	669	685	2.72	1.00	---	---
MR121-5'-T**G**TAAAAC**G**AC**GG**CCA**G**T-3' (G-X)	668	682	2.14	0.47	0.40	0.53

Table 1. Spectroscopic characteristics of MR121 and different oligonucleotide conjugates. The fluorescence lifetimes were measured with the SMD apparatus at concentrations of 10^{-8} M.

In the oligonucleotide G-X containing five guanosine residues the fluorescence quantum yield is drastically reduced. To describe the fluorescence kinetics at least a biexponential model with a short lifetime of 0.4 ns and a long lifetime of 2.1 ns has to be applied. Using the maximum entropy method (MEM) an underlying distribution of fluorescence lifetimes with maximum values at 0.4 ns and 2.1 ns could be recovered.[4] In the present study, the distribution of lifetimes implies a distribution of electron transfer rates between the dye and guanosine residues in the oligonucleotide. Due to the conformational flexibility of the C_6-linker a distribution of relative orientations may result in more effective dipole coupling than other geometries, thus, in effect, varying the electron transfer rate. At this point the question arises whether each individual oligonucleotide exhibits a different but constant fluorescence decay which contributes to the observed behaviour, or each oligonucleotide undergoes conformational transitions between various states with different electron transfer kinetics during the measurement. Thus, if all possible equilibrium states in the oligonucleotide were visited repeatedly on the timescale of the experiment, i. e. during the transition through the detection volume, the same nonexponential kinetics would be observed for every molecule in single-molecule experiments.

We measured more than 200 time-resolved decays of individual oligonucleotide molecules G-0 and G-X and calculated the fluorescence lifetimes. Figure 2 shows a histogram of the determinated lifetimes of single oligonucleotides in water. Our measured data lead to the following conclusion: (a) only oligonucleotides containing guanosine residues exhibit short

fluorescence lifetimes, even on the single-molecule level, and (b) most of the transitions between various conformations in guanosine containing oligonucleotides occur on a ms-timescale, i. e. during the measurement time of 625 µs most of the detected events exhibit either a short or a long fluorescence lifetime.

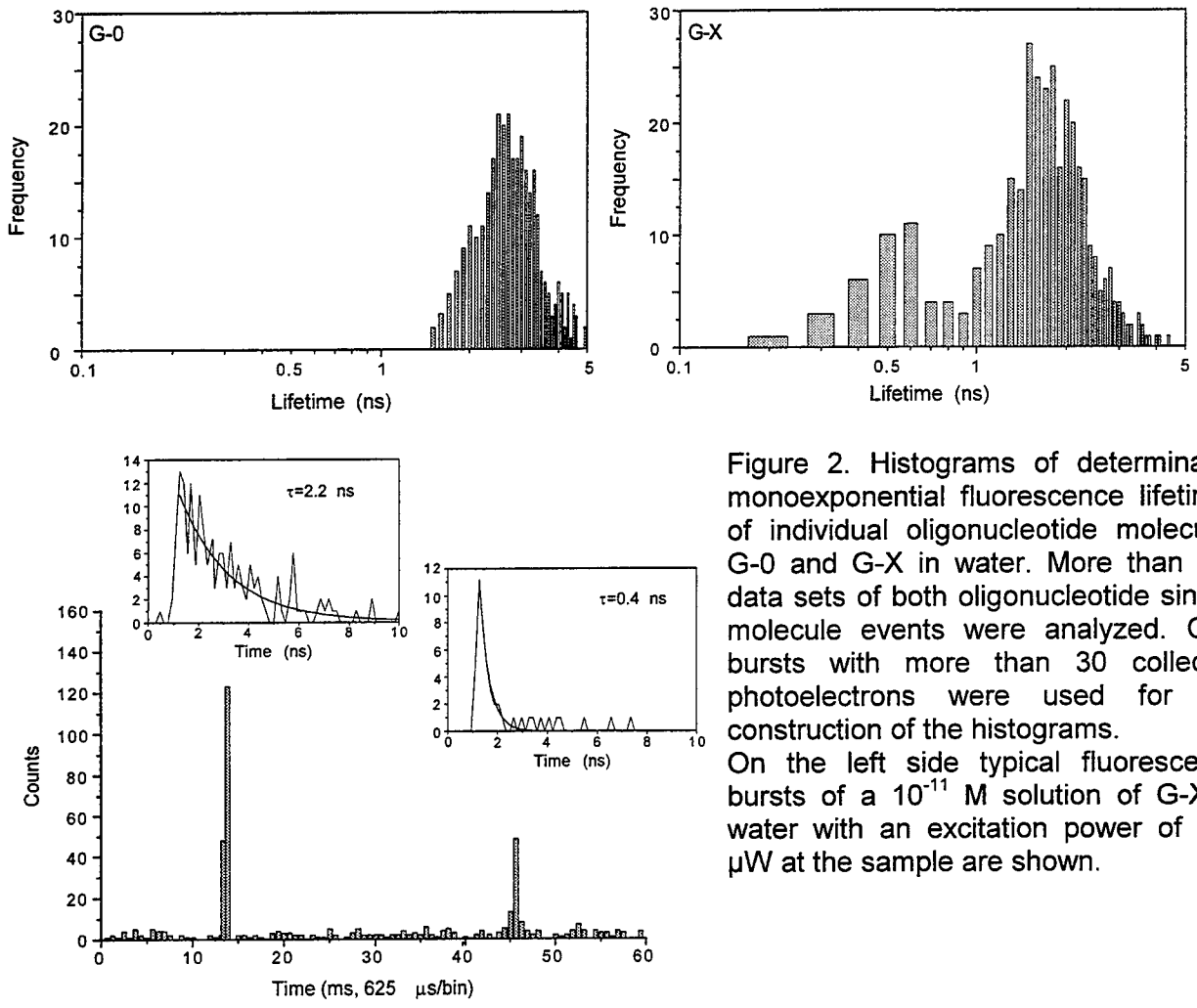

Figure 2. Histograms of determinated monoexponential fluorescence lifetimes of individual oligonucleotide molecules G-0 and G-X in water. More than 200 data sets of both oligonucleotide single-molecule events were analyzed. Only bursts with more than 30 collected photoelectrons were used for the construction of the histograms.
On the left side typical fluorescence bursts of a 10^{-11} M solution of G-X in water with an excitation power of 630 µW at the sample are shown.

References

1) R. M. Dickson, A. B. Cubitt, R. Y. Tsien, W. E. Moerner, *Nature* **388**, 355 (1997).
2) T. Ha, Th. Enderle, D. F. Ogletree, D. S. Chemla, P. R. Selvin, S. Weiss, *Proc. Natl. Acad. Sci. USA* **93**, 6264 (1996).
3) M. Sauer, K.-T. Han, R. Müller, S. Nord, A. Schulz, S. Seeger, J. Wolfrum, J. Arden-Jacob, G. Deltau, N. J. Marx, C. Zander, K. H. Drexhage, *J. Fluoresc.* **5**, 247 (1995).
4) M. Sauer, U. Lieberwirth, K. H. Drexhage, S. Nord, R. Müller, C. Zander, submitted to Chem. Phys. Lett. (1997).
5) S. A. Soper, B. L. Legendre, Jr., D. C. Williams, *Anal. Chem.* **67**, 4358 (1995).

Laser Induced Fluorescence in Inhibited Counterflow Diffusion Flames

Robert G. Daniel, R. Reed Skaggs, Barie E. Homan,
Andrzej W. Miziolek, and Kevin L. McNesby
U. S. Army Research Laboratory
Weapons and Materials Research Directorate
Aberdeen Proving Ground, Maryland 21005-5066

INTRODUCTION: As part of the continuing effort to find an effective, yet safe, replacement compound for the commonly used halon fire suppression agents, we have begun a study of reduced pressure counterflow diffusion flames inhibited with iron pentacarbonyl ($Fe(CO)_5$). Iron pentacarbonyl has been shown to be a very effective fire suppression agent in small quantities, but there is little understanding of the mechanism of its activity. The goal of this study is to understand the mechanism by which $Fe(CO)_5$ inhibits flames by coupling experimental measurements with computer modeling of diffusion flames. This project is part of the Next Generation Fire Suppression Program (NGFSP).

We will present results from the spectroscopic examination of uninhibited and inhibited counterflow diffusion flames via laser induced fluorescence of active flame species at two reduced pressures. The species studied are atomic oxygen (O), atomic hydrogen (H), and hydroxyl radical (OH). The flames under study have also been examined with thermocouple probes to map temperature profiles and emission spectroscopy of active species including OH, CH, C_2, and iron and iron containing compounds. We have also performed flame extinction studies which determine the strain rate for flame extinction as a function of inhibitant concentration.

EXPERIMENTAL: The experiments utilize a counterflow diffusion burner schematically shown in figure 1 as the flame source, an excimer pumped (XeCl) dye laser, and a light collection train. The fuel and any additive flows from the bottom burner head, and the oxidizer (manufactured air) and additive flows from the top. The two flows collide and form a stagnation plane, a region of near zero vertical flow velocity. The fuel will diffuse upward into the oxidizer flow to a stoichiometric region which will support the flame front. The two burner heads are mounted on XZ translation stages to allow the full vertical spatial distribution to be mapped with a fixed optical probe, defined by the laser focus.

The early experiments centered on the emission spectra of the flame, in which many

flame species were mapped by their emission. A two dimensional CCD camera was used to obtain both spatial (distance between burner heads) and wavelength information. The spectra was dispersed with a 500 mm monochromator, which allowed the camera to image a 20 nm region. Spatially, the camera maps approximately 11 mm. A example of the information from an OH spectrum is shown in figure 2.

We are studying reduced pressure (50 and 300 torr) and "atmospheric" (700 torr) flames to increase the understanding of the mechanism of suppression of iron pentacarbonyl, a prototypical fire suppression superagent. Output from the dye laser is focused through a LiF window into the flame, with the fluorescence being collected at a right angle by a 2 inch lens. The fluorescence is focused onto the active element of a photomultiplier tube, whose signal is passed to a lockin amplifier and boxcar for signal averaging.

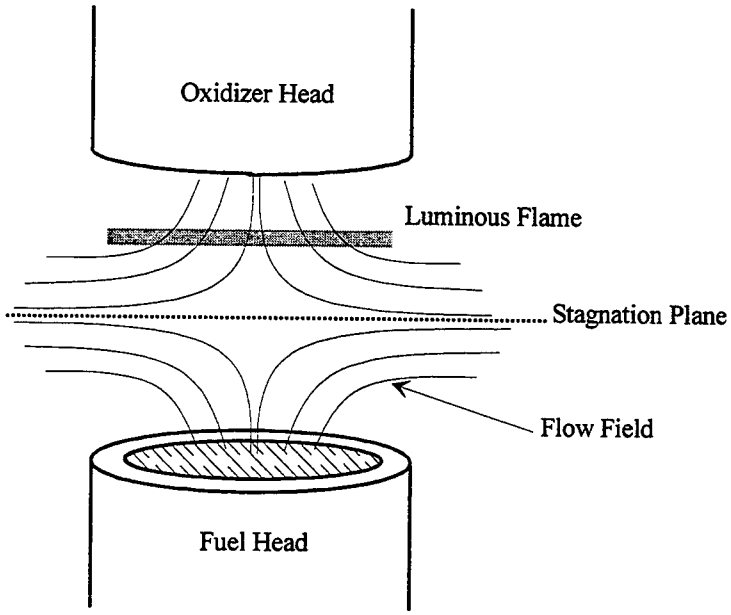

Figure 1. Schematic of a counterflow diffusion burner with the locations of the flame front and stagnation plane indicated. The laser focus will be fixed and the burner heads moved vertically to map the spatial distribution of the species O, H, and OH.

DISCUSSION: We will present the results of continuing experiments designed to map the spatial dstribution of oxygen, hydrogen, and hydroxyl radical. This information will be added to the body of information already existing from emission and thermocouple measurements. The results and their implications will be presented and discussed.

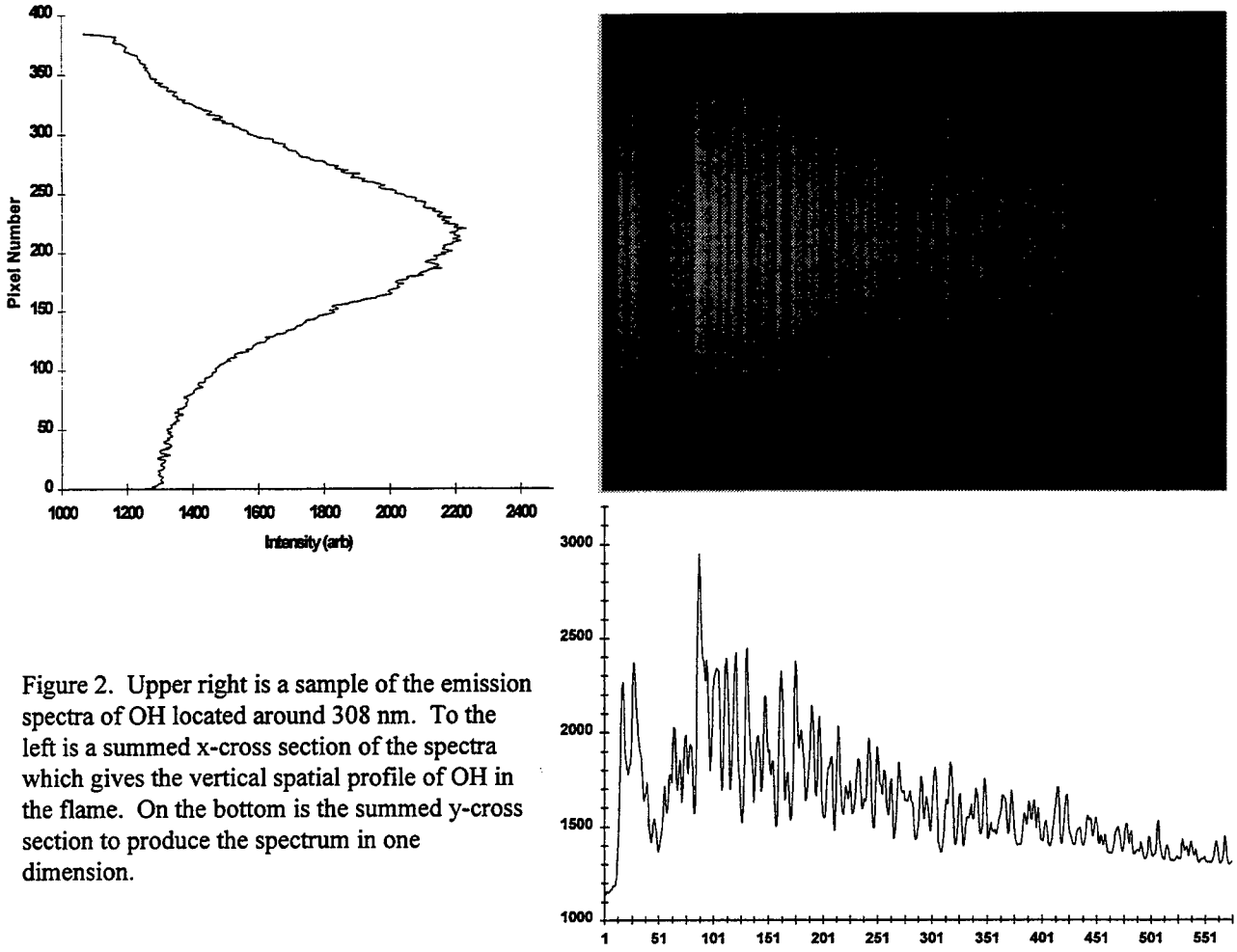

Figure 2. Upper right is a sample of the emission spectra of OH located around 308 nm. To the left is a summed x-cross section of the spectra which gives the vertical spatial profile of OH in the flame. On the bottom is the summed y-cross section to produce the spectrum in one dimension.

CW Diode-Pumped Tunable Nd^{3+}:KY_3F_{10} Laser for Environmental Sensing

M. A. Dubinskii, K. L. Schepler
USAF Research Laboratory, WL/AAJL, 2700 D Street, Suite 2, Wright-Patterson AFB, OH 45433-7405, USA
A. K. Naumov, V.V. Semashko, R.Yu. Abdulsabirov, S. L. Korableva
Kazan State University, Kremlevskaya Street 18, 420008 Kazan, Russia

Introduction

Laser environmental remote sensing is a powerful modern pollution control (atmosphere monitoring) technique. Hydrogen bromide (HBr) is a dangerous pollutant present in the atmosphere as a byproduct of commercial chemical reactions (chemical waste). HBr has quite high intensity molecular absorption lines in the near- and mid-IR (with respect to other species of atmospheric importance). In particular, HBr has a group of absorption lines between 9,300 and 9,800 cm^{-1} (1.020 and 1.075 μm) with typical intensities on the order of 10^{-24} cm^{-1}/(molecule x cm^{-2}), some of them going up to 10^{-23} cm^{-1}/(molecule x cm^{-2}). A simple Nd-activated laser with diode pumping and reasonably wide tunability in this region would be an appropriate source of radiation for HBr monitoring. Wide tunability particularly for wavelengths near 1055 nm not available from commercial Nd lasers will be the key issue for such a device.

A prospective laser material for this application is KY_3F_{10}, first obtained as a single crystal material in the early 80's [1], and then characterized as a laser material with Nd doping under flashlamp [2] and CW Ar-laser [3] pumping conditions. Recently we reported characterization of Nd^{3+}: KY_3F_{10} as a diode-pumped new laser material with low threshold operation [4]. Here we present tuning of Nd^{3+}: KY_3F_{10} as a CW diode-pumped laser configured for environmental sensing needs.

Summary

As was mentioned in [4] , despite the fact that KY_3F_{10} is considered to be a well-ordered crystalline material, Nd^{3+}:KY_3F_{10} indicates unusually wide single *f-f*-fluorescence band features, which make it promising for a variety of tunable, as well as short-pulse, applications. In this effort we have implemented the first tunable CW laser based on $^4F_{3/2} \rightarrow {}^4I_{11/2}$ transitions of diode-pumped Nd^{3+} in KY_3F_{10} .

A Bridgman-Stockbarger grown 2x2x7 mm^3 KY_3F_{10} single crystal, containing ~1at.% of Nd^{3+} ions, was used as an active element. No antireflection coatings were applied to the polished ends for this experiment. The optical layout used for tunability characterization of the CW diode-pumped Nd^{3+}:KY_3F_{10} laser is shown in Fig.1 with optical components comprehensively described in figure caption. A crystal quartz two-plate birefringent filter (BRF) with free spectral range (FSR) of about 5 nm was used as an intracavity tuning element placed between the lens (ARL) and the output coupler (OC) where the laser beam wavefront is nearly flat. Diode end pumping was accomplished using a pair of laser diodes (LD-1 and LD-2) with orthogonally polarized outputs emitting at 798 nm and combined using a dielectric polarization combiner. Both polarizations are efficiently absorbed by the isotropic Nd^{3+}:KY_3F_{10} sample. Spherical collimating lenses

(CL), cylindrical lenses (Cyl. L) and a spherical focusing lens (SL) were used for pump beam shaping to match the $Nd^{3+}:KY_3F_{10}$ laser cavity beam waist inside the crystal.

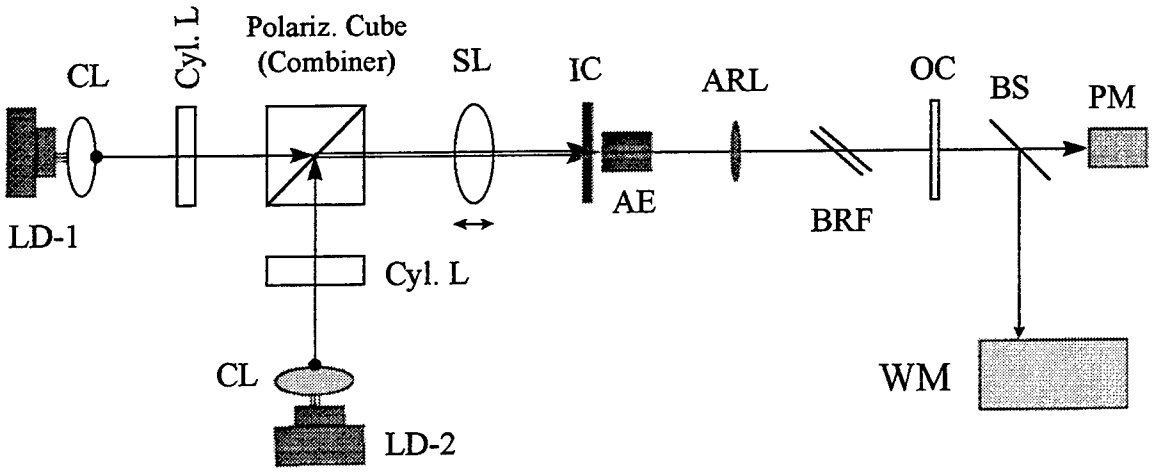

Fig. 1. Optical layout used for tunability characterization of the CW diode-pumped $Nd^{3+}:KY_3F_{10}$ laser. AE - 7 mm long $Nd^{3+}:KY_3F_{10}$ active element; LD-1, LD-2 - pumping laser diodes; CL - collimating spherical lenses; Cyl. L - cylindrical lenses; SL - focusing spherical lens; IC - flat input coupler (HR @ 1056±10 nm, HT @ 790 - 800 nm); ARL - antireflection coated (AR @ 1056±10 nm, f=500 mm) spherical lens; BRF - two-plate crystal quartz birefringent filter; OC - flat output coupler (T = 0.8%); PM -powermeter; WM - wavemeter; BS - beamsplitter.

Tunability between 1053.6 and 1059.1 nm (9442 - 9491 cm^{-1}) and output power of about 300 mW were obtained in this initial experiment. Tunability was only limited by the available birefringent filter FSR, and can be significantly extended. Even with this limited tunability, the laser described is applicable to environmental HBr monitoring. Some other molecules with reasonably strong absorption lines can also be traced. The needle plot below (Fig. 2) indicates the molecular signature lines falling in the above tunability range for three species of atmospheric importance - H_2O, CO_2, and HBr (molecules with the highest intensities in the range). The plot was obtained using the 1996 HITRAN Database (HAWKS) with the line intensities scaled into the standard units of $cm^{-1}/(molecule \times cm^{-2})$ at 296 K. Two more species of atmospheric importance - oxygen (O_2) and hydroxyl (OH), with significantly lower molecular line intensities (therefore not shown in Fig. 2) - can also be detected using long-path DIAL-Lidar systems incorporating the above described tunable $Nd^{3+}:KY_3F_{10}$ laser.

Conclusions

We report on what we believe to be the first tunable CW diode-pumped $Nd^{3+}:KY_3F_{10}$ laser. The continuous tunability (1053.6 - 1059.1 nm or 9442 - 9491 cm^{-1}) obtained in this initial experiment allows for HBr contamination tracing as well as satellite-based H_2O and ground-based CO_2 detection.

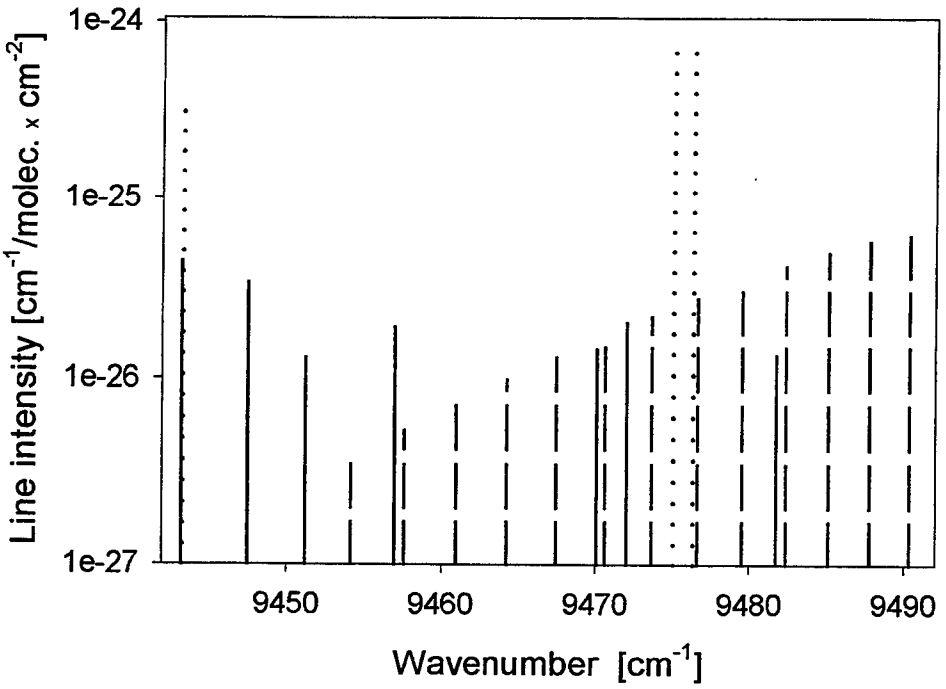

Fig. 2. Molecular absorption line intensities vs wavenumber for three species of atmospheric importance: water (H_2O) - solid line; carbon dioxide (CO_2) - dashed line; hydrogen bromide (HBr) - dotted line. The spectral range shown corresponds to the tunability region of a diode-pumped CW Nd^{3+}:KY_3F_{10} laser.

Acknowledgments. We would like to acknowledge useful input from Dr. C. Prasad of SESI regarding the environmental sensing issues. This work was supported by the US National Research Council, NATO Scientific and Environmental Affairs Division (Grant HTECH.LG 970582) and Russian Foundation for Basic Research (Grant 95-0205518a).

References

1. T. M. Pollak, R. C. Folweiler, E. P. Chicklis, J. W. Baer, A. Linz, and D. Gabbe, US Dep. of Commerce/NBS Spec. Publ. No. 568, 1980, p. 127 - 135.
2. R. Yu. Abdulsabirov, M. A. Dubinskii, B. N. Kazakov, N. I. Silkin, and Sh. I. Yagudin - Sov. Phys. Crystallogr. **32**, 559 - 562 (1987).
3. M. A. Dubinskii, OSA Proceed. on Advanced Solid-State Lasers, G. Dube and L. Chase, eds. (Optical Soc. of America, Washington, DC 1991), Vol.**10,** pp. 348-352.
4. M. A. Dubinskii, K. L. Schepler, A. K. Naumov, V. V. Semashko, R. Yu. Abdulsabirov, S. L. Korableva, OSA Trends in Optics and Photonics, Vol.**10**, Advanced Solid State Lasers, C. R. Pollock and W. R. Bosenberg, eds. (Optical Society of America, Washington, DC 1997), pp. 164 - 167.

Influence Of The Non-Linear Characteristic Of The Laser Source On Detected Signals In Derivative Spectroscopy For Gas Analysis

M. A. Morante, G. Stewart ‡, B. Culshaw ‡, and J. M. López-Higuera

Photonic Engineering Group, TEISA Dept., University of Cantabria
Avda. Los Castros s/n, Santander E-39005, Spain
Tel.: +34 42 201 539 ; Fax: +34 42 201 873

‡ Optoelectronics Group, E&EE Dept., University of Strathclyde
204 George Street, Glasgow G1 1XW, Scotland
Tel.: +44 141 552 4400 ; Fax: +44 141 553 1955

Derivative spectroscopy, or wavelength modulation spectroscopy (WMS), consists in obtaining the concentration of a molecular absorbent by modulating the output wavelength of the optical source and detecting at one of the harmonics of the modulation frequency. The first and second harmonic signals are proportional to the first and second derivatives of the absorption feature, respectively, for small WM amplitude. The maximum gradient of the first and the absolute maximum of the second harmonic signal, which are located at the absorption line center, are directly proportional to the species concentration. [1-3]. In practice, the output power/current characteristic of the laser has a slight degree of nonlinearity which influences the form of the recovered signal. As a result, the detected derivative trace displays a non-constant baseline that degrades the absorption signal. Furthermore, such baseline does not remain unchanged over the operating period of the source, because it is influenced by environmental factors and aging. In this work we analyze the effect of the mentioned nonlinear laser characteristic on the detected harmonic signal, and we propose a simple post-detection processing method to capture the baseline from the demodulated signal in real time.

The survey was applied to detecting methane with an Anritsu DFB laser diode emitting at 1.665 μm. Its output power versus drive current curve was experimentally measured and it was modeled by polynomials of different orders within the operating range. The third order curve proved to be the best fit to the actual laser output:

$$P(\nu) \cong P_0\left[1 - 1.91(\nu - \nu_0) - 0.195(\nu - \nu_0)^2 + 0.193(\nu - \nu_0)^3\right]$$

where ν_0 corresponds to the wavenumber for the Q6 line center, $\nu_0 \cong 6002.82$ cm^{-1}, and P_0 is the power delivered by the source at ν_0, $P_0 \cong 1$ mW.

We have derived theoretical expressions for the first and second harmonic signals and also obtained them experimentally in the laboratory with a dedicated fiber optic system devoted for methane detection. The signal emitted by the laser in a WMS experiment and partially absorbed by a small concentration of gas can be expressed as:

$$S(\nu) = kP(\nu)\exp\left(-\alpha(\nu)CL\right)$$

where $\alpha(\nu)$, C, and L are, the absorption function, the concentration, and the length of absorption of the gas, respectively, and k is a constant that accounts for the optical losses and other optical-electrical conversion factors in the system. The absorption feature of a molecular gas at atmospheric pressure follows a Lorentzian shape [4].

The fact that the laser output power, $P(\nu)$, is not constant over the whole operating range introduces an additional component in the demodulated signal. As a result the first harmonic signal can be expressed as a sum of a gas concentration-dependent component and what can be considered as a baseline, since it is present even in the absence of absorption:

$$f_1(\nu) = k_1\left[f_{1base}(\nu) + f_{1abs}(\nu)\right]$$

$f_{1base}(\nu)$ is a second order polynomial, and $f_{1abs}(\nu)$ is proportional to the first derivative of the absorption function. The gas concentration can be obtained from the value of the maximum gradient of the latter. If we detect at the second harmonic, the expression for the recovered signal can be derived the same way; the baseline is a sloping straight line, and the gas concentration is proportional to the absolute maximum of the absorption signal at the line center. Fig. 1 shows the detected first harmonic signal for 500 ppm.m of methane, and Fig. 2 displays the recovered second harmonic for 750 ppm.m absorption. The baseline in Fig. 1 is a shifted first-derivative of $P(\nu)$, while the baseline in Fig. 2 is a shifted second-derivative of $P(\nu)$, as stated previously.

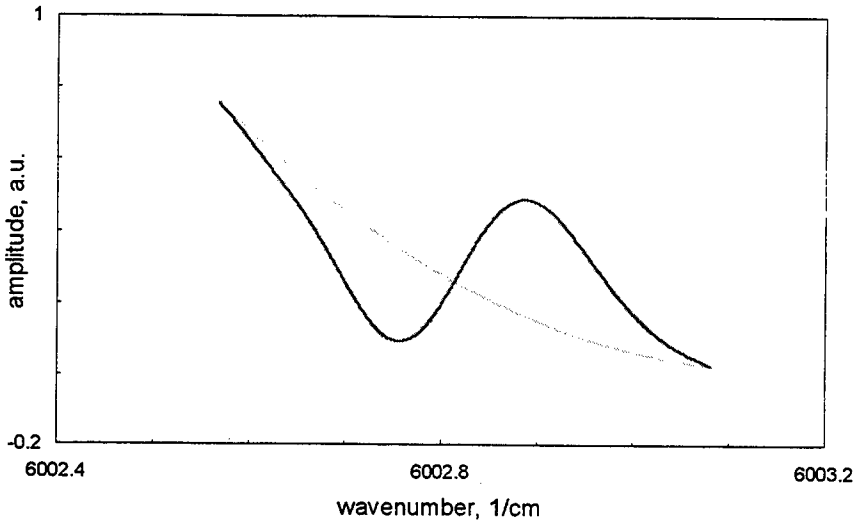

Figure 1. *Detected first harmonic signal for a concentration of methane of 500ppm.m, along with the baseline due to the nonlinearity of the laser characteristic(dashed curve).*

Since the baseline variation is comparable to the absorption signal, its effect must be subtracted before calculating the maximum gradient or the absolute maximum. In the case of first harmonic detection, the baseline can be calculated with the aid of three points on the detected trace; these points are the extremities of the line feature, where no absorption is expected, and the center of the absorption line, where the first derivative of the absorption function is zero and $f_1(\nu)$ coincides with $f_{1base}(\nu)$. If we demodulate at the second harmonic

frequency, the baseline can be obtained from two points -the limits of the absorption line-, since it is a first-order polynomial. Since the baseline is calculated from the detected signal in real time, errors due to change in the laser characteristics are avoided, and the accuracy of the measurement is increased.

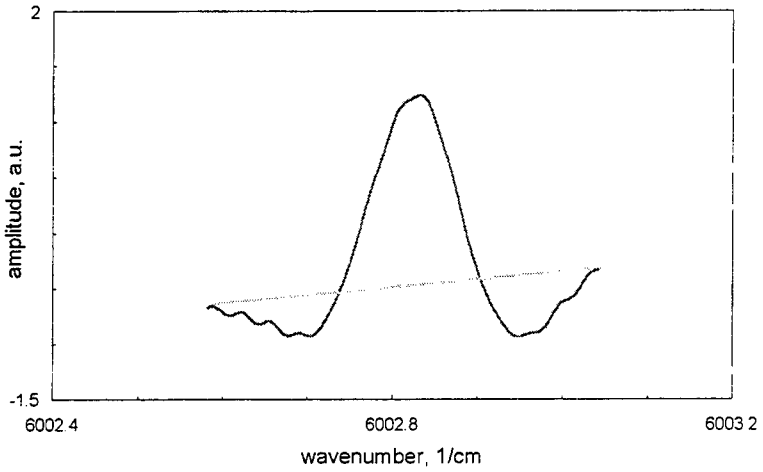

Figure 2. *Detected second harmonic signal for an absorption of 750ppm.m; the weak fringes are due to interference from multiple reflections in the gas cell.*

To sum up, the slight nonlinearity of the laser output characteristic introduces a baseline in the recovered signal in derivative spectroscopy that complicates the removal of the concentration data. The form of such baseline has been analyzed and a straightforward signal processing technique has been proposed to extract it, in real time, from the detected signal. This prevents the need of a reference path without absorption to obtain the baseline, or the need for having the baseline pre-recorded by periodical calibration.

The authors acknowledge support for this work from the LINK Photonics programme in the UK and from the Ministry of Education and Science in Spain.

References

[1] Supplee, J.M., Whittaker, E.A., and Length, W., "Theoretical description of frequency modulation and wavelength modulation spectroscopy". *Appl. Opt.*, **33**(27), pp. 6294-6302, (1994).

[2] Silver, J., "Frequency-modulation spectroscopy for trace species detection: theory and comparison among experimental methods". *Appl. Opt.*, **31**(6), pp. 707-717, (1992).

[3] Reid, J. and Labrie, D., "Second harmonic detection with tunable diode lasers: comparison of experiment and theory". *Appl. Phys. B*, **26**, pp. 203-210, (1981).

[4] Arndt, R., "Analytical line shapes for Lorentzian signals broadened by modulation". *J. Appl. Phys.*, **36**(8), pp. 2522-2524, (1965).

Dual-wavelength temperature measurements in an IC engine using 3-pentanone laser-induced fluorescence

S. Einecke, C. Schulz
Physikalisch-Chemisches Institut, University of Heidelberg, INF 253, D-69120 Heidelberg
Ph. +49 6221 54-8503, Fax: +49 6221 54-4255, email: christof.schulz@urz.uni-heidelberg.de

V. Sick
Dept. of Mech. Eng. and Appl. Mech., University of Michigan, 2023 Automotive Laboratory, Ann Arbor, MI 48109-2121
Ph. (313) 647-9607, Fax: (313) 764-4256, email: vsick@umich.edu

Introduction. Exact knowledge of the local temperature during the compression of air/fuel-mixtures in engines is crucial for evaluating modeling results of the ignition conditions and the flame development after ignition. Especially in ultra-lean burning modern engines using stratified load and exhaust gas recirculation inhomogeneous mixing takes place and causes inhomogeneous temperature distributions. Thus two-dimensional temperature imaging techniques have to be applied to provide the necessary information for model calculations. Temperature measurements in the compression stroke both before and after ignition have been performed in specially designed optically accessible engines using Rayleigh scattering [1]. In more production-like engines, however, due to background scattering the use of Rayleigh scattering for temperature measurements is very limited.
It has been demonstrated before[2,3] that laser induced fluorescence (LIF) of ketones like acetone and 3-pentanone is susceptible to temperature, depending on the excitation wavelength. This is mainly due to a temperature-dependent shift of the common absorption feature which ranges from 220 nm to 340 nm, peaking near 280 nm at room temperature. The resulting fluorescence occurs between 330 nm and 550 nm and is approximately independent of the excitation wavelength for 3-pentanone. Due to evaporation properties similar to those of the non-fluorescent model fuel iso-octane, 3-pentanone is an ideal marker used for mapping fuel distributions in SI engines, particularly when excited close to its absorption maximum where the fluorescence signal is nearly independent of temperature. When excited in the wings of the absorption spectrum, however, the signal is strongly dependent on temperature. This suggests the feasibility to quantitatively measure temperatures, as first demonstrated for static conditions by Grossmann et al. [2]

Theoretical Background. The fluorescence signal for weak laser excitation is given by the following equation:

$$S(\lambda, p, \chi, T) = C\,(Q_{laser}/ E_{photon}(\lambda))\, V\, n(T)\, \sigma(\lambda, p, \chi, T)\, \phi(\lambda, p, \chi, T)$$

where Q_{laser} is the laser irradiance, E_{photon} is the energy of a single photon, V is the detected volume, n is the number density, σ is the molecular absorption cross section of the marker, and ϕ the fluorescence quantum yield. σ and ϕ depend on the exciting laser wavelength λ, pressure p, mixture composition χ, and temperature T. The factor C comprises geometrical arrangements and detection optics properties.

If the same volume is excited by two laser pulses of different wavelengths (with a short temporal delay in to ensure separate detection of the induced fluorescence), the ratio $S(\lambda_1, p, T)/S(\lambda_2, p, T)$ displays the ratio of the pressure and temperature dependent absorption cross sections and fluorescence quantum yields. The detected volume V, the detected species' number density n and the detection efficiency C cancel out. Pressure effects can be corrected for using the data provided by Grossmann[2] and Ossler[4]. Therefore the remaining ratio of both signals is a function of temperature. A strong temperature dependence of the ratio can be expected when exciting in both wings of the absorption feature. In our experiments we used

excitation at 248 nm and at 308 nm: with increasing temperature, the fluorescence intensity decreases after excitation at 248 nm whereas it strongly increases after excitation at 308 nm. After calibration of the fluorescence ratios at known temperatures in static cells, the temperature at any given point in a 2D image can be obtained, even if the physical properties (i.e. mixture ratio) in the measurement volume are transient. This occurs in e.g. the compression phase of internal combustion engines where the knowledge of pre-combustion temperature distribution can enhance understanding of the subsequent ignition and combustion.

Experimental Setup: Measurements were conducted in a modified single-cylinder two-stroke engine (ELO L372) with a bore of 80 mm and 0.372 l displacement. Oil cooling at 50° C was used instead of the original air cooling to achieve stable cylinder wall temperature conditions. The original cylinder head was replaced by a quartz ring of 4 mm height to allow for the entrance and exit of the laser sheets, and a cylindrical full-size quartz window on top through which fluorescence could be monitored. The piston crown had a small pocket spared for the spark plug which enters through the cylinder wall close to TDC. This renders the combustion chamber essentially disk-shaped with a height of 4 mm at top dead center. The fuel was iso-octane (p.a.) doped with 10 % (v/v) 3-Pentanone, freshly mixed before measurements were taken, and fed into the engine via a carburetor. To avoid any fluorescence interference from lubricants, a thin film of MoS_2-grease applied to the cylinder wall replaced the oil usually added to two-stroke fuel. No interfering fluorescence from the grease was fmeasureable. The engine was motored at 1000 rpm. Measurements were performed both without ignition and in a skip-fired mode with four skipped cycles between ignitions. A crank shaft encoder provided a trigger for control of the lasers, image and data acquisition, and ignition. In-cylinder pressure traces were measured using a pressure transducer (Kistler 6001) and charge amplifier.
The excimer lasers (Lambda Physik EMG 150TMSC and EMG 150EST), operated with KrF (248 nm), and XeCl (308 nm) respectivelywere fired with a fixed time delay of 150 ns to prevent crosstalk of the signals. The laser beams were formed into two sheets of approx. 2 cm width and 0.5 mm height employing two cylindrical telescopes carefully adjusted for spatial overlap. Laser output energies were monitored on a shot-to-shot basis. The laser power density at no time exceeded 30 MW/cm^2 to ensure excitation in the linear regime [4].

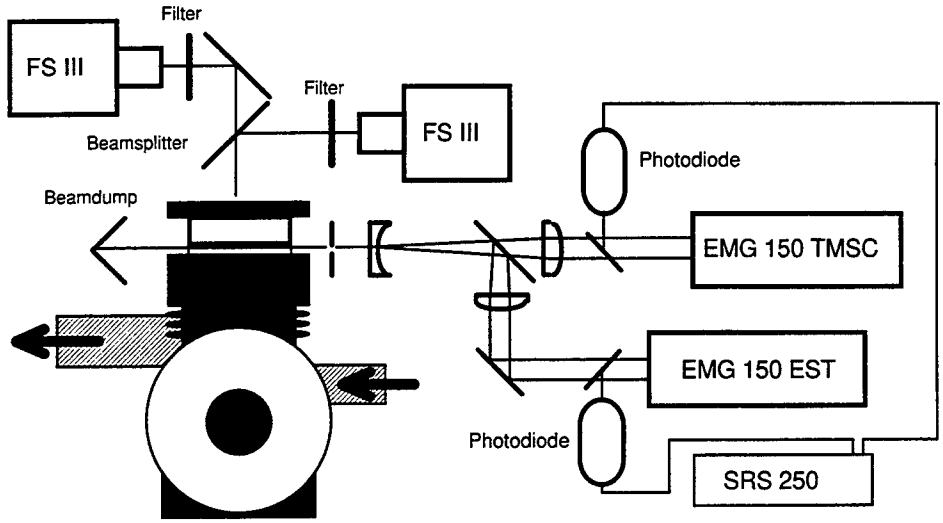

Figure 1: Experimental setup of the dual-wavelength temperature measurements using fluorescence of 3-pentanone in the two-stoke engine

On the detection side, the fluorescence signal was split using a metal-coated beam splitter and each part was imaged onto an intensified CCD camera (LaVision FlameStar III) equipped with an f/2, f=100 mm achromatic UV lens (Halle). A region of 6.7 cm x 5 cm was imaged onto the camera chips (768 x 572 pixels). To avoid detecting scattered light at the excitation wavelengths a Schott WG335 filter was placed in front of each camera. The cameras were triggered so that one of them would only detect fluorescence

from 248 nm excitation, the other that from 308 nm excitation with exposure times of 70 ns for each camera. The camera signals were digitized with a resolution of 12 bit and stored by a computer.

Results: The single-shot images acquired with both laser/camera systems were corrected for background luminosity, laser sheet inhomogeneities, variations of integral laser energy and the pressure influence on the fluorescence signal[2]. Division of corresponding pairs of corrected images yielded the temperature dependant ratio from which the temperature can be extracted using the calibration measurements[2,5].
For the given engine arrangement, with the carburetor fuel system, no spatial variances in the temperature distributions were found at a range of crank angles. Thus averaged temperatures over a field of 24.5 x 17.5 mm are presented here.
Figure 2 shows a histogram over 140 single shot temperature measurements at a fixed crank angle position of 342°ca in independent engine cycles. The averaged pressure for this condition is 10.9 bar. The time dependent increase of temperature with pressure during compression is shown in Figure 3. Averaged temperatures over 140 single measurements for four different detection timings in the compression stroke are shown.

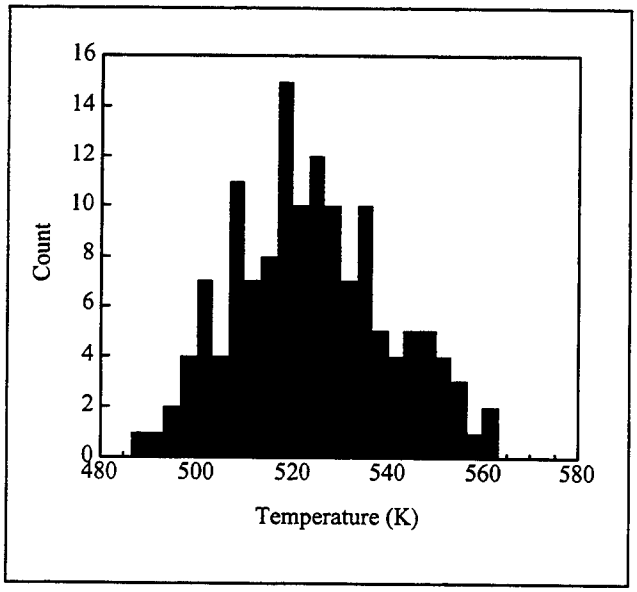

Figure 2:
Temperature histogram; 140 single shot temperature measurements at 342°ca, 1000 rpm, p_{av}=10.9 bar

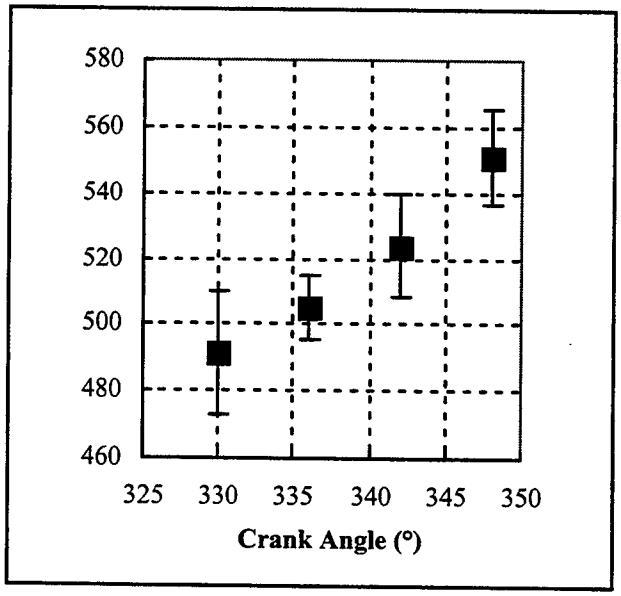

Figure 3:
Increase of temperature during compression.

References:

1. Bräumer, V. Sick, J. Wolfrum, V. Drewes, M. Zahn, R. Maly; SAE Paper 952462 (1995)
2. F. Grossmann, P. B. Monkhouse, M. Ridder, V. Sick, J. Wolfrum; Appl. Phys. B 62, 249 (1996)
3. M. C. Thurber, F. Grisch, R. K. Hanson; Opt. Lett. 22, 251 (1997)
4. F. Ossler, M. Aldén; Appl. Phys. B 64, 493 (1997)
5. R. Tait, D. Greenhalgh; Ber. Bunsenges. Phys. Chem. 97, 1619 (1993)

Instantaneous Velocity Field Measurements of Air Flows by Ozone Tagging Velocimetry (OTV)

Lubomir A. Ribarov, Joseph A. Wehrmeyer, Robert W. Pitz
Department of Mechanical Engineering, Vanderbilt University
Box 1592, Station B, Nashville, TN 37235-1592, USA

Peter A. DeBarber
MetroLaser, Inc., Suite 100, 18010 Skypark Circle, Irvine, CA 92614-6428, USA

Introduction

Although species concentrations and temperature are routinely measured by laser-molecular interactions (laser-induced fluorescence, Raman scattering), velocity is most often measured by the introduction of foreign seed particles, such as oil droplets or ceramic particles. Particle-imaging velocimetry systems are commercially available and provide velocity field measurements based on time-of-flight data from many particles. However, seeding non-uniformities and particle drag can lead to differences between the particle and gas velocity fields. Environmental and operational issues discourage the introduction of particles into large wind tunnel test facilities.

Molecular velocity measurement techniques have been developed where the flow is seeded with a molecular tracer (i.e., iodine, biaceytl, nitric oxide, sodium). Often these tracers are either corrosive or toxic. There remains a need for an optically-based molecular velocity field measurement technique that is "unseeded." A flow tracer or "tag" should be created, photochemically or otherwise, from the nascent gas species to obviate seeding requirements.

High-speed (supersonic) unseeded air velocity fields have been measured using the Doppler shift of Rayleigh scattering.[1] For lower speeds though, direct Doppler methods are not as accurate as time-of-flight methods.

Time-of-flight molecular tagging velocity measurement techniques have been developed that do not require seeding. Most of these techniques create a tag by nonlinear optical processes that limit the length of the tagged line to a few millimeters. For example, using two-photon photodissociation of water vapor, a tag line of OH can be created and subsequently made to fluoresce to profile flow velocity.[2] In the RELIEF method, a nonlinear stimulated Raman process produces a tag line of vibrationally-excited oxygen (O_2) whose enhanced fluorescence strength reveals the line's location when the flowfield is subsequently irradiated by an ultraviolet (UV) laser.[3] The short lifetime of vibrationally-excited O_2, especially in water-laden air, generally limits RELIEF to high-speed, dry flows.

Thus there is still a need for a nascent species molecular flow tagging technique that is amenable to low- or high-speed flows of either dry or humid air. This paper describes a technique being developed to fill that need: ozone tagging velocimetry (OTV).[4] Ozone (O_3), produced from O_2, is the flow tag and is relatively long-lived and insensitive to water vapor's presence. It is produced and detected via single-photon processes, allowing the usage of long tag lines. Tag lines of 40 mm length are used in an instantaneous OTV flow profile presented in this paper. Several OTV developmental issues are also investigated, including the dependence of O_3 production upon temperature, and the merit of using narrowband or broadband lasers.

OTV Photochemistry

Figure 1 shows a conceptual drawing of the OTV technique. First a tag line of O_3 is created from O_2 by a pulsed argon-fluoride (ArF) excimer laser operating at ~193 nm. After a known delay time, the O_3 tag line position is revealed through O_3 photodissociation and subsequent O_2 fluorescence, both caused by a pulsed laser sheet from a krypton-fluoride (KrF) excimer laser operating at ~248 nm. A digital camera images the fluorescence from the initial and final line locations, thus providing means for establishing a velocity profile.

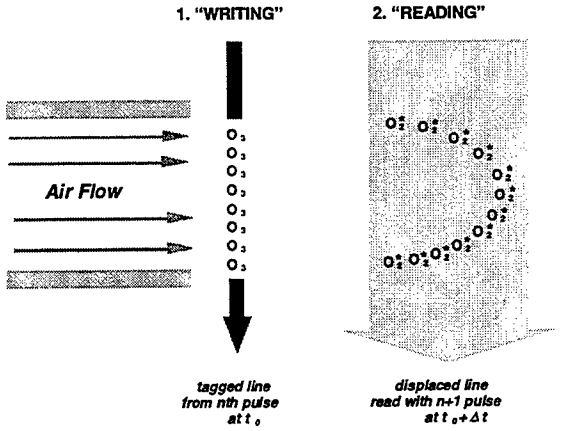

Fig. 1. OTV conceptual diagram.

The following two reactions are involved in photochemically writing the O_3 line:

$$O_2\,(X^3\Sigma^-_g,\, v''=0) + h\nu_{\lambda=193\ nm} \rightarrow O + O \qquad \text{R1}$$

$$O + O_2 + M \rightarrow O_3 + M \qquad \text{R2}$$

In R1, O_2 in the ground ($X^3\Sigma^-_g$) electronic and ground vibrational ($v'' = 0$) state absorbs a photon of 193 nm light and decomposes into atomic oxygen, due to the high predissociation rate of the excited molecular state.[5] The reaction rate for R1 is approximately 10^{11} s^{-1}. In R2 the atomic oxygen combines with O_2, via a three-body reaction with an inert M, forming O_3. The reaction rate (k_2) for R2 governs O_3 production. For M=N_2 or O_2, $k_2=5.7\times10^{-46}$ m^6/s at standard conditions (1 atm and 300 K).[6] The growth time of O_3 (to 50% of steady state concentration) for standard conditions is then $1/(k_2 n_{O2} n_{N2}) \cong 20$ μs, where n is number density.

The displaced O_3 line is "read" by the 248 nm light sheet through reactions R3 and R4:

$$O_3 + h\nu_{\lambda=248\ nm} \rightarrow O\ (^3P) + O_2\ (X^3\Sigma^-_g,\ v''>0) \qquad R3$$

$$O_2\ (X^3\Sigma^-_g,\ v''=6,7) + h\nu_{\lambda=248\ nm} \rightarrow O_2\ (B^3\Sigma^-_u, v'=0,2) \qquad R4$$

The peak of the O_3 Hartley band occurs near 248 nm, and of that portion of O_3 that absorbs 248 nm light, about 10% quickly photodissociates via R3.[7] The O_2 thus created is vibrationally-excited, and O_2 in the $v''=6,7$ vibrational levels can be detected by further 248 nm absorption (from the same laser pulse) and subsequent fluorescence from the ($B^3\Sigma^-_u$,$v'=0,2$) state.

Using the Chemkin-II thermodynamic database and the Senkin[8] chemical kinetics solver, predictions of O_3 concentration vs. time have been made using a set of 108 reversible reactions. For dry air at standard conditions with an arbitrary initial atomic oxygen concentration of 4200 ppm (1% dissociation of ambient O_2), a steady-state O_3 concentration of ~3700 ppm is predicted to occur at ~1 msec and to persist for at least 100 sec.[4] However, as initial temperature is increased O_3 destruction reactions become important, reducing both the lifetime and the peak concentration of O_3. Figure 2 shows these effects for three different temperature/pressure combinations. At 500 K and 1 atm the peak concentration has dropped to ~600 ppm, thus providing only 16% of the OTV signal for standard conditions, disregarding the additional signal loss from total density reduction. Additionally the upper limit to read/write time delay must be less than ~100 msec, though this is not a severe limitation for OTV-measured flow velocities of the order of centimeters per second or greater. The signal loss and time delay are more severe at 600 K, where the peak concentration is now at 200 ppm. While increased temperature is detrimental to O_3 production, increased pressure improves the O_3 peak concentration, due to the three-body formation path of O_3, as compared to its two-body destruction paths.[6] Figure 2 shows a peak O_3 concentration of over 1000 ppm at 500 K and 2 atm.

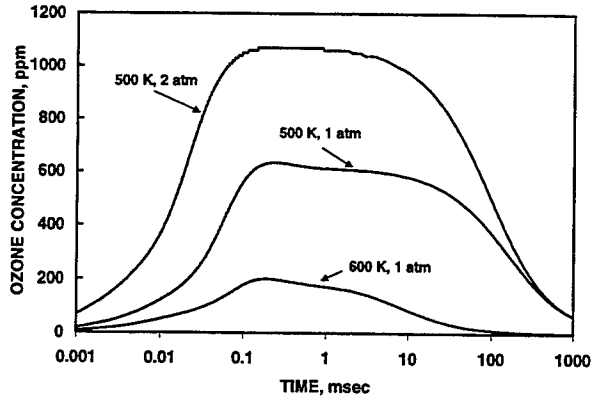

Fig. 2. O_3 concentration vs. time for dry air.

Narrowband/Broadband Experimental Comparison

Time-averaged OTV images have previously been obtained in air using broadband lasers.[4] Narrowband lasers, whose output can be precisely tuned onto O_2 transitions to maximize either photodissociation or fluorescence yields, can enhance OTV signal strength. In the present work two Lambda-Physik lasers are used: a COMPex-150T (0.003 nm linewidth tunable from 192.5 to 193.5 nm) and an EMG-160T MSC (0.001 nm linewidth tunable from 248 to 249 nm). Several O_2 Schumann-Runge transitions are within each of these tuning ranges. Both lasers can be operated broadband with output linewidths equal to their tuning ranges.

Figure 3 shows four time-averaged (20 laser pulse pairs) OTV images obtained in a uniform air flow (~3 m/sec) with each image for a specific combination of narrowband and/or broadband lasers. In narrowband operation the lasers are tuned onto O_2 transitions: 193.293 nm, corresponding to the predissociation-broadened P(17) and R(19) (0→4) lines; or the 248.534 nm R(17) (6→0) lines for the KrF laser. A Nikon UV camera lens and a Princeton Instruments ICCD camera comprise the light detection system, along with two identical interference filters (Laseroptik GmbH, 0° incidence notch filters) used to block 248nm Rayleigh

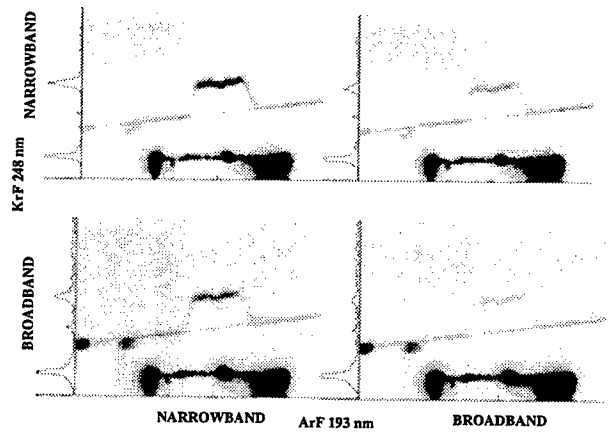

Fig. 3. Time-average OTV images for four laser modes.

scattering. The camera intensifier is gated only during the KrF laser firing, yet 193nm Rayleigh scattering marks the original tag line location, due to photocathode image persistence.

Strength of signal is greatly improved by using two narrowband lasers rather than two broadband lasers, as shown in Fig. 3 by the increased signal of the upper left OTV image compared to the lower right. For single narrowband and single broadband laser operation, a narrowband ArF laser provides slightly better signal than a narrowband KrF laser. Contrast ratios for the four images are 7.5, 3.8, 2.5, and 3.9, clockwise from upper left, estimated by averages of displaced OTV line signal vs. background, mainly due to 248 nm Rayleigh.

Instantaneous OTV Velocity Profile

Figure 4 shows an instantaneous OTV image, obtained from a single laser pulse from each laser. Both lasers are operated narrowband. A nozzle, attached to a loudspeaker receiving a 1 Hz square wave signal, produces a cylindrically-symmetric, mushroom-shaped vortical flowfield. Two tag lines are used to provide a cross whose center provides an unambiguous point to determine velocity. The cross center's 8 mm displacement during the 4 msec delay gives a measured velocity of 2 m/sec. Only one interference notch filter is used and is coupled to a liquid butyl acetate long pass filter that blocks light shorter than ~252nm. As a result 193nm Rayleigh does not mark the original tag line position, though other OTV images with 0 msec read/write delays confirm the tag lines' initial locations.

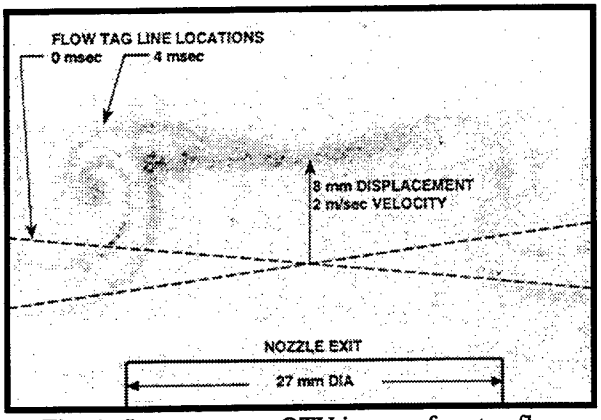

Fig. 4. Instantaneous OTV image of vortex flow.

OTV Filter Selection

Figures 3 and 4 were obtained using two different filter combinations. A butyl acetate filter may be desirable if 193 nm light interferes with OTV signal detection, possibly when scattering surfaces are within the detection system field-of-view. However other filter options exist that block both 193 and 248 nm light but allow fluorescence detection for O_2 transitions between these wavelengths. Figure 5 shows that a liquid acetone filter[9] (10 mm thick, 0.5% acetone in water solution) or a 10 mm thick Schott UG-5 filter both greatly attenuate 193 nm light while allowing through longer wavelength O_2 fluorescence. While the acetone filter is more transmissive from 198 to 228 nm, the glass filter becomes the more transmissive at higher wavelengths. Combinations of these 193 nm filters and 248 nm notch filters can be used when a background of intense scattered light is present at both wavelengths.

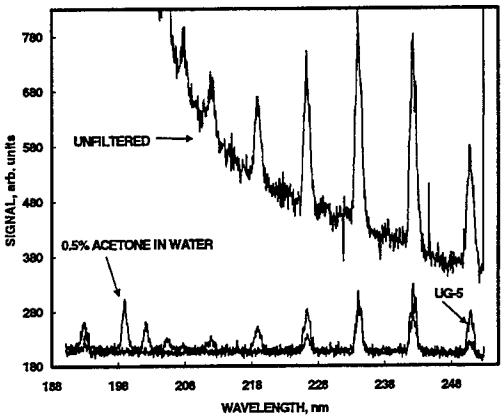

Fig. 5. O_2 fluorescence spectra, 193 nm excitation.

Summary and Conclusions

By using narrowband lasers tuned onto the O_2 Schumann-Runge transitions involved in the read and write steps, the OTV contrast ratio can be improved by a factor of three over that obtained using broadband lasers. The single-photon processes of both steps cause OTV to be insensitive to beam focus, allowing long tag lines to be created, as demonstrated in the instantaneous OTV image presented in this work, where the tag lines are over 40 mm in length. Though the O_3 molecular tag is relatively insensitive to water vapor or pollutants,[4] its peak concentration and lifetime do depend on temperature and pressure of the tagged flow, with the peak concentration dropping from 3700 to 600 ppm, going from 300 to 500 K at 1 atm. By identifying a "hot tag" that is complementary to OTV, velocity profiles of flowfields containing both hot and cold regions (i.e. flames or engine exhausts), can be mapped.

References

1. J. N. Forkey, N. D. Finkelstein, W. R. Lempert, R. B. Miles, *AIAA J.* **34**, 442 (1996).
2. L. R. Boedeker, *Opt. Lett.* **14**, 473 (1989).
3. R. Miles, W. Lempert, *Ann. Rev. of Fluid Mech.* **29**, 285 (1997).
4. R. W. Pitz, T. M. Brown, S. P. Nandula, P. A. Skaggs, P. A. DeBarber, M. S. Brown, J. Segall, *Opt. Lett.* **21**, 755 (1996).
5. G. Laufer, R. L. McKenzie, D. G. Fletcher, *Appl. Opt.* **29**, 4873 (1990).
6. B. Freisinger, U. Kogelschatz, J. H. Schäfer, J. Uhlenbusch, W. Viöl, *Appl. Phys. B* **49**, 121 (1989).
7. H. Park, T. G. Slanger, *J. Chem. Phys.* **100**, 287 (1994).
8. A. E. Lutz, R. J. Kee, and J. A. Miller, *SAND87-8258* (1987).
9. R. L. McKenzie, *Opt. Lett.* **18**, 995 (1993).

High Resolution Hole Burning Spectroscopy of Aluminum Phthalocyanine Tetrasulfonate in MCF-10F Human Breast Epithelial Cells

N. Milanovich, T. Reinot, G. J. Small, and J. M. Hayes
Ames Laboratory USDOE and Department of Chemistry
Iowa State University, Ames, IA 50011

Biological samples when subjected to cryogenic temperatures display an inherent disorder which gives these samples glass-like properties. Thus the high resolution optical techniques such as fluorescence line narrowing (FLN) [1] and hole burning [2] which have been developed to probe into the inhomogeneously broadened absorption spectra of impurity molecules in glasses are increasingly being used to investigate biological samples. FLN, for example, has been used to study DNA-carcinogen complexes at physiological damage levels [3,4] and protein-chromophore interactions [5]. Hole burning has been used extensively to study electron and energy transfer processes in photosynthetic systems [6,7]. Because the band widths obtained by these techniques are so narrow compared with room temperature absorption widths, Stark shifts and broadening and pressure effects on the spectra can be accurately measured.

In this paper, we report the results of hole burning and pressure shifts for a dye molecule within cultured mammalian cells. The results reported here represent the first measurements of hole burning and compressibility for dye molecules within intact cells. The hole burning mechanism will be shown to be non-photochemical hole burning which occurs due to rearrangement of the matrix which solvates the dye rather than due to photochemistry of the dye itself. Non-photochemical hole burning is thus extremely sensitive to the molecular environment of the dye molecule. This opens up the possibility of utilizing hole burning using organelle specific dye molecules to "image" anomalies in sub-cellular structures. As differences in hole burning parameters such as hole width, hole growth and hole shifts with pressure and temperature are due to differences in T_2 optical relaxation, this concept of hole burning imaging is directly analogous to magnetic resonance imaging which measures proton T_1 relaxation times to detect differences in tissue structures.

We report here the hole burning of APT inside MCF-10F human breast epithelial cells. The cells were stained with APT, at which time the cells were prepared for study at liquid helium temperatures (~4.5 K). Spectra obtained for APT in MCF-10F cells was compared to those for APT in hyperquenched glassy water. We also present here the results of pressure effects on the center frequency and width of holes burned in APT's fluorescence excitation spectrum and, subsequently, determine the compressibility of the dye in MCF-10F cells. In general, we are interested in detecting cellular anomalies so that we might eventually apply nonphotochemical hole burning to the early detection of disease.

Acknowledgement

The Ames Laboratory is operated for the U. S. Department of Energy by Iowa State University under Contract W-7405-Eng-82, and this work was supported by the Office of Health and Environmental Research, Office of Energy Research.

References

(1) R. Jankowiak and G. J. Small, *Chem. Res. Toxicol.* **1991,** *4,* 256-269.
(2) R. Jankowiak, J. M. Hayes, and G. J. Small, *Chem. Rev.* **1993,** *93,*1471-1502.
(3) R. Jankowiak, R. S. Cooper, D. Zamzow, and G. J. Small, *Chem. Res. Toxicol.* **1988,** *1,* 60-68.
(4) F. Ariese, G. J. Small, and R. Jankowiak, *Carcinogenesis,* 1996, *17,* 829-837.
(5) A. D. Kaposi, J. Fidy, S. S. Stavrov, and J. M. Vanderkooi, *J. Chem. Phys.,* **1993,** *97,* 6317-6327.
(6) R. Jankowiak and G. J. Small, In *The Photosynthetic Reaction Center,* J. Diesenhofer and J. Norris, Eds., Academic: New York, 1993, Vol. II, p 133-177.
(7) N. R. S. Reddy, P. A. Lyle, and G. J. Small, *Photosyn. Res.* **1992,** *31,* 167-177.

Diode-laser absorption measurements of CO_2, H_2O, and N_2O near 2 μm

R.M. Mihalcea, D.S. Baer, R.K. Hanson
High Temperature Gasdynamics Laboratory
Department of Mechanical Engineering
Stanford University, Stanford, CA 94305-3032
650-725-4016

G. S. Feller
Focused Research Inc.
2630 Walsh Avenue
Santa Clara, CA 95051-0905

A tunable external-cavity diode laser (ECDL) operating near 2.0 μm was used to perform absorption measurements of CO_2, H_2O, and N_2O in a heated static cell at various pressures (15 - 760 torr) and temperatures (294 K - 1460 K). The present work represents an extension of previous diode-laser absorption measurements of weaker vibrational overtones near 1.5 μm[1] and thus offers significantly higher measurement sensitivity. Absorption survey spectra of CO_2, H_2O, and N_2O in the spectral region between 4866 cm^{-1} and 5118 cm^{-1} were recorded, compared to calculations (based on the HITRAN96 and HITEMP databases), and used to select the optimum transitions for concentration measurements. Individual transitions (1-cm^{-1} scans) were measured in order to determine line strength values and self broadening parameters.

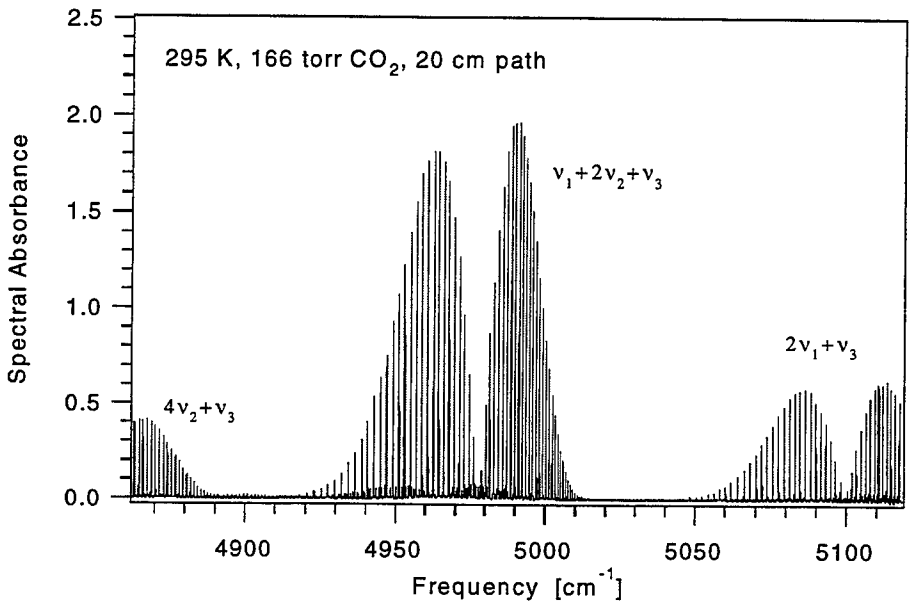

Figure 1. Measured survey spectra of CO_2 between 4866 cm^{-1} and 5118 cm-1 (295 K, 166 torr, 20-cm path).

Figure 1 shows the measured survey spectra of CO_2 between 4866 cm^{-1} and 5118 cm^{-1} (295 K, 166 torr CO_2, 20 cm path). The strongest CO_2 absorption band ($\nu_1+2\nu_2+\nu_3$ band) near 4978 cm^{-1} offers the best opportunity for sensitive CO_2 measurements. Survey spectra of H_2O in this spectral region were also recorded and compared to CO_2 survey

spectra to identify potential interferences. Figure 2 is a plot of the measured survey spectra of H_2O between 4915 cm^{-1} and 5108 cm^{-1} (295 K, 17.6 torr, 60 cm path).

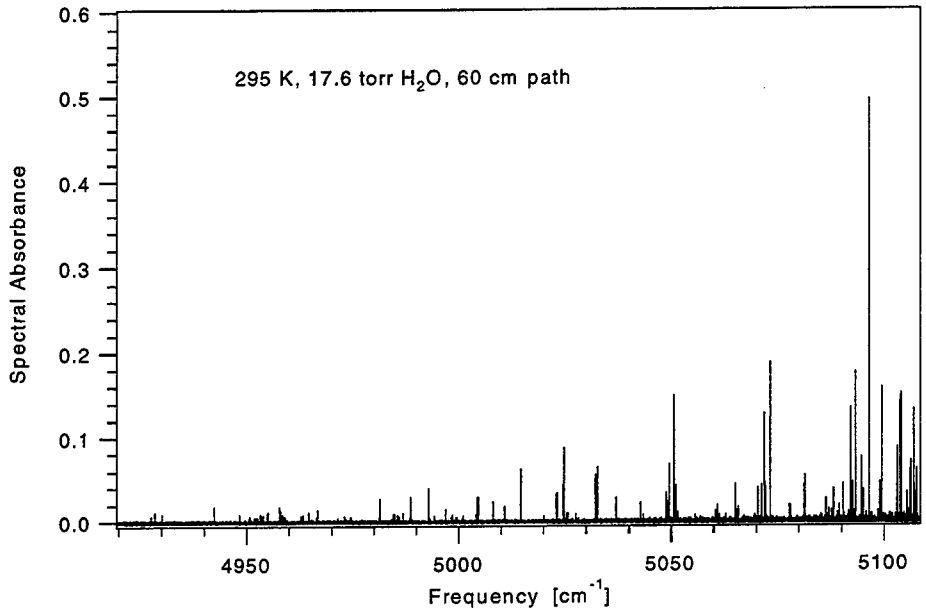

Figure 2. Measured survey spectra of H_2O between 4915 cm-1 and 5108 cm-1 (295 K, 17.6 torr, 60 cm path).

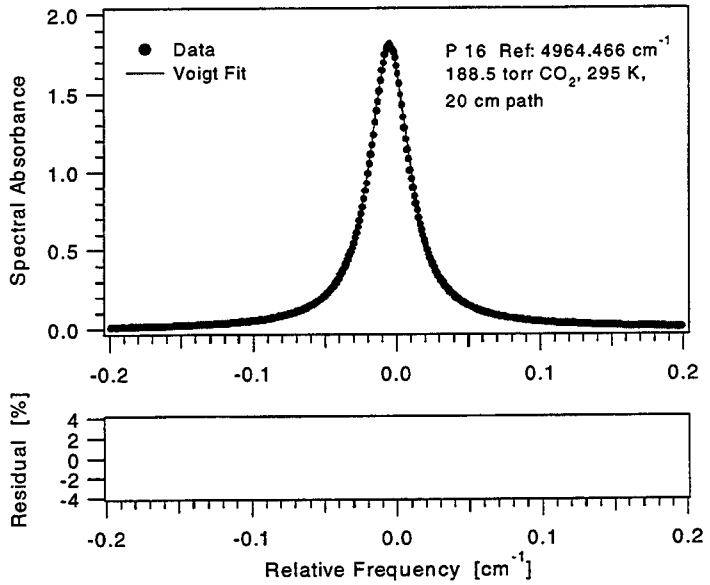

Figure 3. Measured single lineshape of the P16 line of the CO_2 $\nu_1+2\nu_2+\nu_3$ band at 4964.466 cm-1. The residual represents the normalized difference between the data and the best-fit Voigt profile.

The P16 line of the CO_2 $\nu_1+2\nu_2+\nu_3$ band was selected for species concentration measurements of CO_2 near room temperature. Figure 3. shows the P16 line at 4964.466 cm^{-1} and the best-fit Voigt profile. The residual represents the normalized difference between the data and the Voigt fit. The shape of the residual suggests collisional

narrowing of this transition. The P16 line strength at 295 K was determined by various single-lineshape measurements over a pressure range between 114.7 torr and 370.2 torr as shown in figure 4. The measured average P16 line strength (0.0285 cm^{-2}/atm) at 295 K was 9% lower than the corresponding value (0.03131 cm^{-2}/atm) in the HITRAN96 database. The experimental uncertainty was estimated to be 1.5%. The average measured self-broadening parameter (not listed in the HITRAN96 database) was 2γ=0.193 cm^{-1}/atm at 295 K.

Additional survey spectra of CO_2 and H_2O at elevated temperatures and N_2O at 295 K were recorded and will be compared to values in the HITRAN96 and HITEMP databases.

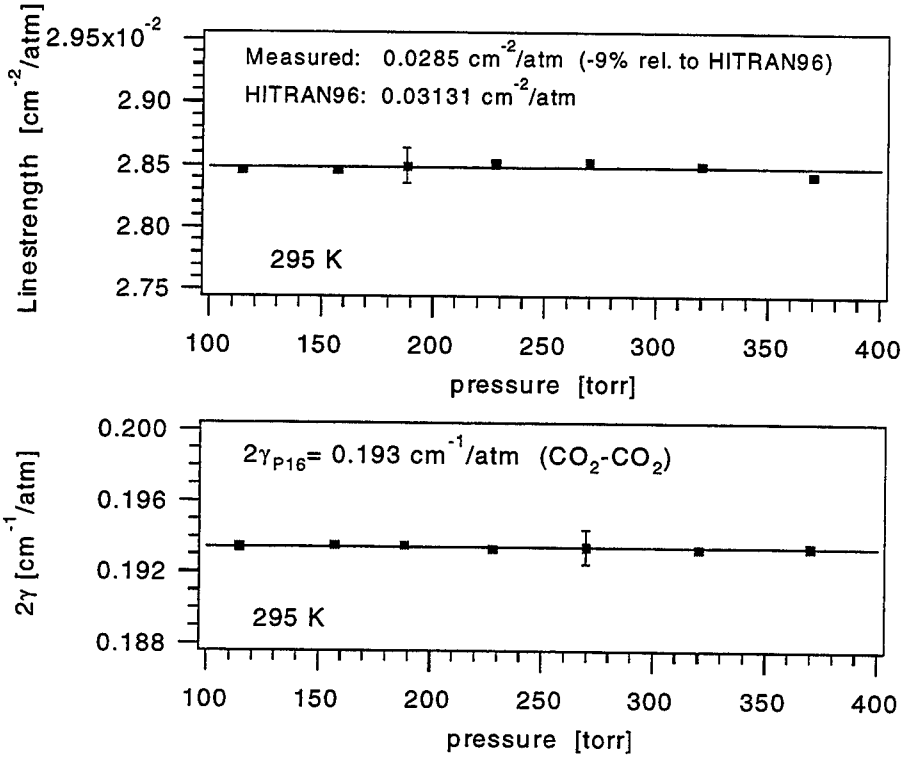

Figure 4. Measurements of line strength and 2γ values of the CO_2 P16 transition ($\nu_1+2\nu_2+\nu_3$ band) at 295 K and various pressures between 114.7 torr and 370.2 torr.

Reference:

1. R.M. Mihalcea, D.S. Baer, and R.K. Hanson, "Diode-laser absorption sensor system for measurements of combustion pollutants," Measurement Science and Technology (submitted for publication July 1997).

Raman measurements of supersonic hydrogen/air mixing

Peter Kasal, Joachim Boltz, Peter Gerlinger, and Dieter Brüggemann

Institut für Thermodynamik der Luft- und Raumfahrt (ITLR),
Universität Stuttgart,
Pfaffenwaldring 31, 70550 Stuttgart, Germany.
Tel.: +49 711 685 2316
Fax.: +49 711 685 2317

Summary

The investigation of fuel/air mixing in high velocity compressible flow is important for a complete understanding of fluid dynamic and for engine development of a future space transportation vehicle with subsonic (ramjet) or supersonic (scramjet) combustion. Numerous configurations with parallel, transverse and oblique fuel injection through walls, ramps or struts have already been investigated[1-5].

Due to its typically lower total pressure drop, parallel injection is preferable for high Mach numbers. The injection of hydrogen at Mach 2.2 into a parallel air flow at Mach 2.0 is studied here. To enhance mixing we injected hydrogen at Mach 2.2. Non-intrusive 1-D Raman spectroscopy was employed to simultaneously determine the distributions of hydrogen, oxygen and nitrogen mole fraction as well as of the temperature. Additional wall pressure measurements and schlieren imaging help to describe the flow in the supersonic mixing channel. Detailed quantitative data for validation of (CFD) calculation are provided.

Our experiments were performed in a rectangular supersonic mixing channel (SMC). It is 35.4 mm high and 40.0 mm wide with a total length of 350 mm and a critical cross section area of 805 mm^2. The air flow was 556 g/s with a temperature of 286.2 K and an absolute pressure of 388.5 kPa before expansion. For pure mixing experiments without combustion the side walls are made of optical quality glass. Upper and lower wall were used as laser beam entrance and exit respectively. The upper wall was additionally perforated with holes of 0.2 mm diameter at 3 mm distance to each other for wall pressure measurements in the channel. The hydrogen was injected with Mach 2.2 parallel into the supersonic air flow of Mach 2.0 through a strut which was placed in the center of the SMC. For the present investigation the injected hydrogen mass flow was 2.4 g/s with a temperature of 287.6 K and an absolute pressure of 427.5 kPa before expansion. The critical cross section area for hydrogen was 11 mm^2. The SMC is fixed on the end of the electrical heater at the ITLR supersonic test facility.

Raman scattering was excited by a 20 W argon-ion-laser (Spectra-Physics) at 514.5 nm. The scattered light was collected with two achromatic collection lenses passed an imaging correction unit and a polychromator (Acton AM-505F-S) and was recorded with a CCD-camera. A narrow band notch-filter between the achromatic lenses suppressed undesirable Mie and Rayleigh scattered light.

Spontaneous Raman scattering was detected from a line along the laser beam. The observed section covered 4 mm on both sides of the SMC centerline. The quantitative determination of species concentrations is straight-forward and reliable. The scattered light intensity I_j from particular species j collected over a solid angle Ω is given by:

$$I_j(\Delta\nu) = N_j\left(\frac{d\sigma}{d\Omega}\right)_{\Delta\nu,j} I_0 C_{\Delta\nu}\Omega L\,.$$

Here I_0 is the intensity of the exciting laser light, N_j the number of scattered molecules from particular species j, $(d\sigma d\Omega)_{\Delta\nu,j}$ its Raman scattering cross section and L the length of the measured volume. $C_{\Delta\nu}$ is an apparatus constant.

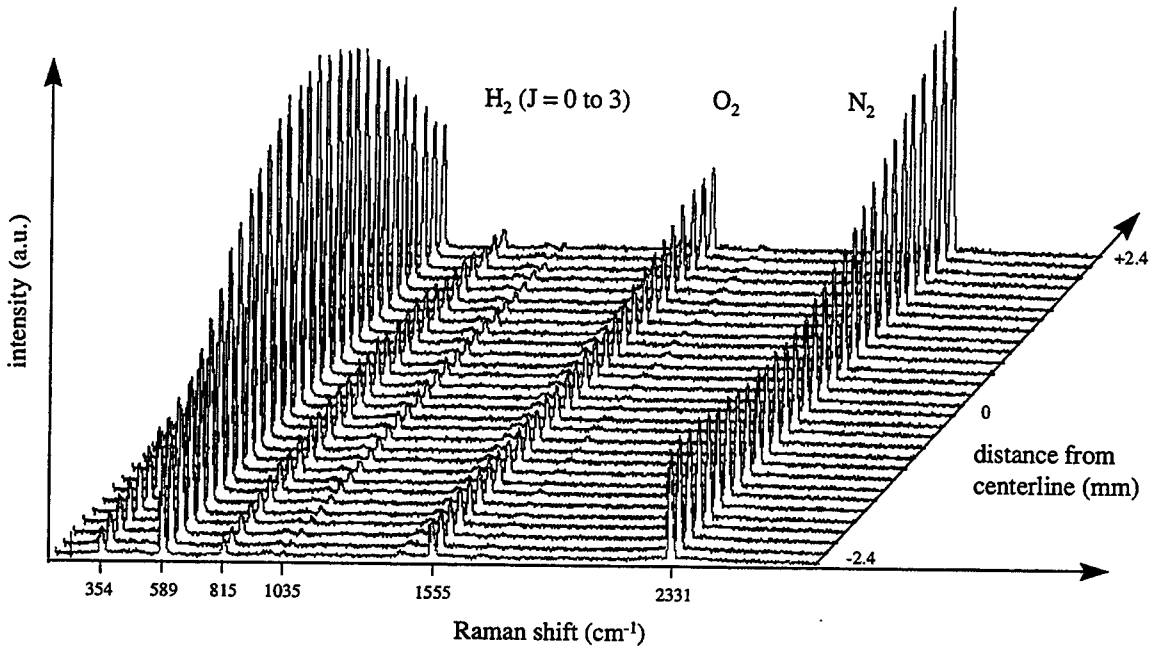

Fig.1: 1-D Raman spectra 150 mm behind hydrogen injection.

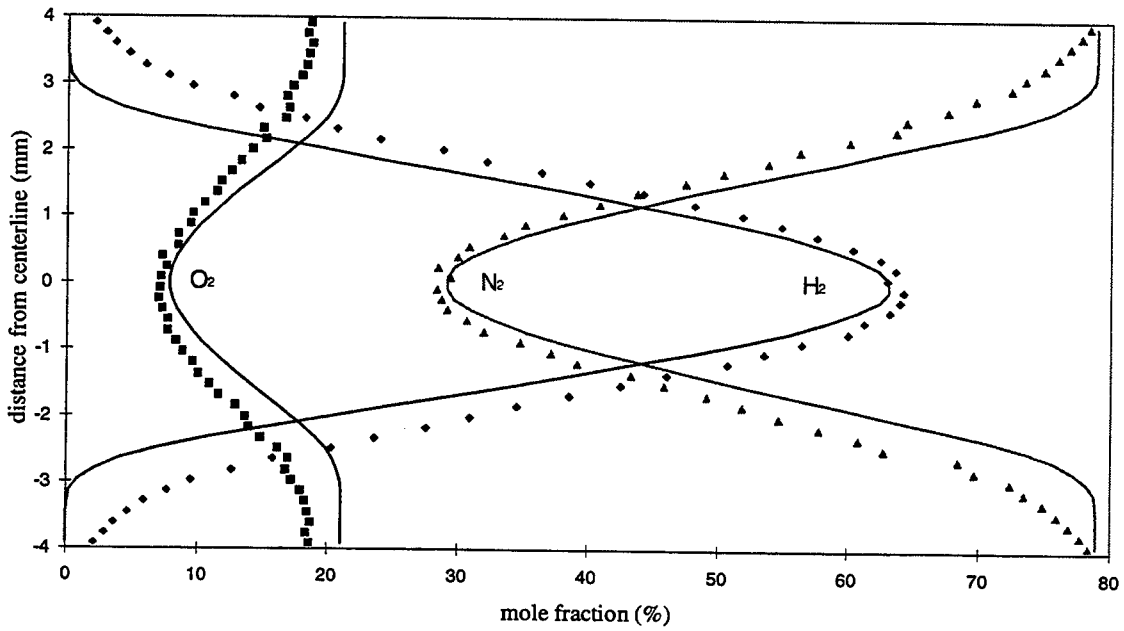

Fig. 2: Mole fractions of hydrogen, oxygen and nitrogen 50 mm behind the hydrogen injection (measurement and CFD calculation).

Fig. 1 shows 1-D Raman spectra 150 mm behind the hydrogen injection. The Raman intensities of the three major species were quantitatively evaluated. Temperature was determined from hydrogen rotational Raman lines. As an example the mole fractions from hydrogen, oxygen and nitrogen at 50 mm behind the hydrogen injection are shown in Fig. 2.
The measured mole fraction profiles are compared with numerical calculation. Details on the used numerical scheme are described elsewhere [6-7]. A comparison of measured and calculated mole fractions shows an excellent agreement (with 3%) on the centerline and some discrepancies in the wings. At all locations the experimental profiles tend to be broader than the calculated distributions. Further parameter studies are in progress to understand the remaining discrepancies.

References

[1] Bayley, D.J. and Hartfield, R.J.,*AIAA Paper 95-2414* (1995).
[2] Foust, M.J.; Pal, S. and Satoro, R.J, *AIAA Paper 96-2766* (1996).
[3] Haibel, M., *Gemischbildung und Struktur schneller Wasserstoff-Luft-Flammen im Nahbereich turbulenter Rezirkulationsgebiete*, Dissertation, Technische Universität München (1994).
[4] Eklund, D.R. and Stouffer, S.D.,*AIAA Paper 94-2819* (1994).
[5] Gauba, G.; Haj-Hariri, H. and McDaniel, J.C., *AIAA Paper 95-2562* (1995).
[6] Gerlinger, P. and Brüggemann, D.,*Int. J. Numer. Methods Fluids24*, 1019 - 1035 (1997).
[7] Gerlinger, P.; Stoll, P., and Brüggemann, D.,*A robust Implicit Multigrid Method for the Simulation of Turbulent Supersonic Mixing* submitted for publication to AIAA J.

High sensitivity detection of molecular oxygen using cavity-enhanced frequency modulation spectroscopy

L. Gianfrani[1], R. W. Fox, and L. Hollberg

National Institute of Standards and Technology
325 Broadway, Boulder, Colorado 80303-3328, USA
[1] Dipartimento di Scienze Ambientali della Seconda Università di Napoli
Via Arena, 22, I-81100, Caserta, Italy

In recent years, high finesse optical cavities have been used for high sensitivity spectroscopy by exploiting the very long absorption path lengths, 10 to 100 times greater than in traditional multipass cells. Cavity Ring Down Spectroscopy applications have been widely performed with both pulsed [1] and CW laser sources [2]. Direct absorption spectroscopy with an optical cavity has also been demonstrated by recording the peak transmitted power around an absorption line [3]. Another relevant application is represented by saturated absorption spectroscopy of overtone molecular transitions. In this case, high finesse and high build-up provide enough intracavity power for saturation of the absorbing gas [4]. More recently, the "NICE-OHMS" method, using frequency modulation techniques, has been used to detect extremely weak saturated signals in a high finesse cavity [5]. In this novel method, the laser beam is frequency modulated at exactly the cavity free-spectral-range (FSR) frequency. Using heterodyne detection of the transmitted power, the phase shift of the central carrier produced by optical dispersion gives rise to the signal. The NICE-OHMS method has reported detection sensitivities for absorption of 10^{-12} cm^{-1} [5]. In this work, we demonstrate how the cavity enhanced frequency modulation technique can be used to perform high sensitivity measurements of small absorption signals, corresponding to weak absorption lines in molecular oxygen.

The experimental setup is shown in figure 1. A single-mode diode laser emitting at a wavelength of 774 nm at room temperature was employed. It was antireflection coated and mounted in a Littman external cavity configuration. The laser wavelength could be tuned down to 762 nm and a sub-MHz narrowing of the laser emission was accomplished. The laser wavelength was measured by means of a 7-digit Michelson wave-meter. An asymmetric optical cavity was used, with a flat input coupler and 1-m radius of curvature output mirror. The cavity length was 26 cm and could be changed by means of a pzt on the output mirror. The cavity was mounted in a stainless steel vacuum chamber into which a sample gas could be introduced. In the present measurements, we typically changed the pressure between few mTorr up to 1 Torr (~0.1 - 130 Pa). The cavity linewidth was measured to be 140 kHz, which corresponds to a cavity finesse of about 4100. The laser frequency was locked to the cavity resonance with the Pound-Drever-Hall method, using sidebands at 8 MHz produced by an electro-optical modulator (EOM1). Phase sensitive detection of the cavity reflected beam provided an error signal that was used to control both the laser injection current and external cavity length. The maximum frequency scan with the laser locked to the cavity was 2 GHz, limited only by the piezo on the cavity. This scan was large enough to allow recordings of the whole absorption profile. Implementation of the NICE-OHMS method, with phase modulation at the cavity FSR frequency (570 MHz), was performed using another electro-optical modulator (EOM2). The transmitted beam was detected by a fast photodiode.

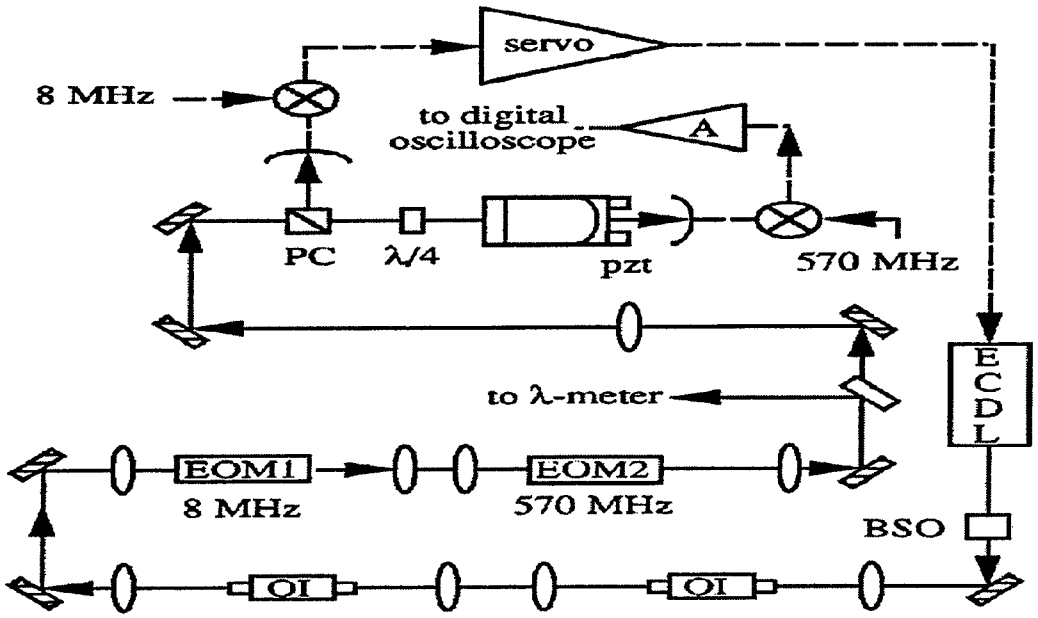

Fig. 1. Experimental setup. ECDL stands for extended cavity diode laser, BSO beam shaping optics, OI optical isolator, EOM electro-optical modulator, PC polarizing cube beam splitter, A current preamplifier.

Weak magnetic dipole transitions of the oxygen $b^1\Sigma^+_g$ (v'=0) ← $X^3\Sigma^-_g$ (v''=0) band around 762 nm were observed. Absorption profiles could be easily recorded by detecting the transmitted power during continuous scans of the cavity length. The transmitted power is given by:

$$P_t = P_{in} \frac{t_1^2 t_2^2}{(1-r_1 r_2)^2} \frac{1}{(1+\frac{\sigma}{\pi} pLF)^2}$$

Here P_{in} is the incident power, σ the absorption cross section, p the oxygen pressure, F the empty cavity finesse, L the cavity length, and t_1, t_2, r_1, and r_2 are the amplitude transmission and amplitude reflection coefficients of the cavity mirrors. When the molecular absorption is small compared to the empty cavity loss, the total fractional change in the transmitted power can be written as:

$$\frac{\delta P_t}{P_t} = \sigma p \frac{2}{\pi} FL.$$

This means that the absorption pathlength is enhanced by a factor F/π. Hence, an equivalent absorption length L_{eq} can be defined as equal to $2FL/\pi$.

We measured, for the $^PP(9)$ line at 763.843 nm, the absorption for several values of the oxygen pressure. Using the equation above and considering that the absorption cross section for the $^PP(9)$ line is $\sigma = 7 \cdot 10^{-6}$ cm^{-1} Torr^{-1} ($5 \cdot 10^{-8}$ cm^{-1} Pa^{-1}), we found a value for L_{eq} of 680 (30) m, in agreement with the value deduced from the measured empty cavity finesse.

An example of the heterodyne detection of an O_2 absorption signal is shown in figure 2. The oxygen pressure was 35 mTorr (4.7 Pa), which gives a single pass absorption of $6 \cdot 10^{-6}$. For the same experimental conditions (detection bandwidth $\Delta f \sim 10$ Hz), the noise spectrum for the output

signal was measured. The signal to noise ratio was about 500, so the minimum detectable single-pass absorption was about 10^{-8}. Detection of $^{16}O^{18}O$ was also performed, in a natural abundance oxygen sample. In the presence of few Torr of oxygen, we observed the $^{P}Q(11)$ line at 763.928 nm, with a signal to noise ratio of about 100.

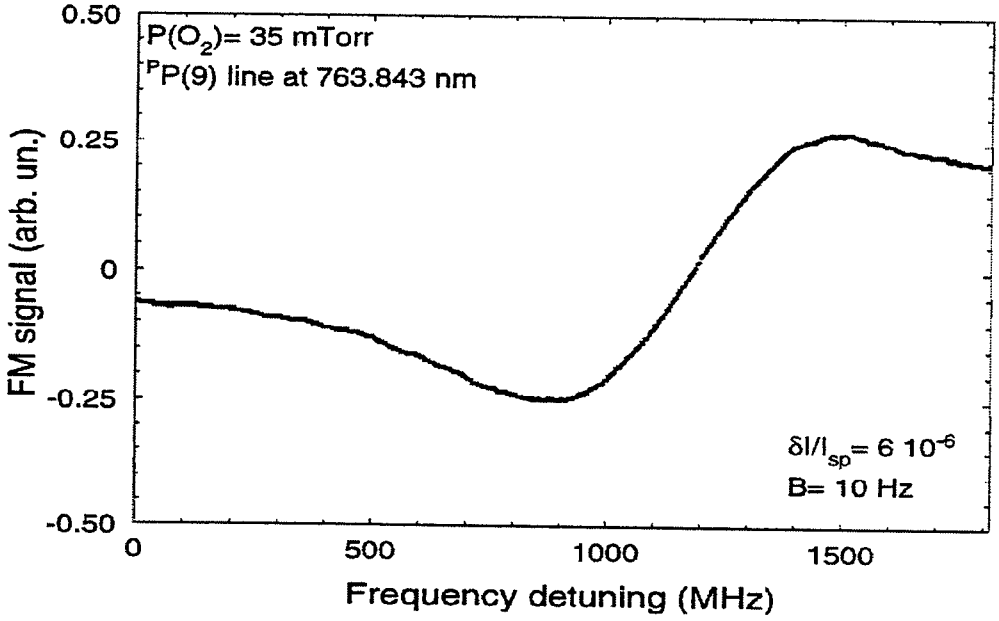

Fig. 2. Example of heterodyne detection of O_2 absorption at 763 nm in a high finesse cavity, corresponding to a single pass absorption of $6 \cdot 10^{-6}$.

The sensitivity of our spectrometer can be improved by at least 2 orders of magnitude, just by optimizing the NICE-OHMS detection method. The minimum detectable variation of the transmitted power was measured to be about $3 \cdot 10^{-5}$ which is about 200 times greater than the shot noise limit. The sensitivity is presently limited by the laser frequency noise that is converted by the cavity into amplitude noise. Hence, with a higher bandwidth on the laser current feedback loop, we should be able to increase the sensitivity and approach shot noise limited detection. In addition, we should be able to use a finesse greater than 10^4 to further decrease the minimum detectable oxygen pressure. This work is a contribution of the US government, and is not subject to copyright.

[1] J. B. Paul, J. J. Scherer, A. O'Keefe, and R. J. Saykally, Laser Focus World, March 1997, p. 71.
[2] D. Romanini, A. A. Kachanov, N. Sadeghi, and F. Stoeckel, Chem. Phys. Lett. 264, 316 (1997).
[3] K. Nakagawa, T. Katsuda, A. S. Shelkovnikov, M. de Labachelerie, and M. Ohtsu, Opt. Comm. 107, 369 (1994).
[4] M. de Labachelerie, K. Nakagawa, and M. Ohtsu, Opt. Lett. 19, 840 (1994).
[5] Jun Ye, Long-Sheng Ma, and J. L. Hall, Opt. Lett. 21, 1000 (1996).

DEGENERATE FOUR-WAVE MIXING SPECTROSCOPY: MULTISTATE RESONANCES AND MULTIMODE LASER EFFECTS

Thomas A. Reichardt, William C. Giancola, and Robert P. Lucht, Laser Diagnostics Laboratory, Dept. of Mech. and Ind. Engineering, University of Illinois, 1206 W. Green Street, Urbana, IL 61801 (Phone: 217-333-5056, Fax: 217-244-6534)

Introduction

Degenerate four-wave mixing (DFWM) spectroscopy is a promising diagnostic technique [1-3], but significant questions remain regarding its application for quantitative concentration measurements in combustion environments with typical laser systems. In this paper we present a summary of two numerical investigations with the goal of quantifying the measurement technique for common experimental situations. Specifically, we investigate both (1) probing a degenerate-level (multistate) resonance with a single-mode laser and (2) probing a two-state resonance with a multimode laser. DFWM signal levels are calculated by solving the time-dependent density matrix equations using direct numerical integration (DNI) [4, 5] for a two or more level system interacting with three laser beams.

Investigation of Multistate Resonances

The previous calculations we have performed with the direct numerical integration (DNI) code [4,5] have been limited to a two-energy-state system. However, for accurate calculation of DFWM saturation with cross-polarized lasers, the degenerate Zeeman states must be included in a multistate model of the DFWM resonance. Cross-polarized laser beams are commonly used for DFWM measurements to reduce the scattered light background [6] and/or to discriminate against the formation of thermal gratings which interfere with the DFWM signal [7]. We consider a multistate system irradiated by multiple laser beams, for which the time-dependent density matrix equations are given by [8]

$$\frac{\partial \rho_{kk}(y,t)}{\partial t} = -\frac{i}{\hbar}\sum_m \left(V_{km}\rho_{mk} - \rho_{km}V_{mk}\right) - \Gamma_k \rho_{kk} + \sum_m \Gamma_{mk}\rho_{mm} \tag{1}$$

$$\frac{\partial \rho_{kj}(y,t)}{\partial t} = -\rho_{kj}\left(i\omega_{kj} + \gamma_{kj}\right) - \frac{i}{\hbar}\sum_m \left(V_{km}\rho_{mj} - \rho_{km}V_{mj}\right) \tag{2}$$

where the diagonal matrix element ρ_{kk} is proportional to the population of level k and the off-diagonal matrix element ρ_{kj} describes the coherence between levels k and j. In Eqns. (1) and (2), $\hbar$ is Planck's constant (J-sec), Γ_{mk} is the population transfer rate from state m to state k ($\sec^{-1}$), Γ_k is the total population transfer rate from state k ($\sec^{-1}$), ω_{kj} is the angular resonance frequency between levels k and j ($\sec^{-1}$), and γ_{kj} is the dephasing rate of the coherence ($\sec^{-1}$). For DFWM, there are two pump and one probe input laser fields. In our analysis, we make the small angle approximation and assume that the propagation axis for all three beams is nearly aligned with the y-axis. The interaction term V_{km} is given in [9].

The manipulation of Eqns. (1) and (2) for solution by direct numerical integration is similar to those for a two-level system [4, 5]. To simulate realistic experimental parameters, we assume a 3.5-nsec Gaussian envelope for the single-mode electric-field intensity of the pump and probe pulses. Unless otherwise stated, we set the peak probe intensity equal to the peak pump intensity. For all of the results presented in this report, we assume a 3° angle between the forward pump and probe.

Recently, Williams et al. [10] used a perturbative solution to determine the signal intensity from different polarization configurations of the pump and probe beams. Results were given for arbitrary combinations of linear and circularly polarized light. The drawback of this perturbative method is that it assumes the laser beam intensities are much less than the saturation intensity of the probed transition. However, the optimal

signal-to-noise ratios are obtained at laser intensities close to the saturation intensity for a transition for which there currently is no analytical solution.

In an effort to predict the characteristics of DFWM with cross-polarized laser beams, we have calculated saturation curves for different polarization configurations and for various transitions. The polarization configuration is specified as '1234', where 1 refers to the polarization of the forward pump, 2 refers to the probe, 3 refers to the backward pump, and 4 refers to the signal. At low laser intensity, the results of our calculations are in excellent agreement with perturbation theory in terms of the relative intensities of the DFWM signal for the various cross polarization and parallel polarization configurations. The results of a DNI calculation of saturation curves for different polarization configurations for the P(1) and Q(1) transitions is shown in Fig. 1. As the laser intensity increases and the resonance starts to saturate, we find that the reflectivity ratio ZXXZ/ZZZZ varies. As expected, the two parallel-polarized cases (ZZZZ and XXXX) yield identical results, as do the cross-polarized cases ZXXZ and ZZXX. We have found that the reflectivity ratio is a function of both the laser intensity and the collision model used in the DNI code. We are currently studying these effects in detail.

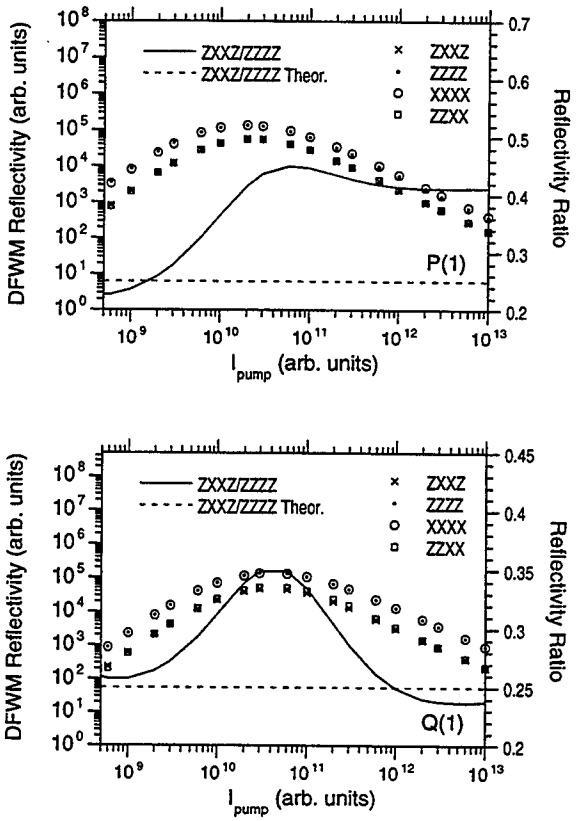

Fig. 1. DNI calculations of the saturation behavior of the DFWM reflectivity for the P(1) and Q(1) transitions for the ZXXZ, ZZZZ, XXXX, and ZZXX polarization configurations. The solid line is the ratio of reflectivities for the ZXXZ and ZZZZ configurations; the dashed line is the low-intensity limit as calculated by Williams et al. [10].

Incorporation of a Multimode Laser Simulation into the DNI Code

The assumption of single-mode laser radiation has been made in virtually every theoretical treatment of DFWM with the exception of papers by Cooper and Ewart and co-workers [e.g. 11, 12], who assume that the laser linewidth is much greater than the collisional and Doppler widths of the molecular resonance. However, most experiments where DFWM has been used as a combustion diagnostic have been performed using commercial pulsed dye lasers; the frequency spectrum of the output of these dye lasers will typically have a linewidth of 0.1 cm^{-1} and will contain several axial modes with slightly different frequencies. We are therefore investigating the effects of probing a two-level resonance with multi-axial-mode laser radiation.

For multi-axial-mode laser radiation, the amplitudes $A_n(t)$ are modeled as the sums of amplitudes from M modes of the laser,

$$A_n(t) = \sum_{m=1}^{m=M} A_{nm}(t)\exp(i\phi_{nm}) = G(t)\sum_{m=1}^{m=M} A_{0nm}\exp(i\phi_{nm}) \quad (3)$$

where G(t) is a Gaussian envelope function, A_{0nm} is the electric field amplitude for mode m and laser beam n at the peak of the pulse, and ϕ_{nm} is the phase of mode m for laser beam n. It is assumed that the amplitudes of the modes are Gaussian-distributed, and that the phases are random and do not change during the laser pulse.

Figure 2 displays some initial results obtained incorporating the multimode laser simulation into the DNI code. At low (non-saturating) laser pulse energies ($< 10^5$), the signal displays the expected cubic dependence on laser energy. The varying constructive and destructive interferences between the electric field components generated by the two laser modes cause significant scatter in the data, especially at low laser energies. However, this scatter decreases significantly at higher laser intensities. We will use this code to investigate the difference in the effective I_{sat} and also in the efficiency of DFWM signal generation (I_{signal} / I_{laser}) when using multimode laser radiation. The dependence of the DFWM signal on collisional rate, especially whether or not the DFWM signal is approximately independent of collisional transfer rates for $I_{pump} \approx I_{sat}$, will also be addressed.

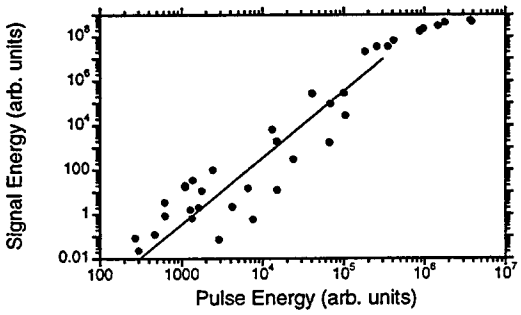

Fig. 2. Saturation curve obtained with a multimode laser. The two longitudinal modes are spaced ±0.02 cm^{-1} from the resonance, for which $\Delta\tilde{\omega}_C = 0.053$ cm^{-1} and $\Delta\tilde{\omega}_D = 0$ cm^{-1}. The solid circles show the shot-to-shot data obtained from the DNI code, while the line is added to illustrate the cubic dependence of the data on the laser pulse energy.

Summary

In this paper we describe the effects of different polarization configurations on DFWM signal generation. We have successfully incorporated the Zeeman state structure of DFWM resonances into our DNI calculations allowing us to investigate degenerate-level resonances. In the second study, we incorporated a multimode laser into our non-degenerate, two-level calculations. We are currently investigating saturation effects and lineshapes for multi-mode laser DFWM in detail.

Acknowledgements

This work is supported by the U.S. Department of Energy, Office of Basic Energy Sciences, Division of Chemical Sciences, under grant DE-FG02-94ER14469. The contract is managed by William H. Kirchhoff and Andrew E. DePristo (interim). T. A. Reichardt gratefully acknowledges the support of graduate fellowships from the Link Foundation and DuPont.

References

[1] A. C. Eckbreth, *Laser Diagnostics for Combustion Temperature and Species*, 2nd ed. Gordon and Breach, Amsterdam, The Netherlands, 1996.

[2] K. Kohse-Höinghaus, Prog. Energy Combust. Sci. **20**, 203-279 (1994).

[3] R. L. Farrow and D. J. Rakestraw, Science **257**, 1894-1900 (1992).

[4] R. P. Lucht, R. L. Farrow, and D. J. Rakestraw, J. Opt. Soc. Am. B **10**, 1508-1520 (1993).

[5] T. A. Reichardt and R. P. Lucht, J. Opt. Soc. Am. B **13**, 1107-1119 (1996).

[6] S. Williams, D. S. Green, S. Sethuraman, and R. N. Zare, J. Am. Chem. Soc. **114**, 9122-9130 (1992).

[7] P. M. Danehy, P. H. Paul, and R. L. Farrow, J. Opt. Soc. Am. B **12**, 1564-1576 (1995).

[8] R. W. Boyd, Nonlinear Optics, Academic, Boston, Mass., 1992.

[9] M. Sargent III, M. O. Scully, W. E. Lamb, Jr. Laser Physics. Addison Wesley, Reading, Mass, 1974.

[10] S. Williams, R. N. Zare, and L. A. Rahn, J. Chem. Phys. **101**, 1072-1092 (1994).

[11] J. Cooper, A. Charlton, D. R. Meacher, P. Ewart, and G. Alber, Phys. Rev. A **40**, 5705-5715.

[12] D. R. Meacher, A. Charlton, P. Ewart, J. Cooper, and G. Alber, Phys. Rev. A **42**, 3018-3026.

POLARIZATION SPECTROSCOPY: CALCULATION OF LINESHAPES AND SATURATION EFFECTS

Thomas A. Reichardt and Robert P. Lucht, Department of Mechanical and Industrial Engineering, MC-244, University of Illinois, Urbana, Illinois 60801 (RPL Email: r-lucht@uiuc.edu, Phone: 217-333-5056)

In recent years there have been several experimental demonstrations of the application of polarization spectroscopy (PS) as a combustion diagnostic technique.[1-3] However, there have been very few theoretical investigations of the technique since the work of Teets et al.[4] in 1977. Teets et al.[4] investigated the low-laser-power limit where saturation effects are small. In this paper we present the initial results of a theoretical investigation of polarization spectroscopy using the method of direct numerical integration (DNI) of the time-dependent density matrix equations to analyze the process. The application of this numerical method allows us to include saturation effects, Doppler effects, non-steady-state effects associated with the finite pulse length of the pump and probe lasers, and will enable us to investigate in great detail the effects of different kinds of collisions.

The physics of polarization spectroscopy is investigated in these initial studies for the case of a strong, circularly polarized pump beam that is counterpropagating with respect to a linearly polarized probe beam. The probe beam intensity is assumed to be much weaker than the pump beam intensity. The pump beam is circularly polarized and propagates in the -z direction,

$$\vec{E}_1(z,t) = E_{01}\exp(-i\omega t - ikz)\left(\frac{1}{\sqrt{2}}\hat{x} + i\frac{1}{\sqrt{2}}\hat{y}\right)$$

The probe beam, initially linearly polarized in the x-direction, is separated into right- and left-circularly polarized components,

$$\vec{E}_2(z,t) = E_{02}\exp(-i\omega t + ikz)\left(\frac{1}{\sqrt{2}}\hat{x} + i\frac{1}{\sqrt{2}}\hat{y}\right) \quad , \quad \vec{E}_3(z,t) = E_{03}\exp(-i\omega t + ikz)\left(\frac{1}{\sqrt{2}}\hat{x} - i\frac{1}{\sqrt{2}}\hat{y}\right)$$

The Zeeman structure of the upper and lower energy levels is included in a multi-state formulation of the density matrix equations. The density matrix elements for single-photon, electric-dipole transitions between a lower state b (J_b, M_b) in a lower level B and an upper state a (J_a, M_a) in an upper level A are discussed in detail by Condon and Shortley.[5] These density matrix elements are also discussed by Sargent, Scully, and Lamb,[6] who have put the results in a particularly convenient form for analysis of laser fields. The density matrix elements are given by

$$\vec{\mu}_{ab} = (\alpha\, J_a\, M_a\, |\vec{\mu}|\, \alpha'\, J_a+1\, M_a \pm 1) = \mp\frac{1}{2}(\alpha J_a \vdots \mu \vdots \alpha'\, J_a+1)\sqrt{(J_a \pm M_a+1)(J_a \pm M_a+2)}\,(\hat{x} \pm i\hat{y})$$

$$(\alpha\, J_a\, M_a\, |\vec{\mu}|\, \alpha'\, J_a+1\, M_a) = (\alpha\, J_a \vdots \mu \vdots \alpha'\, J_a+1)\sqrt{(J_a+1)^2 - M_a^2}\,\hat{z}$$

$$(\alpha\, J_a\, M_a\, |\vec{\mu}|\, \alpha'\, J_a\, M_a \pm 1) = \frac{1}{2}(\alpha\, J_a \vdots \mu \vdots \alpha'\, J_a)\sqrt{(J_a \mp M_a)(J_a \pm M_a+1)}\,(\hat{x} \pm i\hat{y})$$

$$(\alpha\, J_a\, M_a\, |\vec{\mu}|\, \alpha'\, J_a\, M_a) = (\alpha\, J_a \vdots \mu \vdots \alpha'\, J_a)\, M_a\, \hat{z}$$

$$(\alpha\, J_a\, M_a\, |\vec{\mu}|\, \alpha'\, J_a-1\, M_a \pm 1) = \pm\frac{1}{2}(\alpha\, J_a \vdots \mu \vdots \alpha'\, J_a-1)\sqrt{(J_a \mp M_a)(J_a \mp M_a-1)}\,(\hat{x} \pm i\hat{y})$$

$$(\alpha\, J_a\, M_a\, |\vec{\mu}|\, \alpha'\, J_a-1\, M_a) = (\alpha\, J_a \vdots \mu \vdots \alpha'\, J_a-1)\sqrt{J_a^2 - M_a^2}\,\hat{z}$$

where the reduced matrix element $(\alpha\, J \vdots \mu \vdots \alpha'\, J')$ has units of C-m and is given by

$$(\alpha\, J \vdots P \vdots \alpha'\, J') = \sqrt{3A(a,B)\varepsilon_0 \hbar \lambda_{ab}^3 / 8\pi^2 \Gamma(J,J')}$$

Here $A(a,B)$ is the spontaneous emission rate (sec^{-1}) between state a and level B, ε_0 is the dielectric permittivity ($C^2/J-m$), $\lambda_0 = \lambda_{ab} = \lambda_{AB}$ is the wavelength (m) of the transitions ab (assumed the same for all), and

$$\Gamma(J,J+1) = (J+1)(2J+3) \qquad \Gamma(J,J) = J(J+1) \qquad \Gamma(J,J-1) = J(2J-1)$$

The time-dependent density matrix equations and their solution are discussed in our previous publications on resonant wave-mixing processes.[7,8] In the case of polarization spectroscopy a multi-state formulation of the density matrix equations is required and has been developed. We assume pump field 1 is much stronger than the probe field, so that transitions between a lower state b and upper state a are driven by pump field 1 with a Rabi frequency of

$$\Omega_{ab}(t) = -\frac{\left(\vec{\mu}_{ab} \bullet \vec{E}_{01}\right)}{2\hbar} = -\frac{E_{01}}{2\hbar}\left(\vec{\mu}_{ab} \bullet \hat{e}_1\right) = -\frac{E_{01}}{2\sqrt{2}\,\hbar}\left[\vec{\mu}_{ab} \bullet \left(\hat{x} + i\hat{y}\right)\right]$$

The pump field will thus excite transitions for which $\Delta M = M_a - M_b = -1$. After passing through a length L of the medium that is irradiated by pump 1, the probe field amplitudes will be given by

$$\vec{E}_2(L,t) = E_{02}\exp(-i\omega t + ikz)\exp(-\alpha_2 L)\exp(-i\Delta k_2 L)\frac{1}{\sqrt{2}}(\hat{x} + i\hat{y}) = E_{L2}\exp(-i\omega t + ikz)\frac{1}{\sqrt{2}}(\hat{x} + i\hat{y})$$

$$\vec{E}_3(L,t) = E_{03}\exp(-i\omega t + ikz)\exp(-\alpha_3 L)\exp(-i\Delta k_3 L)\frac{1}{\sqrt{2}}(\hat{x} - i\hat{y}) = E_{L3}\exp(-i\omega t + ikz)\frac{1}{\sqrt{2}}(\hat{x} - i\hat{y})$$

The absorption and phase shift terms for beam 2 interacting with a homogeneous resonance are given by

$$\alpha_2 = \left(\frac{2}{3\varepsilon_0\hbar\lambda_0\Delta\omega_{hom}}\right)\left(\frac{1}{1+\left[2(\omega_2-\omega_0)/\Delta\omega_{hom}\right]^2}\right)\sum_a\sum_b\left[(n_b - n_a)\left|\vec{\mu}_{ab} \bullet \hat{e}_2\right|^2\right] \qquad \Delta k_2 = \alpha_2\frac{2(\omega_2-\omega_0)}{\Delta\omega_{hom}}$$

and similar expressions apply for beam 3. There will in general be differences in the absorption and phase shift terms for beams 2 and 3 because of the preferential pumping of $\Delta M = -1$ transitions by the pump beam. After passing through the medium the probe beam is passed through a polarizer aligned at an angle θ with respect to the y-axis, and the transmitted intensity, which is the polarization spectroscopy signal, is given by

$$I_t = c\varepsilon_0 E_t E_t^* = c\varepsilon_0\left|\left[(E_{L2r} + E_{L3r})\sin\theta + (-E_{L2i} + E_{L3i})\cos\theta\right] + i\left[(E_{L2r} - E_{L3r})\cos\theta + (E_{L2i} + E_{L3i})\sin\theta\right]\right|^2$$

The computer code was checked first of all by turning off the pump beam and setting the polarizer angle θ to 90^0. Fig. 1 shows that the absorption line has the expected Lorentzian profile. For Figs. 2-4, the pump beam is turned on and the polarizer angle is set to 0^0. Fig. 2 shows the that the low power PS lineshape for a homogeneously broadened resonance is a Lorentzian cubed, as opposed to the Lorentzian lineshape predicted by Teets et al.[4] Fig. 3 shows saturation curves for the PS signal for constant probe intensity for R(1), R(2), R(10), and R(20) transitions. For the R(20) transition, there are 84 states included in the calculation. Note that the signal saturates and then levels off for the low-J transitions, but peaks and then falls for the high-J transitions. We have also begun to investigate the effect of saturation on PS lineshapes. The Doppler effect is included by solving the density matrix equations for different velocity groups and then summing the resulting absorption and phase shift factors. An unsaturated, Doppler-broadened PS resonance lineshape is shown in Fig. 4 and compared to the homogeneous lineshape and to a Gaussian with the same FWHM as the Doppler width. The Doppler-broadened line is slightly broader than the homogeneous line, but the sub-Doppler nature of the PS lineshape is clearly evident by comparison with the 0.1 cm^{-1} FWHM Gaussian. We are currently investigating the potential of saturated PS for quantitative concentration measurements, and the influence of collisions and Doppler broadening on lineshapes and signal intensities. The effects of window birefringence in cell measurements can easily be incorporated into the computational analysis. The polarization configuration where the pump is linearly polarized at 450 with respect to the probe beam will also be analyzed.

ACKNOWLEDGMENTS

This work is supported by the U. S. Dept. of Energy, Office of Basic Energy Sciences, Division of Chemical Sciences, under Grant DE-FG02-94ER14469. The contract is managed by Dr. William H. Kirchhoff.

REFERENCES

1. K. Nyholm, R. Maier, C. G. Aminoff, and M. Kaivola, Appl. Opt. **32**, 919-924 (1993).
2. K. Nyholm, R. Fritzon, and M. Alden, Appl. Phys. B **59**, 37-43 (1994).
3. C. F. Kaminski, B. Lofstedt, R. Fritzon, and M. Aldén, Opt. Commun. **129**, 38-43 (1996).
4. R. E. Teets, F. V. Kowalski, W. T. Hill, N. Carlson, and T. W. Hänsch, "Laser Polarization Spectroscopy," in *Advances in Laser Spectroscopy I*, A. H. Zewail, Ed., Proc. Soc. Photo-Opt. Instr. Eng. **113**, 80-87 (1977).
5. E. U. Condon and G. H. Shortley, *The Theory of Atomic Spectra*, Cambridge Univ. Press, New York (1951).
6. M. Sargent III, M. O. Scully, and W. E. Lamb, Jr., *Laser Physics*, Addison-Wesley, Reading, MA (1977).
7. R. P. Lucht, R. Trebino, and L. A. Rahn, Phys. Rev. A **45**, 8209-8227 (1992).
8. T. A. Reichardt and R. P. Lucht, J. Opt. Soc. Am. B **13**, 1107-1119 (1996).

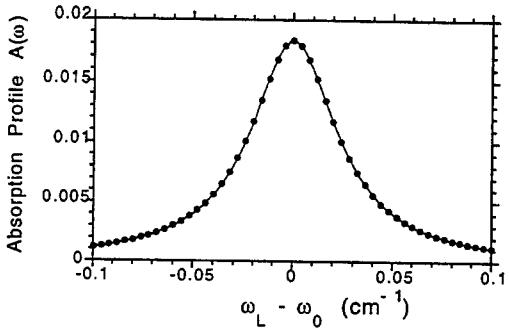

Fig. 1. Calculated absorption profile for a resonance line with a homogeneous FWHM of 0.053 cm^{-1}. The solid line through the calculated points is a Lorentzian fit with a FWHM of 0.053 cm^{-1}. The polarizer transmission angle was set at 90^0 (aligned with the x-axis) and the pump beam intensity was set to zero for these calculations.

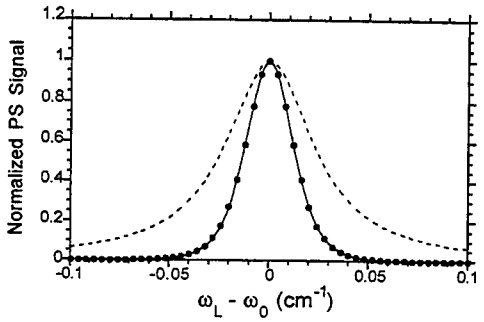

Fig. 2. Calculated polarization spectroscopy lineshape at low pump power. The resonance line has a homogeneous width of 0.053 cm^{-1}. The dashed line is a Lorentzian with a FWHM of 0.053 cm^{-1}, and the solid line through the calculated points is the Lorentzian cubed.

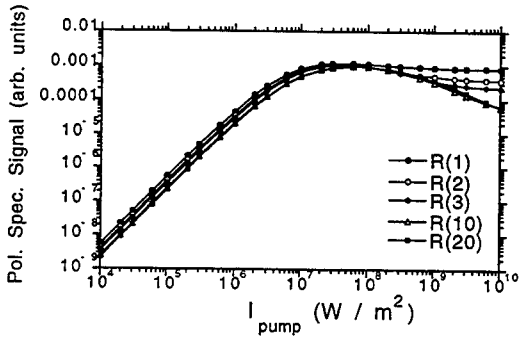

Fig. 3. Calculated saturation curves for five different R-branch transitions. The homogenous FWHM of each transition is 0.053 cm^{-1} and the Einstein spontaneous emission coefficient A(a,B) for each transition is $1.0x10^9$ sec^{-1}.

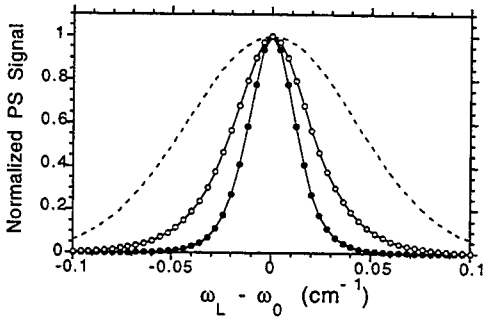

Fig. 4. Calculated PS lineshapes at low pump power. The resonance line has a homogeneous FWHM of 0.053 cm^{-1}. The solid circles are the PS signal calculations for the homogenoeusly broadened line. The open circles are the PS calculations for a line with the same homogeneous width and a Doppler width of 0.1 cm^{-1}. The dashed line is a Gaussian with a FWHM of 0.1 cm^{-1}.

Laser Applications to Chemical and Environmental Analysis

Advances in Diode Laser Sources

Tuesday, March 10, 1998

Alan C. Stanton, Southwest Sciences Inc.
Presider

LTuA
8:00am–10:00am
Coral Room

Single-Frequency Semiconductor Diode Lasers for Gas Sensing

Ramon U. Martinelli

Sarnoff Corporation, CN5300, Princeton, NJ 08543-5300

Building upon the substantial laser technology of telecomminications, Sarnoff has developed single-frequency, distributed-feedback (DFB) semiconductor diode lasers with emission wavelengths of 760 to 2000 nm. These devices are ideal sources for trace-gas monitoring systems employing laser absorption spectroscopy. The devices emitting at 760 to 1000 nm are made from AlGaAs/GaAs compounds, and those emitting from about 1300 to 2000 nm are based on the InGaAsP/InP materials system.

Figure 1 shows a highly schematic diagram of an AlGaAs/GaAs DFB diode laser chip. Other DFB lasers are similar. The various layers are grown epitaxially on the GaAs substrate using organometallic vapor-phase epitaxy. The active region comprises two quantum wells (QWs). The QW thickness (2.5 to 20 nm) determines the gain spectrum of the device. The Bragg grating, incorporated just above the active layer in the clad layer, determines the lasing wavelength.

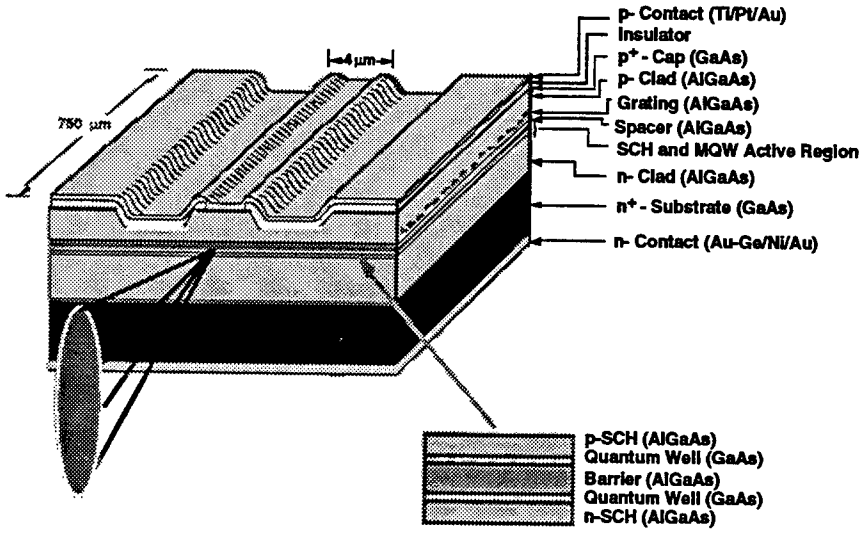

Figure 1. Schematic diagram of a DFB AlGaAs/GaAs diode laser chip

To improve overall efficiency and to promote single-spatial-mode operation, 1.5-µm-thick cladding layers of AlGaAs surround the active region. These layers confine injected carriers to the active region and also form a

dielectric waveguide with the active region that confines the zero-order transverse optical mode to active region.

A ridge is etched into the chip, and contact is made to it. The ridge and its adjacent channels form a waveguide in the lateral direction that supports only the zero-order lateral spatial optical mode.

The chip is typically 300 μm wide, from 500 to 1000 μm long and about 150 μm high. It is usually mounted p-side-up (junction-side-up) to increase the thermal resistance, which, in turn, increases the wavelength current-tuning rate.

Figure 2 shows an output-power characteristic for a 761-nm laser.

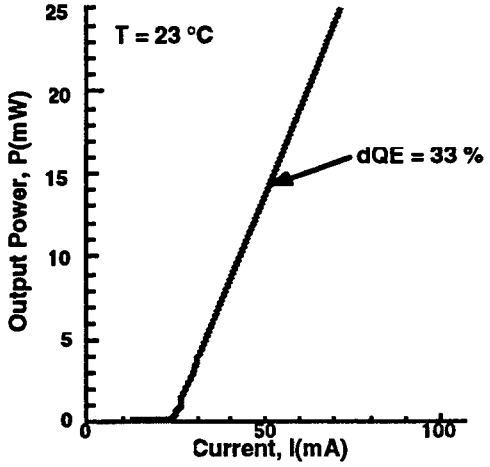

Figure 2. Output-power characteristic of a 761-nm DFB laser.

Above a threshold current of 25 mA the optical power increases linearly with a slope of 0.33 photons per electron. Output powers of tens of mW are typical, and the maximum single-frequency power we have seen is 175 mW for a 1550-nm DFB.

Figure 3 shows the frequency-tuning characteristics of a 761-nm DFB laser.

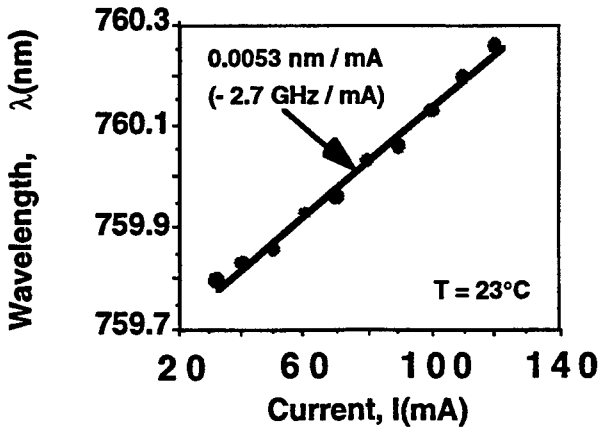

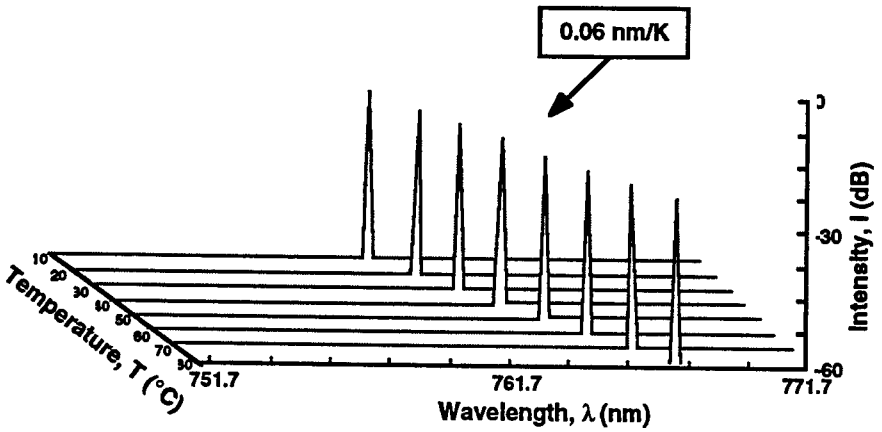

Figure 3. Current- and temperature-tuning characteristics of a 761-nm DFB diode laser.

The current-tuning rate at 23 °C is - 2.7 GHz/mA over 0.4 nm (0.7 cm^{-1}). The temperature-tuning rate is 0.06 nm/K (-31 GHz/K) from 10 to 80 °C. This is a tuning range of 4.2 nm. The output is single frequency with a side-mode-suppression ratio better than - 30 dB.

The linewidth shown in Fig. 3 is instrumentally limited. Figure 4 shows the measured linewidth as a function of output power. It decreases inversely as the output power and spans the interval of 45 to 12 MHz.

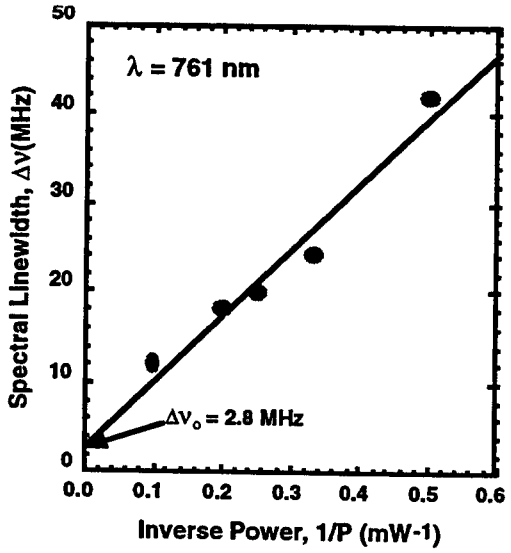

Figure 4. Linewidth of a 761-nm DFB laser.

All of our DFB lasers have linewidths in this range, some as low as 180 kHz. These values are far less than typical Doppler-broadened molecular absorption linewidths of several hundred MHz.

Single-frequency lasers at the other wavelengths have similar characteristics, making them all ideal sources for trace-gas-sensing systems.

Mid-Infrared Interband Cascade Lasers with External and Internal Quantum Efficiencies > 200%

B. H. Yang, D. Zhang, Rui Q. Yang, C.-H. Lin, and S. S. Pei

Space Vacuum Epitaxy Center, University of Houston, Houston, TX 77204-5507

Tel: (713) 743-4433, Fax: (713) 747-7724

Recently, we have proposed [1-3] and demonstrated [4] a new type of mid-IR quantum cascade (QC) lasers based on interband transitions in type-II quantum wells. This interband cascade (IC) laser takes advantage of the broken-gap band alignment in the InAs/Ga(In)Sb heterostructure to recycle electrons from the valence band back to the conduction band, thus enabling sequential photon emission from active regions stacked in series. However, by sticking to the interband transitions, it circumvented the fast phonon scattering which limits the performance of devices based on intersubband transitions such as the QC lasers based on InGaAs/InAlAs quantum wells (QWs). In addition to realizing stimulated emission at wavelengths around 3 and 4 μm,[4-6] room temperature electroluminescence has also been observed at wavelengths up to 15 μm.[7] In comparison, the QC lasers based on intersubband transitions have been successfully demonstrated to operate at wavelengths from 4.3 to 11 μm.

High power and high efficiency operation of the IC laser has also been achieved. A peak optical output power of ~ 0.5 W/facet with a slope efficiency of 211 mW/A per facet at ~3.9 μm was obtained with 1 μs current pulses at 80 K.[5] The threshold current density at 80K was 290 A/cm^2 which is substantially lower than those reported for the QC lasers. The characteristic temperature was 80 K at temperatures up to 165 K. The slope efficiency was 211 mW/A per facet, corresponding to a differential external quantum efficiency of 130%, or 1.3 emitted photons per injected electron. Comparable external quantum efficiency, with a peak output power of 430 mW/facet and a slope efficiency of 274 mW/A per facet were also achieved with a "W" configuration 2.9 μm cascade laser when pumped with 100 ns current pulses at 100K.[6] A maximum operating temperature of 225 K was achieved with a characteristic temperature of 53 K. At 180 K, the maximum output power was 252 mW/facet with a slope efficiency of 188 mW/A per facet. In this presentation, we will report a 4 μm IC laser with both external and internal quantum efficiencies > 200%.

The active region of the IC laser consists of 23 periods of coupled InAs/GaInSb/AlSb QWs which are connected by digitally graded n-type InAs/AlSb injection regions. Both gain-guided and ridge waveguide lasers have been fabricated and tested. The samples with uncoated facets were electrically-pumped with a pulsed current source. The lasing spectra at 80 K under two injection levels are shown in Fig. 1. There is a single mode peaking at 3.97 μm when it was pumped at just above the threshold. At higher injection current, the multi-longitudinal modes appeared which are separated by ~ 25Å as expected from a 0.9 mm Fabry-Perot cavity.

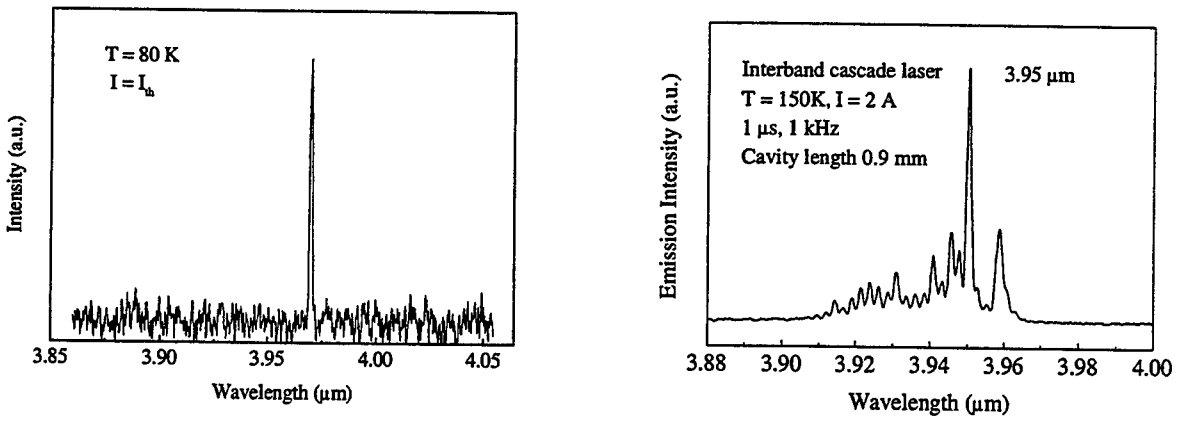

(a) (b)

FIGURE 1 (a) Lasing spectrum with the device biased at just above threshold and (b) at $1.7I_{th}$.

Figure 2 (a) shows the peak output power per facet versus injection current measured with 1 μs long pulses at 1 kHz repetition rate. A slope efficiency of 334 mW/A is achieved at 80 K, corresponding to an external quantum efficiency of 214 % assuming identical emissions from both facets. To our knowledge, this is the highest external quantum efficiency ever reported at this wavelength. The external quantum efficiency was still higher than 100 % at temperatures up to 140 K. Quasi-cw operation was also achieved with pulse lengths of 5-10 μs at 10% duty cycle as illustrated in Fig. 2 (b). At 80 K, peak output powers higher than 160 mW per facet was obtained, corresponding to an average output power >16 mW. The internal loss and internal quantum efficiency were also obtained from the cavity length dependence of the external quantum efficiency as shown in Fig. 3. From the intersection and the slope, the internal quantum efficiencies and the cavity loss were determined to be 220 % and 14 cm^{-1}, respectively. Unfortunately, both parameters degraded rapidly at higher temperature.

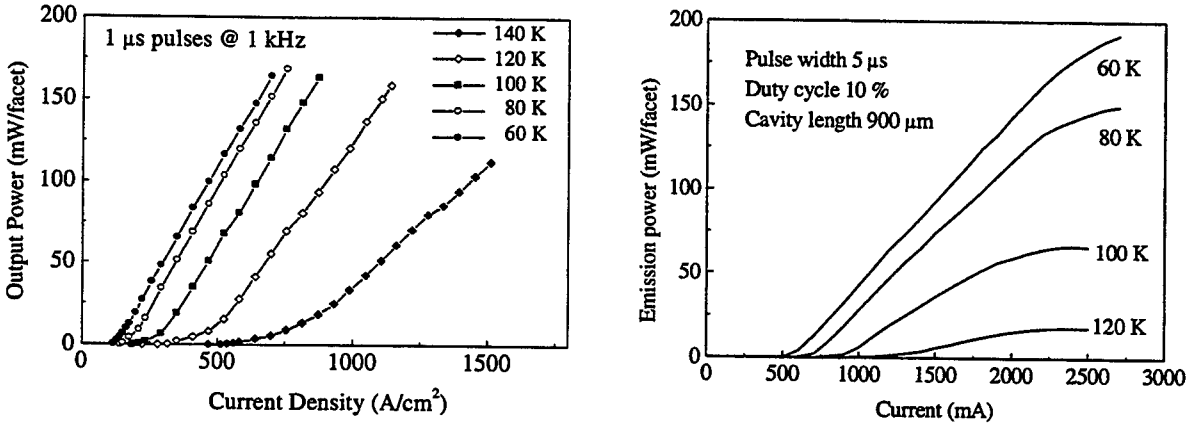

(a) (b)

FIGURE 2 (a) L-I curves of a 430×200 μm^2 ridge waveguide IC laser at various heat sink temperatures with 1 μs pulses at 0.1% duty cycle and (b) of a 900×200 μm^2 device with 5 μs pulses at 10% duty cycle.

In comparison to the interband QW laser based on type-I narrow bandgap semiconductors where the high temperature operation is limited by the Auger recombination, it was predicted theoretically and demonstrated experimentally that the Auger recombination can be suppressed in type-II superlattices.[8] However, detailed analysis of optically-pumped type-II QW lasers showed that the internal loss also play an important role in limiting the type-II QW laser performance at high temperatures.[9-10] Our measured low temperature internal loss of the IC laser is consistent with those of the type-II QW lasers with similar active region structures. We speculate that the inter-valence band absorption may have contributed to the high internal loss at high temperatures. However, it is also clear from the cross sectional scanning tunneling microscopy studies that the quality of the InAs/GaInSb/AlSb heterostructure is not optimum.[11] We believe that significantly better device performance can be achieved with an optimized device design and improved materials in the near future.

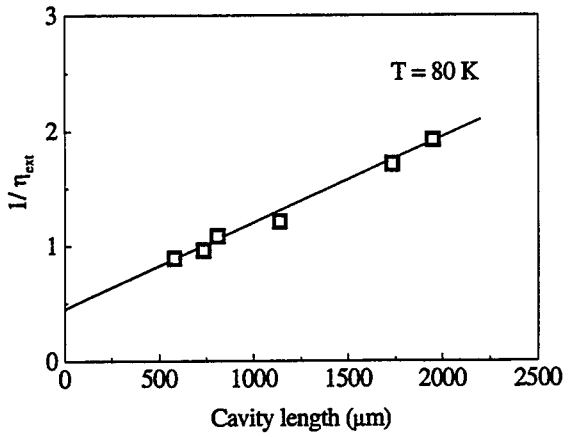

FIGURE 3. Cavity length dependence of external efficiency η_{ext} of an IC laser measured with 5 μs pulses at 10% duty cycle.

References

[1] R.Q. Yang, Superlattices and Microstructures, Vol. **17**, 77 (1995).

[2] R. Meyer, I. Vurgaftman, R. Q. Yang, and L. R. Ram-Mohan, Electron. Lett., **32**, 45 (1996).

[3] R.Q. Yang and S.S. Pei, J. Appl. Phys. **79**, 8197 (1996).

[4] C.-H. Lin, R.Q. Yang, D. Zhang, S.J. Murry, S.S. Pei, A.A.Allerman, and S.R. Kurtz, Electron Lett. **33**, 598 (1997).

[5] R.Q. Yang, B.H. Yang, D. Zhang, C.-H. Lin, S. Murry, H. Wu, and S.S. Pei, to be published in Appl. Phys. Lett. **71** (1997).

[6] C. L. Felix, W. W. Bewley, I. Vurgaftman, J. R. Meyer, D. Zhang, C.-H. Lin, R. Q. Yang, and S. S. Pei, to be published in Photonics Technol. Lett.

[7] D. Zhang, E. Dupont, R. Q. Yang, H. C. Liu, C.-H. Lin, M. Buchanan, and S. S. Pei, Optics Express, **1**, pp. 97-101 (1997).

[8] E. R. Youngdale, et al., Appl. Phys. Lett., **64**, pp. 3160-3162 (1994).

[9] H. Q. Le, G. W. Turner, C.-H. Lin, S. Murry, R. Q. Yang, and S. S. Pei, (to be published).

[10] W. W. Bewley, I. Vurgaftman, C. L. Felix, J. R. Meyer. C.-H. Lin, D. Zhang, S. J. Murry, and S. S. Pei, submitted to J. Quantum Electronics.

[11] J. Harper, M. Weimer, D.X. Zhang, C.-H. Lin, and S.S. Pei, submitted to J. Vac. Sci. Technol..

Mid-IR Vertical-Cavity Surface-Emitting Lasers for Chemical Sensing

W. W. Bewley, C. L. Felix, I. Vurgaftman, E. H. Aifer, J. R. Meyer, and L. Goldberg
Code 5600, Naval Research Laboratory, Washington, DC 20375
Phone: (202)-767-3276, FAX: (202)-404-8613

D. H. Chow and E. Selvig
Hughes Research Laboratory, MS RL63, Malibu, CA 90265
Phone: (310)-317-5330, FAX: (310)-317-5483

Vertical-cavity surface-emitting lasers (VCSELs) are in many ways ideal for chemical sensing. A spectrally-narrow single-mode output beam with relatively low divergence may be obtained by confining the lateral dimensions to the order of a few wavelengths, whereas edge-emitting semiconductor lasers must either undergo extensive processing or employ an external cavity. However, until now the only published report of a short-cavity VCSEL emitting at a wavelength beyond 1.7 μm was a HgCdTe device which operated only to $T = 30$ K and required a threshold pump intensity of 45 kW/cm^2 at 10 K.[1]

Here we discuss the first III-V mid-IR VCSEL. The optically-pumped device emitting at $\lambda \approx 2.9$ μm consists of a 12-1/2 period GaSb/AlAsSb Bragg bottom mirror, an InAs/GaSb/InAs/AlSb type-II "W" active region,[2] and a dielectric top mirror. Figure 1 illustrates the lasing spectrum. The variation with T yields $d\lambda/dT = 0.07$ nm/K, which is a factor of ≈ 20 smaller than for edge emitters since λ is governed by the vertical cavity. The plot in Fig. 2 of peak output power vs pump intensity and temperature for pulsed operation indicates that over 2 W can be generated nearly to ambient temperature (260 K). Pulsed lasing is observed up to 280 K, and the power conversion efficiency of $> 1\%$ at 220 K is much higher than the record for edge-emitters at the same wavelength and temperature.

Figure 3 shows L-L curves for cw operation. For a 10-μm spot, the threshold pump power is only 10 mW at 120 K and 4 mW at 78 K (not shown). Figure 4 plots cw threshold intensity vs T. At $T = 10$ K, I_{th} is two orders of magnitude smaller than the HgCdTe VCSEL result cited above. Note also that the output power exceeds 1 mW for this small spot diameter, which theory predicts will yield a single-transverse-mode output once patterning is employed to achieve index-guiding. The inset of Fig. 3 shows that larger spots produce much higher cw powers (40 mW at $D = 63$ μm). The maximum cw operating temperature of 160 K already approaches the best edge-emitter result to date for this wavelength range, and cw power conversion efficiencies are 5% for $T \leq 80$ K and $> 2\%$ at 130 K.

Our simulations predict that optimized mid-IR VCSELs with W active regions will operate single-mode with mW cw output powers at TE-cooler temperatures ($\geq$ 200 K), which would be especially attractive for chemical detection applications. A diode-pumped instrument with modest pump power would be practical and portable, and high-temperature electrically-pumped type-II mid-IR VCSELs are also projected.[2]

1. E. Hadji, J. Bleuse, N. Magnea, and J. L. Pautrat, Appl. Phys. Lett. 68, 2480 (1996).
2. I. Vurgaftman, J. R. Meyer, and L. R. Ram-Mohan, IEEE J. Quant. Electron. (in press).

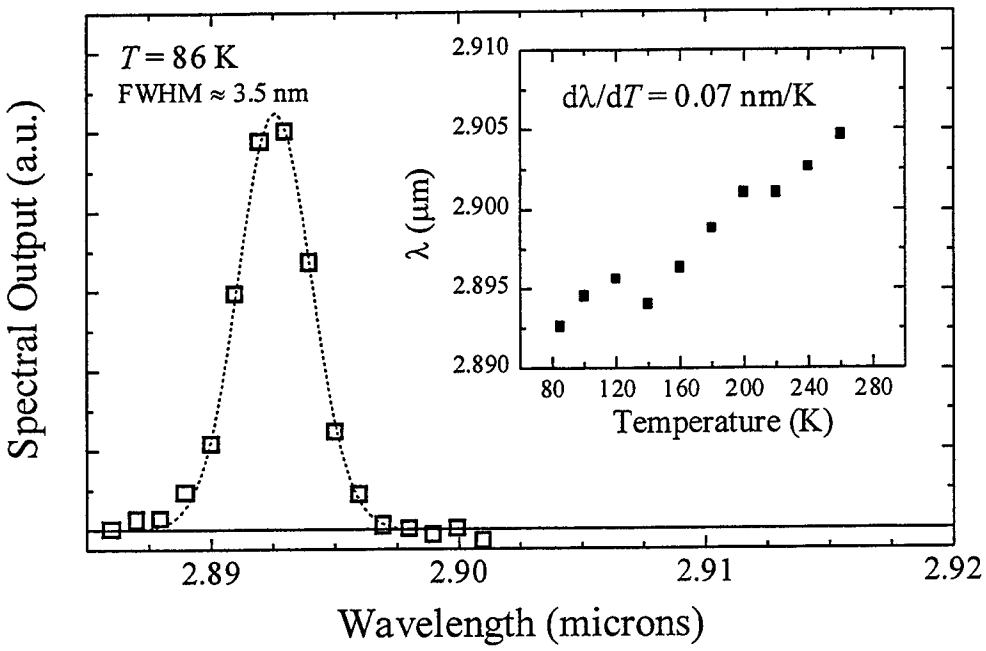

Figure 1. Spectral output (pulsed) vs. wavelength at $T = 86$ K for a 600-μm-diameter spot (multi-mode), and peak wavelength vs. temperature (inset). The 3.5 nm width at 86 K, which is typical of the spectra for all temperatures and spot sizes, is much narrower than typical milti-mode edge-emitter widths in the 15-30 nm range.

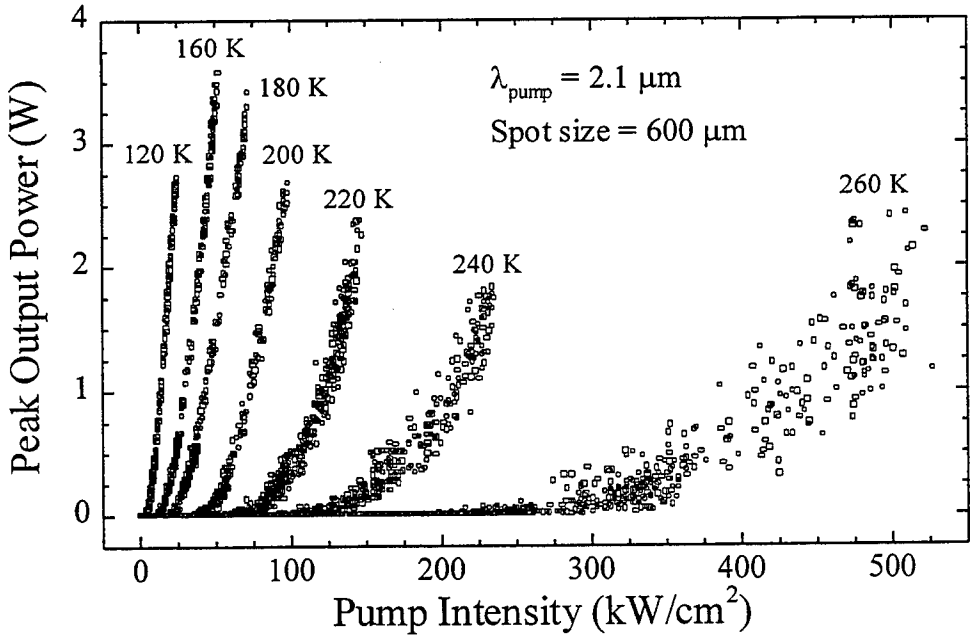

Figure 2. Peak output power (pulsed) vs. pump intensity at several temperatures. The maximum lasing temperature was 280 K.

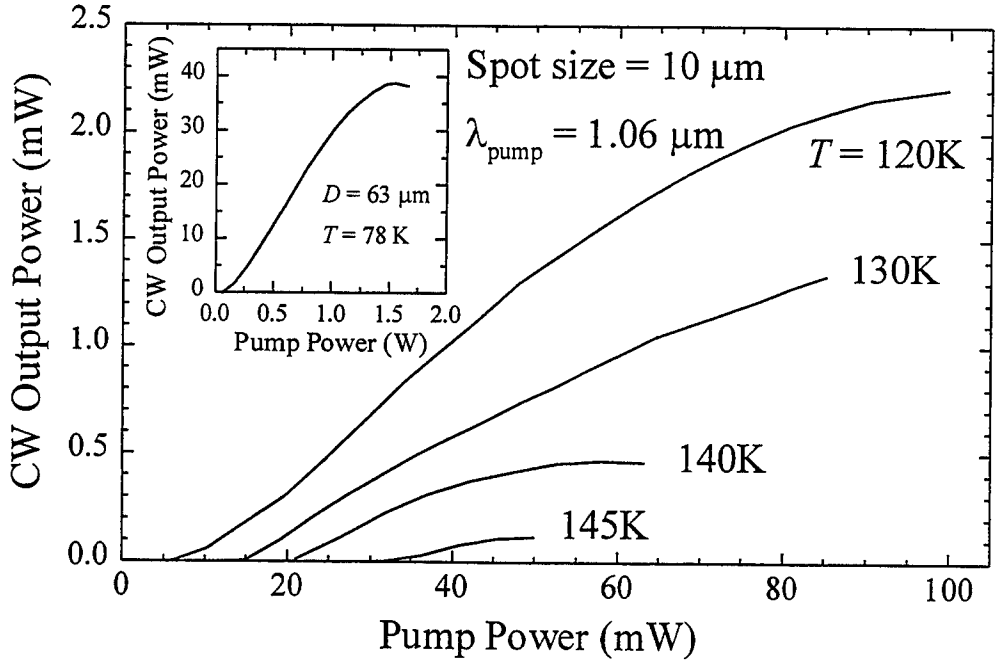

Figure 3. Output power (cw) vs. pump intensity at several temperatures for a spot size of 10 μm. The inset shows data at T = 78 K for a larger spot of 63 μm, with correspondingly higher maximum output power.

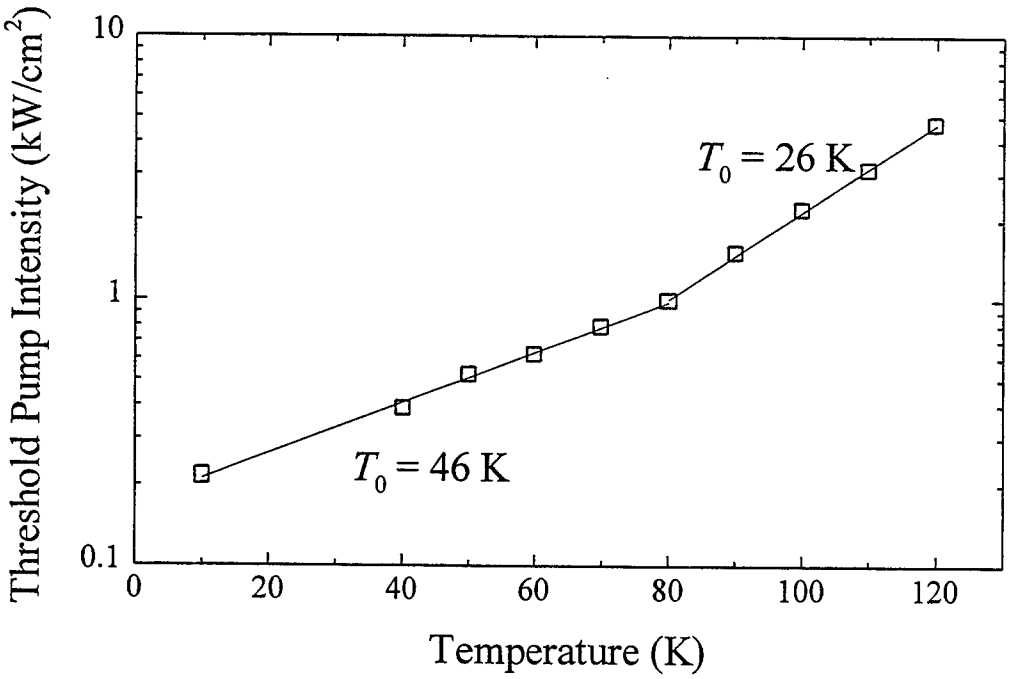

Figure 4. Threshold pump intensity (cw) vs. temperature.

Mid-Infrared Laser Source for Gas Sensing Based on Frequency-Converted Diode Lasers

Douglas J. Bamford, Konstantin Petrov, Andrew T. Ryan, Thomas L. Patterson, Lee Huang, David Hui, and Simon J. Field

Gemfire Corporation, 2440 Embarcadero Way, Palo Alto, CA 94303
Phone: (650) 493-6100
Fax: (650) 493-6493
e-mail: DJBAMFORD@AOL.COM

Compact, room-temperature mid-infrared laser sources have a variety of applications in the quantitative detection of gases. For example, many gases of importance for atmospheric science can be detected quantitatively using strong absorption lines in this spectral region. We are developing a room temperature mid-IR laser source based on the frequency mixing of two diode lasers in periodically poled lithium niobate (PPLN). This laser source has been used to measure strong absorption lines of water vapor (at 2.7 μm), methane (at 3.4 μm) and carbon dioxide (at 4.3 μm).

A schematic diagram of the laser source in its present form is shown in Figure 1. Tunable radiation between 715 nm and 840 nm is provided by a Ti:Sapphire laser pumped by an argon-ion Laser. Tunable radiation between 995 nm and 1040 nm is provided by a grating-stabilized diode laser (SDL-8630). The Ti:Sapphire beam is passed though a chopper, combined with the beam from the SDL laser on a dichroic mirror, and focussed into the PPLN crystal. (The PPLN sample is prepared using an electric field poling process patented by Deacon Research [1].) Radiation emerging from the sample is collimated with a CaF_2 lens, passed through an interference filter with high transmission in the mid-infrared, and focussed with a second CaF_2 lens onto a cryogenically cooled indium antimonide detector. The detector output is preamplified and sent to a lock-in amplifier configured to detect signal at the chopper frequency. The wavelength of the Ti:Sapphire laser is changed by changing the tilt angle of an intracavity etalon.

A typical water vapor spectrum produced by this laser source is shown in Figure 2. The relative power in the mid-IR beam is shown as a function of wavelength. Reasonable signal to noise ratios are obtained with output powers of less than 1 μW. The prominent dips in the detected power are assigned to absorption lines of atmospheric water vapor. Also shown is a theoretical calculation, using the HITRAN database [2]. Good agreement between observed and calculated relative intensities is observed. (Because we did not measure the humidity in the laboratory independently, the calculated spectrum is plotted on a relative scale.)

Future work will be aimed at making the laser source more compact. The Ti:Sapphire laser will be replaced with a diode laser. A tapered waveguide structure following the general design strategy of Arbore and co-workers [3] will be used to increase the device conversion efficiency. With a more efficient PPLN chip, greater output powers can be can be achieved with the same input lasers. Larger output powers will increase the sensitivity of the spectrometer and allow the use of detectors which do not need cryogenic cooling, leading to a truly portable device.

References

1. S.J. Field and D.A.G. Deacon, *Method for Making Devices Having a Pattern Poled Structure and Patterned Poled Structure Devices*. 1996, U.S. Patent #5,519,802.
2. L.S. Rothman, R. Gamache, R. Tipping, *et al.*, "The HITRAN Molecular Database: Editions of 1991 and 1992", *Journal of Quantitative Spectroscopy and Radiative Transfer*, Vol. 48, p. 469-507, 1992.
3. M.H. Chou, M.A. Arbore, and M.M. Fejer, "Adiabatically Tapered Periodic Segmentation of Channel Waveguides for Mode-Size Transformation and Fundamental Mode Excitation", *Optics Letters*, Vol. 21, No. 11, p. 794-796, 1996.

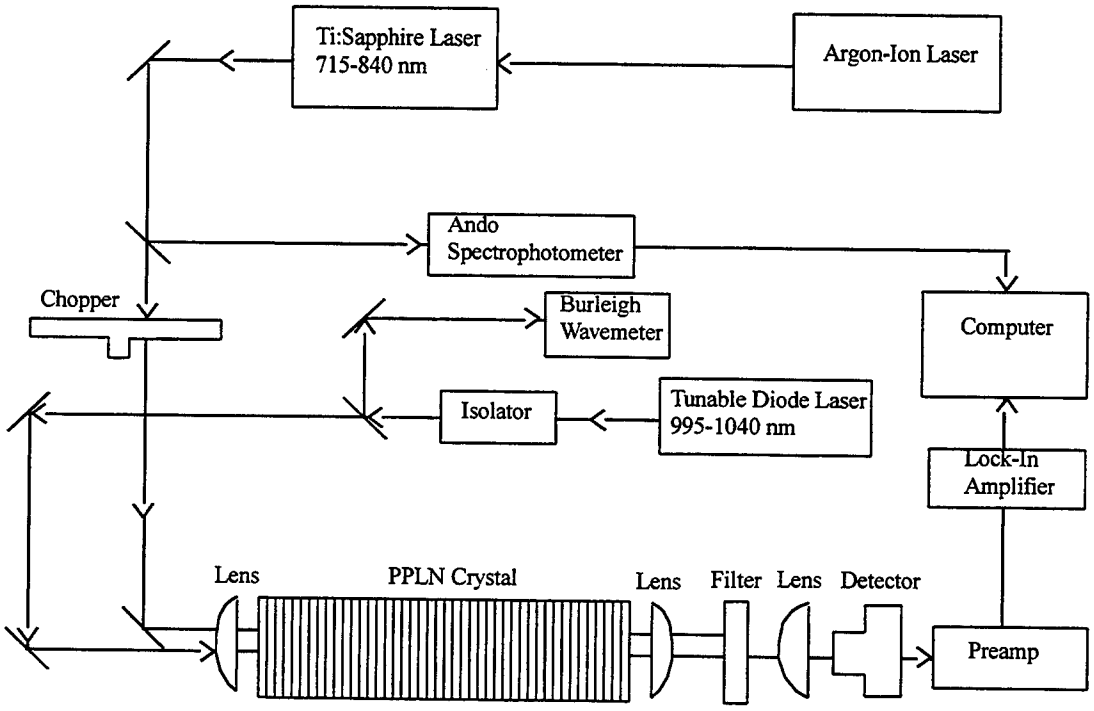

Figure 1. Schematic diagram of the apparatus used for difference frequency generation in PPLN.

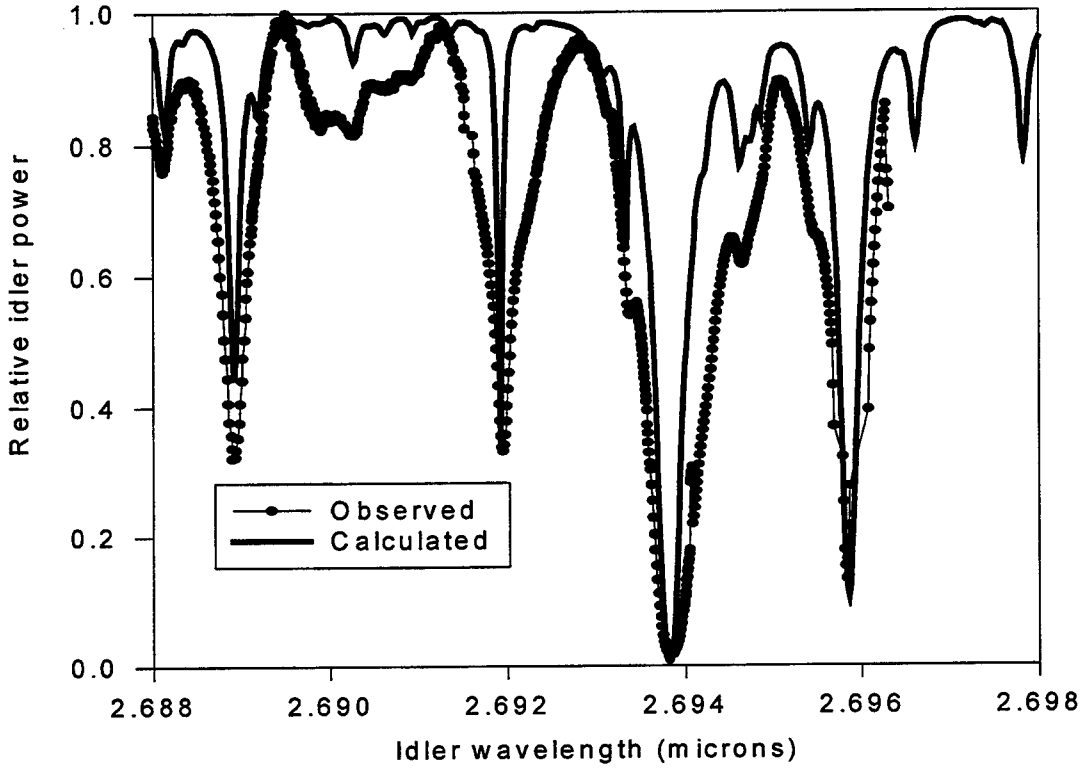

Figure 2. Observed and calculated spectra for atmospheric water vapor.

Trace Gas Monitoring with Antimonide Diode Lasers

Daniel B. Oh and Alan C. Stanton

Southwest Sciences, Inc.,
1570 Pacheco St., Suite E-11
Santa Fe, NM 87505

Tel: (505) 984-1322; Fax: (505) 988-9230
e-mail: sws@rt66.com

Jean-Christophe Nicolas

CEM2, Université de Montpellier II
34095 Montpellier, France

Semiconductor diode lasers, including lead salt lasers operating at wavelengths beyond 3 μm and InGaAlP, GaAlAs, or InGaAsP lasers operating at wavelengths less than 2 μm, have been used extensively for measurement of trace gases by optical absorption.[1] The inherently narrow linewidths of these light sources, combined with high sensitivity detection techniques such as wavelength modulation spectroscopy[2] or frequency modulation spectroscopy,[3] provides a capability for the highly selective and sensitive measurement of a wide range of species important in atmospheric and combustion research, environmental monitoring, and process monitoring. The lead salt lasers, accessing vibrational fundamental bands, generally permit the highest detection sensitivity. However, development of commercial diode laser-based instrumentation for environmental or industrial application has focused on the use of the near-infrared wavelength devices due to their characteristics of room temperature operation, compatibility with silica optical fibers, and availability of single mode operating devices.

Several research groups have been pursuing the development of semiconductor lasers with operating wavelengths in the 2 to 4 μm range based on III-V antimonide materials systems.[4,5] Devices that exhibit room temperature cw operation have been demonstrated at the short wavelength end of this range, and recent results suggest that at least thermoelectrically-cooled operation should be possible at wavelength beyond 3 μm.[4,5] For detection of several trace species of combustion and environmental interest (e.g. carbon monoxide, methane, formaldehyde and nitric oxide), such lasers offer the promise of access to much stronger absorption bands than can be measured with shorter wavelength communication lasers, while retaining the practical advantages of room temperature or thermoelectrically cooled operation. For example, the first overtone band of CO near 2.3 μm that is accessible with antimonide lasers is a factor of 160 times stronger than the second overtone band near 1.57 μm. Although the potential of antimonide lasers for trace gas sensing applications is usually cited as a principal motivation for their development, examples of such applications are not numerous in the literature.

Recently, the measurement of a water vapor absorption line near 2.65 μm using an antimonide laser was briefly described.[6] We reported the laboratory measurement of nitric oxide (NO) using an antimonide laser operating in the 2.65 μm region.[7] By using high frequency wavelength modulation spectroscopy with second harmonic detection, a detection sensitivity for NO of 15 ppm-meter was achieved. Spectral interferences from water vapor, which absorbs strongly in this wavelength region, could be avoided by careful selection of the NO line and by sampling the gas to be analyzed into a reduced pressure cell.

We are currently utilizing antimonide diode lasers that operate between 210 K and 260 K to access H_2CO near 2.28 μm and CO near 2.32 μm. A monochromator is used to isolate a single

longitudinal mode from the multimode Fabry-Perot laser. Figure 1 shows an example of direct absorption and the corresponding wavelength modulation (second harmonic) spectrum of CO measured near 2.32 μm. In order to realize single longitudinal mode operation without the monochromator, we have begun constructing a short external cavity (SXC)[8] laser system with a thermoelectric cooling stage. By inducing feedback from an external mirror separated by a short distance from the back facet of the Fabry-Perot cavity, we force single longitudinal mode operation of the laser diode. Results from our ongoing experiments in detection of CH_4, CO and H_2CO utilizing the SXC arrangement will be presented.

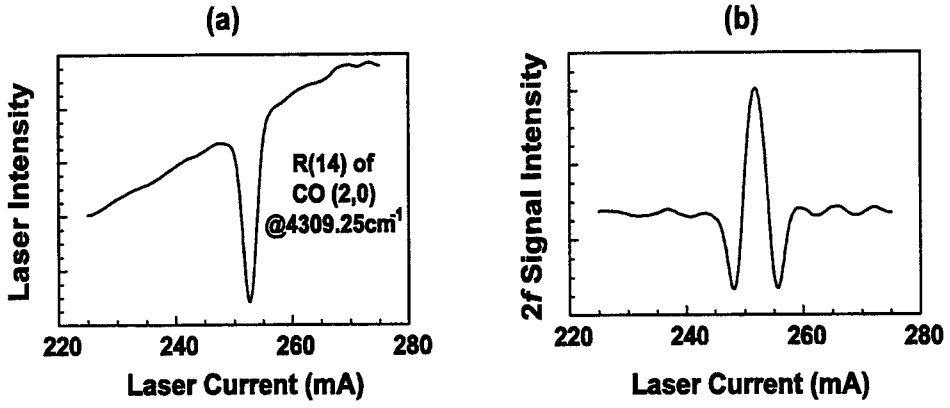

Figure 1 – (a) Direct absorption spectrum, and (b) corresponding 2*f* spectrum of the R(14) line of the CO first overtone band obtained with a 2.3 μm antimonide diode laser.

References

1. D. S. Bomse, "Diode lasers: finding trace gases in the lab and the plant," Photonics Spectra **29**, No. 6, 88 – 94 (1995).
2. D. S. Bomse, J. A. Silver, and A. C. Stanton, "Frequency modulation and wavelength modulation spectroscopies: comparison of experimental methods using a lead-salt diode laser," Appl. Opt. **31**, 718 – 731 (1992) and references therein.
3. P. Werle, F. Slemr, M. Gehrtz, and C. Braüchle, "Quantum-limited FM-spectroscopy with a lead-salt diode laser," Appl. Phys. **B49**, 99 – 108 (1989).
4. H. Lee, P. K. York, R. J. Menna, R. U. Martinelli, D. Z. Garbuzov, S. Y. Narayan, and J. C. Connolly, "Room-temperature 2.78 μm AlGaAsSb/InGaAsSb quantum-well Lasers," Appl. Phys. Lett. **66**, 1942 – 1944 (1995).
5. H. K. Choi, G. W. Turner, M. J. Manfra, and M. K. Conners, "175 K continuous wave operation of InGaAsSb/InAlAsSb quantum-well diode lasers emitting at 3.5 μm," Appl. Phys. Lett. **68**, 2936 – 2938 (1996).
6. R. U. Martinelli, "Mid-infrared wavelengths enhance trace-gas sensing," Laser Focus World **32** (3), 77 – 81 (1996).
7. D. B. Oh and A. C. Stanton, "Measurement of nitric oxide with an antimonide diode laser," Appl. Opt. **36**, 3294 – 3297 (1997).
8. D. T. Cassidy, D. M. Bruce and B. F. Ventrudo, "Short-external-cavity module for enhanced single-mode tuning of InGaAsP and AlGaAs semiconductor diode lasers," Rev. Sci. Instrum. **62**, 2385 – 2388 (1991).

Continuously Tunable, Single Mode, External Cavity Diode Lasers at 2 μm

G. S. Feller, I-Fan Wu, T. Day
Focused Research Inc.
2630 Walsh Ave., Santa Clara, CA 95051
(408) 980-8088

R. J. Menna, R. U. Martinelli, and J. C. Connolly
Sarnoff Corporation
CN5300 Princeton, NJ 08543

R.M. Mihalcea, D.S. Baer, R.K. Hanson
High Temperature Gas Dynamics Laboratory
Stanford University, Stanford, CA 94305

Compact, inexpensive laser sources in the 2-4 μm wavelength region are of growing interest for applications in environmental detection of trace gases as well as medical diagnostics, process control and combustion analysis. Many organic compounds, including hazardous pollutants, have characteristic absorption spectra in this region. Although external cavity diode lasers (ECDLs) are commercially available from 0.6 μm to 1.6 μm[1,2], they have not yet made it into the 2 μm wavelength range. Others have recently demonstrated tunability in an external cavity at 3.3 μm[3] which was not continuous or single mode. We present room temperature operation of single longitudinal and single spatial mode, external cavity tunable diode lasers operating around 2 μm. We also present high-resolution absorption measurements of CO_2 over the 250 cm^{-1} laser tuning range.

Conventional 2 μm strained InGaAs/InP quantum well lasers are used for operation centered at 1.96 μm[4,5]. In order to extend the wavelength of the laser diode, a tensile strained barrier was incorporated into the epitaxial structure. The opposing strain in the quantum wells and the barrier permit a wider quantum well to be used resulting in a longer emission wavelength (centered near 2.02 μm). These lasers are coated with a two layer anti-reflection coating to reduce the front facet reflectivity and suppress lasing in the Fabry-Perot modes of the laser chip. A reflectivity of ~10^{-4} or less is required for continuous tuning across the wavelength range of the laser.

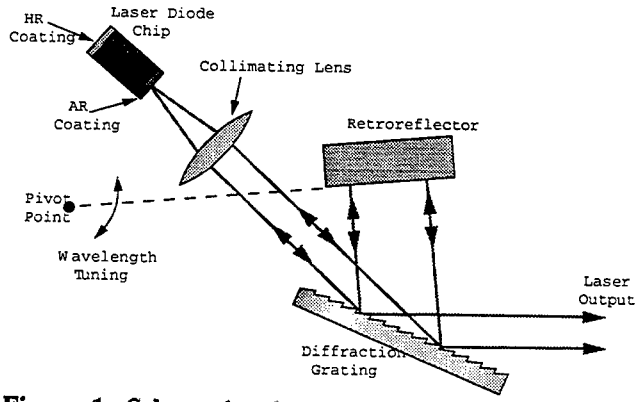

Figure 1: Schematic of a modified Littman-Metcalf laser cavity. The entire base is angled so the beam is parallel to the tabletop.

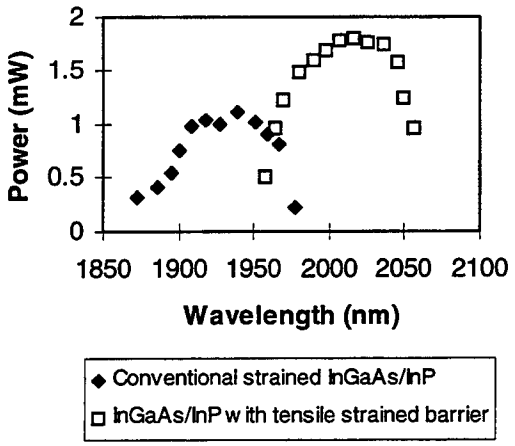

Figure 2: Tuning curves for 2 μm ECDLs. Both lasers contain compressively strained quantum wells, with the addition of a tensile strained barrier region in the longer wavelength laser.

Each laser is then placed into a grazing incidence Littman-Metcalf external cavity[6,7] as shown in Figure 1. The grating acts as a frequency selective output coupler with the angle of the retroreflector determining the output wavelength of the laser. By rotating about a unique pivot point, the feedback angle of the first order reflection and the cavity length track together allowing mode-hop-free tuning. A DC or piezoelectrically controlled motor provides rapid (up to 10 nm/s) tuning while fine control is achieved with a piezoelectric actuator. The conventional strained quantum well laser can be tuned from 1.882 μm to 1.975 μm with output powers greater than 1 mW at the peak. The laser which incorporates a tensile strained barrier region is continuously tunable from 1.960 μm to 2.060 μm, with output powers as high as 1.8 mW at the peak (2.020 μm). The tuning curves for both lasers are shown in Figure 2.

The ECDL was tuned over a wide (250 cm^{-1}) interval using the coarse adjustment motor to quickly record high-resolution CO_2 absorption spectra ($\nu_1+2\nu_2+\nu_3$, $4\nu_2+\nu_3$, $2\nu_1+\nu_3$ bands) near 2.02 μm. The entire survey scan (shown in Figure 3) was recorded in several minutes. Measurements of individual transitions of CO_2 (1.0 cm^{-1} scans) were recorded by adjusting the internal grating to particular center wavelengths and by applying a 6 volt sawtooth voltage waveform at a 1.25 Hz repetition rate to the wavelength modulation input. High-resolution absorption spectra will be presented and compared with calculated lineshapes based on data contained within the HITRAN96 database. The ECDL may also be applied for absorption measurements of other gases in this spectral region (e.g., H_2O, CO_2, N_2O). Measurements of individual absorption lines may be used for accurate determination of gas concentrations in a variety of environments, including high-temperature combustion flows, for emissions monitoring and closed-loop process control applications.

ECDLs at 2 μm open the door to spectroscopic applications for many molecular species and in environments not amenable to some more complicated techniques of generating radiation in this spectral region. Their compact and robust design along with their turnkey operation allow spectroscopy to reach more places. The improvements in the ECDL cavity and AR coating designs will enable steady progress to longer wavelengths and further applications.

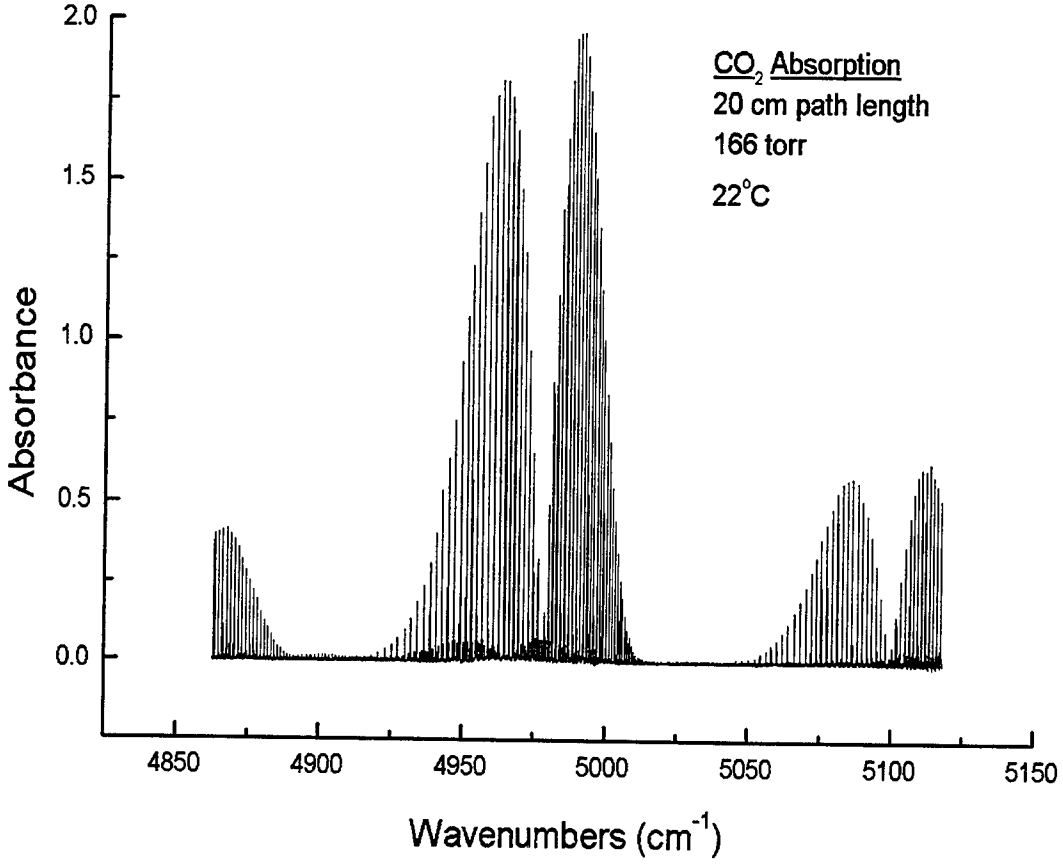

Figure 3: Absorption measurements of CO_2 using the 2.02 μm ECDL

References

[1] K. C. Harvey, C. J. Myatt, *Opt. Lett.*, **16**, (1991), 910-911
[2] New Focus Inc., of Santa Clara, CA and Environmental Optical Systems Inc., of Boulder CO offer ECDLs with wavelengths from 0.63 μm to 1.6 μm
[3] H. Q. Le, et al., *Appl. Phys. Lett.*, **69**, (1996), 2804-2806
[4] S. Forouhar, et al., *Electron. Lett.*, **29**, (1993), 574
[5] R. U. Martinelli, R. J. Menna, G. H. Olsen, and J. S. Vermaak, *IEEE Photon. Technol. Lett.*, **9**, (1997), 431-433
[6] K. Liu, M. Littman, *Opt. Lett.*, **6**, (1981), 117-118
[7] P. McNicholl, H. J. Metcalf, *Appl. Opt.*, **24** (1985), 2757-2761

Laser Based Absorption Sensor for Trace Gas Monitoring in a Spacecraft Environment

D.G. Lancaster, D.Richter*, J.C. Graf** , R.F. Curl, and F.K.Tittel

Rice Quantum Institute, Rice University, 6100 Main St., Houston, TX 77005, USA.
**Fachhochschule Ostfriesland, Dept. of Natural Science Technology, Constantiaplatz 4, 26723 Emden, Germany.*
*** Crew and Thermal Systems Division, Lyndon B. Johnson Space Center, Nasa Road 1, Houston, TX 77058*

Summary

Formaldehyde is a chemical widely used in many industrial manufacturing processes due to its high chemical reactivity and good thermal stability. Commonly used building materials like foams, paint and polymer products can contain formaldehyde. Studies indicate that H_2CO can cause a variety of health effects ranging from irritation of eyes, nose, and throat to nausea and headaches at concentrations above 100 ppb. For extended habitation, NASA has set a more stringent spacecraft maximum allowable concentration of 40 ppb for crew exposure from 7 to 180 days. To reduce formaldehyde levels below this concentration, outgassing materials and equipment need to be identified. In order to monitor the concentration and to locate emission sources, the development of an in-situ, real-time, portable gas sensor capable of detecting formaldehyde of sub-ppm levels in air was developed.

In this paper we present results of a portable laser based sensor for both enclosed volume monitoring of formaldehyde out-gassing from materials to be used in the space station (such as melanine foam) and formaldehyde monitoring of ambient spacecraft air during the 90 day Lunar-Mars life support test at the NASA Johnson Centre Space. During the test we have also demonstrated on-line monitoring of the methane concentration.

For H_2CO detection, direct absorption measurements are made of a fundamental ν_5 band absorption at 2831.64 cm^{-1} (3.5 μm). This line was first identified by Fried [1] to be suitable for atmospheric sensing, although in the presence of a high ambient methane concentration (up to 170 ppm), a weak methane line is close by (0.06 cm^{-1}) and must be taken into account (shown in fig.2). The spectral lines are resolved by conducting the absorption measurements at reduced pressure (60 torr). To calculate the H_2CO concentration, a Lorentzian lineshape is fitted to the H_2CO absorption peak and simultaneously a 5 th order polynomial is fitted to the baseline.

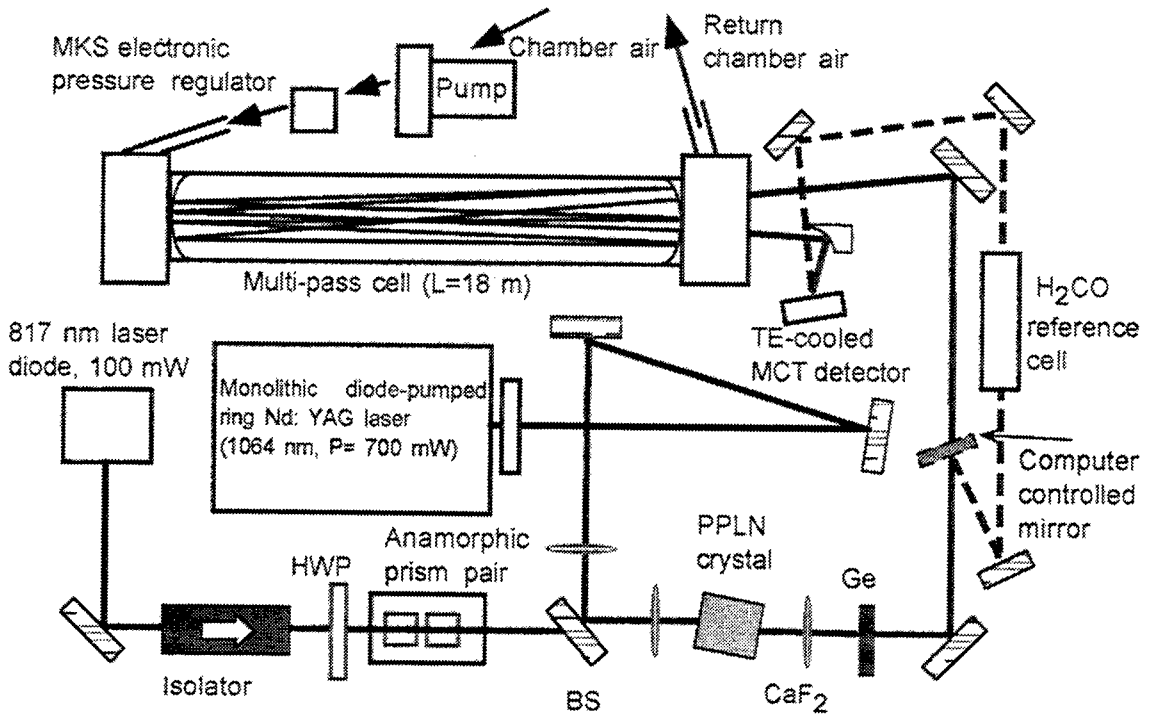

Fig 1: Schematic of the compact (30 cm x 61 cm) diode-pumped difference frequency spectrometer for formaldehyde detection. The computer controlled mirror can be inserted into the beam path to acquire a H_2CO reference spectrum.

The gas sensor described here uses difference frequency generation (DFG) in periodically poled $LiNbO_3$ (PPLN) of a single longitudinal mode (SLM) diode laser (817 nm) and a SLM Nd:YAG laser (1064 nm). Typically, 5 μw of mid-IR light is generated. The sensor layout is shown in fig-1, and is similar in design to that reported previously [2]. Absorption is measured in a 18 m, multi-pass cell. Data acquisition is performed by a laptop computer equipped with a PCMCIA A-D card. Control, data recording and analysis is carried out using Labview software. To provide an absolute frequency calibration, a H_2CO reference spectrum was acquired before every measurement by a computer controlled mirror which re-directed the beam through a 5 cm-long cell that contained a high concentration of formaldehyde (1 part per hundred, by volume).

A typical formaldehyde spectrum which was acquired by the sensor is shown in fig. 2 and corresponds to a concentration of 101 ppb. The measurements of H_2CO concentration in the chamber over a 21 hour period is shown in figure 3. The H_2CO concentration measured over this time has an average value of 34

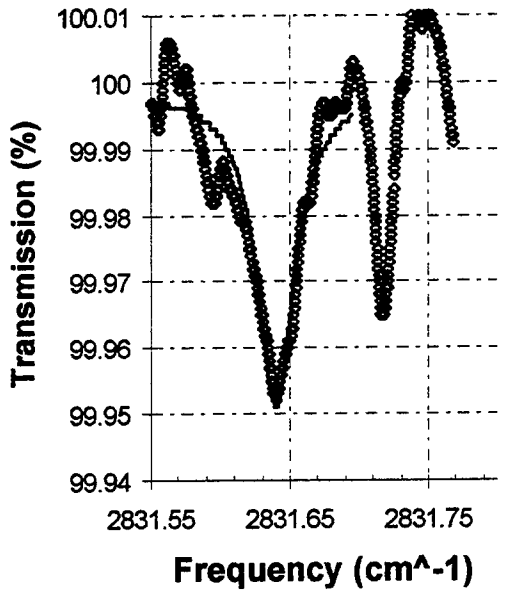

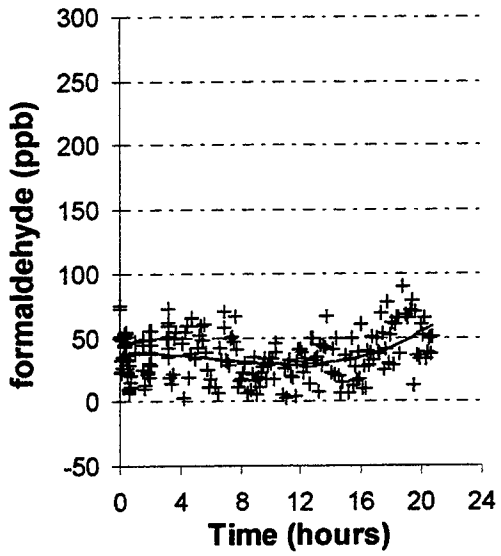

Fig. 2 (left): DFG H_2CO absorption spectra spectrum with a measured concentration of 101 ppb. At 2831.68 cm^{-1} is a CH_4 absorption line corresponding to a methane concentration of ~140 ppm.
Fig. 3 (right): H_2CO concentration recorded by the DFG sensor operating on-line at a closed environment test at the Johnson Space Centre .

± 16 ppb. The absolute calibration of the absorption cross section was performed by using a standard 5.78 ppm (± 5 %) formaldehyde in nitrogen mixture (Scott Specialty Gases). During the 90 day test, we also demonstrated detection of CH_4 over a 24 hour time period by tuning the sensor to an isolated CH_4 line at 2829.59 cm^{-1}.

In conclusion, real-time measurement of H_2CO at sub-ppm concentrations in a space station simulation environment using diode pumped 3.5 μm DFG radiation has been demonstrated. The narrow-bandwidth light and automatic calibration allowed the selective monitorring of a formaldehyde absorption line, from an adjacent CH_4 absorption. A minimum concentration of < 20 ppb H_2CO was detectable.

References

1. T. Toepfer, K. P. Petrov, Y. Mine, D. Jundt, R. F. Curl, F. K. Tittel, Appl. Opt. 36, 8042 (1997)
2. A. Fried, S. Sewell, B. Henry, B.P. West, T. Gilpin and J.R. Drummond, J. Geophys. Research 102, 6253 (1997).

Laser Applications to Chemical and Environmental Analysis

Surface Spectroscopy and Analysis

Tuesday, March 10, 1998

Nicholas Winograd, Pennsylvania State University
Presider

LTuB
10:30am–12:00m
Coral Room

Applications of Surface Nonlinear Optical Spectroscopy

Y. R. Shen

University of California, Berkeley
Department of Physics, 366 LeConte Hall #7300
Berkeley, CA 94720-7300
shenyr@physics.berkeley.edu

Second-order nonlinear optical processes are forbidden in bulks with inversion symmetry, but necessarily allowed at surfaces and interfaces. This intrinsic surface specificity has rendered second harmonic generations (SHG) and sum frequency generation (SFG) exceptionally useful as surface probes. SFG in particular has been developed into an extremely powerful surface spectroscopic tool. It is applicable to all interfaces accessible by light and therefore has provided new research opportunities in many areas of surface science.

We discuss here a few selected examples of how infrared-visible SFG as a surface vibrational spectroscopy has unique capabilities to probe surfaces, interfaces, and films. For gas/solid interfaces, we show that SFG can be used to monitor surface species existing under high gas pressure. This makes in-situ studies of surface reactions possible. For gas/liquid interfaces, we demonstrate the feasibility of using SFG to acquire surface vibrational spectra and hence structural information of surfaces of neat liquids and liquid mixtures. For liquid/solid interfaces, we discuss how SFG can be effective as a probe to study conformational change of surfactant molecules adsorbed at such interfaces in response to change of their liquid environment. For films, we report the first observation of surface-induced ferroelectricity in ice on Pt(111). Other examples will be discussed if time allows.

This work was supported by the Director, Office of Energy Research, Office of Basic Energy Sciences, Materials Science Division of the U.S. Department of Energy, under contract No. DE-AC03-76SF0098.

Spectroscopic Characterization of Semiconductor Surface Impurities by Near-Field Scanning Optical Microscopy

Wolfgang Schade, David L. Osborn, Jan Preusser, and Stephen R. Leone

JILA, University of Colorado and National Institute of Standards and Technology and University of Colorado, Department of Chemistry and Biochemistry, University of Colorado, Boulder, Colorado 80309-0440
SCHADEW@jila.colorado.edu

Near-field scanning optical microscopy (NSOM) is a very promising tool for the characterization of optical and optoelectronic properties of semiconductors and other devices at the nanometer scale [1]. Defect and impurity characterization of surfaces and interfaces is an important field in semiconductor physics. Since these materials are opaque in the visible spectral range, transmission contrast mechanisms which are most common for NSOM can not be applied in these investigations. However, near-field photocurrent (NPC) is a very attractive method for studying surface characteristics of optoelectronic devices [2,3]. The near-field laser light illumination excites electron-hole pairs directly under the fiber tip in the semiconductor material. These photoexcited carriers are collected by p-n junctions and result in a photocurrent that can be measured accurately by lock-in techniques, while moving the sample or the fiber tip to measure images.

The basic experimental set-up is shown in fig. 1. For excitation the fundamental (780 nm) and the second harmonic (390 nm) of a femtosecond Ti-sapphire laser with a pulse duration of 100 fs and 82 MHz repetition rate and the cw output of a HeNe laser (633 nm) are used in these experiments. During all experiments the incident average laser power into the fiber was $P<5$ mW and the transmission through the NSOM fiber tip is about 10^{-4}. The spatial resolution is about 200 nm and a shear-force system is used to set the distance between the fiber tip and the sample surface.

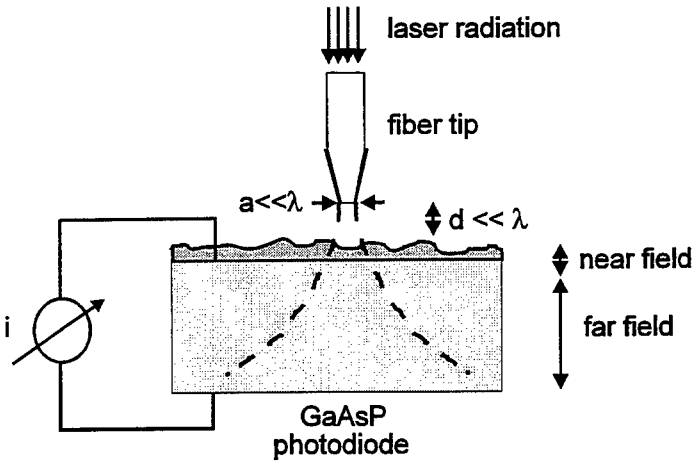

Figure 1: Experimental set-up for near-field photocurrent (NPC) measurements on semiconductors.

In NPC imaging the absorption characteristics of the laser wavelength can change the contrast in the images very dramatically. Also new surface impurity sites become visible by proper choice of wavelengths for the photoexcitation. This is shown in the present investigation for a conventional GaAsP photodiode and the wavelengths λ_1=780 nm, λ_2=633 nm, and λ_3=390 nm.

In order to perform NPC measurements with this photodiode the protective resin coating was carefully removed by chemical etching. The absorption coefficient of GaAs increases significantly when the wavelength is tuned from the infrared to the ultraviolet (uv) spectral range [4]. For GaAs and an incident laser wavelength of 700 nm the penetration depth of the light into the semiconductor is about d=1 μm (1/e decay) while for λ=400 nm it is only d=200 nm. Therefore for laser wavelengths in the red spectral range, where e.g. the GaAsP photodiode shows the best photoresponse, far-field bulk effects are probed. However, if laser wavelengths in the uv are used to probe NPC images the photoresponse is reduced but near-field surface effects are obtained because of the enhanced absorption.

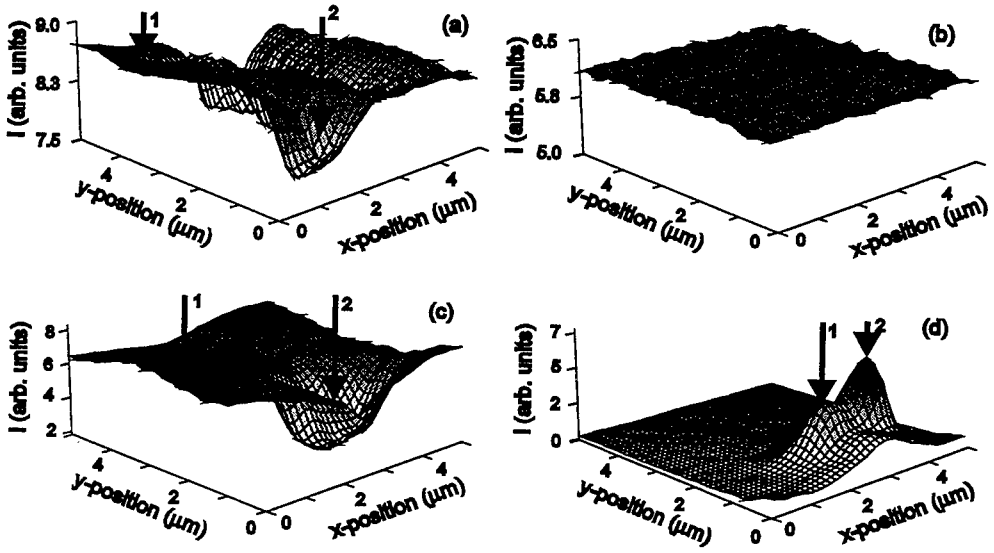

Figure 2: NPC images of a GaAsP photodiode for (a) λ=390 nm, (b) λ=633 nm, (c) λ=390 nm, and (d) λ=780 nm. The scan area is 5×5 μm^2 and I is the measured photocurrent.

Figure 2 shows near-field photocurrent images for three different excitation wavelengths and a scan area of 5 μm × 5 μm. For uv-excitation at λ=390 nm the NPC image in fig. 2a shows several spots with a reduced photocurrent of about 15% that are probably due to impurity sites in the GaAsP material, which has been put into direct contact with the ambient air. Spatially resolved measurements of the photoresponse at the positions that are indicated by the arrows 1 and 2 in fig. 2a show a linear response when the incident laser power is changed. On the normal GaAsP material (arrow 1) the photoresponse is k=0.043 A/W while it is k=0.033 A/W on the impurities (arrow 2). In fig. 2b the same scan area of the GaAsP photodiode and the same experimental conditions are used but the excitation wavelength was λ=633 nm. The NPC image shows a flat surface and no structures are obtained. This is explained by the larger volume of absorption due to the relatively deep penetration depth at λ=633 nm compared to 390 nm.

The density of the impurities on the GaAsP semiconductor is found to differ at different locations. NPC images have been taken at λ=390 nm and different scan areas (figures 2a and 2c). In fig. 2a only a relative change of 15% is obtained between the normal GaAsP and the

impurity spot (arrows 1 and 2), respectively. In the NPC image of fig. 2c the relative change of the photocurrent is about 50% (arrows 1 and 2), which suggests a higher impurity concentration. The optical absorption of a semiconductor is modified by the presence of impurities. The absorption by impurities is temperature dependent and proportional to the impurity concentration [4]. For this GaAsP photodiode the band gap energy is E_g=1.8 eV, which corresponds to a wavelength λ_g=690 nm. However, in the present experiment a broadening of the absorption is observed by as much as 0.29 eV, depending on the impurity density. Therefore, at the impurity sites, the linear response of the photodiode is extended to wavelengths $\lambda_g' <$ 820 nm. This is shown in the NPC image of fig. 2d. Here the same scan area and experimental conditions are used as for the image shown in fig. 2c, but the excitation wavelength is λ=780 nm. For the spot where a reduced photoconductivity was measured in the case of uv-excitation (arrow 2 in fig. 2c) an enhanced photoconductivity is obtained when λ=780 nm is used for the excitation (arrows 1 and 2 in fig. 2d). On those areas where little or no impurity density appears (arrow 1 in fig. 2c) no significant photocurrent signal is detected for λ=780 nm, since in that case the photon energy is below the band gap energy, E_g = 1.8 eV, for GaAsP. However, on locations with impurities a spatially resolved near-field photocurrent signal can be detected, even though the penetration depth of photons at λ=780 nm is about 1 μm. This suggests that the observed impurity spots arise from sites that are close to the surface. Only within the region of the impurities is a photocurrent induced by absorption of 780 nm photons due to the broadening of the absorption, whereas for the normal GaAsP material no photocurrent signal is induced at λ= 780 nm. This mechanism results in an enhanced contrast as indicated in the NPC image of fig. 2d.

In summary, this investigation shows the potential of using multiwavelength near-field photoconductivity for studying surface impurities of semiconductors and optoelectronic devices, which will become important as spatial dimensions miniaturize in the future.

References

1. J.W.P. Hsu, E.A. Fitzgerald, Y.H. Xie, P.J. Silverman, Appl. Phys. Lett. **65**, 344 (1994).
2. M.S. Unlu, B.B. Goldberg, W.D. Herzog, D. Sun, E. Towe, Appl. Phys. Lett. **67**, 1862 (1995).
3. Q. Xu, M.H. Gray, J.W.P. Hsu, J. Appl. Phys. **82**, 748 (1997)
4. K. Seeger, *Semiconductor Physics*, Springer, Berlin (1985)

A Laser Desorption Mass Spectrometer Microprobe for Surface Mapping of Lithium

Grant A. Bickel and Harry M. Adams

AECL
Chalk River, Ontario K0J 1J0, CANADA
Telephone: 613-584-8811 (ext 3172), Fax: 613-584-1220

A laser desorption mass spectrometer microprobe has been utilized to map Li distributions in CANDU® nuclear reactor components. Lithium is present in the Heat Transport System (HTS) of the reactor and can be used as a tracer of HTS leakage. Leakage (in the form of both liquid D_2O and steam) into component crevices, introduces uncontrolled and unknown chemistry within the crevices. One such area is the rolled joint, where the zirconium pressure tube is rolled into the stainless steel end fitting hub. HTS leakage, occurring through cracks and crevices under the rolled joint, may lead to deuterium ingress into the Zr pressure tube and subsequently to pressure tube embrittlement. It is hoped that the results from the laser desorption microprobe, can be used to correlate the HTS leakage through the cracks and crevices under the rolled joint with the deuterium profile in the pressure tube. The laser desorption technique was found to be very sensitive and could provide semi-quantitative Li distributions either at low spatial resolution (the length of the 20 cm hub section) or high spatial resolution (revealing Li in micron sized cracks). Other traditional surface science techniques like SAM and XPS are not sensitive to Li, and commercial SIMS instruments cannot accommodate the large hub samples nor allow for profiling over the hub length.

The laser desorption mass spectrometer microprobe consists of a single laser to desorb and ionize the surface Li species, a vacuum chamber containing a linear time-of-flight mass spectrometer and motorized sample stage, and a computer for data acquisition and sample stage control. The desorption beam wavelength is 229 nm and is produced by a frequency doubled, pulsed dye laser, pumped at 30 Hz with a XeCl Excimer laser. The beam is attenuated and focused onto the sample surface to a diameter ($1/e^2$) of 15 to 200 μm depending on the required spatial resolution. Assuming a Gaussian beam profile, the typical incident fluence at beam center is 20 mJ/cm^2. The time-of-flight mass spectrometer was home built and designed for high ion transmission at the expense of mass resolution. The sample stage is equipped to hold samples up to 20 cm in length. The position of the laser beam is fixed and surface profiling is accomplished by moving the sample with stepping motors.

It is presumed that the Li is on the surface in the form of $LiOH\text{-}H_2O$. The maximum ΔT of the stainless steel hub surface during the laser pulse is approximately 100K according to a finite difference treatment of the heat conduction equations.[1] Tuning the wavelength between 245 and 225 nm always gave a strong Li^+ signal and did not reveal the expected Li photo-ionization threshold at 229 nm. This suggests that Li^+ is produced from the dissociation of desorbed molecular species. No molecular ions were observed in the mass spectrum. The desorption/ionization mechanism is very efficient, and surface coverages of 2.5×10^{13} Li atoms/cm^2 were easily detected and provided persistent Li^+ signals for thousands of laser pulses. The high sensitivity is in part due to the nearly complete overlap of the photo-ionization beam

with the desorption plume.[2] This overlap enables the use of lower desorption fluences, to minimize the influence of surface morphology on the desorption yields.[3] The spatial resolution is limited by the laser beam diameter. However, the desorption process usually depends on laser fluence in a nonlinear way, and thus the effective beam diameter will be less than the actual beam diameter by a factor of $(1/n)^{1/2}$, where n is the order of non-linearity.

A mock-up hub sample was prepared by flooding an offcut hub surface with a saturated LiOH solution, scrubbing it under hot water and finally buffing it with Scotchbrite®. It was presumed that this would leave the Li in the low spots, cracks and crevices. Figure 1 shows a repeated line scan across the surface demonstrating the signal reproducibility and spatial resolution. Figure 2a shows the Li profile acquired with a two dimensional scan. For clarity, a 3×3 Gaussian smoothing filter was applied to the data in Figure 2a. SEM images taken of the laser profiled area showed no discernible morphological changes to the surface as a result of laser irradiation. Because the laser profiling is non-destructive and removes only a fraction of the Li, an exact comparison of the Li profile could be made with SIMS. Figure 2b shows the Li profile of the same area acquired by SIMS. There is nearly complete correlation between the two techniques. In both cases surface topography may have an influence on the magnitude of the Li^+ signal. Even though the ion beam current was extremely low, the SIMS Li profile noticeably changed over the period of a few minutes. This is partially due to removal of Li but, may also be attributed to the high mobility of Li ions on the surface and their exchange into the substrate under the influence of the ion beam.

The laser desorption mass spectrometer microprobe provides semi-quantitative surface distributions of Li on hub surfaces. When benchmarked against SIMS, it is less destructive and provides equivalent results with a more limited spatial resolution. Moreover, the laser desorption method allows for low resolution profiles over large (20 cm) distances.

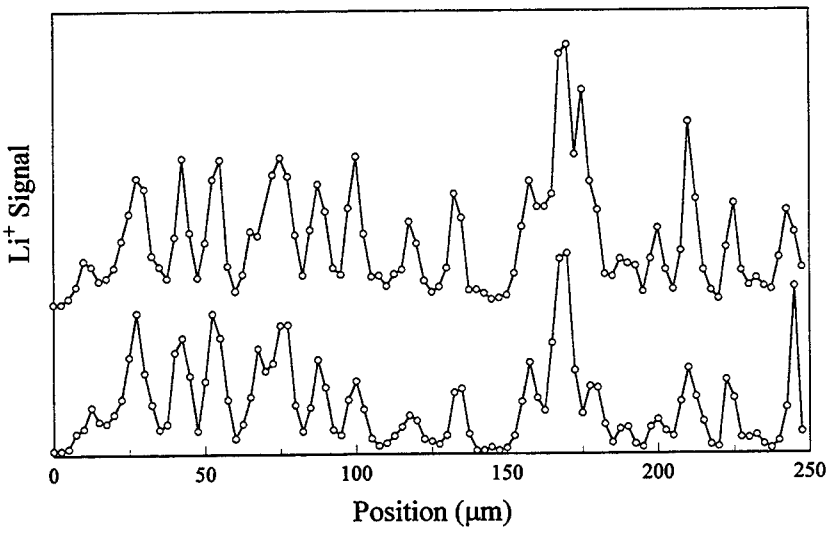

Figure 1. Line profile across portion of rolled joint hub with repeat scan (offset above for clarity). The step size is 2.5 μm. Signals are average of 30 laser pulses at each location per scan. The narrowest features are < 10 μm wide providing an upper limit on the spatial resolution.

Figure 2a. Two dimensional (100 × 100μm) laser profile of Li on a hub surface. The step size is 2.5 μm. The signal intensities are normalized to an 8 bit gray scale with black as the maximum signal.

Figure 2b. SIMS image of Li^+ secondary ions on identical region in Figure 2a. The signal intensities are normalized to an 8 bit gray scale with black as the maximum signal. Acquired with a Cameca IMS 6f operating in the microprobe mode. Primary beam: O_2^+, beam current 6×10^{-12} A, beam diameter: ≈ 1 μm.

References:

1. J-M. Philippoz, R. Zenobi, and R. N. Zare, Chem. Phys. Lett. **158**, 12 (1989).

2. J. E. Anderson, T. E. Allen, A. W. Garrett, C. G. Gill, P. H. Hemberger, P. B. Kelly, and N. S. Nogar, in AIP Conf. Proc. 1997, **388** (Resonance Ionization Spectroscopy 1996), 195, AIP Press.

3. M. R. Savina and K. R. Lykke, Anal. Chem. **69**, 3741, (1997).

Molecular Photoionization and Chemical Imaging

K. F. Willey, V. Vorsa and N. Winograd
Department of Chemistry, Penn State University, 184 MRI Building, University Park, PA 16802
(814) 863-0001; (814) 863-0618 fax

Summary

It is now possible to desorb a variety of organic molecules from surfaces using a tightly focused energetic ion beam. The molecules are detected as secondary ions using time-of-flight mass spectrometry, and may be spatially resolved by rastoring the ion beam over a larger area. A chemically resolved image is then acquired by examining the intensity of a particular mass as a function of x,y position. Presently, liquid metal ion sources using 25 KeV Ga^+ ion projectiles can be focused to a spot of less than 20 nm in diameter. The limiting factor for molecule-specific imaging is sensitivity. The ion dose must be kept less than 1% of the total number of surface molecules to prevent chemical damage. Moreover, the ionization probability of desorbed molecules is generally less than 1 in 10^4. Since the molecules desorb from the first layer and since there are at most 4 x 10^6 molecules per square micron (depending on size of course), the signal rapidly approaches zero as the spatial resolution or beam probe size is reduced below 1 micron.[1] Here we investigate the use of high intensity 100 fs laser pulses to photoionize the desorbed neutral molecules in an attempt to increase the measurement efficiency of this type of experiment. Our model system is dopamine, an important neurotransmitter that has aromatic character, but is subject to significant fragmentation using ns laser pulses. The results suggest that this approach can indeed expand the performance of mass-spectrometry based imaging experiments and can open new applications in bioimaging.

The experiments presented here were performed on a specially designed reflectron-based imaging time-of-flight secondary ion mass spectrometer (ToF-SIMS). A schematic diagram of the equipment configuration is shown in Figure 1. The fs laser source employed for the postionization experiments is a Ti:sapphire based regenerative amplifier system manufactured by Clark-MXR, Inc. as described previously[2] except that an additional 4 pass YAG-pumped amplifier was employed to further increase the laser energy to 3.5 mj/pulse at 800 nm or 350 mj/pulse at 267 nm at a repetition rate of 1 kHz. The high repetition rate is essential for imaging experiments. Each image contains 128 x 128 mass spectra and with 1-5 laser pulses per pixel, acquisition times can be extensive with 10-30 Hz systems.

The photoionization properties of thermally evaporated dopamine molecules are shown in Figure 2 using the three available photoionization wavelengths. There are three major species observed including the molecular ion M^+ at m/z = 153, a fragment ion M^+-CH_2NH at m/z = 124 arising from the McLafferty rearrangement (McL^+) and the side chain fragment $CH_2NH_2^+$ at m/z = 30. Note that M^+ is observable at all ionization wavelengths including 800 nm where at least 5 photons are required for ionization. As the wavelength is reduced toward the UV, the relative amount of M^+ increases, suggesting that UV radiation will yield the best detection efficiency during ion desorption experiments. The ionization does not appear to involve tunnel

or barrier suppression ionization since better molecular photoionization is expected in near IR than in the UV.

The corresponding spectral profile of dopamine sputtered from a thin film deposited onto a Si substrate is shown in Figure 3. Note that the M^+ signal is virtually undetectable via postionization but that MH^+ is a significant peak in the SIMS spectrum. The reasons for this discrepancy are unclear at the moment. It is possible that the sputtered molecule is formed in highly excited vibrational states and that photoionization leaves the ion on a dissociative potential energy curve. It is also possible, however, that there are fewer neutral dopamine molecules which are sputtered intact than there are protonated molecular ions formed during desorption. This is an interesting issue that merits further study. The intensity of the other fragment ions is, however, about 4 times greater than that found by SIMS.

An example of the chemical imaging approach is shown in Figure 4. This image shows a 200 micron field of view and is recorded with 152 x 128 pixels. The dopamine image is shown by summing the counts from m/z 123 and 124. The molecule was coated onto a Cu grid and placed over an In substrate. The In photoionization image at m/z 115 is shown on the right.

Acknowledgment

We gratefully acknowledge the financial support of the National Institutes of Health and the National Science Foundation.

References

1. N. Winograd, *Anal. Chem.* **65**, 622A (1993).

2. C. L. Brummel, K. F. Willey, J. C. Vickerman, N. Winograd, *Inter. J. of Mass Spec.*, **143**, 257 (1995).

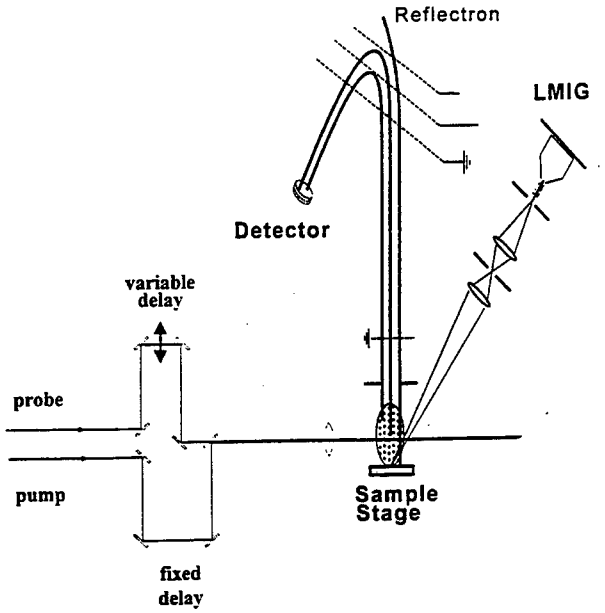

Figure 1. Block diagram of ToF-SIMS system.

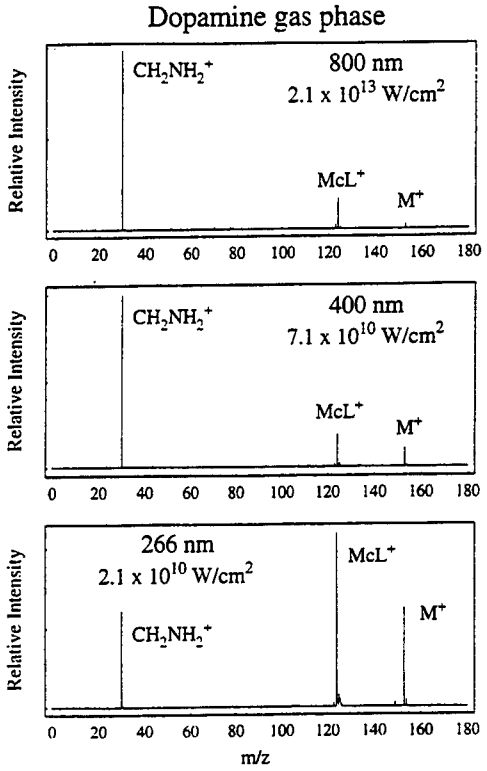

Figure 2. Photoionization of dopamine at various ionization wavelenths.

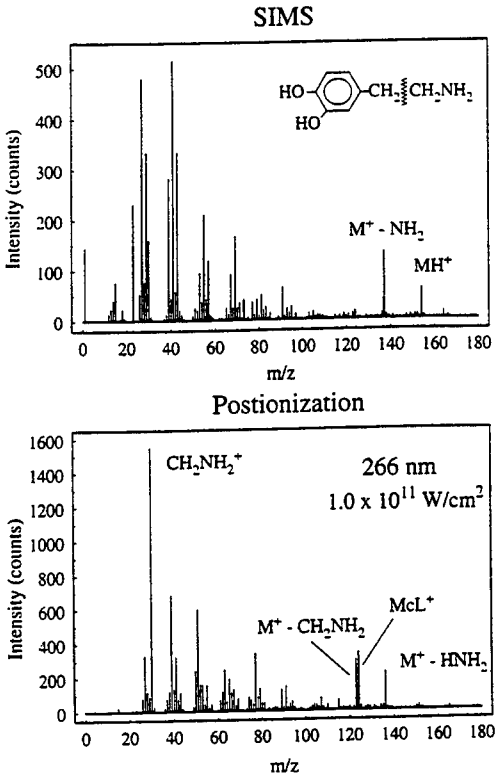

Figure 3. Comparison of SIMS and postionization spectra for dopamine.

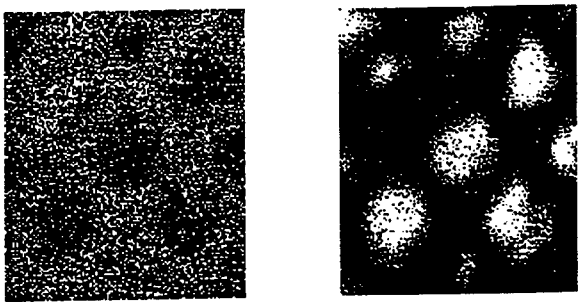

Figure 4. Postionization with 267 nm light of a grid coated with dopamine.

Laser Probe Of Surface Reaction Dynamics

Xiaoyang Zhu
Department of Chemistry, University of Minnesota, Minneapolis, MN 55455
Phone: (612) 624-7849; Fax: 626-7541; E-mail: zhu@chem.umn.edu

Understanding surface chemical kinetics is essential to the advancement of the frontiers of many vital technologies, such as semiconductor device fabrication and heterogeneous catalysis. This indisputable driving force, along with the rapid development of a large repertoire of atomic, molecular, and structural sensitive surface probes, has been responsible for the built-up of an immense literature on the chemical pathways and kinetics of a large number of molecules on an equally large number of solid surfaces. A typical example of a surface chemical study may involve the identification of surface chemical species and gas phase products in a certain parameter phase space, as well as the measurement of kinetic parameters for key reaction steps. This practice is widely employed today to tackle a seemingly inexhaustible number of important surface chemical problems. Such a pragmatic approach is by no means mundane since the problems we are tackling are increasingly more complex while the tools at hand are ever more powerful. However, to some in the field, obtaining chemical kinetics of another molecule on another surface is not as gratifying as taking perhaps even a blurred glimpse into the elementary chemical act responsible for the surface chemical reactivity. It is the purpose of surface reaction dynamics to probe and understand the elementary chemical acts responsible for the macroscopic kinetic behavior. Understanding at such a fundamental level may allow us not only to explain but also to predict surface reaction rates.

The field of surface reaction dynamics has progressed significantly in the last decade or so, thanks in part to the successful migration of many of the concepts and tools from the much more advanced field of gas phase reaction dynamics. On the experimental side, two techniques stand out: molecular beams and laser spectroscopies. In a molecular beam-surface scattering experiment, one can investigate the role of translational energy in chemical reactivity or the extent of energy transfer in inelastic scattering. A more complete microscopic picture can be obtained by characterizing reaction products using laser spectroscopic techniques, which yield product density, velocity, and, more importantly, quantum state distributions (rotational, vibrational, and electronic). With the availability of this level of microscopic information, we can now compare experiment and theory on a *quantitative* basis, a sign of maturity in this research field. Past attempts in state-resolved characterization of surface reaction products have concentrated on diatomic species in molecule-surface scattering, recombinative desorption, and photodesorption. Here, I address more complex problems, i.e., the dynamics of surface reactions involving polyatomic species. These studies clearly illustrate the multidimensional nature of surface reaction dynamics.

Examples I: Thermal desorption of methyl radical from GaAs [1]

The thermal desorption of methyl radical at ~700 K from GaAs(100) is the rate-limiting step in the surface reaction controlled metalorganic chemical vapor deposition (MOCVD) of GaAs from $Ga(CH_3)_3$. This reaction is also a model surface reaction for MOCVD in general. Fig. 1 shows a resonance enhanced multiphoton ionization (REMPI) spectrum of CD_3 thermally desorbed from the GaAs(100) surface. Each data point in this spectrum is obtained from state-resolved thermal desorption at a particular wavelength. The vibrational distribution in the umbrella mode of CD_3 is superthermal. Using calculated FC factors the vibrational population ratios are $N_{v''=2}/N_{v''=0} = 0.6$ and $N_{v''=3}/N_{v''=1} = 0.5$, which are more than four

times those expected from a thermal equilibrium at the desorption temperature. In contrary to vibration, the translational distribution of the methyl radical is nearly thermal neutral ($<E_{trans}/2K>$= 860 ± 60 K). These results can be interpreted by a hypothetical potential energy surface, Fig. 2, for the desorption of a methyl group from the GaAs surface. The main feature of this hypothetical PES is that there is an "early" barrier in the desorption coordinate, i.e., the transition state involves a significantly bent CD_3 group. This study is of general significance to the understanding of M-C bond cleavage in surface reaction controlled MOCVD processes. It also provides a quantitative basis for further theoretical investigations.

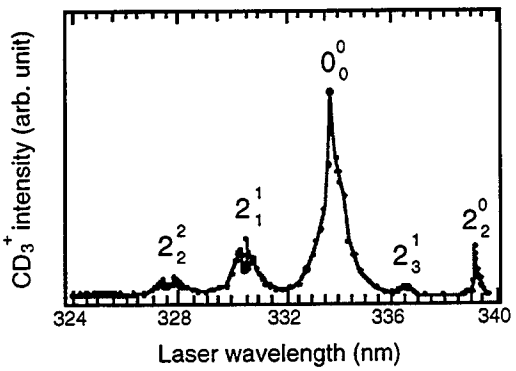

Fig. 1. Resonance enhanced multiphoton ionization spectrum of CD_3 thermally desorbed from GaAs(100) surface at 700 K.

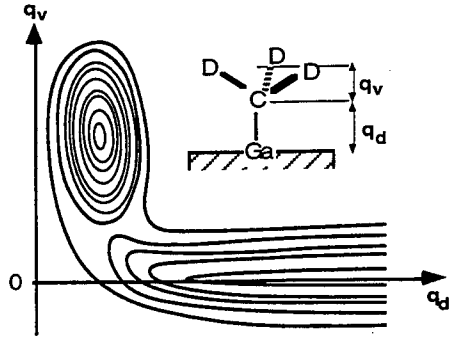

Fig. 2. A hypothetical potential energy surface for the desorption of methyl radical from GaAs. Note the location of an "early" transition state in the desorption coordinate.

Example II: Photodissociation of phosgene on Ag [2]

Exothermic reactions are perhaps the most common type of surface reactions. The common perception is that the excess energy released by a surface reaction is quickly absorbed by the vast number of energy states within the substrate, both electronic and nuclear. However, nuclear motion leading to chemical consequences can in some cases compete efficiently with these energy relaxation pathways. Here, I provide state resolved evidence for energetic and concerted dynamics in surface reactions. The Cl_2CO/Ag system because (i) Previous surface studies have shown that Cl_2CO readily dissociates on metal surfaces upon photon irradiation, yielding CO as the gas phase product; (ii) In the gas phase, the first step in the UV photodissociation or the dissociative electron attachment of Cl_2CO yields the unstable ClCO radical, which promptly dissociates to CO and Cl. If this reactive ClCO radical is formed on metal, its dissociation serves as a probe to the dynamics of an energetic surface reaction.

Cl_2CO is weakly adsorbed on Ag at 90 K. Photo-irradiation of 1 ML Cl_2CO leads to dissociation, with Cl retained on the surface and CO desorbed into the gas phase. Fig. 3 shows the mean translational energy of CO from monolayer phosgene, $<E_{trans}>$ = 0.26 ± 0.2 eV (or $<E_{trans}/2k>$ = 1500 ± 100 K), which is independent of hν. Also shown is the mean translational energy of CO from the photodissociation of Cl_2CO on the surface of a multilayer film. For monolayer, in contrast to $<E_{trans}>$, the initial photodissociation cross section decreases by more than two orders of magnitude when hν approaches the threshold (~1.9 eV). The observed independence of $<E_{trans}>$ on hν, particularly when it is near the threshold, indicates that CO is not a product of the primary DEA reaction. The translational energy distribution of CO (g) is determined by the dynamics of ClCO dissociation on the Ag surface, independent of the electron excitation energy. The $<E_{trans}>$ of CO from direct photodissociation of Cl_2CO on the surface of the molecular film is clearly lower than that from

the DEA process on Ag. The same trend is also seen in internal state distributions, Fig. 4. Here, the rotational state distributions are extracted from REMPI measurements.

The observation of higher translational and rotational energy of CO from the monolayer DEA reaction than that from the direct photodissociation on the surface of the molecular film is unexpected. Previous surface photochemical studies have often shown the opposite. The explanation for the surprising result from Cl_2CO lies in the intermediate, ClCO. For monolayer dissociation, the surface is not a bystander during Cl-CO bond cleavage. It is known that Cl adsorbs strongly on metal and Cl-Ag bond formation should be highly exothermic (81 kcal/mole or 3.5 eV in the gas phase). The high $\langle E_{trans} \rangle$ and $\langle E_{rot} \rangle$ from the surface reaction is evidence for concerted reaction dynamics on the surface: the high exothermicity in the Cl-Ag bond formation on the surface exerts part of the energy to the Cl-CO coordinate, leading to the observed high translational and rotational energy in CO (g). The gas phase product essentially provides probe to the local "hot" spot resulting from Ag-Cl bond formation.

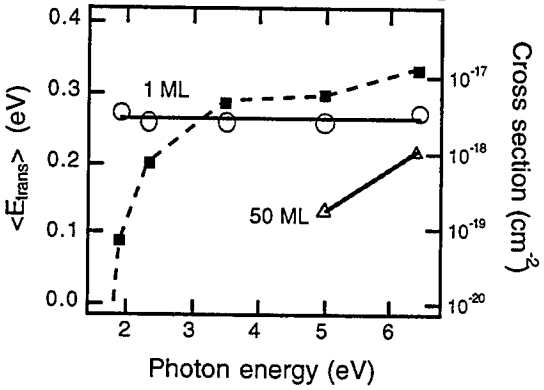

Fig. 3. Mean translational energy of CO (open circles and triangles, left axis) and initial photodissociation cross section (filled squares, monolayer, right axis) as a function of photon energy.

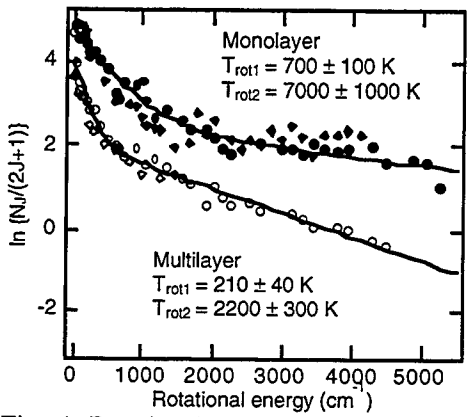

Fig. 4. Rotational state distribution of CO from the photodissociation of monolayer and multilayer Cl_2CO on Ag.

Perspectives

State resolved characterization of model surface processes involving diatomic species, along with molecular beam-surface scattering experiments, have been mainly responsible for many of the current vocabulary and concepts in surface dynamics. The advancement of this field is inevitably faced with the challenge of understanding more complex surface reactions, those which usually involve more than two atoms. The successful examples illustrated here represent initial efforts in this direction. While model systems involving diatomic species will continue to dominate the field of surface reaction dynamics, increasing efforts on polyatomic systems will certainly appear. This progress also calls for the advancement in theoretical calculation and modeling. I am hopeful that, in the near future, one can construct potential energy surfaces, such as that in figure 2, using theoretical results from first principles. Quantitative comparisons between dynamic simulations and state resolved measurements will become feasible for surface reactions in general. Thus, predicting surface reaction rates will not remain an illusive goal.

[1] Q.-S. Xin and X.-Y. Zhu, J. Chem. Phys. 104 (1996) 8829; H. Wang, Q.-S. Xin, and X.-Y. Zhu, J. Vac. Sci. Technol., to be published.

[2] Q.-S. Xin and X.-Y. Zhu, Phys. Rev. Lett. 75 (1995) 4776; J. Chem. Phys. 104 (1996) 7904.

Laser Applications to Chemical and Environmental Analysis

Environmental Applications: 1

Tuesday, March 10, 1998

Robert P. Lucht, University of Illinois–Urbana
Presider

LTuC
2:00pm–3:30pm
Coral Room

Use of a Fiber Optic-Based, Laser-Induced Breakdown Spectroscopy (LIBS) Probe for In Situ Determination of Metals in Soils

Gregory A. Theriault
Stephen H. Lieberman
Code D361
Space and Naval Warfare Systems Center, San Diego
53475 Strothe Road
San Diego, CA 92152
Phone: (619) 553-2779
Fax: (619) 553-2876
Email: theriaul@nosc.mil

Scott Bodensteiner
Richard Tripoli
San Diego State University Foundation
San Diego, CA 92182

A Cone Penetrometer-deployed fiber optic probe for the *in-situ* assessment of metal contamination of soil is described. In this talk both system design features and field-testing results will be discussed.

Microanalysis of solids by laser ablation with one shot

H.E. Bauer[1] and K. Niemax[2]

[1]Institute of Physics, University of Hohenheim, Garbenstrasse 30, 70599 Stuttgart, Germany
phone: +49-711-459-2145, fax: +49-711-459-2461, e-mail: bauerhe@uni-hohenheim.de

[2]Institute of Spectrochemistry and Applied Spectroscopy, Bunsen-Kirchhoff-Strasse 11,
44139 Dortmund, Germany
phone: +49-231-1392-101, fax: +49-231-1392-310, e-mail: niemax@isas-dortmund.de

Introduction

Sampling by pulsed lasers (LA: laser ablation) is a fast and simple method which, in principle, can be used for all types of solid samples. The technique is well established in combination with the inductively coupled plasma (ICP) and is also commercially available. Optical emission spectrometry (OES) of the laser produced plasma, called LIBS (laser induced breakdown spectrometry), is the more direct method. However, LIBS is still regarded as the less accurate technique in comparison with LA-ICP-OES or -MS, because the analytical data are strongly dependent on the parameters of the laser produced plasma which can change dramatically from laser shot to laser shot if the matrix composition and the ambient conditions vary. One way to compensate for the variation of the plasma is the simultaneous spectroscopic measurement of the analyte lines and all relevant plasma parameters. This requires simultaneous and time gated measurements of the total emission spectrum of the laser spark.

We have coupled a high resolution Echelle spectrograph with an intensified charge coupled device detector (ICCD) which allows to detect simultaneously the major part of the total emission spectrum of the laser produced plasma. The Echelle/ICCD system is used in LIBS as well as in combination with a microwave induced plasma (MIP) as emission source for laser ablated vapour [1].

Experimental

A Nd:YAG laser (wavelength: 1.06 μm, pulse length: 5 ns, pulse power: 10 mJ) was used for

ablation. Depending on the matrix, typical masses of 1 - 150 ng were ablated. The Echelle spectrograph spans the total spectrum (180 - 880 nm) over about 100 orders. Approximately one third of the total spectrum could be measured simultaneously using a 576×384 pixel ICCD chip. The actual resolution of the measured spectra was about 20 000. The spectra were stored in a PC and evaluated with the help of a home-made software. The software includes a NIST atomic database and fit routines necessary for evaluation.

Results

Steel as well as aluminum samples were used for the first measurements. For example, Fig. 1 shows the spectrum from 240 - 880 nm of a standard steel sample. 73 spectral orders were detected simultaneously (n=100 to n=27). Fig 2 displays a section of the Echelle spectrum of an aluminum sample with 0.56 % Mg in 86th order. The spectrum was measured with one shot. Ar

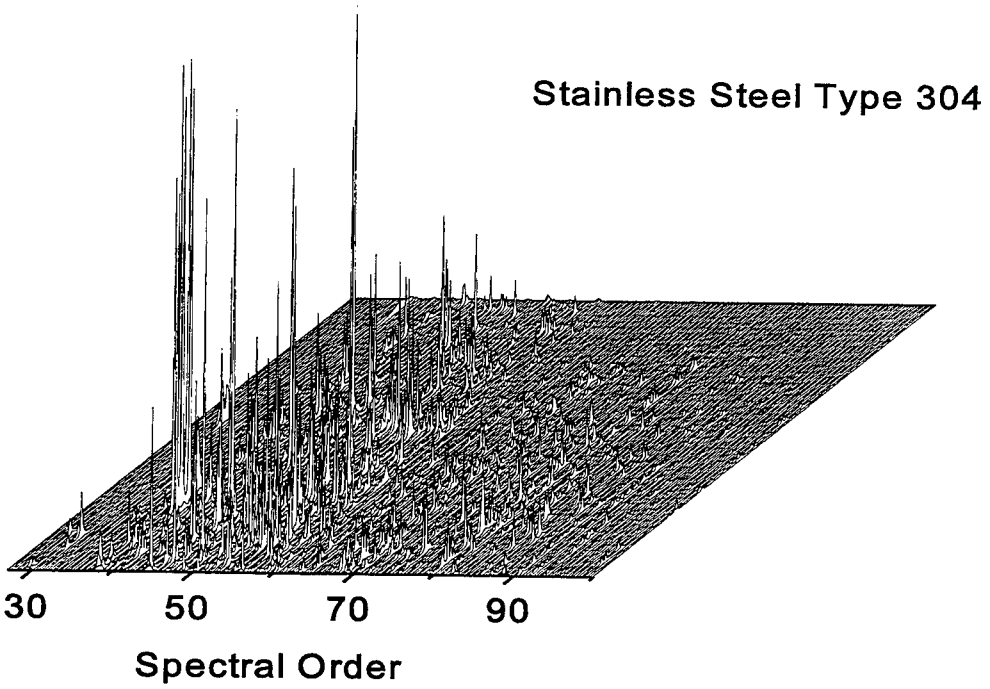

Fig. 1: Echelle spectrum of a standard steel sample measured with the ICCD camera.

was used as ambient gas (pressure: 1013 hPa). The line shown is the Mg(II) resonance line at 279.55 nm. The 3σ detection limit of Mg in Al with one laser shot was about 10 ppm. Taking into account the Al mass ablated with the shot (about 150 ng), the absolute detection limit was about 1 pg. This indicates the analytical power of LIBS with the Echelle/ICCD instrument. Complete analysis of Al with one laser shot were made taking into account major, minor and

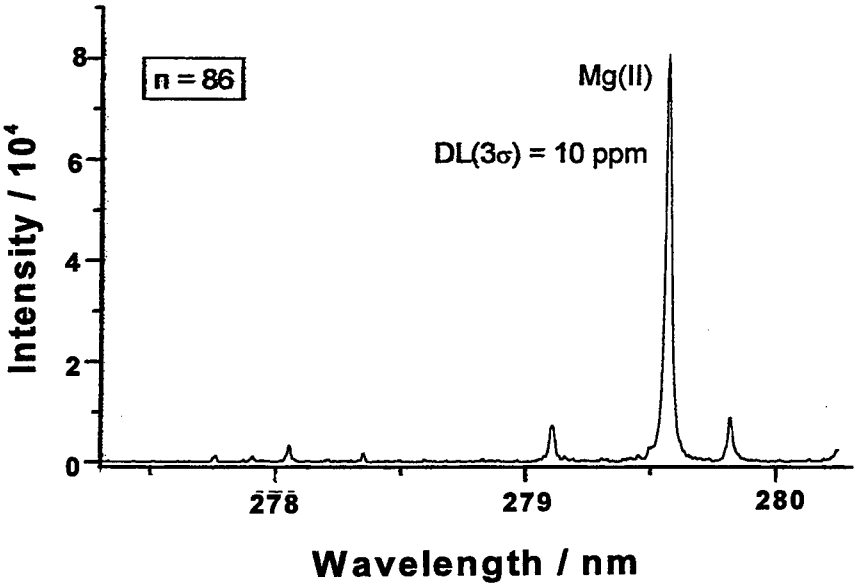

Fig. 2: Spectrum of the 86th order obtained with one laser shot on an Al sample (c_{Mg}: 0.54%).

trace elements. Typically eight different elements (total: about 99.95 %) could be measured simultaneously. It should be stressed that the analytical precision in single shot measurements is improved by taking into account all strong lines of a particular element. Furthermore, it is interesting to note that the plasma excitation temperatures from single shot spectra determined from the line intensities, the excitation energies and the relevant transition probabilties of different element by the Boltzmann plot technique agreed within the limits of uncertainty. Preliminary Echelle/ICCD measurements with the MIP [1] revealed significant improvements of the one shot detection limits in comparison with LIBS which is in agreement with earlier observations [2].

References

[1] J. Uebbing, A. Ciocan and K. Niemax, *Spectrochim.Acta* **47B** (1992) 601.

[2] A. Ciocan, J. Uebbing and K. Niemax, *Spectrochim.Acta* **47B** (1992) 611.

Single-Shot Laser-Induced Breakdown Spectroscopy (LIBS) of Energetic Materials

Edwin D. Lancaster, Kevin L. McNesby, Robert G. Daniel, and Andrzej W. Miziolek
U.S. Army Research laboratory
Aberdeen Proving Ground, MD 21005

The application of Laser-Induced Breakdown Spectroscopy (LIBS) is being investigated as a tool for the determination of energetic/explosive materials for a variety of applications.

LIBS is a very simple and straightforward technique requiring very little sample (pg to ng per LIBS event) and no preparation of the sample. It is possible to develop rugged and field-portable instrumentation since all of the components can and are being miniaturized. Each LIBS event produces a microplasma that is spectrally rich with atomic, ionic, and molecular fragment emissions characteristic of the chemical composition of the sample being irradiated. Traditionally, LIBS studies involve the analysis of metals using relatively narrow spectral ranges where a particular element emission occurs. However, in our laboratory LIBS is being explored in new ways as a means for the detection of energetic materials/explosives. We are exploring LIBS for its utility in the detection and identification of taggants, residues, and precursor materials.

A laser induced plasma is formed by focusing the pulse of a Nd:YAG laser to a fluence sufficient to produce ionization/breakdown of the compound of interest. Spectrochemical analysis based on the collection of the emission from atomic and molecular constituents occurs after the plasma continuum radiation decays (2-100 μsec). The full spectrum can be captured per single laser shot, and immediately analyzed by comparing to reference spectra of various explosives. With the powerful chemometric software it is possible to determine whether the LIBS spectrum is due to explosive particles or not. Through this technique it is possible to analyze single particles for energetic materials.

The following compounds are being studied by the LIBS technique:

Compound	Components
RDX	*1,3,5-trinitro-1,3,5-triazacyclohexane*
DMNA	*dimethylnitramine*
Comp A3	*91% RDX, 9% wax*
Comp B	*63% RDX, 36% TNT, 1% wax*
Comp C4	*91% RDX, 5.3% di(2-ethylhexyl)sebacate, 2.1% polyisobutylene, 1.6% motor oil*
Ammonium Nitrate - Prill	*purchased from Southern States*
LX-14	*95.5% HMX (1,3,5,7-tetranitro-1,3,5,7-tetrazacyclooctane), 4.5% Estane 5704-F1*
PBX 9502	*95% TATB (triaminotrinitrobenzene), 5% Kel-F 800*

Below are three emission spectra of compounds (RDX, Ammonium Nitrate, and Comp B) evaluated by LIBS. The detector was gated to allow the collection of emission spectra for 150 ns beginning 2 us after the plasma generation.

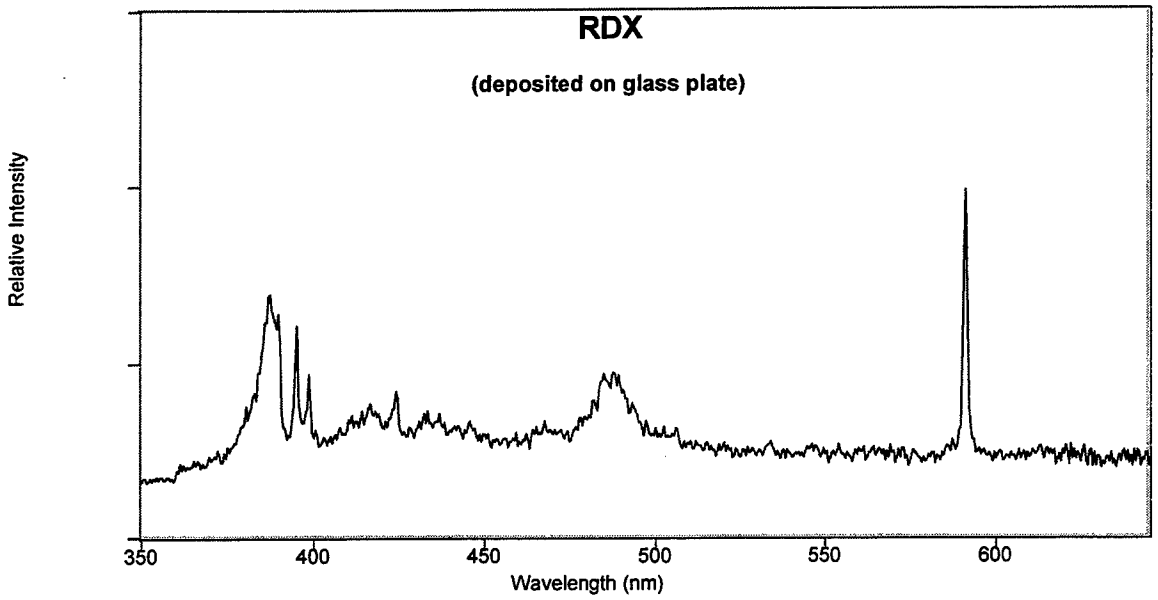

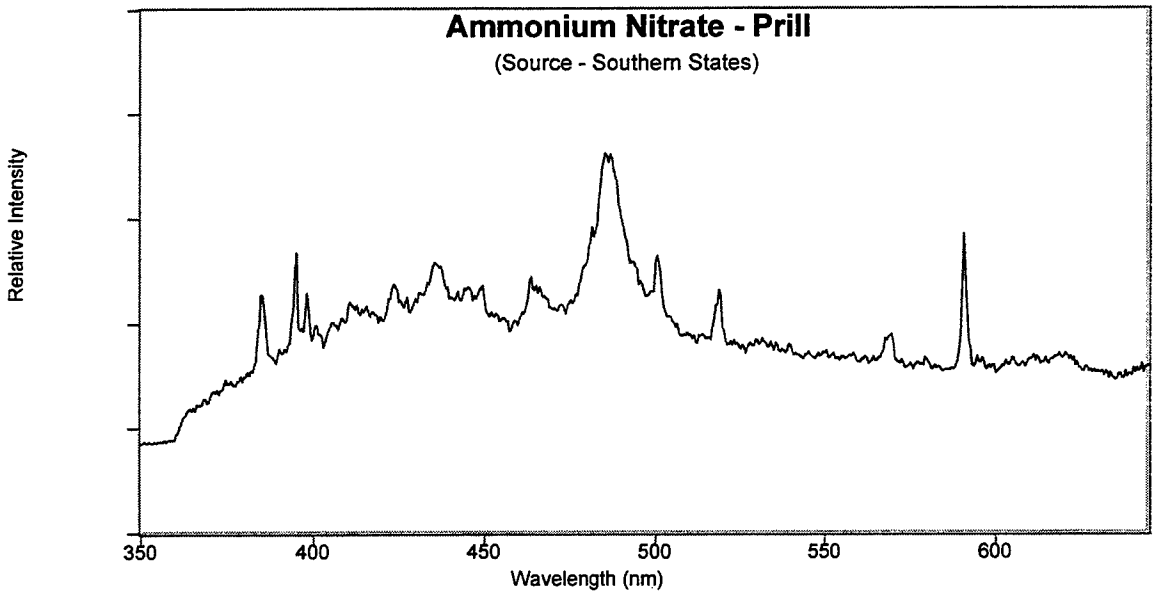

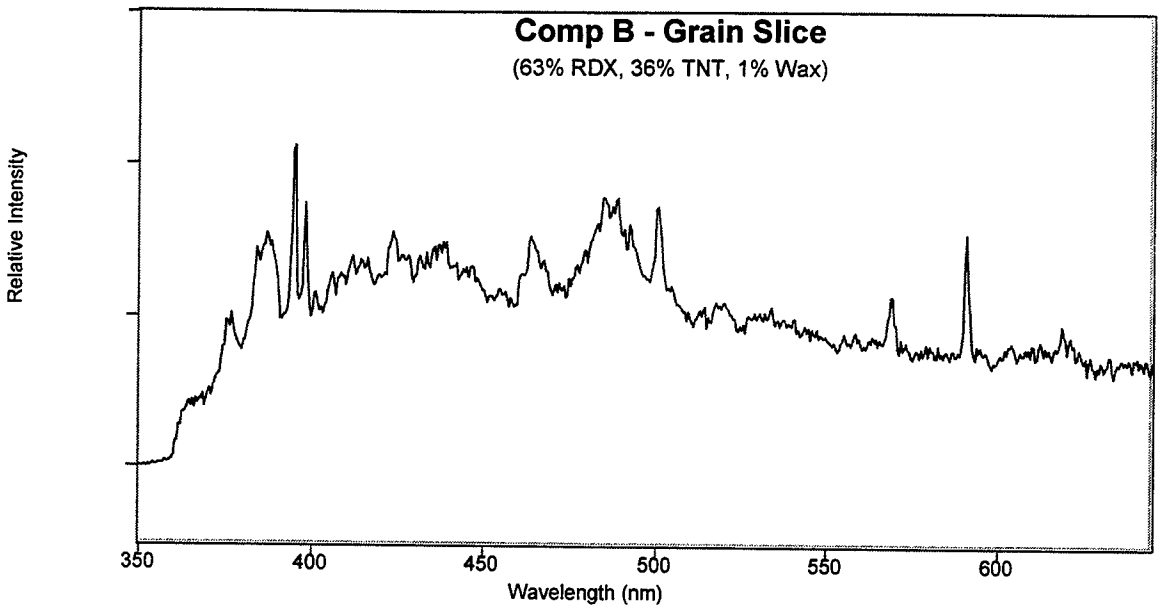

Single-shot LIBS spectra have been obtained for various energetic materials without any sample preparation. These spectra are rich with spectral signatures and are of sufficient quality to be useful for analysis. It is possible to develop methods utilizing this technique that will allow for the stand-off detection (up to 20 meters) of energetic materials. Since rapid screening of suspect areas are possible, This method would allow for the direct investigation of pre- and post- blast areas.

We are investigating the shot-to-shot variability within a given sample to verify the uniqueness of LIBS spectra for various members of the nitro-organic family. Also, we are determining whether single-shot LIBS spectra for composite materials are simple additives of each individual component.

A DIODE-LASER BASED RESONANCE IONIZATION MASS SPECTROMETER FOR SELECTIVE ULTRATRACE ANALYSIS

K. Wendt, K. Blaum, B.A. Bushaw[1], C. Geppert, P. Müller, W. Nörtershäuser, A. Schmitt, N. Trautmann[2] and B. Wiche

Institut für Physik, [2]Institut für Kernchemie, Universität Mainz, D-55099 Mainz, Germany
[1]Battelle Pacific Northwest Laboratories, P.O. Box 999, Richland, WA 99 352, USA
Tel: ++49-6131-39-2882, Fax: ++49-6131-39-2991, Email: Klaus.Wendt@UNI-MAINZ.DE

Resonance ionization mass spectrometry (RIMS) has become a widely used technique for isotope-selective ultra-trace analysis[1-4]. It provides complete isobaric suppression, high overall efficiency and strongly increased isotopic selectivity in respect to conventional mass spectrometers. Still a major drawback for the application of this technique is the complexity of the experimental set-up, particularly the laser system, which restricts utilization of the technique to a small number of university and research institutes so far.

Presently the rapid development and commercialization of diode-lasers and the combination with standard mass spectrometers can strongly reduce the experimental complications of RIMS and overcome the limitations mentioned. A refined diode-laser based resonance ionization mass spectrometer for highly selective ultra-trace analysis is presented, which combines coherent narrow-band multistep resonance ionization with a compact quadrupol mass spectrometer. Its advantages over existing conventional analytical instruments are demonstrated in the determination of trace and ultra-trace isotopes of calcium for cosmochemical studies, medical investigations and radiodating. Here, the general analytical requirements are: complete isobaric suppression, a maximum isotopic selectivity (isotopic abundance sensitivity) of up to 10^{15} for determination of the longest lived isotope ^{41}Ca ($t_{1/2}$= 1.03×10^5 a) and a good overall efficiency to enable studies of micro amounts. Furthermore a high precision and reliability in the determination of the isotopic ratios is mandatory.

Apart from the laser system, the actual analytical system is mainly consisting of the atomic beam oven and the quadrupole mass spectrometer, which have already been described in detail elsewhere[5]. We have in addition analyzed the performance of the quadrupol mass spectrometer (QMS) in respect to provide maximum isotopic abundance sensitivity in combination with high transmission. These extensive studies, carried out by ion trajectory simulations and comparison to experiment will be published separately[6], discussing the capabilities and limitations of the mass spectrometer system. By carefully optimizing the

working conditions concerning the location of ionization, the acceleration field and geometry and the parameters of the QMS rod system itself, isotopic abundance sensitivities of more than 10^8 of the pure QMS without selective optical ionization are demonstrated. This number is to be multiplied with the major contribution to isotopic (and isobaric) selectivity, stemming from the selective optical resonance ionization. Hence, the laser system has been specifically taylored to suit the requirements of coherent narrow-band multistep resonance excitation, which are discussed e.g. by Bushaw[5]. Laser line widths in the order of 1 MHz and comparable long term stability is mandatory and is realized by using tunable, continuous wave, extended-cavity diode lasers with active temperature and current stabilization and a computer controlled frequency stabilization and control system. The latter is constructed around a 300 MHz scanning spectrum analyzer through which the diode lasers are referenced to a stabilized He:Ne laser.

Three different excitation ladders in Ca I have been worked out. The schemes include single-, double- and triple-resonance excitation with subsequent non-resonant ionization from the corresponding highest excited state. The resonant excitation uses the individual steps of the $4s^2\ ^1S_0 \rightarrow 4s4p\ ^1P_1 \rightarrow 4s4d\ ^1D_2 \rightarrow 4snf\ ^1F_3$ ($n \approx 30$) excitation ladder[7]. Subsequently, non-resonant ionization from the low-lying and intermediate atomic states is achieved with the intensive uv (364 nm) or visible (514 nm) light from an existing Ar^+-laser. The first-step excitation at 422,7 nm requires frequency doubling of 855.4 nm diode laser light in a $KNbO_3$ crystal, placed inside an external resonance enhancement cavity. Apart from this, the single resonance excitation involves only the non-resonant uv ionization. This simple scheme already provides full isobaric but only very low isotopic selectivity of just about a factor of 10, restricted by the residual Doppler width of the optical resonance line. Furthermore, the efficiency is limited due to the low cross section of the non-resonant ionization process. Nevertheless, this simple scheme is well suited for precise measurements of isotope ratios, e.g. in cosmochemical studies, and for medical applications with stable tracer isotopes. Both the selectivity and efficiency is strongly increased by using one or two additional resonant excitation steps and, finally, by applying efficient infrared ionization with the 10.6 μm photons from a CO_2 laser. The necessary second and third steps are directly excited with the extended cavity diode laser light around 733 nm and 835 nm, respectively.

Recently, high resolution spectroscopical data on the isotope shifts and hyperfine structures of the two step resonant excitations $4s^2\ ^1S_0 \rightarrow 4s4p\ ^1P_1 \rightarrow 4s4d\ ^1D_2$ have been obtained for all stable isotopes. The line shapes and line widths, which govern the accessible optical selecitivy, are analyzed as a function of the experimental parameters. For this detailed theoretical understanding of the different coherent multi-step excitation processes the density matrix formalism is used and a complete theoretical description for the excitation and ionization processes involved is worked out. This approach results in a number of differential equations for the diagonal and off-diagonal elements of this matrix, which can be identified with the populations and coherences of the atomic levels concerned. The numerical solution of the strongly coupled system gives theoretical predictions for the ionization rates as a function of the experimental parameters of all laser fields involved, like laser power, laser line width and detuning. From the resulting complex peak shapes the optical selectivity and the efficiency can

be extracted for each individual excitation and ionization path. The theory perfectly reproduces and explains the experimental results and yields predictions for optical isotopic selectivities of maximum up to 10^{11} and ionization efficiencies of up to 5 %. A precise description of this approach will be given in the near future after completion of the corresponding experimental verification[8].

Analytical studies with the single- and double-resonance excitation schemes so far cover isotope ratio measurements in meteorite samples and blood as well as ^{41}Ca-determination for medical applications. They exhibit complete suppression of potassium and titanium isobaric interferences and confirm the expected precision in the determination of isotopic rations of about 2%[8]. Continuing work focusses on the spectroscopy as well as the refinement and final application of the full triple-resonance scheme for ultra selective low-level measurements of ^{41}Ca and shall establish resonance ionization mass-spectrometry as a competitive technology to accelerator mass spectrometry[9].

REFERENCES:

1. G.S. Hurst, M.G. Payne, S.D. Kramer, and J.P. Young, „Resonance ionization spectroscopy and one-atom detection", Rev. in Mod. Phys. 51(4), 767-819 (1979)
2. V.S. Lethokov, *Laser Photoionization Spectroscopy,* Academic Press, Orlando, 1987
3. G.S. Hurst and M.G. Payne, *Principles and Applications of Resonance Ionization Spectroscopy,* Hilger Publ., Bristol, 1988
4. M.G. Payne, L. Deng and N. Thonnard, „Applications of resonance ionzation mass spectrometry", Rev. Sci. Instrum. 65(8), 2433-2459 (1994)
5. B.A. Bushaw, „High-Resolution Laser-Induced Ionization Spectroscopy", Prog. Anal. Spec. 12, 247-276 (1989)
6. K. Blaum, P. Müller, W. Nörtershäuser, A. Schmitt, N. Trautmann and K. Wendt, „Ions going cracy - Optimizing a QMS", Int. Jour. of Mass. Spec and Ion Proc. to be published
7. B.A. Bushaw, F. Juston, W. Nörtershäuser, N. Trautmann, P. Voss-de Haan and K. Wendt, „Multiple Reosnance RIMS Measurements of Calcium Isotopes Using Diode Lasers", AIP Conference Proceedings 388, 115 (1997)
8. B.A. Bushaw, W. Nörtershäuser, P. Müller and K: Wendt, „Coherent narrow-band multistep resonance ionization in calcium, experiment and theory", to be published
9. D. Fink, J. Klein and R. Middleton, „^{41}Ca: past, present and future", Nucl. Instr. and Meth. in Phys. Res. B52, 572-582 (1990)

Isotope-Selective Analysis by Diode Laser Spectrometry

H.D. Wizemann[1] and K. Niemax[2]

[1]Institute of Physics, Universität Hohenheim, Garbenstraße 30, D-70599 Stuttgart, Germany. Phone: +49-711-459-2144 Fax:+49-711-459-2461
[2]Institute of Spectrochemistry and Applied Spectroscopy (ISAS), Bunsen-Kirchhoff-Straße 11, D-44139 Dortmund, Germany. Phone: +49-231-1392-101 Fax: +49-231-1392-310

Single-mode laser diodes of the etalon-type generate radiation of very narrow bandwidth, typically 0.04 nm, in the red and near-infrared wavelength range [1]. The linewidth of such diodes is considerably narrower than the line widths of free atoms in thermal atomizers, analytical flames, or plasmas. Therefore, these laser diodes are proper tools for analytical high-resolution laser spectroscopy. The necessary condition for high-resolution measurements is the atomization of the samples in low-pressure atmospheres ($\leq$ 10 hPa), where pressure broadening of the analyte lines is small and line broadening is dominated by the Doppler effect. If the shifts of spectral lines by the isotope effect are larger than the Doppler-widths of the individual components, the isotope composition of the elements can be measured by Doppler-limited laser spectroscopy. This is often sufficient for light and heavy elements, where large isotope line shifts occur due to the classical Bohr mass shift or due to the volume or field shift, respectively. For medium heavy elements the dominating contribution to isotope shift is the relatively small specific mass shift. This means in general, that for these elements Doppler-free spectroscopic methods are required, such as saturation spectroscopy or Doppler-free two photon excitation [2].
Exemplary analytical measurements of all the mentioned topics will be reported. A low-pressure electrothermal graphite furnace was used for the atomization of aqueous samples. Isotope-selective Doppler-limited diode laser atomic absorpion spectrometry was performed with lithium and lead as representatives of light and heavy elements, respectively. Rubidium stands for the medium heavy elements. Here, Doppler-free saturation spectroscopy was used because of the small isotopic shift. For each natural lithium and rubidium isotope the limits of detection were determined comparatively by two different modulation techniques, namely intensity modulation and wavelength modulation (table 1). Although atomization takes place at reduced pressure (1 - 10 hPa), the obtained limits of detection are comparable with or better than the results obtained with conventional hollow cathode graphite furnace atomic absorption spectrometry. In a further experiment two laser diodes were used to measure both naturally abundant lithium isotopes simultaneously (figure 1). This provides a better accuracy for the determination of isotope ratios.
Whereas resonance lines were used for the alkali elements, no transition from the groundstate is reachable for lead with commercial laser diodes, whether by use of the fundamental wavelength nor by use of the frequency-doubled radiation. Thus, the absorption measurements of the lead isotopes were performed in a FANES-cell (FANES: Furnace Atomic Non-Thermal Excitation Spectroscopy), a graphite tube furnace with integrated low-pressure dc discharge [3], using frequency-doubled laser

Table 1. Limits of detection (3σ) for Li and Rb obtained by intensity modulation (IM) and 2f-wavelength modulation (WM)

Isotope	IM	AM
^{6}Li	550 pg/ml	29 pg/ml
^{7}Li	220 pg/ml	11 pg/ml
^{85}Rb	140 pg/ml	790 pg/ml
^{87}Rb	130 pg/ml	860 pg/ml

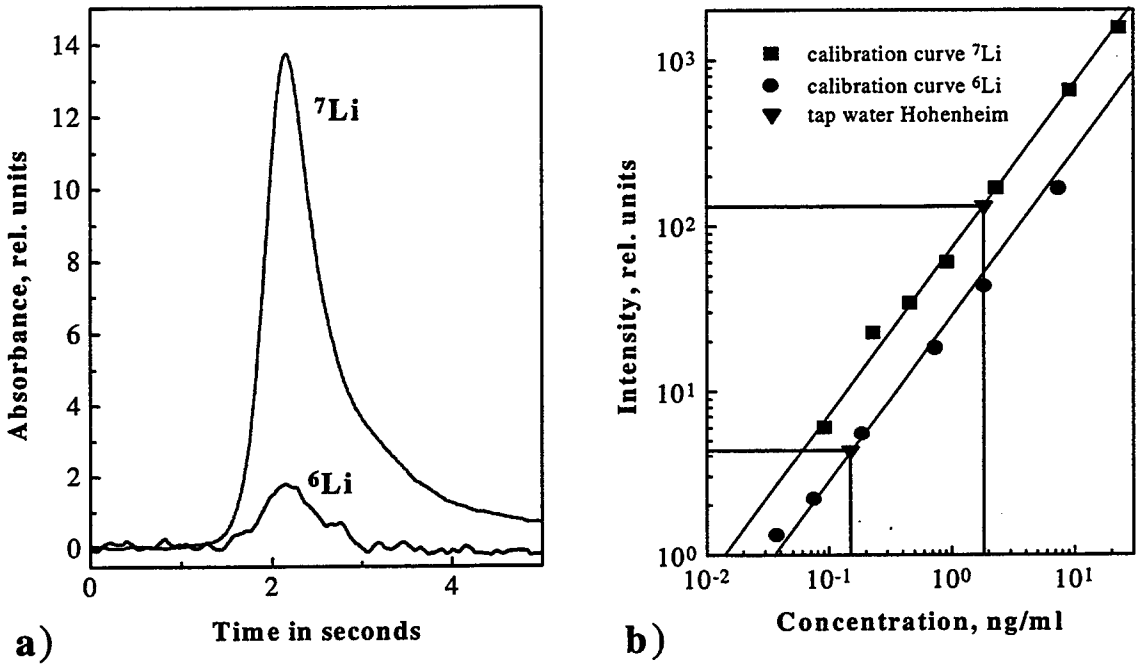

Figure 1. a) Simultaneously processed transient signals of the lithium isotopes in the tap water at Hohenheim. b) Evaluation of the measured concentrations with a calibration curve.

diode radiation. In the course of these experiments we demonstrated the application of the isotope dilution technique to calibrate measurements in analytical diode laser spectroscopy, the major advantage of isotope selective diode laser spectrometry [4]. Furthermore, it was demonstrated by addition of salt to the aqueous samples, that isotope dilution is also an effective technique for optical spectrochemistry to minimize or cancel severe matrix effects.

A possibility to obtain better isotope selectivity is the application of Doppler-free two photon excitation. The technique was tested with lithium, where the first laser diode saturated the resonance transition (2s → 2p) and a second laser diode probed the 2p → 3s transition. In preliminary experiments performed in a low pressure graphite furnace different applications of intensity and wavelength modulation were compared to get best sensivity. A 3σ detection limit for ^{7}Li better than 90 pg/ml was found.

The results indicate that isotope-selective diode laser atomic absorption spectrometry can be a powerful technique in isotope selective element analysis and in the

determination of isotope ratios. Severe physical and chemical matrix effects can be minimized because of the applicability of the isotope dilution technique. This allows accurate element analysis in all spectrochemical atomizers. The forced development of green and blue laser diodes will increase the number of elements which can be probed effectively by laser diodes.

[1] Franzke,J.; Schnell,A.; Niemax,K. *Spectrochim. Acta Rev.* **1993**, *15* , 379
[2] Demtröder,W. *Laser Spectroscopy*; Springer Verlag, Berlin, 1981
[3] Falk,H.; Hoffmann,E.; Lüdke,Ch. *Prog. Anal. Spectrosc.* **1988**, *11*, 417
[4] Wizemann,H.D.; Niemax,K. *Anal. Chem.* accepted for publication

Laser Applications to Chemical and Environmental Analysis

Environmental Applications: 2

Tuesday, March 10, 1998

Jay B. Jeffries, SRI International Inc.
Presider

LTuD
4:00pm–5:30pm
Coral Room

Feasibility Study of On-line Detection of Sulphuric Acid Aerosols in the Atmosphere by Laser Photofragmentation and Plasma Spectroscopy

M. Hidalgo Nuñez, P. Cavalli, G.A. Petrucci and N. Omenetto

European Commission, Joint Research Centre, Environment Institute, 21020 Ispra (Varese), Italy
Phone: +39-332-789801; FAX: +39-332-789210; e-mail: nicolo.omenetto@ei.jrc.it

SUMMARY

A major interest of our Institute lies in the study of the atmospheric sulphur cycle and in the oxidation mechanism(s) of Dimethylsulfide (DMS) in air. DMS originates from the ocean biota and its crucial role in the formation of atmospheric aerosols is well-documented (1,2). When DMS is oxidized, it generates SO_2 that can be further oxidized to H_2SO_4, inducing the production and growth of new aerosol particles that can act as cloud condensation nuclei and affect the Earth's albedo (2). The possibility of detecting sulphuric acid aerosols with laser excitation has been discussed, to the best of our knowledge, only in one paper (3), where the aerosols generated by mixing SO_3 and H_2O were addressed with laser photons at 193 nm. The resulting broadband emission was attributed to sulphuric acid and was similar to the emission spectrum of gaseous SO_2.

A very similar emission spectrum was observed (4) by direct nebulization of aqueous sulphuric acid solutions at different concentrations and excitation of the resulting aerosols with 193 nm photons from an ArF excimer laser. It was found, however, that this mode of aerosol generation was not reproducible. In fact, a relation between the intensity of the emission signal and the acid concentration in the solution could not be established in any meaningful way, mainly because of the inconstant environment (in terms of humidity and temperature). Another approach was then followed, that is, the generation of sulphuric acid aerosols by homogeneous nucleation (5). In this case, a small amount of vapour is swept into a particle-free air stream and then allowed to condense in small

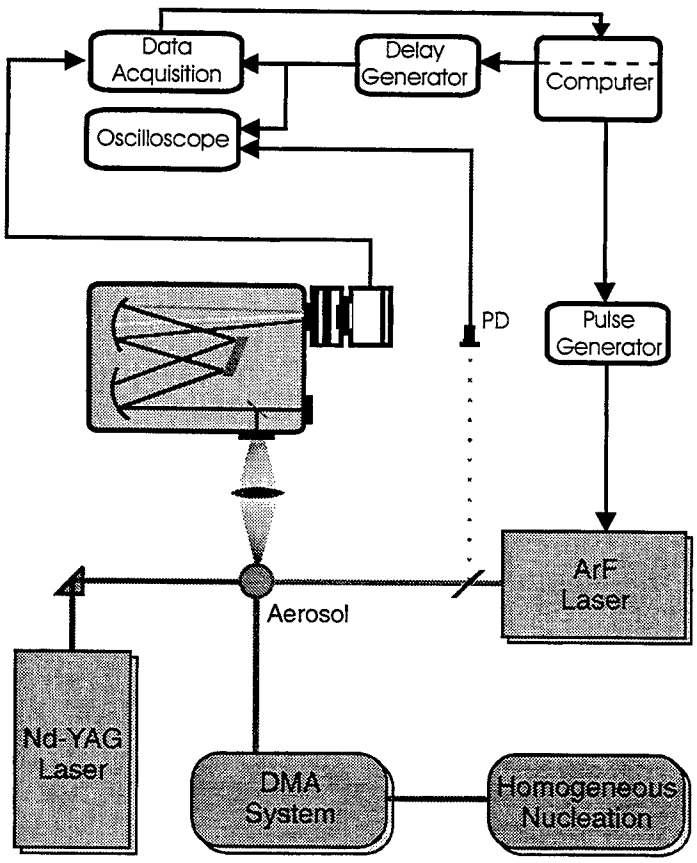

Figure 1. Experimental setup.

droplets, resulting in the formation of homogeneously grown particles. The general experimental setup is shown in Figure 1. The resulting emission spectrum was similar to that obtained with the nebulization of aqueous sulphuric acid solution, but was much more reproducible. To obtain the total mass of sulphuric acid contained in the aerosol generated, a Differential Mobility Analyzer (DMA) was used. This has the advantage of giving not only the mass, but also the size distribution of the particles generated.

Even though this system could be successfully operated, the sensitivity was not sufficient. In addition, since the broadband emission lies in the blue region, it is difficult to avoid completely extraneous fluorescence from optical components, which also occurs in the blue under 193 nm excitation. It was then decided to attempt Laser Spark Emission Spectroscopy. This can be done by focusing the beam from a Nd:YAG laser (1.064 μm) into the aerosol and monitoring the resulting emission from atomic sulphur around 180 nm. The optical path between the spark and the spectrometer, as well as the spectrometer itself, was purged continuously with nitrogen. The results obtained were encouraging. A linear relationship (see Figure 2) was repeatedly obtained (on different days and for independent aerosol generation events) between the peak of the emission line at 1806.65 Å and the mass of sulphuric acid, calculated as the integral under the size distribution obtained with the DMA. The spectral background in this wavelength region is such than the limit of detection, calculated as the concentration resulting in a signal-to-root-mean-square-background noise of 3, is 6 ng ml^{-1} of air.

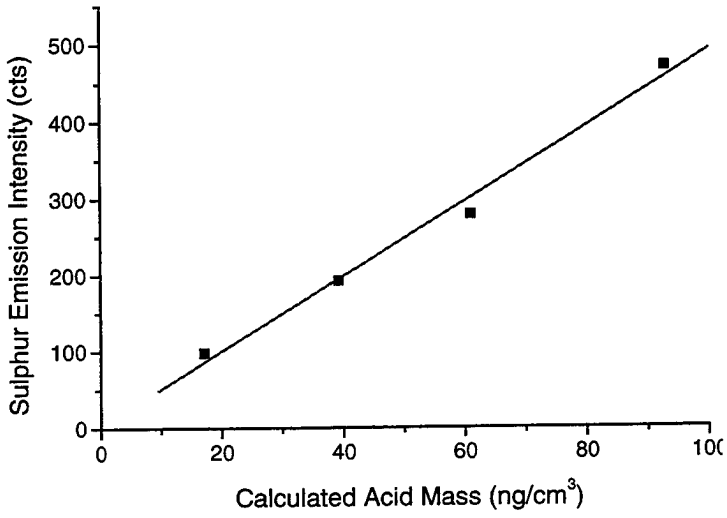

Figure 2. Calibration curve obtained for Laser Spark Emission of H_2SO_4 aerosols produced by homogeneous nucleation.

An independent, interesting approach was also found during the course of these studies. The idea consists in the possibility of measuring sulphuric acid indirectly, i.e., by taking advantage of the depressive effect that the presence of sulphuric acid has on the sodium emission resulting from the photofragmentation of sodium hydroxide aerosols. We have found that, when 193 nm photons are mildly focussed on sodium compounds (NaCl, NaOH, Na_2SO_4) in the form of aerosols, even without forming a plasma (pre-breakdown conditions), an intense emission from atomic sodium is observed, due to instantaneous vaporization and photofragmentation of the molecular species. This has already been reported in the literature (see, for example, Ref. 6). The interesting outcome is that the sodium signal resulting from the photofragmentation of NaOH is about 10 times greater than that due to Na_2SO_4, which can be attributed to the difference in the relevant thermochemical constants (7). This fact has led us to hypothesize that sulphuric acid aerosols, reacting with NaOH aerosols, would form Na_2SO_4 aerosols, therefore leading to a significant decrease in the sodium emission. To prove this, increasing amounts of

H_2SO_4 solution were added to a NaOH solution, which was nebulized and continuously monitored for sodium emission. This is borne out experimentally in Figure 3. A simple calculation shows that the limit of detection that can be obtained by this method for sulphuric acid aerosols is of the order of 10 ppb H_2SO_4 per minute of collection time of the aerosol into a solution of NaOH at a given low concentration, which is continuously nebulized and interrogated by the focussed excimer laser beam.

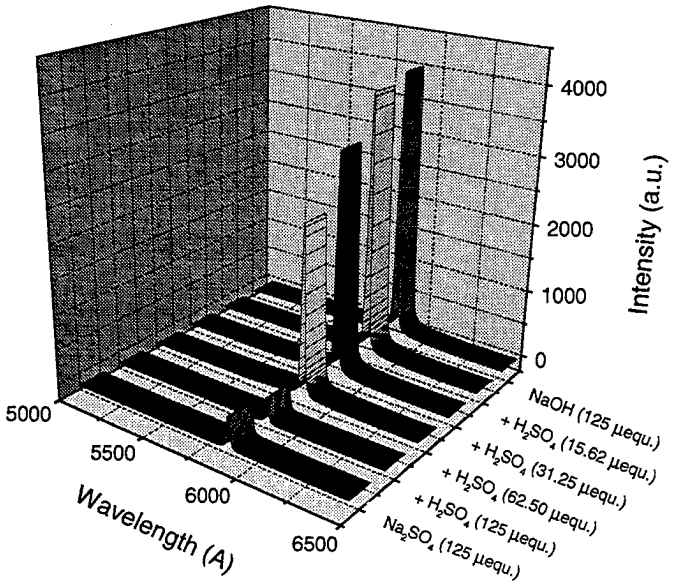

Figure 3. Decrease of Na atomic emission after conversion of NaOH to Na_2SO_4 by reaction with sulphuric acid.

Work is still in progress to better quantify these methods. In all the cases illustrated, the laser techniques have the significant advantage of providing on-line detection capabilities at a level which is considered to be adequate for the direct study of many simulated (e.g., Teflon bag) atmospheric reactions leading to the formation of sulphuric acid aerosols.

REFERENCES

1. G.S. Tyndall and A.R. Ravishankara, Int. J. Chem. Kin., 23, 483 (1991).
2. F. Raes, J. Wilson and R. Van Dingenen, in "Aerosol Forcing of Climate," R.J. Charslon and J. Heintzenberg, Eds., Jophn Wiley and Sons, New York (1995).
3. Y.G. Yin, H.C. Zhou, M. Suto and L.C. Lee, J. Photochem. Photobiol. A, 52, 255 (1990).
4. N. Omenetto, P. Cavalli, M. Hidalgo and G.A. Petrucci, Ann. Chim., 87, 241 (1997).
5. R. Niessner and D. Klockow, Anal. Chem., 52, 594 (1980).
6. N. Cheung, E.S. Yeung, Appl. Spectrosc., 47, 882 (1993).
7. R.C. Oldenborg and S.L. Baughcum, . Chem., 58, 1430 (1986).

Application of LIBS to Monitor Compositions for Plant Control

Yoshihiro DEGUCHI , Seiji IWASAKI,
MITSUBISHI HEAVY INDUSTRIES, LTD., Nagasaki R & D Center, Applied Physics Lab.,
5-717-1, Fukahori-Machi Nagasaki 851-03, Japan, tell: 0598-34-2321, fax: 0958-34-2345

Naohiko ISHIBASHI,
MITSUBISHI HEAVY INDUSTRIES, LTD., Hiroshima Machinery Works, Steel Manufacturing Machinery Designing Department, Electrical & Automatic Control Equipment Section, 6-22, 4-chome, Kan-No-Shin-Machi, Nishi-ku, Hiroshima, 733, Japan, tell: 082-291-2187, fax: 082-294-0952

1. Introduction

It has become more and more important to monitor the condition of material to cope with environmental disruption and improve the efficiency of industrial plants. As the situation now stands, the on-line monitoring techniques of plant controlling factors are necessary to enhance the control ability of the overall operation of industrial plants.

Because of its strong signal intensity and simplicity of its apparatus, laser induced breakdown spectroscopy (LIBS) is suitable for material composition measurement for the plant control[1),2,3)]. The delection limit can be enhanced combining LIBS and LIF. In this study LIBS has been applied to several fields such as fry ash, alkali metals and cement raw material composition measurements.

2. Experimental Apparatus and Signal Processing

A LIBS analyzer, which was developed by MHI for the plant application, is shown in Figure 1.A laser beam is focused into a small area and makes a hot plasma. The atomized material emits the emission attributed to the material contents. This signal is a function of material components and plasma temperature. In this study several emission lines, which are emitted from the same atom but from the different energy levels, are used to correct the temperature effects in LIBS signal. A typical LIBS signal is shown in Fig. 2. A monochrometer with two gratings was used to detect different (high and low) resolution LIBS spectra at the same time. Fig 3 shows the ratio of LIBS signal of Si and Ca in $CaSiO_3$ particles with and without temperature correction. The stability of the signal is much improved using the temperature correction method.

3. Application

3.1 Pulverized Coal and Fry Ash Particles

The unburned carbon control of the fry ash is necessary for the better operation and the utilization of the fry ash itself in the coal thermal power plants. Figure 4 shows the comparison between the unburned carbon amount in fry ash and the LIBS signal ratio of C and Si. The LIBS signal has a good relationship with the unburned carbon in fry ash measured by the conventional method. LIBS has an ability to detect the main composition of the ash and this can expand its application to different types of the coal combustion fields.

3.2 Alkali Metals

Alkali metals such as Na and K are the cause of the corrosion and deposition in power generation turbines. The ppb-ppt level detection is required for the safety regulation. The normal LIBS has a detection limit around ppm-ppb and its enhancement will be necessary for the power plant application. A tunable laser was added to excite the Na and K after the LIBS process. The detection of Na and K in water was performed and the results are shown in Figure 5. They show the good linearity between the LIBS/LIF signal and the contents of Na and K. The arrow in the figure shows the LIBS detection limit without the LIF process. LIBS/LIF can enhance the signal intensity by 1-2 orders of magnitude. The ppt level detection can be possible by improving the efficiency of the experimental conditions. In the gaseous condition the detection limit will be much better because of the less quenching affection.

3.3 Application to Cement Materials

The LIBS analyzer was automated and tested in the plant field. Emission signals by Ca, Si, Al, and Fe components, which are the main controlling factors of the cement plants, have been detected and analyzed using the plasma temperature correction method. Stability $2\sigma < 1\%$ in each composition was achieved in the same cement material sample in the laboratory experiment. This analyzer was applied to the plant field for a month and the results were compared with the conventional X-ray analyzer (see Figure 6). These two results show a good agreement. The LIBS analyzer has an on-line measurement ability (LIBS:a minute, X-ray:30 minutes) and will make a significant contribution for the quality control systems in cement plants.

4. Conclusion

LIBS was applied to the several materials and its applicability was tested in the plant field. It shows the better characteristics in the on-line ability and sensitivity compared to the conventional method. Combining with the solid state laser technology, it will overcome the conventional methods in various fields to control the plant performance.

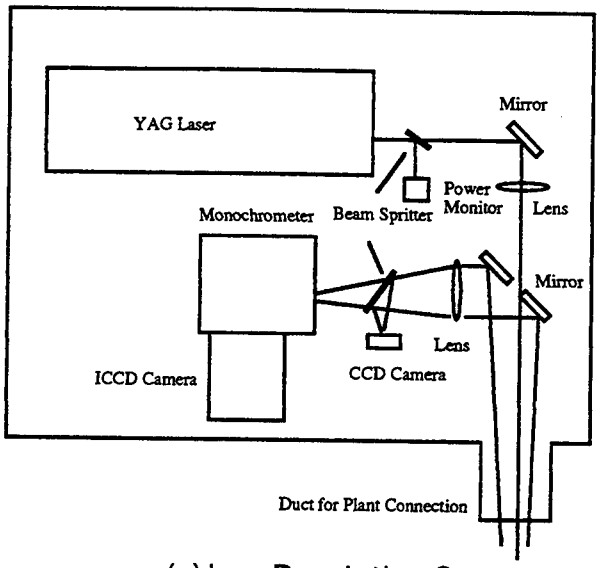

(a) Low Resolution Spectrum

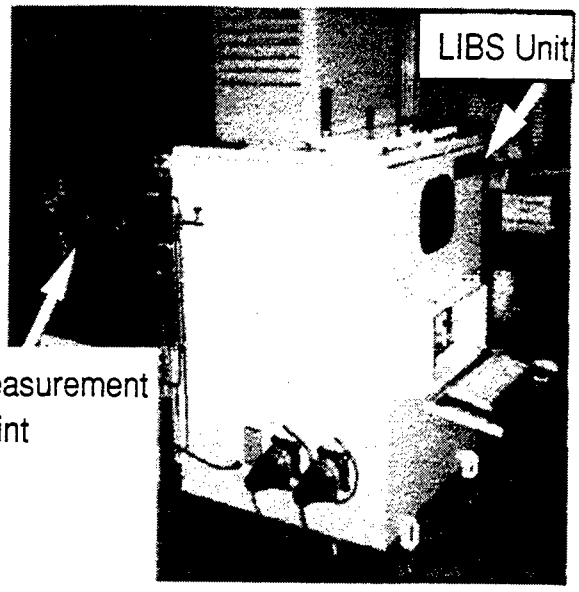

(b) Picture of LIBS Unit

Figure 1 LIBS Unit

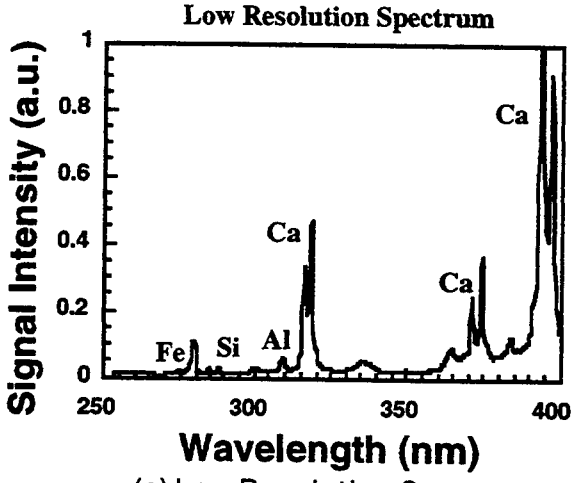

(a) Low Resolution Spectrum

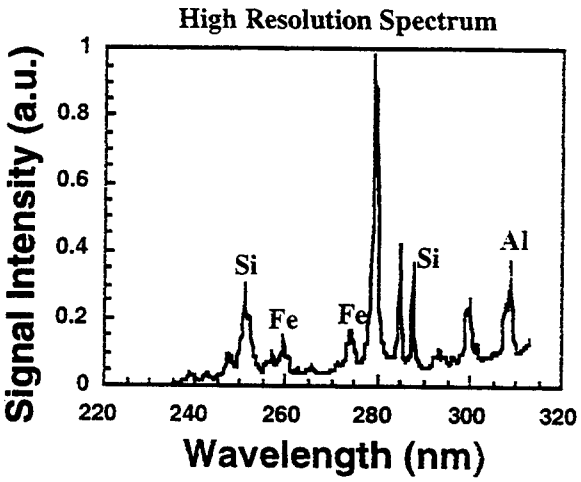

(b) High Resolution Spectrum

Figure 2 LIBS Spectra

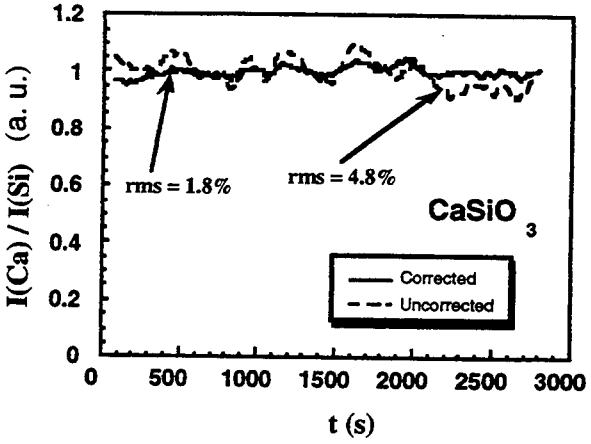

Figure 3 Plasma Temperature Correction

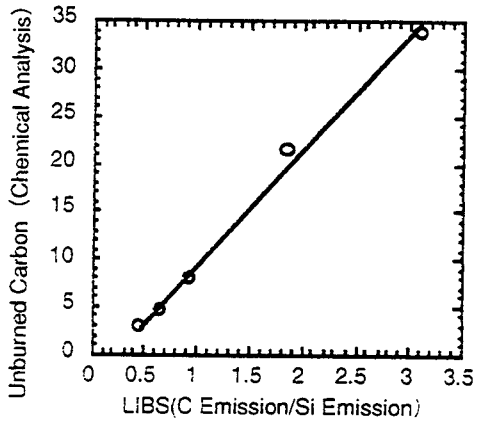

Figure 4 Comparison of Unburned Carbon in Fry Ash to LIBS Signal

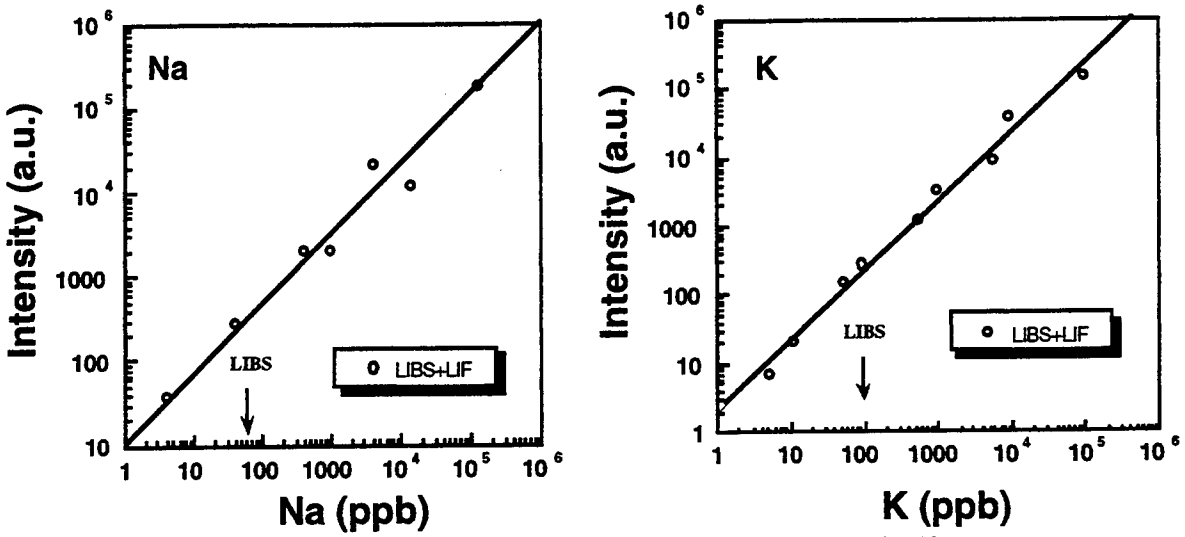

(a) Na (b) K

Figure 5 Alkali Metal Detection Using LIBS/LIF

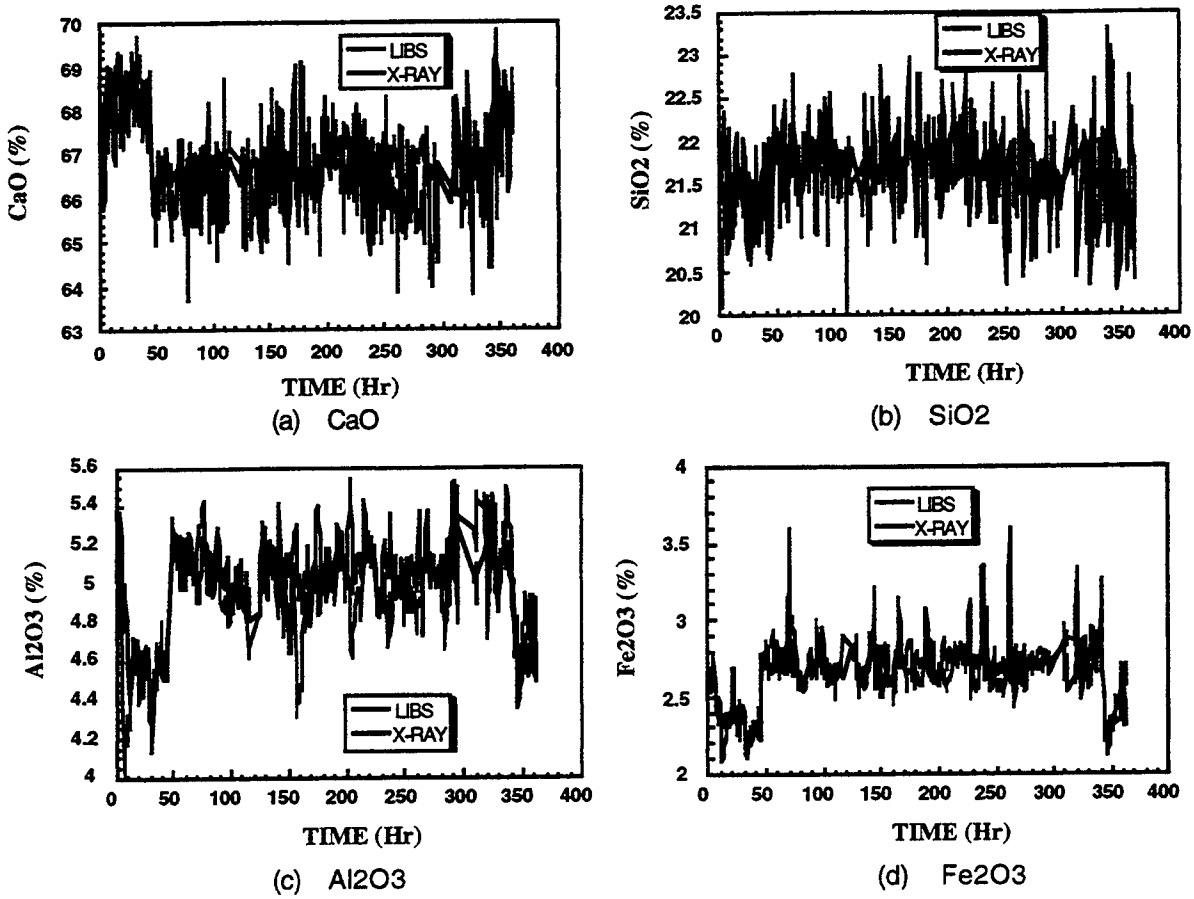

(a) CaO (b) SiO2

(c) Al2O3 (d) Fe2O3

Figure 6 Cement Material Composition Measurement

References

1) Ottensen D.K., et. al., Energy & Fuels VOL.5,NO.2 P.304, 1991.
2) Peng L.W., et. al., Process Control Qual., VOL.7, NO.1, P.39,1995
3) Rensberger Weiland K.J., et. al., Applied Optics, Vol.32, NO.21, p.4066, 1993

Toxic Multi-Metal Continuous Emission Monitoring by Laser-Induced Breakdown Spectroscopy

Hansheng Zhang, Fang-Yu Yueh and Jagdish P. Singh
Diagnostic Instrumentation and Analysis Laboratory
Mississippi State University, P.O. Drawer MM, Mississippi State , MS 39762-5932
Singh@DIAL.MSSTATE.EDU

SUMMARY

Laser-induced breakdown spectroscopy (LIBS) is a laser-based, advanced diagnostic technique for measuring the concentration of various elements in the test medium.[1-3] In LIBS, a pulsed laser beam is focused at the test point to produce a spark. The spark in the focal region generates a high density plasma which atomizes and electronically excites the various atomic elements in the test volume. Atomic emission from the plasma is collected and analyzed to obtained the concentration of the atomic species in the test medium.

Toxic metal emissions from various waste-processing off-gas systems represent a significant health hazard. The real-time measurement of selected toxic metals in smoke stack emissions would be useful in order to control the quantities of these species emitted into the atmosphere. LIBS is currently being evaluated as a near real-time measurement technique for monitoring the concentration of metal species in the off-gases from waste- processing facilities.[4,5] In the present paper, the results of recent LIBS measurements at the U.S. Environmental Protection Agency (EPA)'s Environmental Research Center, Research Triangle Park, North Carolina, are presented.

The experimental arrangement of the LIBS system is described in Reference 3 and is shown in Figure 1. A frequency-doubled Nd:YAG laser was focused by an ultraviolet (UV) grade quartz lens of 300 mm focal length was to produce the spark. The same lens was also used to collect light from the laser induced spark. Two UV-grade quartz lenses of focal length 100 mm and 50 mm were used to couple the LIBS signal into an optical fiber bundle. The other end of the fibler was coupled to a spectrograph. The spectrograph was equipped with 1200 and 2400 line/mm diffraction gratings of dimensions 75 mm x 75 mm. A 1024-element intensified diode array detector with a pixel width of 0.022 mm was used to detect the light from the laser spark. The detector was used in a gated mode and was synchronized to the laser output. To maximize the signal, a gate pulse delay of 5-10 μsec and width of 10 to 20 μsec were used in most of the work. The spectral window monitored by the array was 19 nm wide with a resolution of 0.16 nm with the 2400 line/mm grating. Data acquisition and analysis were performed using a notebook computer. A user-written macro program was employed to analyze and display the data in near real-time.

The tests were conducted using a simulated flue gas stream produced by the EPA Rotary Kiln Incinerator Simulator (RKIS).[6] The hot flue gas was spiked both by injecting particulates and by injecting an aqueous metals feed solution of appropriate concentration. The flue gas conditions at the location of the RM and multi-metal CEM sampling ports are discussed on reference 6. The LIBS system was calibrated for all toxic, volatile metals (As, Be, Cd, Cr, Co, Hg, Mn, Ni, Pb, and Sb) with an ultrasonic nebulizer system at the DIAL laboratory. The calibration was based on the peak area of each selected analyte line. The peak area, or peak height, of the analyte lines from the test LIBS spectra were normalized using the calibration factor to obtain metal concentrations.

The concentration of Be, and Cr were sucessfully measured in all the tested metal levels. The concentration of Cd was measured in the medium and high metal tests. Pb concentration was

measured in the high concentration test. The LIBS system was not able to monitor Sb and Hg in this test due to fact that the target concentrations were below the LIBS detection limit. The concentrations of Be, Cr, Cd and Pb were inferred from LIBS spectra recorded in the 230 and 420 nm spectral regions. The results of LIBS measurement at the three metal concentrations have been compared with the results from the RM, and are summaried in Table I.

In the low metal concentration test, although Pb and Cd lines were monitored during the low metal concentration test, the results of the analysis of these two metals were not reliable due to (1.) spectral interference and (2.) a target concentration near the LIBS detection limit. Concentrations of Cr, Y, and Be were successfully measured during the test.

In the medium metal concentration test, Cr, Cd, Be and Y were monitored using two spectral regions. Each spectral region was monitored for ~20 - 40 minute during EPA sampling. The real-time LIBS data clearly shown that the metal concentrations gradually increased during the first half hour of the test after the metal injection. The metal concentration quickly dropped to zero when metal injection was stopped. The metal concentration level was found more stable during the later part of the test.

During the high metal concentration test, LIBS system was the first CEM to detect the injected ash and the metal levels were all below specifications in the beginning of the test. The facility operator was informed of the problem. It took some 20 minutes before the problem was really recognized by the facility monitors which was then corrected immediately. Cd, Be, Cr and Pb were sucessfully measured after the facility problem was corrected. This incident shows the importance and need for real-time, on-line CEM operation.

The LIBS system was sucessfully used to monitor concentrations of selected toxic metals in near real-time under field-simulated conditions. Althought, the present LIBS system can only be used as a CEM to monitor concentrations of Be, Cr, Cd and Pb, its capability to provide instant indication of system problems has been well-demonstrated by this test. Further work on improving the detection limits of Pb, Hg, As and Sb will continue.

REFERENCES

1. L.J. Radziemski, and D.A. Cremers, "Spectrochemical Analysis Using Plasma Excitation", in *Laser Induced Plasmas and Applications,* L.J. Radziemski, and D.A. Cremers, Eds. (Marcel Dekker, New York, NY, 1989), Chap. 7, p. 295-325.
2. J.P. Singh, H. Zhang, F.Y. Yueh, and K.P. Carney, "Investigation of the Effects of Atomspheric Conditions on the Quantification of Metal Hydrides using Laser Induced Breakdown Spectroscopy", Appl. Spectrosc. 50, 764-773 (1996).
3. H. Zhang, J.P. Singh, F.Y. Yueh and R.L. Cook, "Laser Induced Breakdown Spectra in a Coal-Fired MHD Facility", Appl. Spectrosc. **49**, 1617-1623 (1995).
4. W.L. Flower, L.W. Peng, N.B. French, H.A. Johnson and D.K. Ottesen, "A Laser- Based Technique for Continuously Monitoring Metal Emissions from Thermal Waste Treatment Units", Proceedings of International Incineration Conference, Houston, Texas, May 9-13, 1994, pp.73-76.
5. J.P. Singh, F.Y. Yueh H. Zhang, and R.L. Cook, "Laser Induced Breakdown Spectroscopy as a Process monitor and control for Hazardous Waste Remediation", Process Control and Quality 249, xxx (1997).
6. "Final Report for Performance Testing of Multi-Metal Continuous Emissions Monitor", Ames Laboratory, Iowa (1996).

Table I. Comparison of the results of LIBS and RM. [a,b]

Date	Test	Be(LIBS)	Be (RM)	Cd(LIBS)	Cd(RM)	Cr(LIBS)	Cr(RM)	Pb(LIBS)	Pb(RM)	Y(LIBS)	Y(RM)
4/22/96	1	38.2	50.0			69.7	65.7			66.9	100
4/22/96	2	39.0	61.6			43.7	61.0			27.3	119
4/22/96	3	41.9	55.2			31.0	56.9			24.4	110
4/22/96	4	40.3	53.8			29.3	52.3			85.0	105
4/22/96	5	32.8	47.7			30.9	47.2			68.8	92.2
	RA	**38%**				**53%**				**89%**	
4/24/96	1	29.2	14.5			22.6	19.0			202.6	115
4/24/96	2	20.1	12.8			17.0	20.1			133.4	99.8
4/24/96	3	33.0	12.3			16.8	19.8			108.3	97.2
4/24/96	4	42.3	11.0			15.4	13.7			96.1	91.7
	RA	**273%**				**31%**				**93%**	
4/25/96	1	73.8	52.1	55.8	45.5	17.5	33.0			108.6	110
4/25/96	2	65.7	52.6	52.4	46.0	27.7	38.1			100.5	114
4/25/96	3	45.5	51.6		43.8	18.5	35.0			55.4	112
	RA	**86%**		**73%**		**61%**				**86%**	
4/26/96	1	103	272		356	197	176	275	375		
4/26/96	2	490	474	631	447	276	180	536	458		
4/26/96	3	526	436	554	377	299	153	608	375		
4/26/96	4		509		441	236	169	488	446		
4/26/96	5	398	549	534	500	272	216	540	489		
	RA	**57%**		**77%**		**76%**		**49%**			

a. Analyte concentration are in ug/dscm
b. Relative Accuracies (RA) of the LIBS results are in bold type.

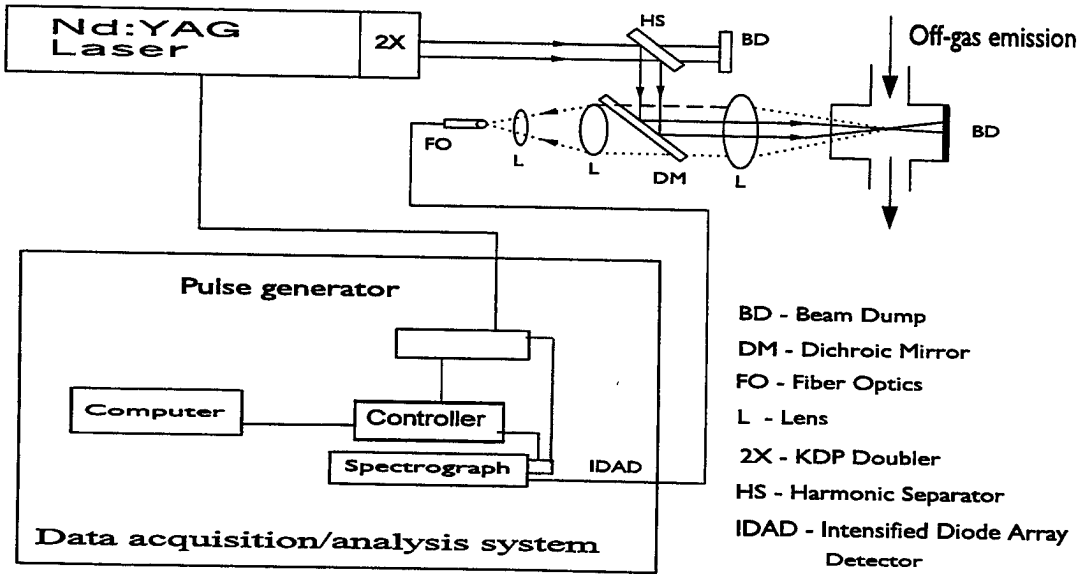

Figure 1. Experimental setup of laser-induced breakdown spectroscopy.

Real Time, *in Situ* Measurement of Aerosol Light Absorption with a New Photoacoustic Instrument: Quantification of Black and Elemental Carbon Aerosol

Hans Moosmüller
Desert Research Institute, P.O. Box 60220, Reno, NV 89506
Tel.: 702-677-3194, Fax: 702-677-3157, e-mail: hansm@sage.dri.edu

W. Patrick Arnott
Desert Research Institute, P.O. Box 60220, Reno, NV 89506
Tel.: 702-677-3123, Fax: 702-677-3157, e-mail: pat@sage.dri.edu

C. Fred Rogers
Desert Research Institute, P.O. Box 60220, Reno, NV 89506
Tel.: 702-677-3178, Fax: 702-677-3157, e-mail: fredr@sage.dri.edu

Abstract

A photoacoustic instrument has been developed to measure *in situ* light absorption by aerosol. The current lower detection limit for light absorption is 0.4 Mm^{-1} which corresponds to an elemental carbon mass density of ≈ 40 ng/m^3 assuming an efficiency for light absorption of 10 m^2/g. Calibration is performed using simple theory for the instrument along with use of a calibrated microphone and laser. Two compact, efficient lasers were used during instrument evaluation performed in the North Front Range Air Quality Study (Colorado, 1996/97). Laser wavelengths were 532 nm and 685 nm, and corresponding average powers were 60 mW and 87 mW. Nearby measurements of black and elemental carbon aerosol show good correlation with the photoacoustic measurement of aerosol light absorption and shed further light on the question of absorption efficiencies of black and elemental carbon aerosol.

Introduction

Black carbon aerosol is a common type of aerosol that strongly absorbs visible light. It has a significant graphitic carbon content, and is typically formed by incomplete combustion.[1] This aerosol negatively impacts visibility,[1] is a health hazard when inhaled,[2] and may alter the global radiation balance. A number of techniques have been devised to measure light absorption by aerosol. Many use the capture of aerosol on filters, followed by an optical measurement to determine aerosol light absorption. It may be desirable to measure aerosol light absorption by means that do not require the use of filters, are not influenced by aerosol and filter substrate scattering, and can observe the aerosol closer to its natural state. The photoacoustic technique is one method for doing this.[4] By taking advantage of technological innovation in laser efficiency and compactness, and applying photoacoustic ingenuity, we have built a useful photoacoustic instrument for aerosol light absorption measurement in most common field conditions.

The Photoacoustic Instrument

A schematic view of the photoacoustic instrument is shown in Figure 1. The principle of operation is as follows. The laser beam power is modulated at the acoustic resonance frequency of the photoacoustic resonator. Light absorbing components (gas or aerosol) convert laser beam power to an acoustic pressure wave through absorption induced gas expansion. A microphone detects the acoustic signal, and hence a measure of light absorption is produced. The

piezoelectric disk is used to determine the acoustic resonance frequency and the resonator quality factor (gain) to calibrate the system. Acoustic notch filters block most of the air-flow pump noise and spurious sound produced by absorption of light on the windows from entering the resonator. Holes for the laser beam (not shown) are placed at pressure nodes to minimize their coupling to the resonator mode.

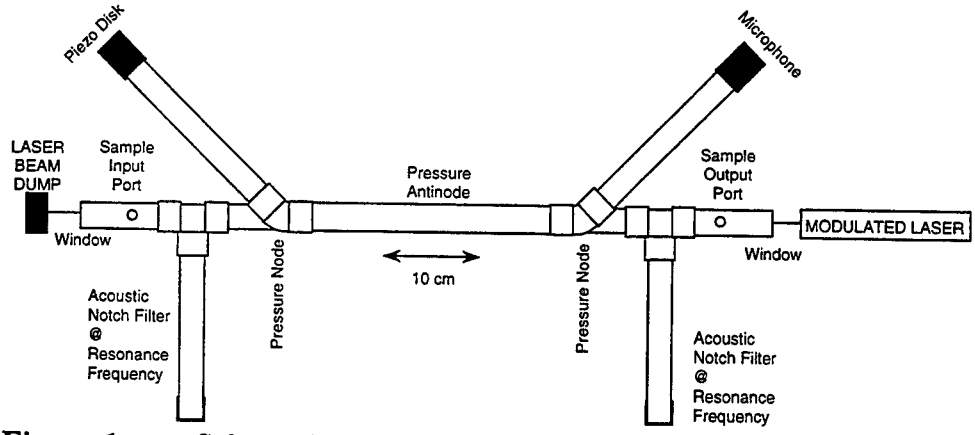

Figure 1. Schematic view of the prototype photoacoustic instrument.

Light absorption, B_{abs}, in dimensions of inverse distance, is determined from the acoustic pressure P_m, measured with the (calibrated) microphone and corrected for preamplifier gain; resonator quality factor Q; resonance frequency f_0; the Fourier component of laser beam power P_L at f_0; and resonator cross sectional area A_{res}. The expression for B_{abs} is

$$B_{abs} = P_m \frac{1}{P_L} \frac{A_{res}}{\gamma - 1} \frac{\pi^2 f_0}{Q} ,$$

where $\gamma = 1.4$ is the ratio of isobaric and isochoric specific heats for air. Typical instrumental values were P_L = 50 mW to 105 mW, A_{res} = 5.07 cm^2, f_0 = 500 Hz, and Q = 80. The photoacoustic coefficient for the resonator from Eq. (1) is $P_m (P_L B_{abs})^{-1}$ = 12.8 Pa $(W m^{-1})^{-1}$. The broadband acoustic and electronic noise combined to produce a background level equivalent to B_{abs} = 0.4 Mm^{-1} at about 10 min time resolution.

The all-solid-state lasers used were both very compact and efficient: a 532 nm doubled Nd:YAG laser and a 685 nm laser diode provided ≈ 60 mW and ≈ 87 mW modulated average power, respectively. The entire measurement procedure was automated with use of the computer which also analyzes the microphone signals after phase sensitive detection with an Fast Fourier Transform (FFT) analyzer.

Photoacoustic Light Absorption and Black and Elemental Carbon Measurements.

During the 96/97 winter intensive study period of the Northern Front Range Air Quality Study (NFRAQS) our photoacoustic instrument was operated at the Brighton, CO site, collocated with black carbon and elemental carbon instrumentation. The aethalometer measures the concentration of black (i.e., light absorbing) carbon (BC) aerosol based on deposition of aerosol on a quartz filter tape and subsequent light attenuation measurement of the loaded filter.[3] The aethalometer was operated with a time resolution of 10 min, quite comparable with the photoacoustic instrument. Elemental carbon (EC) aerosol concentrations were measured *via* aerosol deposition on quartz filters and laboratory analysis with the thermal/optical TOR

method.[7] Aerosol was accumulated on the filter for six or twelve hour periods. For the comparison of photoacoustic aerosol light absorption with aethalometer BC and TOR EC shown in Figure 2, photoacoustic and aethalometer measurements were averaged over the respective TOR filter sampling periods. Linear regression analysis yields excellent correlation (R^2 = 0.94) between photoacoustic light absorption measurements made with the 685-nm laser and the aethalometer BC measurements indication an absorption efficiency of 4.3 m^2/g for BC aerosol at 685 nm. Correlation with TOR EC measurements is good (R^2 = 0.85) indicating an absorption efficiency of 3.1 m^2/g for EC aerosol. Similar measurements made on different days with the photoacoustic instrument using the 532-nm laser indicate an absorption efficiency of 9.1 m^2/g for BC and of 7.0 m^2/g for EC aerosol.

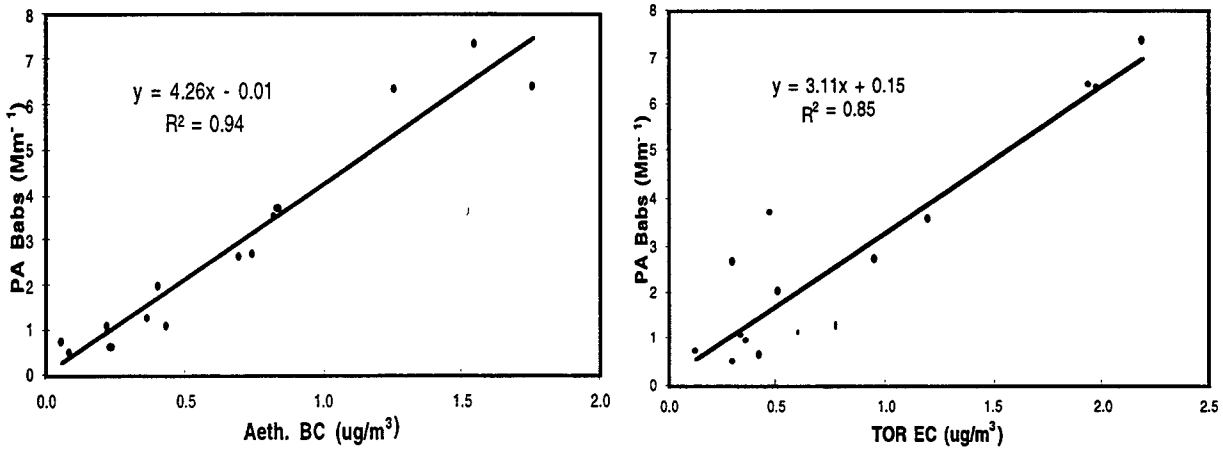

Fig. 2: Correlation of 685-nm photoacoustic measurements (PA) of aerosol light absorption with black (BC) and elemental carbon (EC) measurements taken on January 3, 6, 7, 8, 9, 1997.

While these absorption efficiency calculations are based on a relatively limited number of measurements they raise a number of interesting points:

1. Absorption efficiencies are about a factor of two higher at 532 nm than at 685 nm. The magnitude of this change cannot be explained by simple Mie calculations.
2. Photoacoustic measurements show excellent correlation with aethalometer BC measurements and good correlation with TOR EC measurements.
3. TOR EC aerosol measurements are significantly higher than aethalometer BC measurements resulting in lower absorption efficiencies for EC aerosol.

References

1. H. Horvath, Atmos. Environ. **27A**, 293-317 (1993).
2. D. Muir and D. P. H. Laxen, Atmos. Environ. **29**, 959-962 (1995).
3. A. D. A. Hansen, H. Rosen, and T. Novakov, Sci. Total Envir. **36**, 191-196 (1984).
4. R. W. Terhune and J. E. Anderson, Opt. Lett. **1**, 70-72 (1977).
5. K. M. Adams, Appl. Opt. **27**, 4052-4056 (1988).
6. A. Petzold and R. Niessner, Appl. Phys. **B 63**, 191-197 (1996).
7. J. C. Chow, J. G. Watson, L. C. Pritchett, W. R. Pierson, C. A. Frazier, and R. G. Purcell, Atmos. Environ. **27A**, 1185-1201 (1993).

In situ Sensing of Atmospheric Trace Gases Using Airborne Near-IR Diode Laser Sensors

David M. Sonnenfroh, William J. Kessler, Mark G. Allen
Physical Sciences Inc.
20 New England Business Center
Andover, MA 01810
tel: 978.689.0003 fax: 978.689.3232 e-mail: sonnenfroh@psicorp.com

John Barrick
NASA Langley Research Center
Hampton, VA 23681-0001

Over the last few years, there has been considerable effort at Physical Sciences Inc. (PSI) and elsewhere to develop ultrasensitive trace gas sensors for *in situ* monitoring of several important atmospheric species including H_2O, CO_2, and CH_4. At PSI, high performance field sensors have been created by combining near-IR diode laser absorption with balanced ratiometric detection. One such sensor is a laser hygrometer developed for NASA which is capable of monitoring water vapor from ground level to the tropopause. The laser hygrometer monitors water vapor through absorption via a strong, isolated line at 7181.172 cm^{-1} in the $\nu_1 + \nu_3$ combination band. Through a series of laboratory measurements, we have demonstrated a sensitivity of 2 x 10^{12} molecules cm^{-3} which corresponds to ~0.3 ppmv water vapor at typical mid-latitude tropopause conditions (12 km or 40 kft) using a 50 cm absorption pathlength. We have also demonstrated a dynamic range of 4 orders of magnitude and a measurement rate of 10 Hz. The hygrometer uses a unique, compact, external air probe for true *in situ* sampling, thereby obviating well-known limitations in time-response and sensitivity imposed by extractive air sampling systems.

The PSI laser hygrometer was designed for deployment on the NASA DC8 research aircraft but is easily adaptable to other aircraft. The sensor was designed as a turn-key, stand-alone instrument requiring minimal user interaction. All aspects of laser control, laser health monitoring and measurement parameters are fully accessible through the system computer via a simple graphical user interface developed using LabView™. Data reduction provides for signal averaging of single sweep absorption spectra followed by baseline subtraction and integration. Data is reported as number density or dew point using ancillary meteorological data. Single absorption spectra are acquired at 200 Hz; 20 such spectra are averaged to achieve a 10 Hz measurement rate.

Recently, we successfully demonstrated airborne operation of the laser hygrometer aboard the NASA P3B aircraft during the course of the Southern Great Plains mission during June and July of 1997. We had the opportunity to intercompare the laser hygrometer with two NASA chilled mirror hygrometers. This presentation will provide a summary look at the data collected during this demonstration over 10 separate flights.

Data from a portion of Flight 7 is presented in Figure 1. The aircraft was in nominally level flight in clear air at 25 kft; the static air temperature was 252 K and the static air pressure was 377 mB. The aircraft made a turn at 55880 s and retraced its flight path back through the same airmass. This produced the high degree of symmetry (about 55880 s) observed in the number density temporal history.

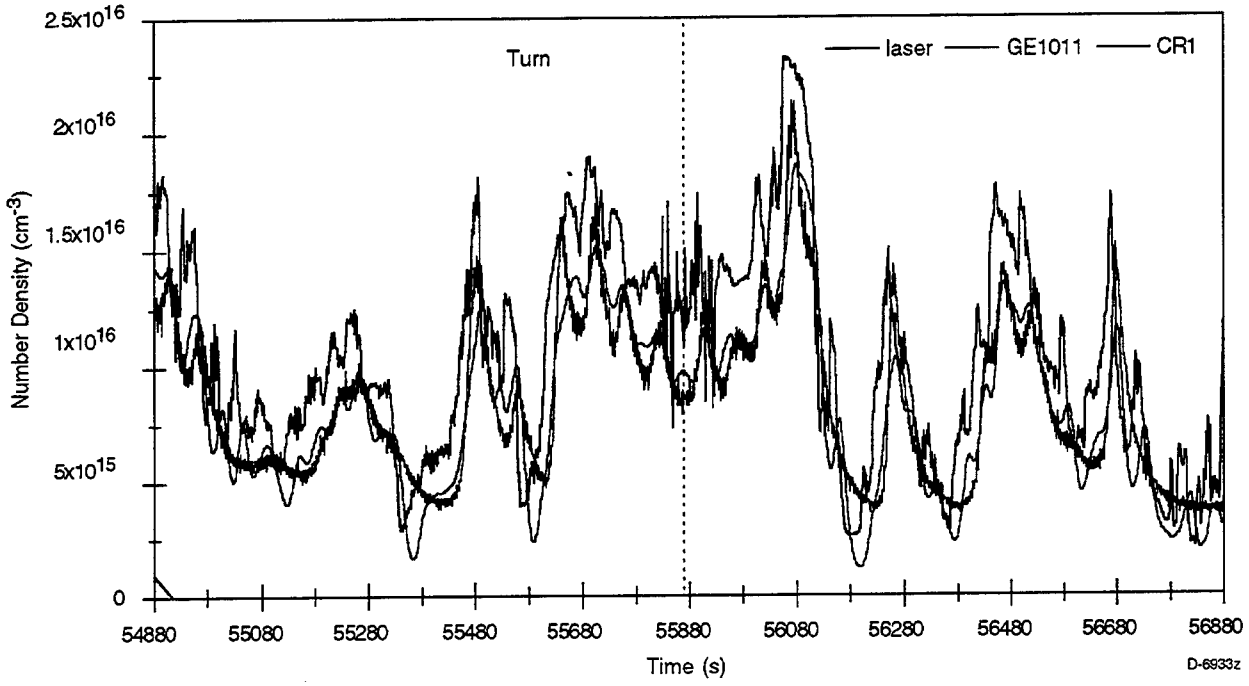

Figure 1. Flight data for part of Flight 7, 25 June 1997. The altitude was 25 kft, static air temperature was 252 K and the static air pressure was 377 mB. The aircraft was halfway through a turn at 55880 s.

Additional flight data is presented in Figure 2. During Flight 10 while cruising at 25 kft, the laser hygrometer recorded an encounter with a very moist air parcel. The relative humidity, nominally at 5% before and after the encounter, reached ~80% inside the air parcel. The excellent temporal response of the laser hygrometer is evidenced by the fine structure observable in the number density at the leading edge of the encounter.

This basic platform is evolving toward a variety of related applications. Currently we are implementing full automation and downsizing the sensor for deployment on an unmanned aerial vehicle (UAV). Capability to monitor additional trace gases such as CH_4 will also be included. In this multispecies monitor, a separate laser is included for each species to be detected. These fiber-coupled lasers are multiplexed onto a common send fiber optic for transport to the external air probe. The multiplexing is achieved by tailoring of the drive current waveforms. We have used such techniques to simultaneously detect three separate species as illustrated by the spectrum presented in Figure 3. This presentation will review the design criteria and performance parameters for this sensor.

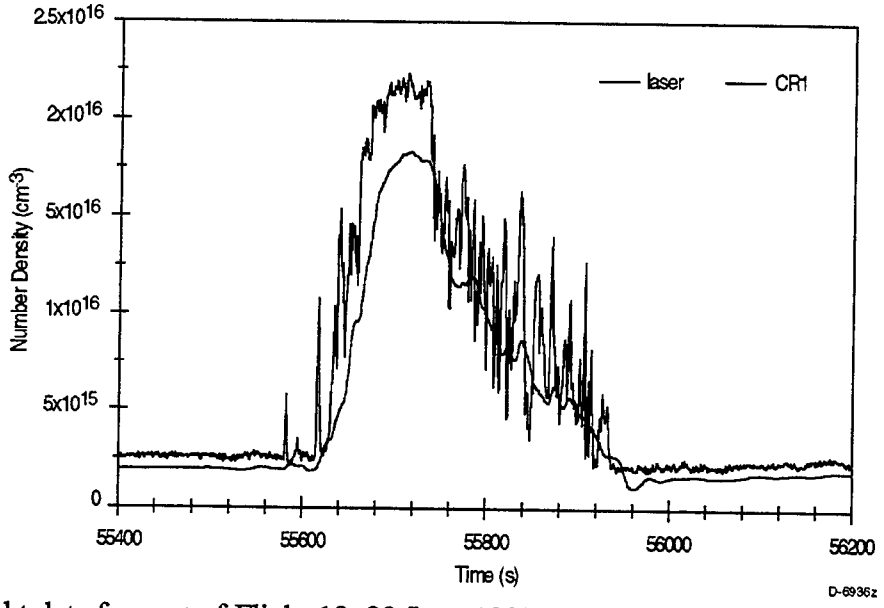

Figure 2. Flight data for part of Flight 10, 29 June 1997. The altitude was 25 kft, static air temperature was 251 K and the static air pressure was 378 mB. Data rates were 1 Hz for the laser hygrometer and 0.1 Hz for the cryogenic chilled mirror hygrometer.

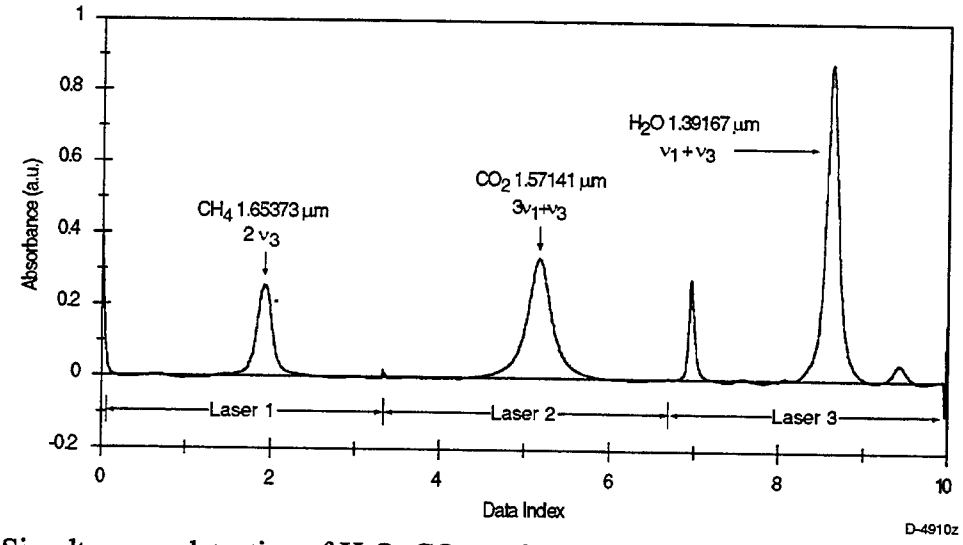

Figure 3. Simultaneous detection of H_2O, CO_2, and CH_4 using three separate, multiplexed diode lasers operating at 1.39, 1.57, and 1.65 µm.

INTRACAVITY LASER SPECTRAL ANALYSIS OF TRACE ELEMENTS IN ENVIRONMENTAL SAMPLES

V.S.Burakov, P.Ya.Misakov, and S.N.Raikov

Institute of Molecular and Atomic Physics
National Academy of Sciences of Belarus
70 Scorina av., 220072 Minsk, Belarus
Tel.: 375172685763, Fax: 375172393064, E-mail: lldp@imaph.bas-net.by

Laser spectroscopic techniques have significantly enhanced the performance of atomic spectrometry [1,2]. Despite the impressive detection power of laser methods, they are as a rule still far from being practically applied in routine analyses especially of complex natural samples of environmental interest. The main reason for this situation hitherto remains the comparatively higher complexity and cost of tunable lasers and their power supplies excluding low-power semiconductor laser diodes, that have excelent potential spectroscopic and operational properties for spectral analysis [3]. Of course, these laser sources of radiation at present also have some specific disadvantages, that restrains their wide practical application. On the other hand, the common tunable dye laser-based instruments can compete with established analytical techniques and have a chance to be routinely used for the direct elemental analysis espesially at trace levels or for solving some narrowly specific problems.

Intracavity laser absorption spectroscopy is based on the extremely high sensitivity of a laser output to intracavity frequency dependent losses especially when the linewidth of the absorber placed inside the cavity of a multimode laser is much narrower than the spectrum width of the laser used [4,5]. The intracavity laser spectrometer (ICLS) based on a broadband tunable laser is very similar to that employed in conventional continuum source atomic absorption spectrometry (AAS) [6]. In fact, apart from the primary light source, all other modules, analytical procedure and data processing and storing remain practically unchanged. Nevertheless, the ICLS has much lower limits of detection. Lately a number of works has been published demonstrating the extremely low analyte concentrations measured by the intracavity technique [7-10].

Experimental section

The ICLS that can be used for the determination of ultra-low concentrations of the desired trace elements in liquid, gaseous and solid samples is described below. The ICLS consists of three basic modules: (i) broadband dye laser (DL), (ii) high-resolution spectrograph (HRS), and (iii) data processing system (DPS). Also it includes different types of atomizers and samplers: (iv) electrothermal atomizer (ETA), (v) electrostatic precipitator (ESP), and (vi) pulsed laser sampler (LS).

(i) The tunable multimode flash lamp-pumped DL is used as the primary light source with the broadband smooth spetrum and following output parameters: spectral range of 400-700 nm, spectral width of 10-15 nm, pulse duration of 1-10 μs and beam aperture in the cavity of 6-8 mm. Taking into account the progress in the development of the dye lasers and their power supplies, since the absorption measurements in the ICLS do not need high-power radiation, and the efforts made on the spectral narrowing of the output and the stabilization near the line centre, the compact, inexpensive and easy to operate DL is used.

(ii) The laser spectrum including the absorption lines of the analyte is recorded with the help of the HRS of a special design. As a dispersion element, an echelle grating (300 lines/mm) operating in the 6-25 spectral orders with double dispersion is used. The focal length of the objective is 1377 mm. Reciprocal linear dispersion is about 0.5 nm/cm in the yellow spectral range and accordingly the spectral resolution is about 1 pm.

(iii) The DPS includes an optical multichannel analyzer (OMA) and a personal computer (PC). Absorption lines are registered by the OMA on a base of a CCD array. The array has 2048 pixels with a size of one pixel of 12x10 μm. The width of spectral window of observation usually is about 1 nm. Processing and storing of obtained data as well as monitoring of the ICLS modules are performed with the help of the PC.

(iv) The graphite-tube furnace ETA located in the DL cavity allows to analyze ultra-trace concentrations of elements in solutions. The standard graphite tube is 28 mm long with a 6-mm inner diameter. Heating temperature control is between ambient and 3070^0C at 1^0C increments. The program of the ETA has 64 steps with a 1-799 s/step at 1 s increments.

(v) For direct accumulation on the inner surface of a graphite furnace of small particles suspended in atmosphere or another gaseous medium the compact and portable ESP is used. It contains a special holder for graphite tube and a thin tungsten wire as a negative electrode, that can be inserted in the desired position into the tube. The gas is drawn through the graphite tube by a micropump, and gas volumes are controlled by a flow meter and a timer. The ESP has the following main parameters: potential $\leq$ 3.1 kV, gas flow rate $\leq$ 800 cm^3/min, sampling time of 1-99 min with step duration of 1 min.

(vi) For direct elemental analysis of solid samples without their pretreatment the pulsed LS is used. Ablation plasma is generated by focusing a beam of the ruby laser, operating at the fundamental wavelength in the Q-switched (25 ns) mode with a maximum pulse energy of 0.5 J on the target surface. The radiation of the LS used may be focused down to 100 μm (in spot diameter) on a sample permitting surface microanalysis. A sample holding positioner is used to maintain the ablation plume in the DL cavity and to preselect the irradiated surface zone. The device is located within a hermetic chamber in which a costant gas (usually argon) flow creates the desired environment.

Results and discussion

The use of a typical 5-μs DL makes it possible to increase a length of the absorbing layer in the laser cavity by a factor of about $3 \cdot 10^3$ as compared with a geometrical length of the absorbent. Therefore, an absorption can be measured not only in the strongests spectral lines.

For the ICLS with the graphite tube ETA or the LS the calibration procedures and reagents are conventional and are described in detail in commercial literature as well as in our papers [7-10]. The analytical curves were obtained by plotting the relative intensity of an absorption line versus the element concentration in a standard solution or solid sample. Besides, the dynamic range of calibration curves was greatly extended by measuring a value of integral absorption or equivalent width of absorption line in the DL spectrum.

The ICLS parameters, operating conditions and analytical procedures were optimized for each element to be analised. As compared with conventional

analytical methods a significant reduction in measurable absorbance was demonstrated and limits of detection were as a rule considerably decreased for absorbing centres having suitable analytical lines in the visible spectral range. The table presents for some metals the comparison with the limits of detection reported by other modern conventional spectroscopic methods (the most sensitive ones): graphite furnace (GF) AAS [11] and inductively-coupled plasma mass-spectrometry (ICP-MS) [12].

Element	Detection limit, ng/L		
	ICLS	GFAAS	ICP-MS
Al	1	10	6
Ba	0.2	40	2
Cr	2.5	4	20
Li	0.03	10	0.1
Sr	0.15	10	0.8

Statistical characteristics of the ICLS have been determined for as a rule 50-60 measurements of the absorption line relative intensity, when the same volume of the standard solution with a constant concentration of a chosen element is introduced into the furnace. It has been shown that the error distribution is normal and the relative standard deviation of the analysis in the middle of the dynamic range is about 10%. The precision of the ICLS is determined mainly by the stability of the spectral distribution of laser radiation intensity near the absorption line.

The mentioned metals and some others elements, for example iodine, were determined at trace levels without pre-concentration in different real environmental samples such as: mineral water, air, solid materials (silicates and slags) and human urine.

Literature cited

1. Omenetto, N.J. *Trace Microprobe Tech.* 1992, 10, 277.
2. Jackson, K.W.; Chen, G. *Anal. Chem.* 1996, 68, 231R.
3. Niemax, K. et al. *Anal. Chem.* 1996, 68, 351A.
4. Pakhomycheva, L.A. et al. *Sov. JETP Lett.* 1970, 12, 43.
5. Campargue, A. et al. *Spectrochim. Acta Rev.* 1990, 13, 69.
6. Jones, B.T. et al. *Anal. Chem.* 1989, 61, 1670.
7. Burakov, V.S. et al. *J. Anal. At. Spectrom.* 1994, 9, 307.
8. Burakov, V.S. et al. *Microchem. J.* 1994, 50, 365.
9. Burakov, V.S. et al. *Fresenius J. Anal. Chem.* 1996, 355, 361.
10. Burakov, V.S. et al. *Fresenius J. Anal. Chem.* 1996, 355, 883.
11. Guide to Analytical Values for Thermo Jarrell Ash Spectrometers.
12. Atomic Spectroscopy Detection Limits, Perkin-Elmer.

Laser Applications to Chemical and Environmental Analysis

Laser Diagnostics for Combustion Analysis

Wednesday, March 11, 1998

Dieter Brüeggemann, University of Stuttgart, Germany
Presider

LWA
8:00am–10:00am
Coral Room

Diagnostics and Sensors for Turbine Engines

J. M. Seitzman, R. T. Wainner and R. Tamma

Georgia Institute of Technology, Aerospace Combustion Laboratory
School of Aerospace Engineering, Atlanta, GA 30332-0150
(404)894-0013, Fax 894-2760, jerry.seitzman@ae.gatech.edu

Introduction

There is a growing urgency for improved performance of combustion devices, for example higher efficiency and lower pollutant emissions. Because of high power requirements and strict size limitations, turbine engines for aircraft propulsion present a particularly difficult challenge. In order to increase specific thrust, improve efficiency and reduce engine size, recent efforts in turbine engine technology have been directed toward increased operating pressures (>30 atm). Maintenance of optimum conditions, e.g., turbine inlet temperature profiles, becomes more difficult as these engines are obliged to achieve optimal performance closer to materials limits and in off-design conditions. Active control of turbine engines offers great potential for such improvements. However, active control of turbine engine combustors requires sensors that are capable of monitoring high temperature and high pressure combustion gases. In such a hostile environment, optical techniques are a natural solution, as they offer the possibility of non-intrusive measurements. At the same time, measurement of combustion particulates, primarily soot, is of great interest. Soot plays a key role in radiative heat transfer in the combustor, and therefore, represents a significant source of combustor liner heating. Soot emissions from aircraft during takeoff are of interest since small particulates like soot have been determined to pose respiratory health risks. Finally, soot emitted from aircraft engines at higher altitudes may act as water condensation sites and therefore play an important role in global climate through changes in the earth's albedo.

In this paper, we describe development of optical techniques to address each of these problems. For active engine control, we describe efforts to develop sensors based on line-of-sight absorption to monitor turbine inlet conditions (combustor exit conditions). For measurement of soot in both flames and engine exhausts, we present the development of a technique known as laser-induced incandescence (LII).

Absorption-Based Sensors for Combustor Control

For active optical sensing, line-of-sight absorption based on IR diode lasers have shown great promise. While many species have been measured using IR absorption, water and carbon dioxide are the best candidates for combustor exhaust temperature sensors. Line-of-sight absorption measurements are based on the absorption of light as it propagates across a region of interest. The transmission of narrow linewidth radiation at frequency ν through a nonscattering gaseous medium of length L may be described by

$$T_\nu = I_\nu / I_{\nu 0} = \exp\left[\int_0^L -k_\nu(x,p,T,n_i)dx\right] \quad (1)$$

where T_ν is the spectral transmittance of the medium (=1-absorbance), I_ν is the spectral intensity after propagation to L, $I_{\nu o}$ is the incident spectral intensity from the light source (at x=0). The spectral absorption coefficient $k_\nu(x,T,p,n_i)$ at a distance x is a property of the gas, and therefore, it is a function of thermodynamic variables such as temperature (T), pressure (p) and composition (n_i). Species concentration or temperature measurements are obtained by determining the transmittance of the gas at one or more frequencies/wavelengths and inverting Eq. 1 to obtain the parameters of interest. Because the gas transmittance is integrated over the path length L, the resulting measurement must be recognized as some path averaged value. Also, the above expressions represent nonlinear relationships; therefore the measured values are not true linear averages, but weighted averages based on the exact path distribution of the gas properties. When accurate, spatially resolved measurements are required in nonuniform, turbulent flows, this may represent a significant problem. The measurement requirements of a sensor used for active control are, however, less demanding. For example, it may be sufficient to know whether the overall gas temperature is simply increasing or decreasing, or perhaps, if the temperature distribution is uniform to within some amount. These questions are answerable with properly designed absorption sensors.

For in-situ sensing of turbine inlet temperature profiles, the high pressure environment is a significant challenge compared to atmospheric absorption-based sensors. Figure 1 shows a calculated absorption spectrum of water in the 1.4 μm region at 1 and 30 atm. At the high pressures present in the combustor, much of the spectral structure is lost and there are few regions of low absorption where background corrections can be made. Thus sensors for this environment must be widely tunable or involve multiple fixed-frequency sources. In addition, the

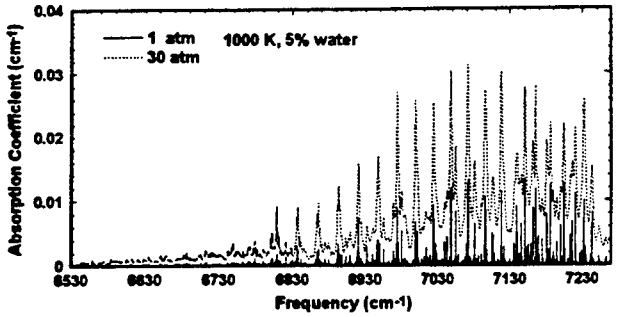

Figure 1. Calculated absorption spectra of water (1.4 μm region) at 1000 K based on 5% water concentration by volume at 1 and 30 atm total pressure.

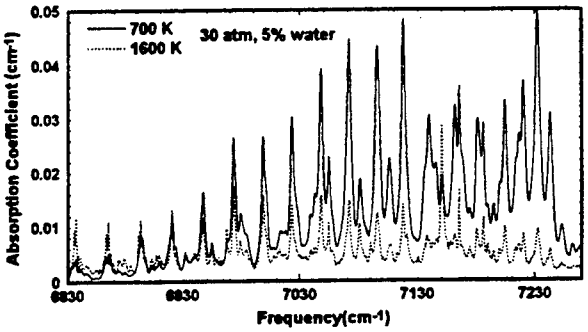

Figure 2. Calculated temperature dependence of water absorption at high pressures.

choice of spectral locations with appropriate temperature dependence is also reduced. Figure 2 shows calculated spectrums in the 1.4 and 2 μm regions at two temperatures. While there are a number of wavelengths where the absorption decreases rapidly with increasing temperature, the opposite trend is much more difficult to find. Wavelengths with low or comparable absorption at low temperatures compared to high temperatures are needed when the inlet profile contains even small "clumps" of cold gas. Otherwise, the sensor may significantly underestimate the turbine inlet temperatures.

Laser-Induced Incandescence of Soot

When illuminated by a sufficiently high intensity laser, a soot particle will absorb enough energy to experience a rapid temperature rise and even vaporization. At the high temperatures (>3900 K) reached by the soot, significant incandescence, essentially blackbody emission, occurs. Since the small primary soot particles (<100 nm typically) are much smaller than the laser wavelength (>500 nm), their absorption is in the Rayleigh limit where it is proportional to the particle volume (or mass). For this reason, the LII signal is nearly proportional to the soot fraction (or soot concentration) in the measurement volume. Compared to the alternative soot measurement approaches: elastic scattering, extinction, and intrusive sampling measurements, LII is more robust. LII is nonintrusive, easily extended to planar imaging for spatially resolved measurements in unsteady flows, and relatively insensitive to particle geometry.

The experimental arrangement for the LII measurements presented here is shown in Fig. 3. The LII signal

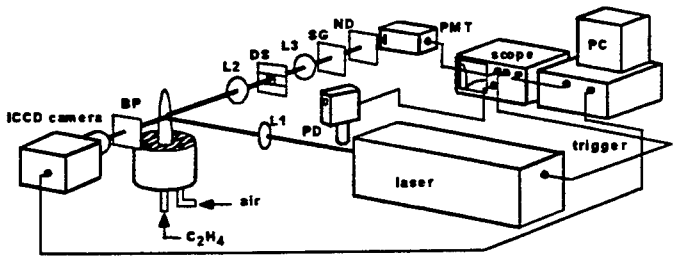

Figure 3. Laser-induced incandescence experimental setup. L1: 500 mm cylindrical lens, L2: 150 mm spherical, L3: 50 mm spherical, DS: adjustable rectangular aperture, BP: bandpass filter, ND: neutral density filter, SG: Schott glass long-pass filter and PD: photodiode.

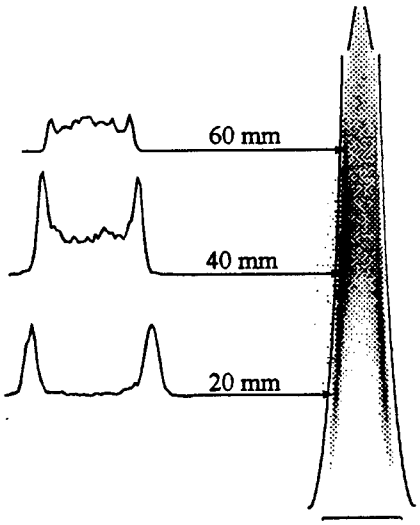

Figure 4. Single-shot LII image of soot from an ethylene air diffusion flame detected at 430 nm and with a gate of 30 ns beginning with the laser pulse. The vertical height of the image is approximately 80 mm, and the plots to the left are horizontal sections (vertically averaged over 4 pixels, ~0.4 mm) through the image at the heights indicated.

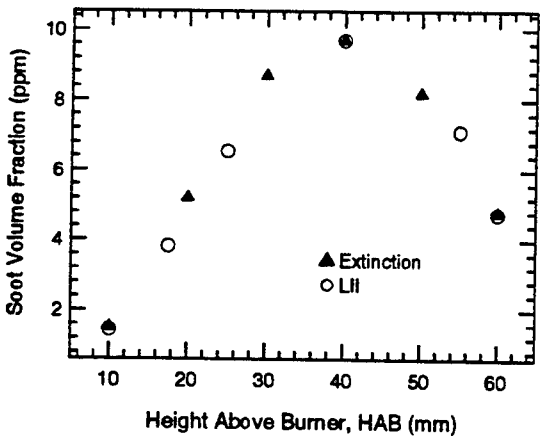

Figure 5. Soot volume fraction measurements along the path of maximum soot volume fraction in the ethylene flame. The LII signal at 650 nm detection is compared to extinction data.[1] The Nd:YAG (532 nm) is focused to an 8 mm tall sheet (550 MW/cm^2). The detection gate is 30 ns, and the data are normalized at 40 mm HAB.

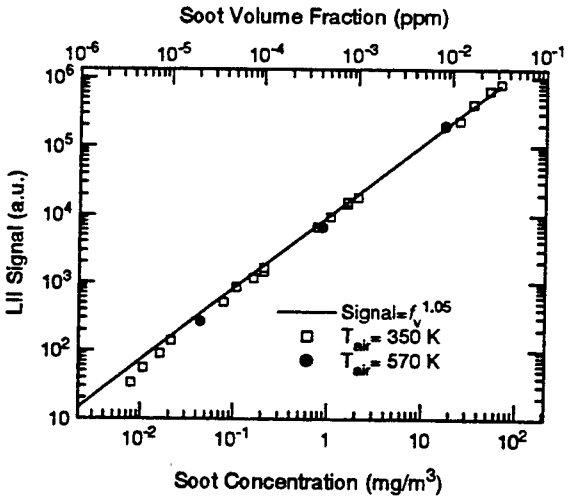

Figure 6. Linearity of LII soot measurements determined in a hot air jet seeded with small carbon black particles. The LII was produced by an unfocused Nd:YAG laser (1064 nm) and detected by a PMT with long pass filters (>580 nm). Each data point represents an average of 128 laser shots.

was produced by the output of a Nd:YAG laser, and collected either on an ICCD camera (Princeton Instruments) with an f/4.5 photographic lens or by a photomultiplier (PMT, Hamamatsu 928B) with an f/4.5 collection system. Spectral filters were used to isolate the LII signal from scattering and other interferences. Neutral density (ND) filters were used to extend the dynamic range of the PMT. Measurements have been acquired in two flows: an ethylene-air diffusion flame and a hot-air jet (14 mm exit diameter) containing carbon black particles.

As an example of the imaging capability of LII, Fig. 4 shows a single-shot image of the soot fraction in the diffusion flame. This image has not been corrected for vertical variations in the laser sheet intensity. Except near the edges of the sheet, however, the soot measurements are quite reliable because the LII signal can be made weakly dependent on laser intensity for high laser intensities. This image was acquired with 550 mJ of laser energy at 532 nm spread into a sheet of 80×0.3 mm, and detected through a 10 nm bandpass filter at 650 nm. The ICCD camera operated with a 30 ns gate that was prompt with the laser pulse. The horizontal profiles shown in the figure display the excellent signal-to-noise attainable with LII. Figure 5 shows the excellent agreement between soot volume fraction (f_v) measurements obtained from the LII data, compared to previous extinction measurements.

While the soot concentration only varies by a small amount in the flame, the soot loading in jet engine exhausts can vary over a much greater range. Figure 6 shows measurements of the LII signal from a heated jet of air containing known amounts of carbon black particles. This flow is intended to simulate the temperature and soot loading of engine exhausts. In this case, 250 mJ of unfocused 1064 nm output from the laser passed through the soot-laden air stream and were detected from a 1.5×4×8 mm region defined by the collection aperture and the laser beam width (8 mm). To improve the detection limits of the system, the LII signal was collected from 580 nm (set by long-pass glass filters) to ~850 nm (the 0.1% quantum efficiency point of the PMT). Even at the lowest soot loading investigated (~4 parts per trillion or 8 μg/m^3), the raw LII signal still exceeded the saturation level of the PMT and required an ND 1 filter. Thus with the current experimental arrangement, we expect a soot detection limit better than 1 ppt. These measurements also show the LII signal to be nearly linear with soot fraction over at least 4 orders of magnitude. For a range of ~100 ppt to 0.1 ppm, the LII signal scales roughly as $f_v^{1.05}$.

Acknowledgements

This work was supported under an NSF CAREER Award with Drs. M. Linevsky and F. Fisher as technical monitors, by the Army Research Office with Dr. D. Mann as monitor, and by AEDC and MetroLaser, Inc.

References

[1]Quay, B., Lee, T.W., Ni, T., and Santoro, R.J., "Spatially Resolved Measurements of Soot Volume Fraction Using Laser-Induced Incandescence," Combust. and Flame 97, 384-392, 1994.

CAVITY RINGDOWN CALIBRATION OF LASER-INDUCED INCANDESCENCE

Dr. Randy L. Vander Wal
Nyma, Inc.
Brook Park, Ohio 44142
M.S. 110-3
email: randy@rvander.lerc.nasa.gov

Prof. Thomas M. Ticich
Department of Chemistry
Centenary College of Louisiana
2911 Centenary Blvd.
Shreveport, LA 71134
email: tticich@beta.centenary.edu

Summary

Laser-induced incandescence (LII), a technique which determines relative soot volume fraction, requires calibration to yield quantitative results. Spatially resolved LII signals from soot within a methane/air diffusion flame are calibrated using cavity ring-down (CRD) which avoids extrapolation required of less sensitive methods in current use. Using CRD, quantification of LII for ppb f_v levels is demonstrated.

Introduction

Laser-induced incandescence (LII) has emerged as a versatile method for soot volume fraction (f_v) determination. By observing the incandescence from pulsed laser heated soot, f_v can be detected with high temporal and spatial resolution. Recent applications of LII include f_v determinations in premixed [1,2] and diffusion flames [3-10]. While some experimental studies have investigated the excitation and detection conditions that yield accurate f_v values [2,9,10], a particularly important aspect of the technique that has received less attention, however, is calibration [2,8,10]. The signal intensity depends upon several parameters such as the excitation laser fluence [1-3,6-10], excitation laser wavelength [1], detection wavelength [2,9], and the duration and delay of the detection gate [2,9]. Therefore, the signal magnitude reflects the excitation and detection conditions and thus provides only a relative measure of f_v, therefore requiring calibration to extract absolute values [1-4,7-10].

Currently used methods of calibration include light extinction [10] and gravimetric sampling [8]. The limited sensitivities of these methods require extrapolation of the LII signal to obtain absolute values for low f_v levels, thus magnifying uncertainties. Furthermore, differences in soot primary particle size and aggregate morphology may further complicate such calibration procedures limiting the transferability of the LII measurements [2]. Thus, a method which offers highly sensitive f_v determination for direct comparison to LII in the system of interest is desirable. In response to this need, we report the first use of cavity ring-down (CRD) [11-13] for calibration of LII in a methane/air diffusion flame to achieve absolute quantification of part-per-billion (ppb) f_v levels.

Experimental Approach

Figure 1 illustrates the experimental arrangement. A pulsed Nd:YAG provided light at 532 nm for CRD measurements and 1064 nm light for LII measurements. Two telescopes were used to achieve a down collimated beam with a spatial mode character compatible with the CRD cavity. In the first telescope, a Galilean arrangement, a 50 μm diamond pinhole placed between two 200 mm focal length, BK-7 glass lenses spatially filtered the laser beam. A second telescope formed by 400 and -50 mm focal length lenses served to down collimate the spatially filtered beam.

The pulsed laser light was then directed into an optical cavity formed by two mirrors with 1.0 m radius of curvature and 99.7 percent nominal reflectivity at 532 nm. To achieve stability and minimize the effects of longitudinal and transverse cavity spatial modes on the ringdown time, the spacing between the mirrors was set at 307 mm with the burner placed at the center of the cavity. Light emerging from the cavity was relayed via a 1 m quartz optical fiber bundle into a 1/4 m monochromator serving as an optical filter for stray light rejection. A Thorn EMI 9781R photomultiplier tube with nominal 2 ns response served as the detector. A digital oscilloscope collected and coaveraged 100 temporal scans for subsequent analysis. Temporal decays were fit to a single exponential function using nonlinear regression between the 90 and 10 percent peak intensity points using commercial software.

LII images were acquired using 1064 nm light provided by a Nd:YAG laser. A beam expansion telescope formed by a -50 and + 500 mm lens expanded the laser beam while a single 1500 mm focal length cylindrical lens formed the laser sheet. The beam focus was adjusted to create a sheet width of 1 mm based on burn patterns, which was comparable to the beam waist maintained by the CRD mirrors. LII signals were collected unfiltered using an intensified video array camera fitted with a 105 mm UV Nikkor lens. A frame-grabber captured 3 sequential LII images which were subsequently coaveraged together. Radial intensity profiles were then taken from the averaged image.

A methane gas-jet diffusion flame was established on a central fuel tube of 11 mm inner diameter fuel tube surrounded by an air coflow from a 101 mm diameter ceramic honeycomb. A chimney with open aperatures for optical access served to stabilize the flame and shield it from room drafts.

Results and Discussion

Analysis of CRD data

To analyze the CRD data, which provide a path integrated absorption, the observed ringdown decays were fit to a single exponential to determine the decay rate [12-13]. The path-

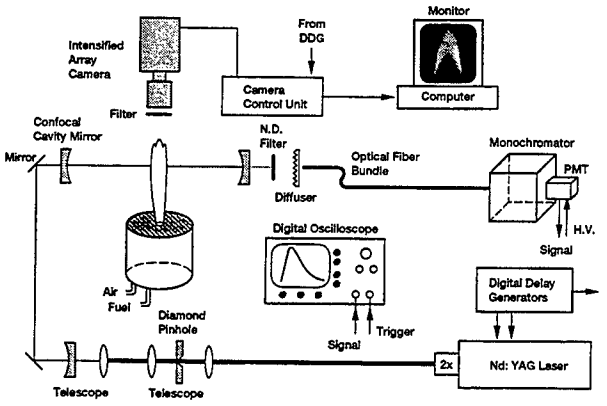

Figure 1.—Experimental diagram.

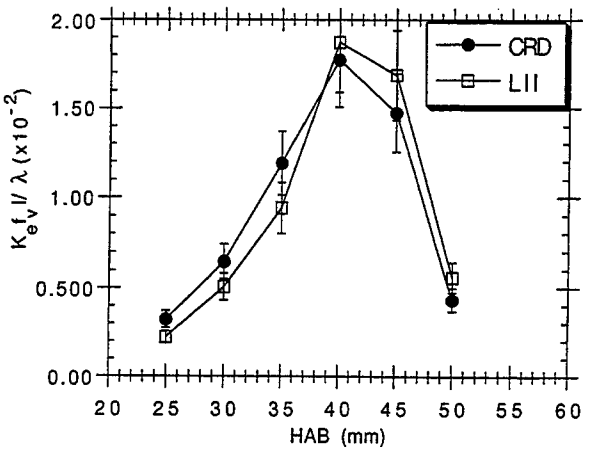

Figure 2.—Path-integrated absorbance through the methane/air diffusion flame. Shown also for comparison are the calculated path integrated LII based absorbance values as a function of axial position. The error bars represent one standard deviation. See text for details.

integrated absorption due to soot can be calculated from this decay rate using equation (1),

$$k^{-1} = \tau = \frac{d}{c(1 - R + K_e f_v L/\lambda)} \tag{1}$$

where k is the measured decay rate (τ is the ringdown time), d is the cavity mirror spacing, c is the speed of light and R is the mirror reflectivity. The remaining term $K_e f_v L/\lambda$ describes the path integrated attenuation due to soot through Beer's law expressed as,

$$T = \frac{I}{I_o} = \exp(-K_e f_v L/\lambda) \tag{2}$$

where T is the percent transmission with I and I_o being the attenuated and reference transmitted light intensities, respectively. Using Eq. (1), the mirror reflectivity can be calculated in the absence of absorption. In practice, additional losses due to cavity misalignment or background absorption will increase the ringdown decay rate and lower the observed R. With these additional losses contained within R, the absolute path integrated absorption due to soot can be readily computed.

The absorption term in Eq. (2) differs from that in Refs. 11-13, which expresses it as the product of the molecular absorption, absorption cross section and pathlength. In Eq. (1), the absorption is instead expressed as a product of soot aerosol absorption, K_e, soot concentration, f_v, and pathlength, L, for an aerosol in the Rayleigh size regime at wavelength λ. This analysis of the CRD data to extract the absorbance from soot does follow a premise of Beer's law in that the light source (laser light) spectral bandwidth is narrow relative to the absorption "linewidth," in contrast to some instances involving molecular absorption. Figure 2 plots the absorption product obtained from CRD data taken at a series of axial positions in a methane/air diffusion flame using Eq. (1).

Comparison with LII

Although the ultimate purpose of using the CRD measured extinction is to calibrate the spatially resolved LII signal, we first checked the agreement between the path-integrated absorption from CRD and the path-integrated LII signal. As demonstrated elsewhere [1-11], LII yields a relative measure of the soot volume fraction. Thus, the path-integrated absorption across a flame of width $2R$ at a particular axial height can be related to the relative value of f_v provided by LII according to Eq. (3),

$$\int_{-R}^{R} \frac{K_e f_v dL}{\lambda} = C \int_{-R}^{R} \frac{K_e f_{v,rel}}{\lambda} dL \tag{3}$$

where C is a constant. In a digitized image, the path length, L, is proportional to the spatial distance mapped to an individual camera pixel, a constant for all images and can be carried through the summation. Additionally, because the terms K_e, λ and elemental path length are constant, they may also be subsumed into the constant C to yield Eq. (4).

$$\int_{-R}^{R} \frac{K_e f_{v,rel}}{\lambda} dL = C' \sum_{x(-R)}^{x(R)} \mathrm{LII}(x) \tag{4}$$

Here, C' is the calibration constant and $x(-R)$ and $x(R)$ are the pixels spanning the radial width of the LII signal, LII(x). Equations (3) and (4) may be written for each axial position at which CRD and LII measurements are made since the value of C' is common to all positions. To determine C', the LII summation was calculated from radial intensity profiles at axial positions ranging from 5-60 mm in 5 mm vertical intervals. The ratio of the CRD measured absorption, summed over all axial positions, to the radially integrated LII intensities, also summed over all axial positions, then determines the constant C'. This procedure effectively weights C' by those path-integrated absorption values which are largest.

Applying C' to the radially summed LII intensity at a given axial position yields the soot absorption product. Figure 2 compares these LII-determined values with the CRD results. At axial positions preceding the maximum f_v value, the LII measurements slightly underpredicts the absorption factor. This may reflect some slight absorbance by PAHs and other fuel

pyrolysis products within the soot inception and growth regions. This error is mollified by the fact that the absolute soot volume fraction computed from absorption can vary by more than 25 percent depending upon the choice of refractive index, a widely-recognized uncertainty in soot measurements [14]. Measurements throughout the growth and oxidation regions show good agreement, illustrating the robustness of LII for f_v determination using these excitation and detection conditions. The sensitivity of both techniques is best illustrated at a height of 25 mm HAB where the path integrated absorption of 0.002 corresponds to a transmission of 0.9978.

Calibration of Spatially Resolved LII

Given the agreement between the CRD and LII path-integrated measurements, the path-integrated CRD value of f_v may be used to assign absolute f_v values to the spatially resolved LII signals. Multiplication of the spatially resolved LII radial intensity profiles by C' calculated above yields absolute values of f_v. These results are plotted in Fig. 3. No correction was applied to the LII profiles for soot attenuation because it is negligible at such low f_v values. To convert the absorption factor product $K_e f_v L/\lambda$ to f_v, we used a value for K_e of 4.9 [14]. This value was obtained from Eq. (5)

$$K_e = \frac{36\pi nk}{\left(n^2 - k^2 + 2\right)^2 + 4n^2k^2} \qquad (5)$$

using values for n and k, the real and imaginary components of the refractive index, respectively, of 1.57 and - 0.56i [14]. Even though this particular flame is axisymmetric, such a calibration method can be applied to any arbitrary spatial distribution of soot. As Fig. 3 shows, soot volume fraction levels of 0.001 ppm can readily be quantified.

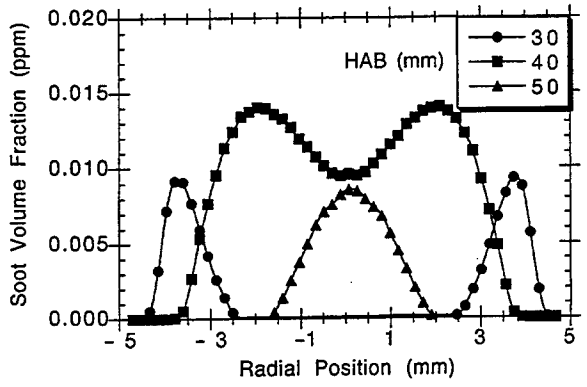

Figure 3.—Radial intensity profiles converted to f_v.

Conclusions

CRD presents an attractive method for calibration of LII. In contrast to other calibration methods, CRD provides straightforward quantification of LII for sub ppm f_v levels. Furthermore, this calibration method eliminates effects due to different aggregate morphology and primary particles size that often are associated with very low f_v levels by permitting direct calibration of the system of interest. The ease of implementation and equipment cost provide additional incentives. The same laser and wavelength can be used for performing both CRD calibration and LII measurements. As demonstrated here, harmonic mirrors with reflectivity greater than 99.7 percent appear adequate for CRD measurements of f_v at these concentration levels. Mirrors with reflectivity values up to 99.9 percent are routinely produced as stock items for high energy pulsed laser optics at common pulsed laser wavelengths in the visible and near-infrared.

Acknowledgements

This work was supported through NASA contract NAS3-27186 with Nyma Inc. Professor Ticich gratefully acknowledges support through the Ohio Aerospace Institute ASEE summer faculty fellowship.

References

1. R.L. Vander Wal, and K.J. Weiland, Appl. Phys. **B59**, 445 (1994).
2. J. Appel, B. Jungfleisch, M. Marquardt, R. Suntz and H. Bockhorn, Twenty-Sixth Symposium (International) on Combustion, The Combustion Institute, Pittsburg, PA p. 2387 (1996).
3. B. Quay, T.W. Lee, T. Ni, and R.J. Santoro, Combust. and Flame **97**, 394 (1994).
4. C. R. Shaddix, J. E. Harrington and K. C. Smyth, Combust. and Flame, **99**, 723 (1994).
5. F. Cignoli, S. Benecchi and G. Zizak, Appl. Opt. **33**, 5778 (1994).
6. N.A. Tait and D.A. Greenhalgh, Ber. Bunsenges Phys. Chem. **97**, 1619 (1993).
7. T. Ni, J.A. Pinson, S. Gupta and R.J. Santoro, Appl. Opt. **34**, 7083 (1995).
8. R.L. Vander Wal, Z. Zhou and M. Y. Choi, Combust. and Flame **105**, 462 (1996).
9. R.L. Vander Wal, Appl. Opt. **35**, 6548 (1996).
10. C.R. Shaddix and K.C. Smyth, Combust. and Flame **107**, 418 (1996).
11. J.J. Scherer, J.B. Paul, A. O'Keefe and R.J. Saykally, Chem. Rev. **97**, 25 (1997).
12. J.J. Scherer and D.J. Rakestraw, Chem. Phys. Lett. **265**, 169 (1997).
13. R.T. Jongma, M.G.H. Boogaarts, I. Holleman and G. Meijer, Rev. Sci. Instrum. **66**, 2821 (1995).
14. K.C. Smyth and C R. Shaddix, Combust. and Flame **107**, 314 (1996).

Vapor/liquid mass fraction measurements by linear Raman spectroscopy

Bernd Mewes, Gerd Bauer, and Dieter Brüggemann

Institut für Thermodynamik der Luft- und Raumfahrt (ITLR),
Universität Stuttgart,
Pfaffenwaldring 31, 70550 Stuttgart, Germany.
Tel.: +49 711 685 2316
Fax: +49 711 685 2317

Summary

In almost all combustion systems the liquid fuel is injected into the combustor as a spray. Spray formation, vaporization, and mixing with the oxidizer determine the quality of the combustion process and thereby the amount of unwanted emissions. A laser diagnostic is needed which can monitor these processes in order to optimize them. Especially the distributions of vaporized fuel and of oxidizer are of interest including regions where liquid fuel is coexisting. A well-known method to discriminate between different phases of the fuel is the exciplex fluorescence technique developed by Melton and Verdieck [1]. Quantitative results are difficult to obtain if oxygen, the oxidizer in almost all combustion systems, is present. Another technique is based on the fluorescence of acetone which is practically independent of its phase. Phase discrimination is done by using the huge difference in molecular density [2]. The high absorption coefficient for the used UV light prevented saturation of the CCD camera by liquid droplets.

In contrast to LIF, spontaneous light scattering is inherently free from quenching. Linear Raman scattering is widely used to measure mole fractions and temperature of gas phase components in reacting and non-reacting flows. Its ability for phase discrimination was studied by Johnston [3] to distinguish between vapor and liquid phase of propane. Unfortunately spectra from the different phases were found to be too similar. Alternatively Raman scattering has been combined with Mie scattering as a marker for the liquid phase [4] or with laser induced fluorescence from droplets doped with an organic dye [5].

Johnston's conclusions are valid for most of the hydrocarbons but not for water as found by Schweiger [6]. It was demonstrated that vapor and liquid in aqueous systems can be separated and that the Raman signal from polydispersed sprays or droplet streams is linear to the concentration [7]. This separation is based on the phase dependent Raman signal from the OH stretching vibration. In the liquid phase hydrogen bonding accounts for a broad Raman signal ranging from 2900 to 3700 cm^{-1}, whereas water vapor results in a peak at 3653 cm^{-1}.

We have examined Raman spectra of methanol and found the same effect as shown in Figure 1. The upper spectrum was recorded from liquid methanol at 298 K. The lower one is from a defined mixture of methanol vapor and nitrogen at 323 K and 0.1397 MPa with mole fractions of 23.6 % and 76.4 %, respectively. The spectra are only corrected for CCD dark charge. The liquid spectrum intensity is divided by 40. The huge difference in background between the two phases is obvious. In sprays the spectrum of the vapor is expected on top of the liquid one, since the scattering process is linear and therefore additive.

The sharp OH stretching vibration peak only appears in the vapor phase at 3683 cm^{-1}. In the liquid it is broadened by hydrogen bonding to a band reaching from 3200 to 3600 cm^{-1}. The symmetrical

CH stretching vibration at 2837 cm^{-1} as well as the asymmetric one at 2942 cm^{-1} are existent in both phases.

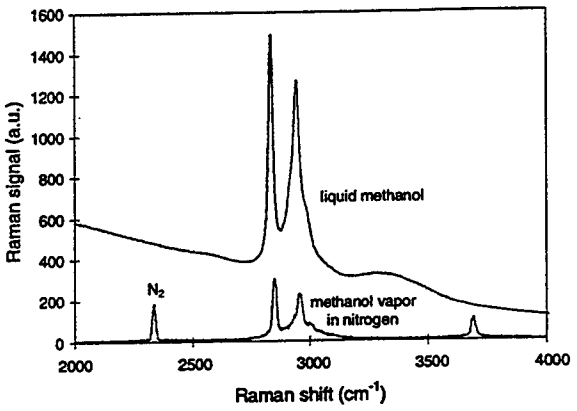

Fig. 1. Raman spectra from methanol in its liquid phase (upper) and from the vapor in nitrogen atmosphere (lower). Spectra are only CCD dark charge corrected.

This effect was used to visualize the mass fraction distribution across a methanol droplet stream. Excitation source was an Ar^+ laser from Spectra Physics at 514.53 nm. The laser beam was focused to a spot diameter of 170 µm by a reflection coated lens with 150 mm focal length. The detector system consisted of two lenses, a dove prism to rotate the image by 90°, a Kaiser Notch filter to suppress Rayleigh and Mie scattering, an imaging polychromator Acton AM505 and a PI back-illuminated CCD camera with 1100 (26.4 mm) pixels in horizontal (wavelength dispersed) and 330 (7.9 mm) in vertical (spatial axes) direction. The slit width was 250 µm. The observation lens combination resulted in a magnification of 1:1.25. Since the 330 vertical stripes were binned to 16 stripes, the 16 measurement volumes were 400 µm wide, 170 µm high, and 170 µm deep. A measurement across a methanol droplet stream, 15 mm below the orifice of the droplet generator, is shown in Fig. 2. The methanol was preheated to 323 K and injected as 140 µm droplets in a high pressure chamber at 0.4 MPa.

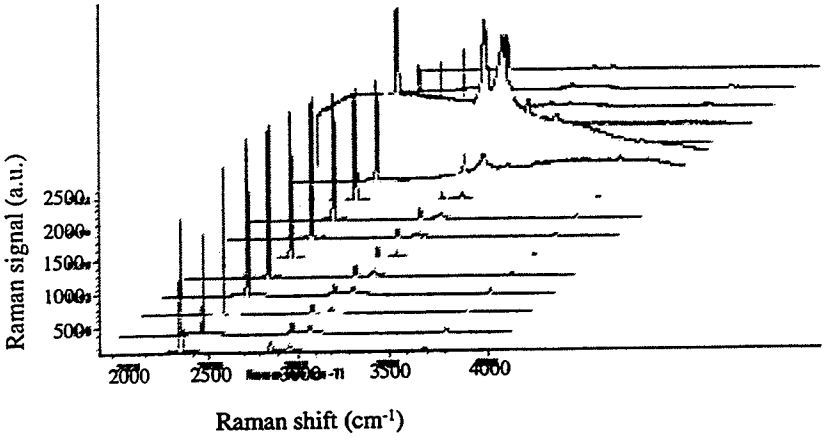

Fig. 2. One-dimensional Raman spectra of an evaporating methanol droplet stream.

Quantitative results from these spectra can be obtained by considering liquid and vapor of methanol as two different species. The Raman band intensity I_j of species j with a shift $\Delta\nu$ is given by

$$I_j(\Delta\nu) = N_j\left(\frac{d\sigma}{d\Omega}\right)_{\Delta\nu,j} I_0 C_{\Delta\nu} \Omega L \qquad (1)$$

where N_j is the number density of species j, $(d\sigma/d\Omega)_{\Delta\nu,j}$ the absolute Raman cross section of the band with the Raman shift $\Delta\nu$, I_0 the energy of the exciting laser, $C_{\Delta\nu}$ an apparatus dependent constant, Ω the solid angle of observation, and L the length of the measurement volume. Here, the vapor forms the OH vibration band at 3683 cm^{-1} whereas the liquid correlates to the CH vibration band from 2800 to 3000 cm^{-1} subtracting the vapor contribution. Mass fractions can be derived by dividing each integrated Raman intensity by its cross section and apparatus constants and subsequent division by the sum for all species. Vapor/liquid ratios as well as fuel/air ratios can also be obtained.

The apparatus constants have to be measured in a calibration experiment using a known methanol/air or for safety reasons methanol/nitrogen mixture. The Raman cross section of the liquid can be calculated by multiplying the vapor cross section [8] by an internal field effect constant [8] L_{lg}. With calibrations for every binned stripe of the CCD camera the spectra in Fig. 2 can be evaluated to the mass fractions shown in Fig. 3.

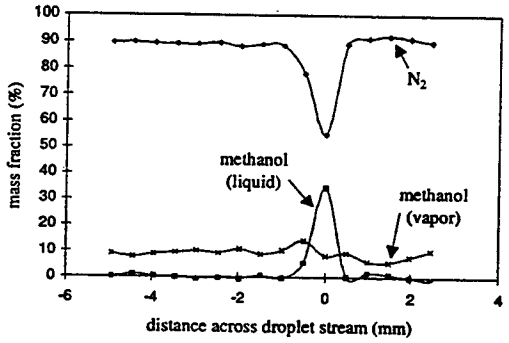

Fig. 3. Measured mass fractions across an evaporating methanol droplet stream.

In conclusion, by using methanol as fuel or as a substitute linear Raman spectroscopy can discriminate between the liquid and vapor phase even if droplets are existent. Due to its linearity mass fractions of all flow components and of the liquid fuel can be directly measured. In order to open this technique to a wide variety of applications from internal combustion engines to airplane turbines further studies are in progress using high energy pulsed lasers on evaporating fuel sprays.

References

[1] Melton, L. A. and Verdieck, J. F., *Twentieth Symposium (International) on Combustion / The Combustion Institute,* 1283-1290 (1984).

[2] Bazile, R. and Stepowski D., *Exp. in Fluids 20,* 1-9 (1995).

[3] Johnston, S., *Proc. ASME Fluid Eng. Conf., Boulder, Colorado,* 107-118 (1981).

[4] Masri, A. R., Dibble, R. W., Barlow, R. S., *J. Raman Spec. 24,* 83-89 (1993).

[5] Bazile, R. and Stepowski D., *Exp. in Fluids 16,* 171-180 (1994).

[6] Schweiger, G., *Proc. 3rd Int. Aerosol Conf. (ed. by Masuda, S. and Takahashi, K.), Kyoto, Japan,* 321 (1990).

[7] Schweiger, G., *J. Opt. Soc. Am. B 8,* 1770-1778 (1991).

[8] Schrötter, H. W. and Klöckner, H. W., *Raman Spectroscopy of Gases and Liquids (ed. by Weber, A.),* 123-166 (1979).

Simultaneous Laser-Induced Fluorescence and Rayleigh Scattering Measurements for Precise Determination of Flame Structure

Jay B. Jeffries, Norbert Heberle, Gregory P. Smith, and David R. Crosley
Molecular Physics Laboratory
SRI International
333 Ravenswood Ave.
Menlo Park, California 94025
Phone 650-859-6341
Fax 650-859-6196

Nearly one third of all natural gas is consumed in Bunsen-type burners, partially premixed flames which have a fuel-rich premixed flame forming an inner core surrounded by a diffusion flame. Pollutant emissions of nitrogen oxides, NO_x, in these flames are an important concern. The NO is produced by two chemical pathways, the thermal (Zeldovich) and the prompt (Fenimore) mechanisms. For temperatures below 2000 K, the thermal pathway is minimized because of the high activation energies of the rate-limiting chemical reactions. Thus, at the flame temperatures found in partially premixed flames, the prompt mechanism produces much of the NO.

CH radicals play an important role in the total amount of NO_x emissions. The Fenimore mechanism begins with the CH + N_2 reaction which forms HCN, breaking the strong N_2 bond. CH radicals can also initiate reburn reactions that consume some of the NO that is produced and reduce the total NO_x emissions. Thus, any predictive model for pollutant formation must provide an accurate CH prediction. Models of the reactive flame chemistry and prompt NO formation are quite sensitive to the steep spatial gradient in gas temperature. Therefore, it is important to locate the CH radical distribution spatially with respect to the variation in gas temperature. We have combined laser-induced fluorescence (LIF) of reactive intermediate radicals CH or OH with simultaneous Rayleigh scattering measurements to determine the location of the spatial distributions of these radicals with respect to the temperature gradient. The technique described here is generally applicable to steady reactive flows.

Our laboratory Bunsen burner stabilizes the premixed inner flame cone on a 1.65-cm-diameter tube surrounded by a homogeneous air co-flow with a diameter of 20 cm. This large diameter is necessary to stabilize the upper regions of the diffusion flame, some 15 cm from the

exit from the inner tube. The beam from a Nd:YAG pumped dye laser is directed through the flame, tuned to excite either OH and CH, and the subsequent fluorescence collected f6 perpendicular to both the laser beam and the gas flow. The laser beam and optical collection system is fixed; the burner is translated vertically and horizontally to determine the spatial distribution of the LIF signal. Spatial resolution of 0.1-0.2 mm is defined by the laser beam diameter.

Figure 1 shows the OH LIF versus radial position taken at two different heights (indicated in the inset) in a fuel-rich (Φ=1.36) flame, using a filtered photomultiplier. The lower trace shows rapid rises in the OH at the flame front of the premixed flame and again in the diffusion flame, steady levels of OH between the flame zones, and no OH in the unburned core of the premixed cone. The upper trace, above the premixed flame front, shows the OH structure throughout the upper part of the diffusion flame. The OH LIF signal is more than 20 times larger than the Rayleigh scattering signal from the atmospheric pressure flame. However, by detuning the excitation wavelength so that only light in the wings of the laser bandwidth are resonant with the OH transition, we have adjusted the OH LIF signal to be roughly equal to the Rayleigh scattering in the cold gas surrounding the flame. The lower trace in Figure 2 shows the simultaneous OH LIF and Rayleigh scattering signals, at the lower position of the Figure 1 data. The Rayleigh signal is high at the cold edge of the premixed flame and declines with changes in gas temperature and composition in the hot flame zone. The onset of the OH appears delayed until most of the flame front density decline (temperature rise) has occurred.

CH LIF is observed only in the premixed cone; no CH was observed in other regions of any of the flames studied. The CH LIF signal is nearly 100 times smaller than the Rayleigh scattering signal. For simultaneous LIF and Rayleigh measurements, we used a small monochromator to disperse the wavelength of the collected light, and adjusted the center wavelength slightly off-resonance with the laser. If we tune the laser to excite P(9) of the CH(A-X) (0,0) band and center the detection wavelength on the Q-branch bandhead, we can effectively adjust the Rayleigh scattering signal to be approximately equal to the CH LIF signal. The upper trace of Figure 2 shows these simultaneous CH LIF and Rayleigh scattering signals.

The two traces in Figure 2 precisely locate both the CH and OH structures in the flame with respect to the temperature gradient. This allows us to test flame models of the chemistry. The dashed line in the Figure 2 is the result of a simple one-dimensional, laminar, premixed model

of the inner cone flame, using the Sandia Premix flame code with the GRI-Mech 2.11 mechanism. Only the position of the computed temperature and the heights of the species profiles are adjusted. Excellent agreement is seen in the timing of the OH rise and the CH peak with respect to temperature, as well as the CH width and slope of the OH.

This research was sponsored by the Basic Research Group of the Gas Research Institute.

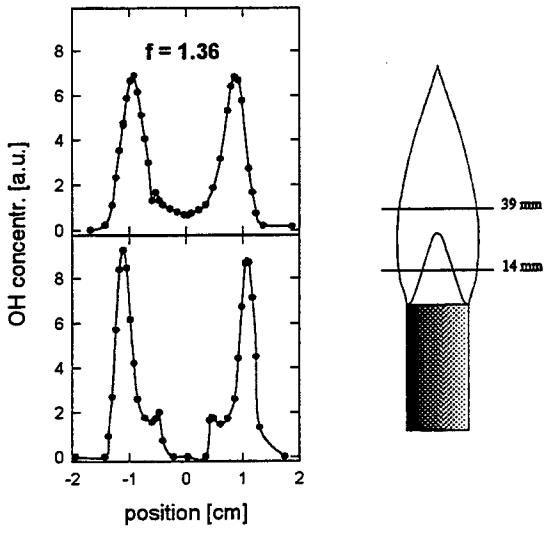

Figure 1

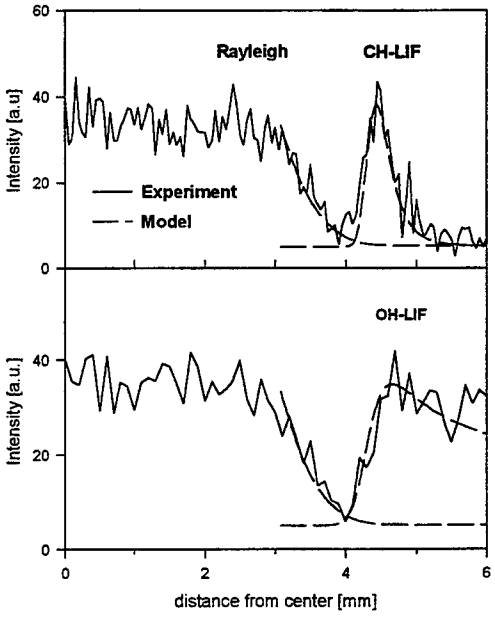

Figure 2

Evaluation of 2 Line Laser Induced Atomic Fluorescence for Two Dimensional Thermometry in Practical Combustion Applications

C. F. Kaminski and J. Engström
Department of Combustion Physics, Lund Institute of Technolgy,
P.O. Box 118, 22100 Lund, Sweden.
Tel: +46 (0)46 2229858 Fax: +46 (0)46 2224542
E-Mail: clemens.kaminski@forbrf.lth.se

Introduction

The measurement of temperature field distributions in practical combustion devices is an important task in combustion diagnostics because of the sensitive temperature dependence of rate coefficients of chemical reactions. For example, the production of toxic by-products during combustion may be influenced by local temperature variations. Spatially resolved temperature data is thus highly relevant from a theoretical as well as practical point of view: In the former case it may serve for the refinement and validation of models describing the process under investigation. In view of the latter, visualisation of temperature field distributions may aid engineering intuition and ultimately help in the design of more efficient and environmentally friendly combustion systems.
For turbulent combustion planar laser induced fluorescence thermometry (PLIF) has been shown to be a valuable tool to accomplish this measurement task [i,ii]. Almost without exception PLIF approaches to thermometry have been based on molecular species. Molecular PLIF requires high power densities distributed homogeneously over the laser beam cross section, a task which is difficult to accomplish, especially in the UV region where most suitable species absorb. Often excitation is in a spectral region where interferences from other, unwanted, species can occur which renders the interpretation of measurements difficult.
Atomic species, on the other hand, have much higher oscillator strengths and many species suitable for thermometry absorb in the visible region where spectral interferences are low. Adequate signal to noise ratios can be obtained at much lower laser power densities. The use of metal atoms as seeder species for flame thermometry has been discussed in detail in the literature [iii,iv].
The potential and first applications of single shot two line PLIF thermometry using atomic indium have been reported by the authors [v]. The present paper reports on the principles of the technique and presents preliminary results obtained in a commercial 4-stroke automotive engine.

Theory

In two line LIF thermometry transitions from the ground and first excited states of the seeder species are excited by two laser sources. The resulting fluorescence corresponding to each transition is proportional to the populations in the respective lower state. Thus if thermal equilibrium prevails, a temperature can be obtained from the ratio of the two fluorescence signals. The spin orbit splitting in the ground state of atomic indium provides an energy spacing which makes its population distribution temperature-sensitive over a range encountered in many practical combustion environments (ca. 700 - 3000K).
The principle of the technique is described in detail in reference v. It can be shown that in the linear excitation regime the temperature of the system is given by the ratio:

$$T = \frac{\varepsilon/k}{\ln\left(\frac{F_{21}}{F_{20}}\right) + \ln\left(\frac{I_{21}}{I_{20}}\right) + 4\ln\left(\frac{\lambda_{21}}{\lambda_{20}}\right) + \ln C} \qquad \ldots(1)$$

Where the subscripts j=0,1,2 refer to the ground, first, and upper electronic states of the system, F_{2j} are the respective fluorescence signal intensities with constant background noise subtracted, I_{2j} are the excitation intensities normalised

by the laser bandwidths, λ_{2j} are the excitation wavelengths, and C is a system dependent calibration constant. A striking feature of equation (1) is that due to the symmetry of the excitation and detection processes neither the oscillator strength of the transitions involved nor effects of collisional quenching enter the temperature calculation. Equation (1) holds under the assumption that the signal is not saturated and no laser absorption and fluorescence trapping occurs. The latter has to be ensured by keeping the seeder concentration sufficiently low.

Results and conclusions

An example of a single shot temperature field distribution obtained from a fluctuating methanol/air pool flame is shown in figure 1. In this case the fuel was directly seeded with small amounts of $InCl_3$ salt. The picture on the left corresponds to a single shot PLIF signal corresponding to F_{21} at 451 nm. In the middle the corresponding image for F_{20} at 410 nm is displayed. Processing these images according to equation (1) yields the corresponding temperature distribution shown on the right. Details on the experimental conditions and the computational procedures employed to obtain such profiles are given in reference v. The accuracy and precision of the technique has been investigated in well characterised flames with simultaneously performed vibrational CARS measurements from N_2 and will be subject of another publication.

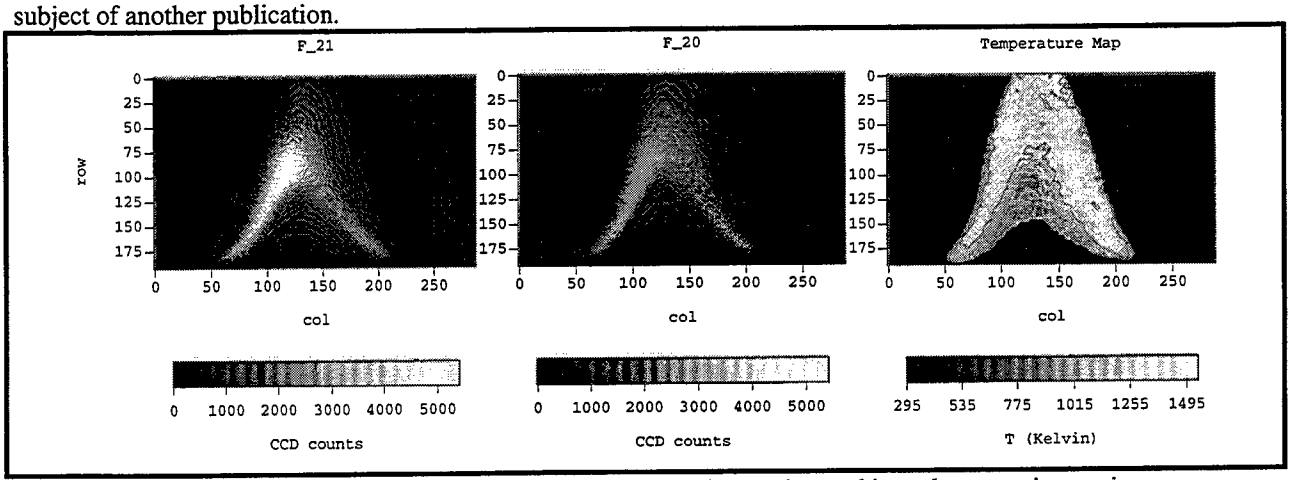

In this paper we would like to highlight the potential of the technique to be used in real automotive engines. Measurements were conducted in a commercial 4 stroke engine (Volvo N1P) equipped with a transparent cylinder liner and a transparent piston. The engine was run under stoichiometric conditions on isooctane fuel which was directly seeded with small amounts of $InCl_3$. Two lasers were used to excite F_{21} and F_{20} respectively, with a time delay of 500 ns between subsequent pulses. Two cameras then imaged the resulting fluorescence, gated to F_{21} and F_{20} respectively. The cameras were exactly aligned on a pixel by pixel basis [v]. The entire system was triggered to allow gating to any desired crank-angle with 1 degree resolution. The left picture in figure 2 shows the section of the engine chamber seen by the cameras. Inlet and outlet valves to the left and right of the picture respectively as well as the position of the spark plug (middle) and a pressure sensor (top) can be identified. Subsequent pictures correspond to single shot images (F_{21}) at 345, 351, 366, 492, and 600 degrees crank angle respectively (ignition occurs at 330 degrees, peak pressure at 366 degrees, exhaust valve opening 492 degrees, intake valves open at 716 degrees). These measurements are to our knowledge the first reported PLIF images from atomic seeder species in any internal combustion device. Currently temperatures are being evaluated from such data which will be used for the validation of detailed combustion models and will be correlated with NO_x measurements performed in the engine under similar condtions [vi]. In a separate measurement campaign the motor was run under identical conditions but here OH PLIF was used to obtain temperature profiles [vii]. These measurements will allow a detailed comparison of advantages and disadvantages of these two techniques for 2 dimensional thermometry under practical conditions. One advantage of the atomic two line technique is apparent from figure (2) and is that signals can be obtained over the entire

combustion cycle and even in the exhaust gas cycle. OH in contrast is present only over a very limited range of crank angles (between 20 to 30 degrees) before temperatures have become too low for significant amounts of OH to be produced.

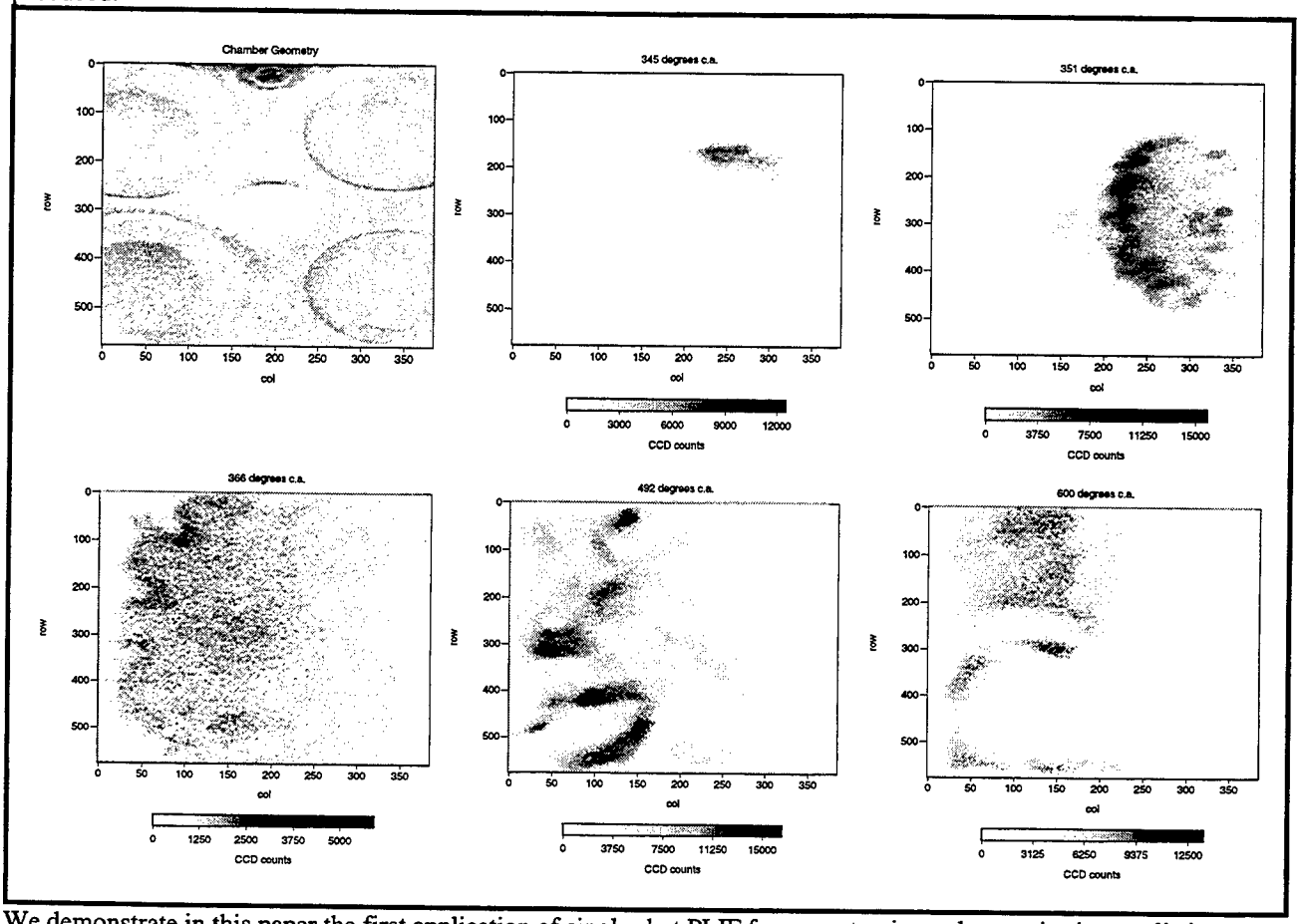

We demonstrate in this paper the first application of single shot PLIF from an atomic seeder species in a realistic combustion engine. The temperature sensitivity of the ratio of the 2 line PLIF signals from indium over a very large range of temperatures may prove to make this technique a valuable tool in turbulent combustion diagnostics.

---

[i] Long, Marshall: Simultaneous Two-Dimensional Mapping of Species Concentration and Temperature in Turbulent Flames. Opt. Lett. **10**, 267, 1985.

[ii] Cattolica, Robert: OH Rotational Temperature from Two Line Laser Excited Fluorescence. Appl. Opt. **20**, 1157, 1981

[iii] Omenetto, N et al: Flame Temperature Measurements by Means of Atomic Fluorescence Spectrometry. Spectrochim. Acta **27B**, 453, 1972.

[iv] Alkemade, C. Th.: A Theoretical Discussion on some Aspects of Atomic Fluorescence Spectroscopy in Flames. Pure and Applied Chem. 23, 73, 1970.

[v] C.F. Kaminski, J. Engström, and M. Aldén: Quasi Instantaneous 2-Dimensional Temperature Measurements in Combustion by Atomic Laser Induced Fluorescence. VDI Berichte **1313**, 555-560, 1997.

[vi] F. Hildenbrandt, C. Schulz, V. Sick, G. Josefsson, I. Magnusson, Ö. Andersson, and M. Aldén: Laserspectroscopic Investigation of Flow Fields and NO-Formation in a Realistic SI Engine. *submitted to SAE journal*

[vii] U. Meier, D. Wolff: Deutsche Forschungsanstalt für Luft und Raumfahrt

Measurement of fluorescence of formaldehyde in atmospheric pressure flame

Susumu YAMAGISHI

Ship Research Institute, Ministry of Transport,
6-38-1 Shinkawa, Mitaka, Tokyo, Japan 181
Phone +81-422-41-3113, Fax. +81-422-41-3115

Summary
Formaldehyde (H_2CO) is one of the key intermediate species in the initial state of combustion and is also a harmful exhaust constituent, especially in alcohol combustion. A detailed understanding of the reaction system of H_2CO can be obtained by comparison between measured and calculated density profiles. LIF is often used for in-situ measurement of flame but the estimation of quenching effects under atmospheric pressure is difficult (1). The electronic band spectrum of H_2CO has been discussed in many papers (1,2), but most spectral experiments were performed under low pressure at room temperature. Also the red shaded branch of 350nm band which is important for the YAG THG has been seldom used for measurement.
In order to determine the concentration we use the following basic relationship of the fluorescence process. If we know the quantum efficiency, we could measure the concentration of the species of interest from Eq.(1).

$$I_f = N_e \sigma V I_L \frac{k_R}{k_R + k_{NR} + \sum_Q k_Q M_Q} G\,\Omega \qquad (1)$$

where k_R is the radiative constant and k_{NR} is the non-radiative constant. k_Q is the quenching rate of collisions with partner molecules, N_e is the concentration of the molecule of interest, σ is the absorption cross section, V is the target volume, I_L is the laser intensity, G is the optical constant of the system and Ω is the collection angle.
$\tau_r = 1/k_R$ is termed the life time for the case of molecules free from quenching. The quantum efficiency of fluorescence is defined and determined by:

$$\Phi_F = \frac{k_R}{k_R + k_{NR} + \sum_Q k_Q M_Q} = \frac{\tau_f}{\tau_r} \quad . \qquad (2)$$

The life time can be measured from temporal measurement of fluorescence decay. If the detector system responds linearly to the excitation light, fluorescence intensity $I_0(t)$ is a convolution integral of its response to the light P. It can be expressed as:

$$I_0(t) = \int_0^t P_0(t')G(t-t')dt' \quad . \qquad (3)$$

$G(t)$ is assumed to be the sum of exponential and is expressed by :

$$G(t) = \sum_{i,j=1}^{l} a_i e^{-t/a_i} \qquad (4)$$

The best fit can be obtained from the magnitude of the sum of the squares of weighted residuals between observed fluorescence and an assumed function(3). Hence, the parameters of pre-exponential term and life time term can be determined.
The LIF/Raman measurements(5) were performed using the pulsed laser, and the streak camera. The exciting source is the third harmonics of the YAG laser with FWHM of 0.8cm^{-1} (5-6ns). The scattered light was collected from the focused part in a direction perpendicular to the incident axis. The collected light was then dispersed with spectrometers (f=25cm, CHROMEX). The diameter of the laser beam focused at the measuring section was approximately 80 μm and its image was focused at the slit with a magnification ratio of 1.0. We measured the sample gas in a cell at NTP and in a flame on a single

nozzle burner. A typical band spectrum is shown in Fig. 1 . It contains a large number of closely spaced rotational lines. By comparing with the predicted vibrational spectra (2) this band spectra has been identified as the fluorescence spectra of H_2CO. The average decay times of H_2CO fluorescence branches, measured at NTP is $\tau = 44.58n$ sec. Also, the value of the radiative life time reported in references 3 is 3.6 ± 0.3. Using these values in Eq.(2) a quantum efficiency of 0.0124 was obtained. There were considerable variation among the branches. The causes of the variation include uncertainties of overlapping of adjacent branches, noise, and the inherent characteristics of each branch. Further research is needed.

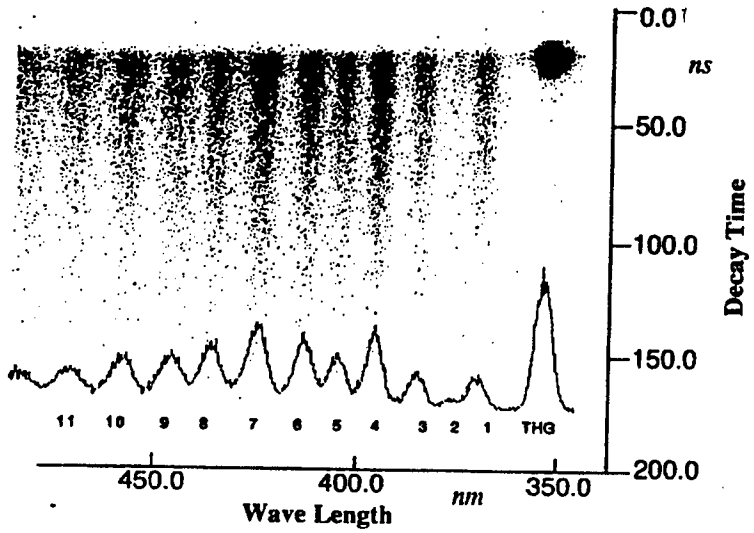

Fig. 1 Observed fluorescence of formaldehyde diluted with nitrogen under atmospheric pressure excited by third harmonics of the YAG laser.

Both LIF and Raman spectra were observed in C_2H_4/air flame. At higher temperatures portion, the strong unidentified fluorescence spectra overlap with those of Raman spectra. The principal component analysis(PCA) approach was used to analyze the observed spectra and to evaluate the noise level. Let $\mathbf{Y}$ represents the NWxNS data matrix, $\mathbf{X}$ represents the NWxNC spectral matrix. β represents the NCxNS concentration matrix. Here, NW is the number of wavelengths, NS is the number of positions, and NC(=p) is the number of scattering species. $\mathbf{Y}$ can be expressed in matrix form as:

$$\mathbf{Y} = \mathbf{X}\hat{\beta} \quad . \tag{5}$$

Variance of $\mathbf{Y}$ is expressed by

$$\mathrm{var}(\mathbf{Y}) = \hat{\beta}'\mathbf{S}\hat{\beta} \quad ,$$

where, $\mathbf{S}$ is termed the covariance matrix. (6)

Let $\hat{\lambda}$ to be the lagrangean multiplier and it will be turned out to be eigenvalues of $\mathbf{S}$, the problem is maximizing the function.

$$\phi = \hat{\beta}'\mathbf{S}\hat{\beta} - \hat{\lambda}\left(\hat{\beta}'\hat{\beta} - 1\right) \tag{7}$$

under the following condition,

$$\hat{\beta}'\hat{\beta} = \hat{\beta}_1^2 + \hat{\beta}_2^2 + \cdots + \hat{\beta}_p^2 = 1\,, \qquad (8)$$

The solution can be expressed by the equation.

$$\hat{\beta}'\mathbf{S}\hat{\beta} = \hat{\lambda} \qquad (9)$$

In this case rank $\mathbf{Y}$ equals NC. The rank $\mathbf{Y}$ is determined by examining the eigenvalues and eigenvectors of the square matrix of dimension NSxNS. If the spectra were free from noise, the PCA values would be equal to NC. It is necessary to search for the minimum number of base vectors by statistical method.

In Fig. 2, the spectral profiles of major components evaluated from magnitudes of eigenvalues were shown, where NW is equal to 512 and NC is equal to10. From the eigenvector, we can estimate the spectral matrix and the concentration of each position.

To analyze the observed spectra without references, the principal component analysis(PCA) appears to be a promising method.

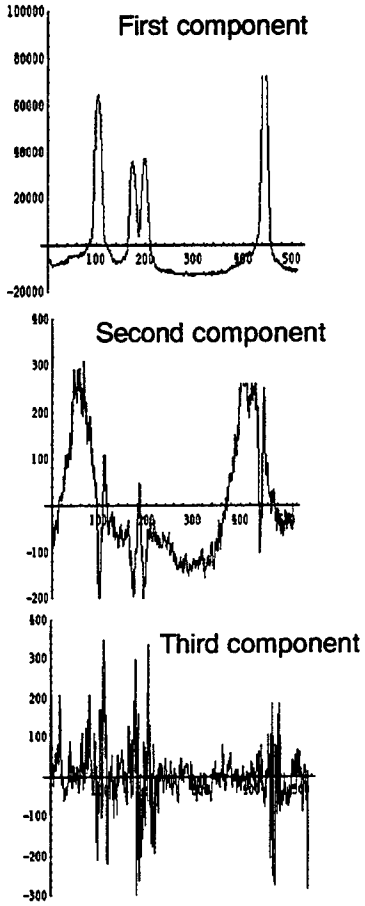

Fig. 2 Plots of major components of the spectral data obtained in C_2H_4/air flame.
The first component contains the stokes-Raman spectra of O2, C2H4, CO2 and N2 in the 370-390nm. A major portion of the second component turned out to be H_2CO .
The third component represents almost the noise level.

REFERENCES
1. K.Shibuya, R.A.Harger, and E.K.C.Lee,J.Chem.Phys.,69,751(1978)
2. Job, V.A.,Sethuraman,V. and Innes,K.K.,J.Mol. Spec.,vol.30,p365(1969)
3. A.C.Luntz,J. Chem. Phys. 69p3436(1934)
4. D.V.O'Connor and D.Phillips, Time-correlated single-photon counting(1985)Academic Press.
5. Yamagishi,S.Tsuchiya,M. 34th Symp.(Japan)on Combustion (1996)
6. S.Kawata,K.Sasaki,and S.Minami, J. Opt. Soc. Am. A(1987)p2101

THEORETICAL INVESTIGATION OF PHASE MATCHING SCHEMES FOR DEGENERATE FOUR-WAVE MIXING SPECTROSCOPY

Thomas A. Reichardt and Robert P. Lucht, Laser Diagnostics Laboratory, Dept. of Mech. and Ind. Engineering, University of Illinois, 1206 W. Green Street, Urbana, IL 61801 (Phone: 217-333-5056, Fax: 217-244-6534)

Introduction

Degenerate four-wave mixing (DFWM) spectroscopy is a potentially powerful technique for quantitative measurement of minor species in gas-phase media [1-3]. In this paper we compare the DFWM signal levels and lineshapes obtained using two different phase-matching geometries: the phase-conjugate geometry and the forward phase-matched geometry. DFWM signal levels are calculated by solving the time-dependent density matrix equations using direct numerical integration (DNI) [4, 5] for a two-level system interacting with three laser beams. This numerical analysis includes the effects of molecular motion, intermolecular collisions, and high laser intensities, all of which have been shown to affect the DFWM signal level.

Comparison of Forward Phase-Matching and Phase-Conjugate Geometries

Our previous investigations of DFWM spectroscopy using the DNI methodology have focused almost exclusively on the commonly-used phase-conjugate phase-matching geometry with counterpropogating pump beams (see Fig. 1(a)). A disadvantage of this geometry is that the signal level decreases as the square of the Doppler width in primarily Doppler-broadened environments. This is because the frequencies of all three input laser beams are Doppler shifted in the rest frame of a molecule moving along the laser beam axis. The probe and the forward pump beams have the same frequency (assuming a small crossing angle), but the backward pump beam has a different frequency in the molecular rest frame. The lasers will couple with the resonance effectively only with those molecules moving slowly enough that their Doppler shift is equal to or less than the collisional width of the resonance. If the ratio of Doppler to collisional broadening increases, the lasers will couple effectively with a smaller fraction of the molecules, leading to a decrease in signal level.

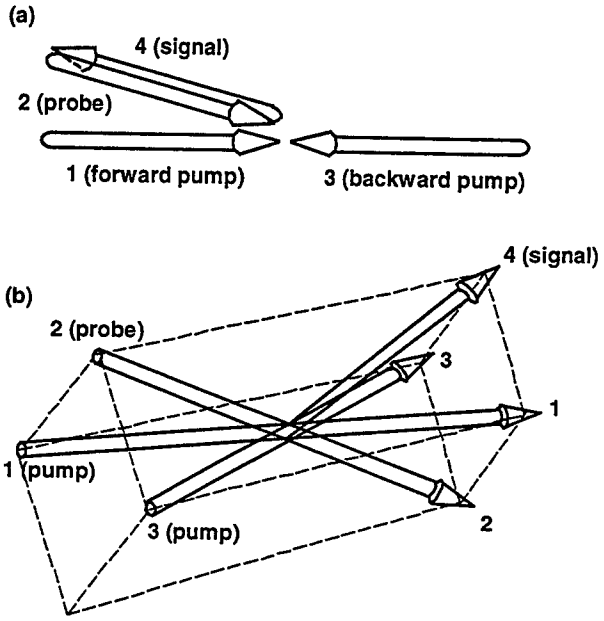

Fig. 1. Illustrations of (a) the phase-conjugate geometry and (b) forward-phase-matched geometry.

Another less-commonly-used phase-matching scheme is the forward-phase-matching configuration, illustrated in Fig. 1(b). With this geometry, the probe and two pump beams propogate approximately from the same direction into the probe volume, similar to the folded BOXCARS arrangement in coherent anti-Stokes Raman scattering (CARS). Because the Doppler shift is the same for each of the three input beams (assuming a small crossing angle), the lasers couple effectively with the molecules regardless of their velocity. Therefore, in primarily Doppler-broadened environments, we expect greater signals from the forward-phase-matched geometry. In addition, the forward-phase-matched geometry is expected to be more effective than the

phase-matched geometry in turbulent environments because it should be less sensitive to beam-steering effects [6].

Figures 2 and 3 compare the signal levels and lineshapes obtained using the phase-conjugate and forward-phase-matched geometries. For all the results displayed in this work, the population transfer rate Γ_{21} and the coherence dephasing rate γ_{21} are set equal to 5×10^9 sec^{-1} (resulting in a collisional width $\Delta\tilde{\omega}_C = \Delta\omega_C / 2\pi c = 0.053$ cm^{-1}), and the peak probe intensity (I_{pr}) is set equal to one-fourth the peak pump beam intensity (I_{pump}). For Fig. 2, the pump intensity is set equal to one percent of the saturation intensity of the resonance [3], while the Doppler width $\Delta\omega_D$ is varied so that $\Delta\omega_D / \Delta\omega_C = 0$ and 2. The spectra for the forward-phase-matched geometry are normalized so that the line center signals for both geometries are the same for the low-laser-intensity limit ($I_{pump} / I_{sat} = 0.01$) for homogeneous conditions ($\Delta\omega_D / \Delta\omega_C = 0$). The difference in the signal strengths obtained from the two geometries is discussed by Bervas et al. [7]. For the homogeneous low-laser-intensity limit displayed in the top figure, the two lineshapes are identical. As the Doppler width is increased such that $\Delta\omega_D / \Delta\omega_C = 2$, the line center signal decreases by a factor of 7 for the forward-phase-matched geometry, and a factor of 29 for the phase-conjugate geometry. The signal for the phase-matched geometry decreases more than the signal for the forward-phase-matched geometry because the beams interact more effectively with the resonance for the former geometry.

For Fig. 3 the laser intensity is varied such that $I_{pump} / I_{sat} = 0.1$, 1, and 10 while $\Delta\omega_D$ held constant. For the left column of figures, $\Delta\omega_D = \Delta\omega_C$, while for the right column $\Delta\omega_D = 2\Delta\omega_C$. Because the two gratings for the forward-phase-matched geometry constructively interfere, the lineshapes for this geometry demonstrate a greater degree of saturation. In particular, for $I_{pump} / I_{sat} = 10$, the lineshape for the forward-phase-matched case shows a significant dip at line-center due to saturation of the resonance.

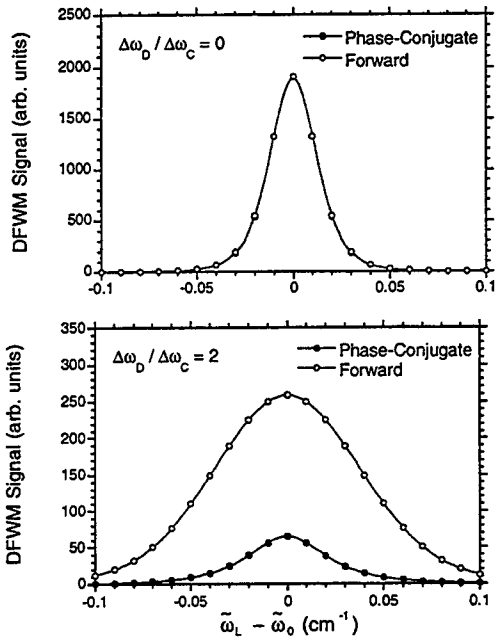

Fig. 2. Effect of molecular motion on the phase-conjugate and forward-phase-matched geometries. For both spectra, the pump intensity $I_{pump} = 0.01 I_{sat}$. The laser detuning is given as $\tilde{\omega}_L - \tilde{\omega}_0$, where $\tilde{\omega}_L = \omega_L / 2\pi c$ is the laser frequency (cm^{-1}) and $\tilde{\omega}_0 = \omega_0 / 2\pi c$ is the resonance frequency (cm^{-1}).

Summary

In a comparison between the phase-conjugate and forward-phase-matched geometries, we found the latter geometry to generate larger signal strengths for non-saturating laser intensities and also to display the effects of saturation at lower laser intensities. At higher laser intensities, we find that even for lines with significant Doppler broadening that phase-conjugate signals are comparable. These lineshapes will be compared to the results of a simplified analytical model of the DFWM process proposed by Farrow [8] which applies to the moderate saturation regime and includes Doppler broadening.

Acknowledgements

This work is supported by the U.S. Department of Energy, Office of Basic Energy Sciences, Division of Chemical Sciences, under grant DE-FG02-94ER14469. The contract is managed by William H. Kirchhoff and Andrew E. DePristo (interim). T. A. Reichardt

gratefully acknowledges the support of graduate fellowships from the Link Foundation and DuPont.

References

[1] A. C. Eckbreth, *Laser Diagnostics for Combustion Temperature and Species*, 2nd ed. Gordon and Breach, Amsterdam, The Netherlands, 1996.

[2] K. Kohse-Höinghaus, Prog. Energy Combust. Sci. **20**, 203-279 (1994).

[3] R. L. Farrow and D. J. Rakestraw, Science **257**, 1894-1900 (1992).

[4] R. P. Lucht, R. L. Farrow, and D. J. Rakestraw, J. Opt. Soc. Am. B **10**, 1508-1520 (1993).

[5] T. A. Reichardt and R. P. Lucht, J. Opt. Soc. Am. B **13**, 1107-1119 (1996).

[6] K. Nyholm, M. Kaivola, and C. G. Aminoff, Opt. Commun. **107**, 406-410 (1994).

[7] H. Bervas, S. Le Boiteux, L. Labrunie, and B. Attal-Tretout, Molecular Phys. **79**, 911-941 (1993).

[8] R. L. Farrow, Combustion Research Facility, Sandia National Laboratories, Personal communication (1997).

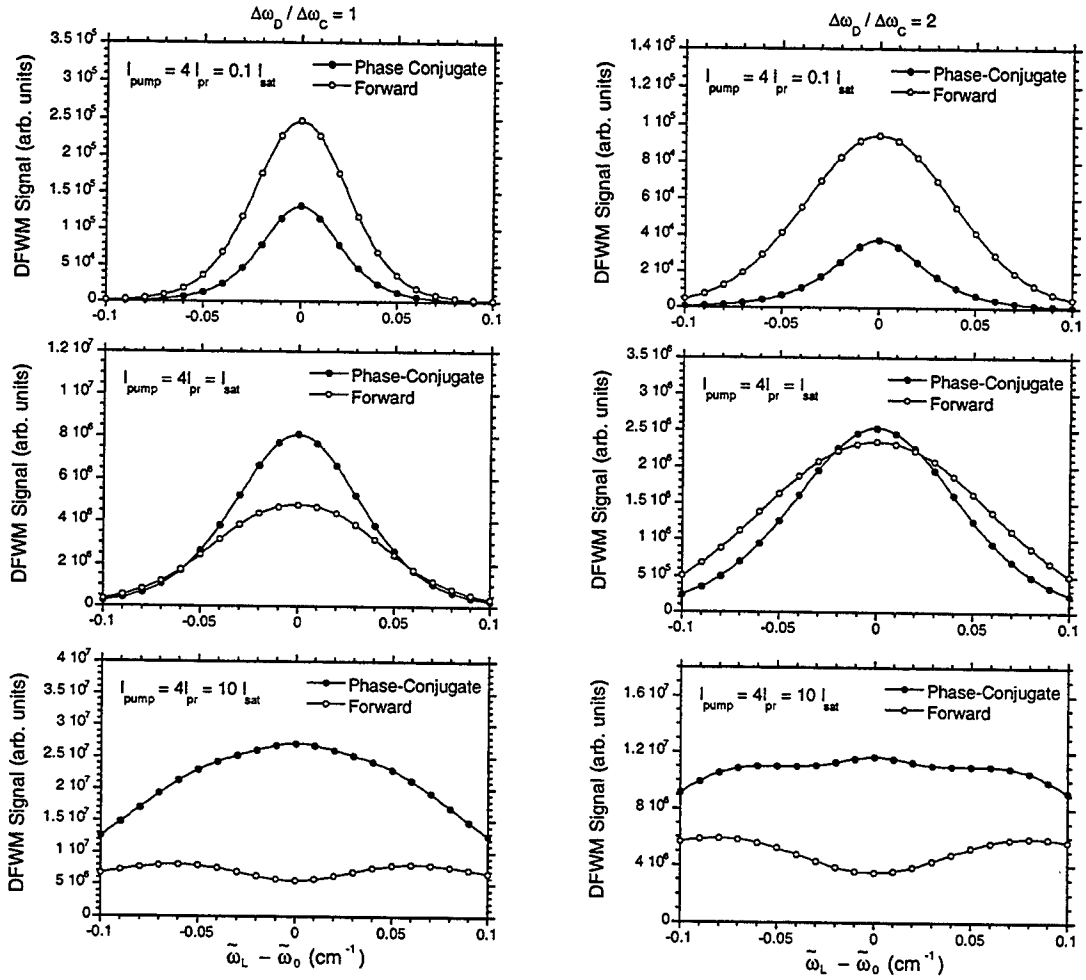

Fig. 3. Effect of saturation on a resonance that is both collision- and Doppler-broadened. For figures on the left $\Delta\omega_D = \Delta\omega_C$, while for the figures on the right $\Delta\omega_D = 2\Delta\omega_C$.

Laser Applications to Chemical and Environmental Analysis

Diode-Laser Sensors for Combustion Monitoring

Wednesday, March 11, 1998

Kay Niemax, Institute of Spectrochemistry and Applied Spectroscopy, Germany
Presider

LWB
10:30am–11:30am
Coral Room

Diode-laser sensor system for combustion monitoring

R.M. Mihalcea, D.S. Baer, R.K. Hanson
High Temperature Gasdynamics Laboratory
Department of Mechanical Engineering
Stanford University, Stanford, CA 94305-3032

A diode-laser sensor system, comprised of a tunable external-cavity diode laser (ECDL) operating near 2.0 μm and fiber-optic components, has been developed to measure the gas temperature and the concentrations of CO_2 and H_2O in the combustion and exhaust regions of a flat-flame burner (C_2H_4/air) using absorption spectroscopy techniques. The present system extends the techniques developed previously[1-4] for the measurement of H_2O and CO_2 by probing relatively stronger vibrational bands and thus offers higher measurement sensitivity. Measurements of individual transitions (1-cm^{-1} scans) were recorded by adjusting the internal grating to particular center wavelengths and by applying a 6-volt sawtooth voltage waveform at a 1.25-Hz repetition rate to the wavelength modulation input. Temperature may be determined either from the ratio of measured H_2O ($\nu_1+\nu_2$, $\nu_2+\nu_3$ bands) or CO_2 ($\nu_1+2\nu_2+\nu_3$ band) absorbances. Species (H_2O, CO_2) concentrations were determined from the measured temperature and absorbances of appropriate transitions recorded by tuning the ECDL wavelength across selected transitions within the 250 cm^{-1} laser tuning range centered at 2.02 μm.

Figure 1 is a schematic of the experimental setup consisting of the burner, the fast-sampling apparatus, and the diode-laser system. A water-cooled, premixed, flat-flame burner (McKenna) with a 6-cm diameter served as the combustion test facility. Measurements were recorded both in the burned gases near the flame and in the exhaust region. For the flame measurements, the beam was directed through the flowfield using a fiber-coupled GRIN lens. For measurements in the exhaust region, the fast-sampling system consisting of a water-cooled probe and a multi-pass, 36-meter path flow-through cell was used to extract a portion of the combustion products at various distances along the burner axis (at a rate of ≈0.4 liters/sec) for increased measurement sensitivity.

An on-line data analysis system was used for real-time analysis of the recorded signals which included the difference between the laser transmission (through the flowfield or multipass cell) and reference intensities ($I-I_0$), reference laser intensity (I_0), and etalon transmission intensity. A Pentium personal computer served as a computational platform using LabVIEW® as the graphical programming language.

Figure 2 illustrates a measured CO_2 survey spectra recorded in a 20-cm heated quartz cell at 1360 K by tuning the ECDL across the $\nu_1+2\nu_2+\nu_3$, $4\nu_2+\nu_3$, $2\nu_1+\nu_3$ bands. The spectra will be compared with the HITRAN96 and HITEMP databases and used to determine the appropriate CO_2 transitions for thermometry and mole fraction measurements. Similar absorption measurements will be performed for H_2O in this spectral region.

The sensor system may be applied to probe additional species by measuring other species which also absorb appreciably within this spectral region (e.g., N_2O and NH_3) and thus is very well suited for a variety combustion diagnostics and control applications.

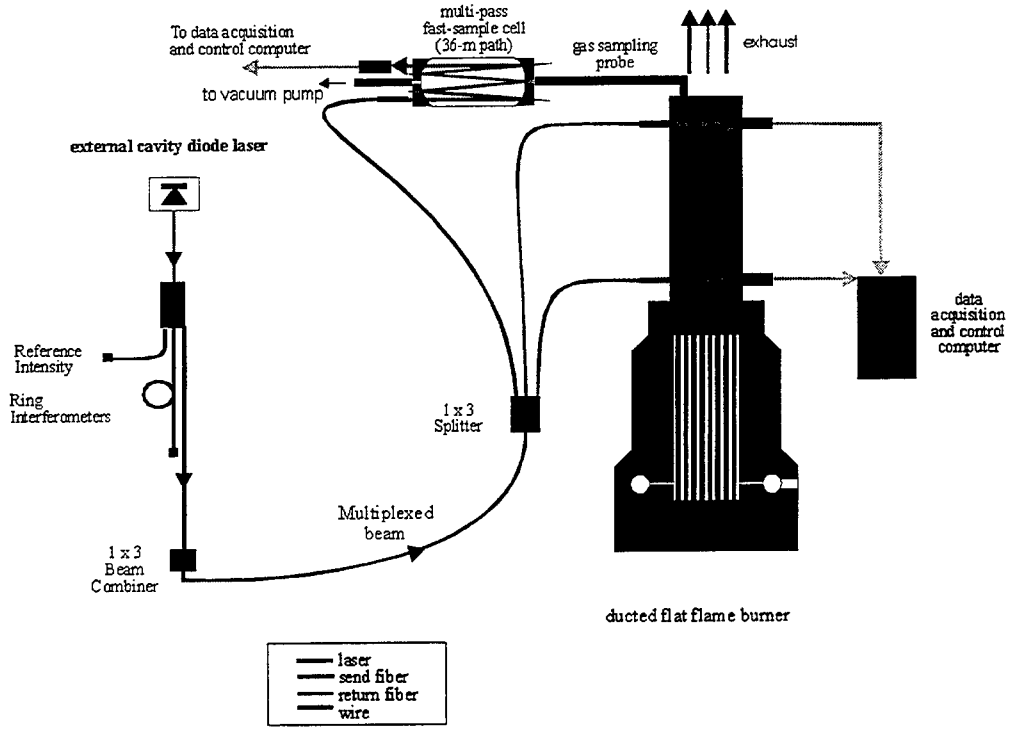

Figure 1. Schematic diagram of the sensor system used to measure CO_2 and H_2O absorption near 2.0 μm for the determination of gas temperature and species mole fractions in a combustion system.

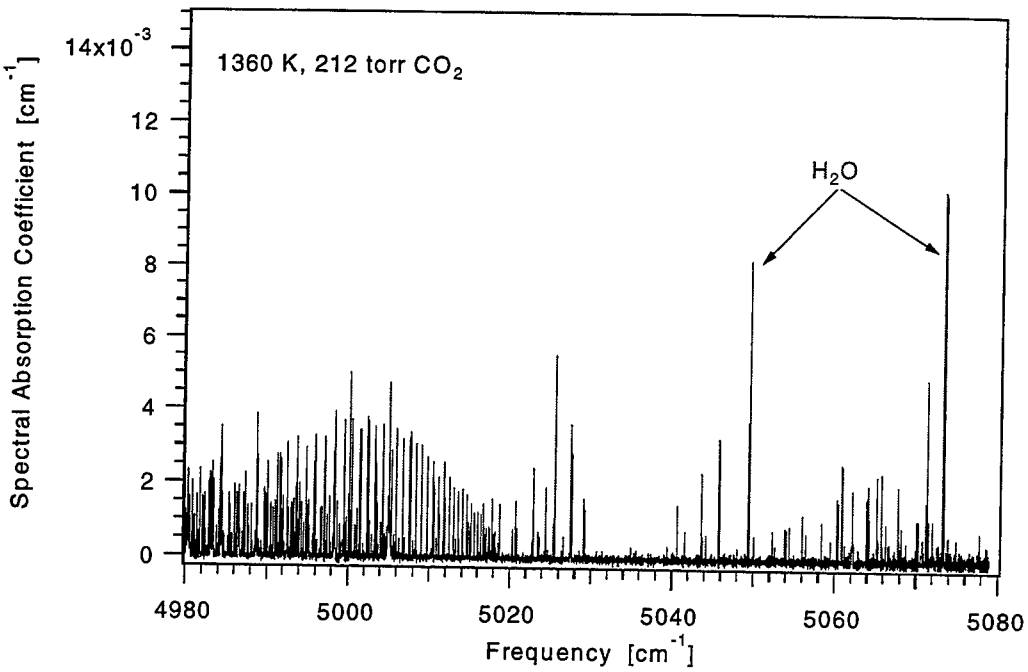

Figure 2. Measured CO_2 survey spectra ($\nu_1+2\nu_2+\nu_3$, $4\nu_2+\nu_3$, $2\nu_1+\nu_3$ bands) recorded over the 4980-5080 cm^{-1} region in a heated quartz cell (1360 K, 212 torr, 20-cm path).

References:

1. E.R. Furlong, D.S. Baer, and R.K. Hanson, "Combustion control using multiplexed diode-laser absorption sensors," *26th Symposium (International) on Combustion*, Naples, 1996.

2. E.R. Furlong, D.S. Baer, R.K. Hanson, "Real-time process control using diode-laser absorption sensors," *Proceedings of the SPIE (Denver)*, 1996, paper #2834-29.

3. E.R. Furlong, R.M. Mihalcea, D.S. Baer, and R.K. Hanson, "Measurement and control of temperature and CO using multiplexed diode lasers," SPIE Optical technology in fluid, thermal, combustion flows III San Diego, paper 3172-33 (July 1997).

4. R.M. Mihalcea, D.S. Baer, and R.K. Hanson, "Diode-laser absorption sensor system for measurements of combustion pollutants," Measurement Science and Technology (submitted for publication July 1997).

Near -Infrared Tunable Diode Laser Diagnostics in Laboratory and Real-Scale Inhibited Flames

Kevin L. McNesby, Robert G. Daniel, R. Reed Skaggs, and Andrzej W. Miziolek
U.S. Army Research Laboratory
Craig S. Miser
U.S. Army Aberdeen Test Center
Aberdeen Proving Ground, MD 21005

The goal of this research project is to develop and demonstrate/validate new laser-based instrumentation for the measurement of concentrations of candidate suppressants, oxygen, fuels, and combustion byproducts during suppression of flames and explosions. Time resolved measurement of concentrations of suppressants, oxygen, fuels, and combustion byproducts serve as a check on the repeatability of the tests and help determine why a suppressant is behaving well or poorly in a given full-scale suppression test.

The approach used in the investigation of gas species produced during suppression of crew and engine compartment fires involves a close interaction between laboratory based combustion diagnostics facilities currently in place at ARL and similar, ruggedized, facilities in place at ATC. Instrument utility, response, and quantitative calibration are performed at ARL prior to application of a particular technique to large scale fire scenarios. This protocol has been used successfully for the quantification of HF gas produced during chemical inhibition of JP-8 fuel pool fires[1].

Key benefits to implementation of laser-based sensing devices derive from real-time sensing and the ability to use multiple sensors from a single laser source. Real time sensing is important because it provides information on how and at what rate fuel and oxidizer are consumed, the time required following agent release for suppressant to be effective, and the rate at which toxic gases are produced during a suppression event. Typically, fire suppression on-board military vehicles is accomplished within 250 milliseconds of fire detection. Gases measured using NIRTDL absorption spectroscopy include HF, CO, CH_4, O_2, NO_2, and H_2O. Use of multiple sensors, enabled because the lasers and detectors are fiber coupled, is required because of the need to know how well a given agent suppresses a fire at different locations within the vehicle. Together, the use of real-time sensing and multiple sensor measurement provide a means to judge why a suppressant behaves the way it does in different fire scenarios.

Examples will be presented of NIRTDL absorption spectroscopy of several gases in laboratory-scale, atmospheric pressure opposed flow flames and in full scale testing on board military vehicles (see Figure 1).

1. Applied Optics, vol. 35, p4004 (1996).

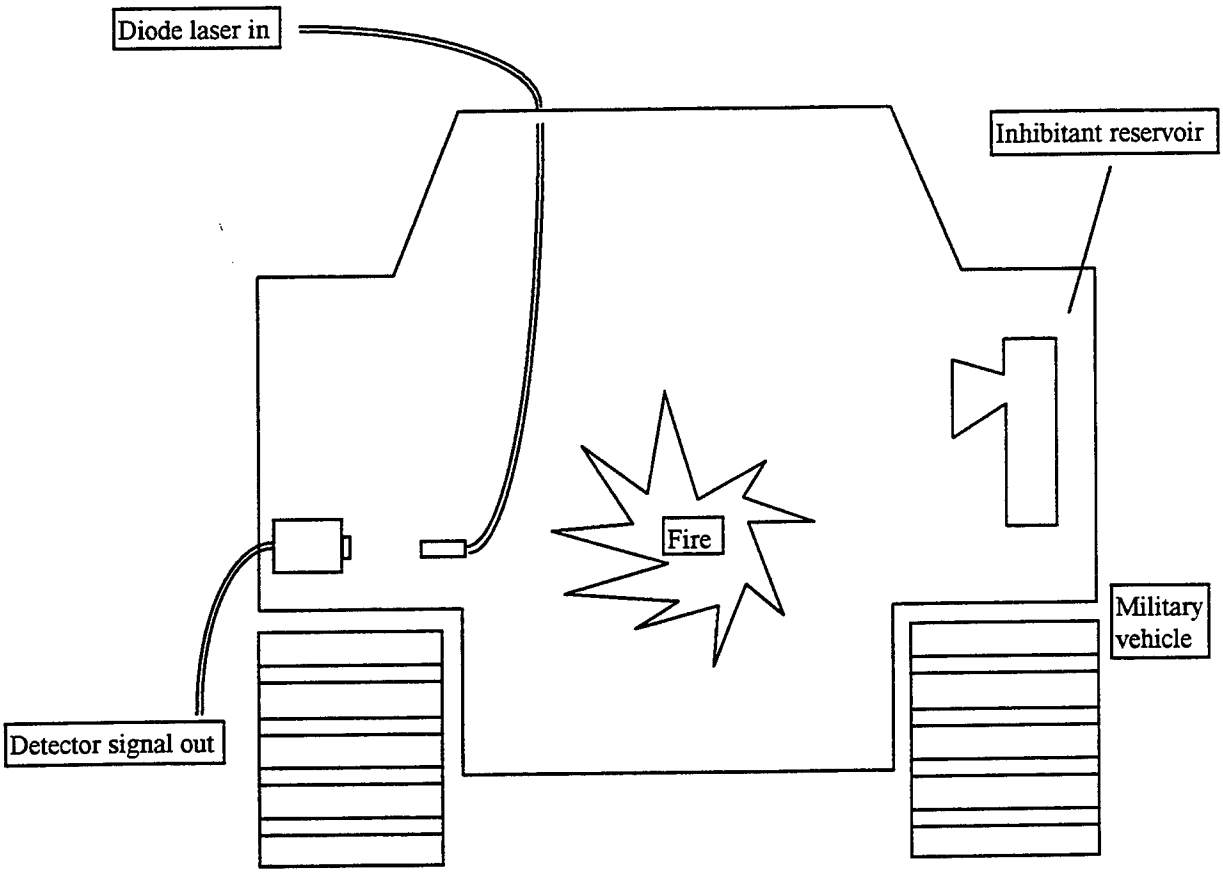

Figure 1: Schematic of experimental setup for measurement of combustion species produced during suppressant testing on board military vehicles.

In-situ Oxygen-Monitoring using Near-Infrared Diode Lasers and Wavelength Modulation Spectroscopy

V. Ebert, K.-U. Pleban, J. Wolfrum
Institute of Physical Chemistry, University of Heidelberg,
Im Neuenheimer Feld 253, 69120 Heidelberg, Germany
Phone: 00-49-6221-544258, Fax: 00-49-6221-544255
e-mail: volker.ebert@urz.uni-heidelberg.de

Despite increasing recycling quota the removal or long time storage of the remaining municipal waste remains a difficult task. This is valid especially in densely populated countries like Germany or Japan where there is little space for waste disposal sites. Hence waste combustion is used as a effective way to reduce the waste volume and to utilize the energy stored therein. However due to the large inhomogeneities of the refuse its combustion is a very demanding task. To minimize emission of pollutants and corrosion damage and to optimize energy production simultaneously fast in-situ diagnostics and active combustion control systems, like TACCOS [1], a thermography system based on an mid-infrared scanner camera which directly measures local imbalances in the fuel bed temperature or LISA [2], a CO_2-laser based in-situ ammonia sensor used for on-line control of NO_x removal systems (SNCR or SCR), are required. A very promising tool for the development of fast in-situ sensors are tunable diode lasers. They are inexpensive, compact, rugged, and relatively simple to operate. Due to their fast tunability, high spectral resolution and spectral power density they offer the opportunity for specific, nonintrusive, chemical sensors with a fast time response making them attractive for active combustion control. Since oxygen is one of the most important molecules for all combustion processes and not accessible by alternative optical detection methods there is a strong need (e.g. to adapt the secondary air flow or distribution in incinerators or other combustors) for a fast in-situ oxygen sensor which can measure at high temperatures and close to the reaction zone. Hence in a first attempt we tried to develop a diode laser based in-situ oxygen sensor which had to be fast enough for active control purposes e.g. in incinerators.

Experimental Details

The spectrum of molecular oxygen in the near infrared shows only a few very weak bands (A, B, γ, δ). They belong to vibrational subtransitions of the $b^1\Sigma_g^+ \leftarrow X^3\Sigma_g^-$ magnetic dipole transition and reach in the case of the A-band (759-770nm) line strengths of about $2 \cdot 10^{-4}$ cm^{-1} atm^{-1} at 300K. With increasing temperature the maximum absorption coefficient is decreasing even further. For a typical in-situ application (4m path, 800°C, 10Vol.-% O_2) the peak fractional absorption by O_2 is below 1%. In addition to that severe and strongly varying interferences (like radiation emission, broad band absorption by dust, or beam deflection by index of refraction fluctuations) are caused by the in-situ absorption path. They can can lead to transmission fluctuations which are orders of magnitude larger than the required absorption resolution. Until the absorber density or concentration can be extracted from the absorption signal, it has to be precisely corrected for these transmission changes. We report an approach to these corrections using wavelength modulation spectroscopy and harmonic detection. The setup used is shown in

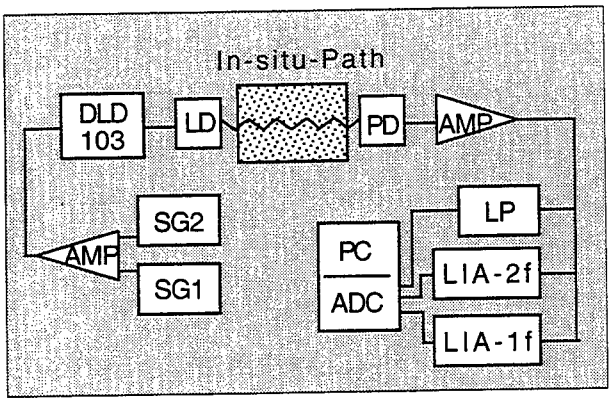

Fig.1: Schematics of the O_2-in-situ-sensor

figure 1. The signal generators (SG1+2) and the summing amplifier are used to modulate the current (and hence the wavelength) of the laser diode (LD) simultaneously with a slow ramp (9Hz) and a fast sinusoidal modulation (41kHz) via the laser diode driver (DLD103). The modulated laser light is collimated, guided through the in-situ path, and detected and converted into a current signal by the photodiode (PD) and the preamplifier. Two analog lock-in amplifiers (LIA1+2) are used to demodulate the first and second harmonic of the absorption signals simultaneously. Both waveforms are digitized with a 12-bit ADC and can be averaged and stored in a PC. Even though inexpensive Fabry-Perot-type laser diodes are available for the A-band of O_2 we decided to use the more expensive, but continuously tunable distributed feedback laser (DFB-DL) to avoid the severe restrictions on the design of the sensor caused by the discontinuous tuning behaviour of the FP-type. Even under in-situ conditions it was possible to record the complete 2f spectrum of the band head of the R-branch wit a DFB-DL as shown in figure 2 and select any of the lines.

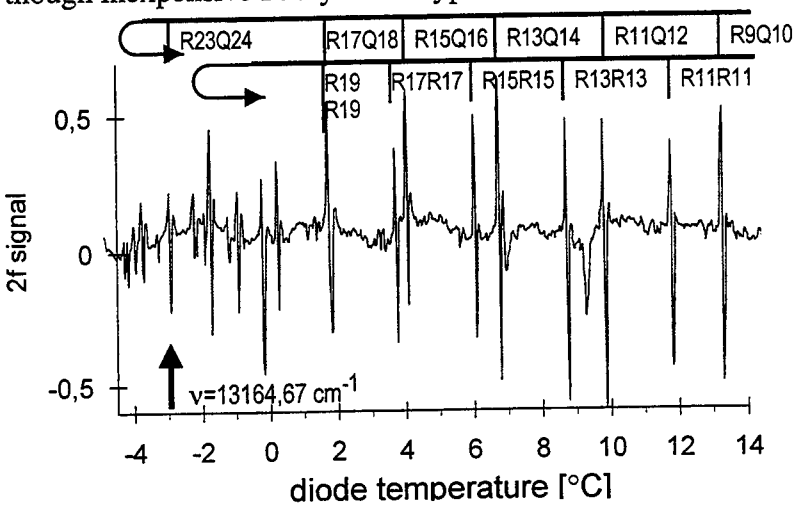

Fig.2: In-situ O_2-absorption spectrum in a 20 MW incinerator gained by temperature tuning of the DFB diode laser

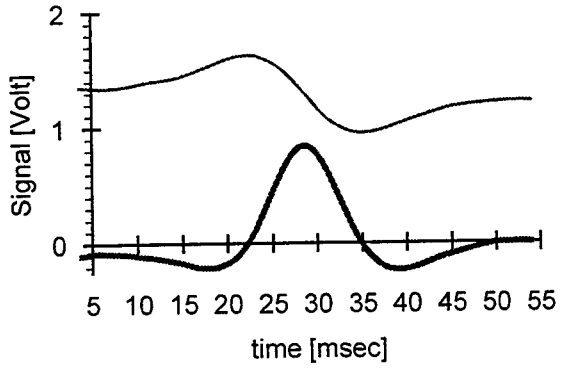

Fig.3: Derivative in-situ O_2-absorption signals gained by current tuning of the laser

Data Analysis and Results

Typical 1f and 2f in-situ signals recorded under standard load conditions in a 20 MW_{th}-incinerator with a cross section of 4x4m are shown in figure 3 (an average over 20 scans or 2 sec is shown). The recorded 1f and 2f signals have not been corrected for transmission fluctuations. But since they both have been measured simultaneously they should be distorted in the same way. Due to the high amplitude modulation (AM) of the laser, which is a result of the steep L-I-curve of the laser diode, the 1f component shows a significant positive offset. As the laser wavelength is current scanned over the absorption line this offset (or AM) should be constant - a consequence of the linearity of the L-I-curve- and is only be-

ing changed by transmission fluctuations. The constant AM is therefore used to sense the variations in the transmission of the in-situ path. In removing the portion of the 1f signal which is caused by the O_2 absorption line the remaining offset can be used to do a point by point transmission correction of the 2f line shape. The removal of the resonant 1f contributions is realized by applying a fit to the 1f signal assuming a Lorentzian and subtracting the fitted resonant 1f contribution. The resulting time dependent 1f offset is then used to correct the 2f signal before the oxygen concentration is extracted from the corrected 2f signal with another fit to the corrected 2f line shape. As a result of this procedure transmission drops down to 40-50% could be removed with little effect on the O_2-signal.

A test of this setup was performed in a full scale waste incinerator (20 MW_{th}). Due to the lack of adequate in-situ oxygen sensors the laser signal (thin line) could only be compared to a relatively slow ZrO_2-sensor (thick line) located about 45 m downstream of the laser measurement plane in the cold fluegas duct. The result of this comparison is shown in figure 4. As expected the laser sensor shows a much quicker time response (time resolution 3 sec) indicated by the steeper O_2-changes. It is about 25 to 35 sec faster than the reference sensor (no gas transport to the sensor). Assuming that the temperature did not vary significantly in the detection volume (thermocouples indicated a ± 25 K variation over the full 40 min.) the laser resolves concentration fluctuations in the order of 0.1 Vol% and shows that fast O_2 variations are underestimated by the ZrO_2-sensor either due to the slow response of the reference sensor or due to mixing effects.

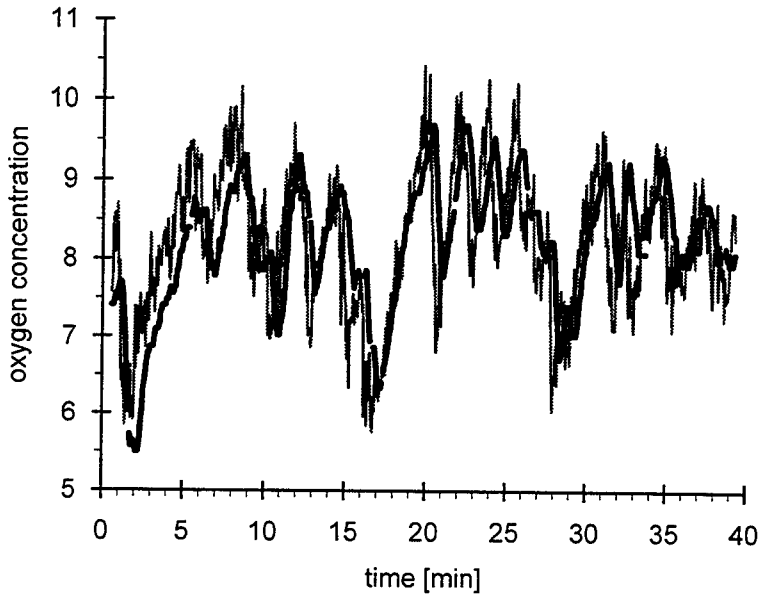

Fig.3: Comparison of the laser in-situ O_2 absorption signal (thin line) and the ZrO_2-sensor (thick line) gained at a 20MW incinerator

Conclusions: It has been shown that even under strong transmission fluctuations -characteristic for in-situ applications- wavelength modulation spectroscopy can be used to quantitatively determine oxygen concentration in a full scale waste incinerator, if the 2f signal is normalized by the offset in the 1f signal. In the demonstrated case the laser signal is about 30 sec faster than any available method and shows superior time response. Based on this results active combustion control for incinerators or other large scale combustion systems via the O_2-content in the fluegas seems feasible and will be approached in the near future to allow e.g. secondary air control. The detection scheme can be fairly easy adapted to other species like CH_4 or NH_3 by changing the laser diode and the detector.

[1] F.Schuler, F.Rampp, J.Martin, J.Wolfrum ; "TACCOS- A Thermography-Assisted Combustion Control System for Waste Incinerators.", Combustion and Flame 99: 431-439 (1994)

[2] Meienburg, W., Wolfrum, J.: 23 rd Symp. (Int.) on Combustion, The Combustion Institute, Pittsburgh, 231 (1990)

In-Situ Measurements of Combustion Species Using Near-IR Diode Laser Sensors

Mark G. Allen, Bernard L. Upschulte, David M. Sonnenfroh
Physical Sciences Inc.
20 New England Business Center
Andover, MA 01810
tel: 978.689.0003 fax: 978.689.3232 e-mail: allen@psicorp.com

The rapid improvements in room-temperature diode laser technology for communications and data storage applications has given rise to a entirely new class of potential optical sensors for species composition and gasdynamic parameter measurements. These sensors are finding widespread application to chemical processing, environmental monitoring, and, increasingly, aerodynamic and propulsion needs. High quality devices are now commercially available in a number of discrete spectral windows between 630 nm and 2.0 μm. For aerodynamic and propulsion applications, most activity to date has focussed on O_2-based measurements using 763 nm AlGaAs lasers and H_2O-based measurements using 1.31 to 1.39 μm InGaAsP lasers. These devices are characterized by a rapid time response, extreme sensitivity, and opto-mechanical robustness consistent with practical industrial installations.

The sensors are based on the path-integrated absorption of the diode laser radiation. A fortuitous coincidence of transitions between 1.5 and 2.0 μm allows a small number of lasers to monitor CO, OH, H_2O, and CO_2, important intermediate and product species in hydrocarbon-fueled combustion systems. Multiple transitions may be probed for simultaneous temperature measurements. The Doppler shift of the molecular absorption feature with respect to a known stationary frequency can be used to determine the velocity and mass flux. Using fiber-optic delivery systems, a single laser and detector can monitor multiple stations, thereby reducing capital costs, maintenance, and calibration requirements. Remote citing also allows the sensor to make reliable measurements in harsh industrial or engineering environments. By scanning resolved absorption transitions, the sensor provides pressure-independent concentration data and is relatively immune to aerosol, particulate, or other broad spectral interference sources.

A significant technical goal of the present work was to demonstrate the application of a new diode laser architecture to gas sensing. In a typical single-section DFB laser, an index grating is fabricated above or within the laser gain region, providing wavelength-selective feedback to force the cavity to oscillate in a single and narrow mode. Rapid wavelength tuning of this mode is accomplished by modulating the injection current into the gain medium. The principal effect of the injection current modulation is to modulate the refractive index of the gain medium, thereby changing the optical period of the grating and, hence, the output wavelength. Because the current is also pumping the laser gain, the maximum available current tuning range is constrained between lasing threshold at the low end and output facet damage at the high end. A large power modulation (or amplitude modulation) is also inevitable with current modulation in single-section lasers. The best available DFB lasers typically exhibit maximum current tuning ranges on the order of 3 cm^{-1}. This range is sufficient to scan a single, atmospheric-pressure-broadened lineshape, but is rarely capable of resolving more than one

lineshape. Hence, the general approach to multi-species detection is to apply a separate laser for each species.

In contrast, we used a multi-section, Grating-Coupled Sampled Reflector (GCSR) laser that consists of four electrically-isolated sections fabricated using conventional InGaAsP laser materials. The gain section includes the output facet and the InGaAsP active layer. The rear-section consists of a periodically-modulated Bragg-reflector. In a conventional DFB or DBR laser, a single-period Bragg grating provides wavelength feedback (or reflectivity) at a single frequency peak. The periodically-modulated Bragg-grating produces a comb of reflectance peaks. The coupler section consists of single-period Bragg-grating with a broad spectral transmission peak. This section is designed so as to transmit only a single peak from the comb spectrum of the rear-reflector. The final phase section provides a small optical phase adjust to correct for round-trip phase accumulation within the cavity.

The various laser sections provide a flexible and wide tuning control. At a fixed value of gain and phase section injection current, the coupler and reflector sections can be tuned to access 10's of nm of tuning range - far larger than with any conventional single section laser and comparable to bulky external cavity lasers. Figure 1 shows a typical tuning surface of the particular laser we ordered from Industrial Microelectronics Center (IMC) in Kista, Sweden. This data was acquired with a fixed gain and phase section currents and at a fixed laser temperature of 20°C. As the coupler current increases for a fixed reflector current, the output wavelength tunes discontinuously across the reflection peaks of the super-structure DBR grating. At a fixed coupler current, the reflector current can be varied to sweep the output wavelength

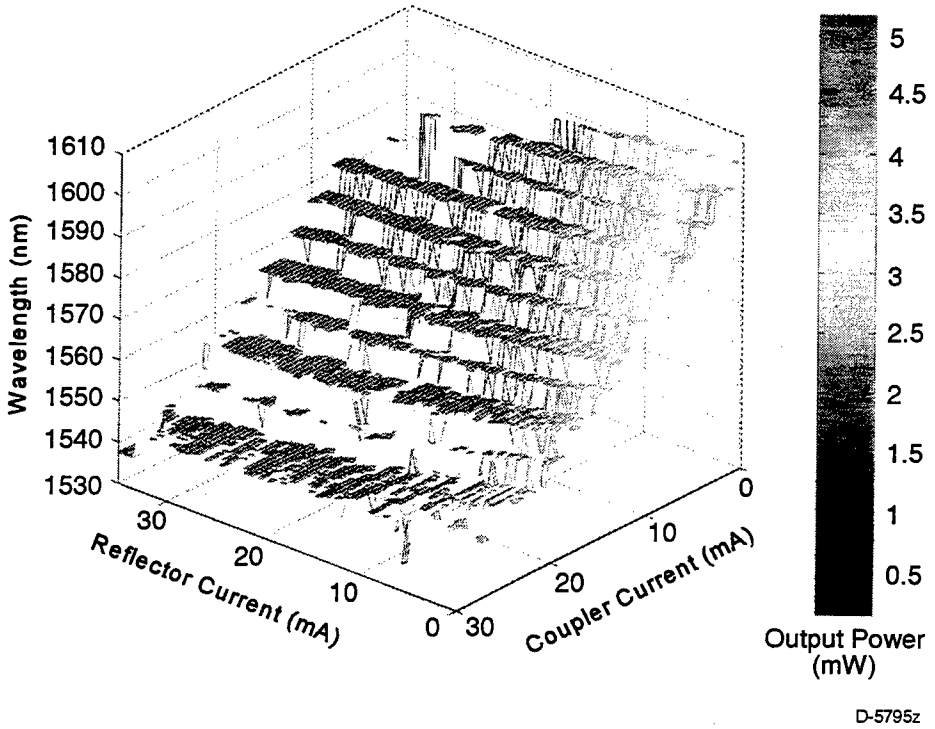

Figure 1. Example GCSR laser tuning surface.

across the transmission bandpass of the grating coupler. The reflector current variation introduces minimal output power variations, although high coupler currents reduce output power considerably because higher electron densities result in a high optical loss in the laser cavity. Any of these currents can be selected on micro-second time-scale, allowing the laser to select any wavelength within this space at 10's of kHz rates. This laser is fabricated out of conventional InGaAsP materials, so it should be straightforward to achieved ~ 100 nm tuning anywhere between about 1.3 and 2.0 μm with other lasers.

Measurements of several gases were demonstrated in room-temperature and combustion gases. The combustion measurements were completed above a flat-flame burner with separate methane, oxygen, and nitrogen flow control. The fuel-air stoichiometry of the flame was adjusted to vary the concentration of target compounds and the overall flame temperature. A multi-pass mirror arrangement was added to increase the total absorption pathlength in the 2.54 cm cross-section burner to 71 cm. As an example, we report *in-situ* measurements of the CO molecule using the R24 transition of the (3,0) overtone band at 6412.06 cm^{-1} (1.560 μm). Figure 2 shows the measured CO concentration as a function of fuel-air equivalence ratio. The concentration was determined from the integrated area of the absorption lineshape and calibrated against the equilibrium flame concentration at an equivalence ratio of 1.5. The equilibrium behavior of CO is shown as a solid line, in good agreement with the measured values.

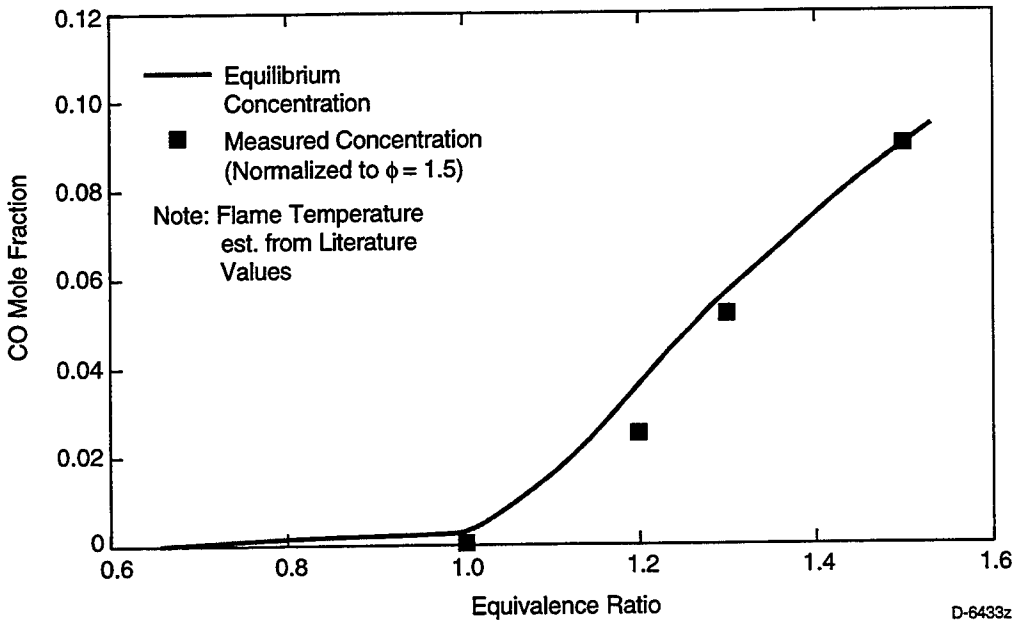

Figure 2. Example *in-situ* measurements of flame CO concentration.

The presentation will discuss these and other measurements of CO_2, OH, H_2O, as well as two-line absorption thermometry based on OH. Applications to practical combustor, aeroengine, and utility furnaces will also be described.

Key to Authors and Presiders

Laser Applications to Chemical and Environmental Analysis

Postdeadline Papers

March 9–11, 1998

Sheraton World Resort Orlando
Orlando, Florida

CONTENTS

High sensitivity CO_2 detection based on a 2 μm room temperature diode laser

P. Werle[1], R. Mücke[1], F. D'Amato[2] and T. Lancia[3]

[1] *Fraunhofer-Institute for Atmospheric Environmental Research, D-82467 Garmisch-Partenkirchen, Germany (Fax :+49-8821/73573, E-mail : Werle@ifu.fhg.de)*

[2] *Ente per le Nuove tecnologie, l'Energia e l'Ambiente (ENEA), Frascati (Roma), Italy*

[3] *Tecsa Ricerca & Innovazione srl (TRI), Scanzorosciate (BG), Italy*

Abstract. Experimental data from a CO_2 monitor designed for field applications using room temperature diode lasers are presented. Near-infrared DFB-lasers operating at 1.57 μm and around 2.0 μm have been used for CO_2 measurements. At ambient concentration levels a resolution of more than two orders of magnitude has been demonstrated at 1.57 μm, at 2 μm the precision is in the order of 0.1 ppm CO_2, and for trace analysis a detection limit of 10 ppb has been obtained. The measurements demonstrate the suitablity of near-infrared DFB-diode lasers for the precise determination of CO_2 concentrations as required for climatological, medical or industrial applications.

When semiconductor lasers were first introduced in the mid-1960s they found immediate application as much needed tunable sources for high-resolution infrared laser absorption spectroscopy and now, more than three decades later, laser based analysis techniques are at the threshold of routine applications in environmental monitoring and industrial process gas analysis. The features of diode laser spectroscopy rendering it such a valuable technique for gas analysis are that it is specific and as a high resolution spectroscopic technique it is virtually immune to interferences by other species. Modulation techniques allow absorptions as low as 1 part in 10^6 to be measured within a 1 Hz bandwidth [1]. While mid-infrared (lead-salt) lasers operated at cryogenic temperatures cover the fundamental absorption bands required for ultrasensitive gas analysis, near-infrared room temperature diode lasers give access mainly to significantly weaker overtone and combination bands. Therefore, the selection of the optimum operating conditions for a gas analyzer is always a trade off between the required sensitivity and an operational system. Historically, most applications have been reported in the field of atmospheric research, where still better and faster instrumentation is required. Many of these applications require instruments with higher time resolution and better sensitivities.

CO_2	*Wavelength λ*		*Linestrength*	*Detection limit*	
Band	[cm^{-1}]	[μm]	[cm/molec]	[pptv]	[$\mu g/m^3$]
$3\nu_3$	6983.019	1.432	$6.043 \cdot 10^{-23}$	$73 \cdot 10^3$	144
$2\nu_1 + 2\nu_2 + \nu_3$	6359.968	1.572	$1.846 \cdot 10^{-23}$	$220 \cdot 10^3$	430
$\nu_1 + 4\nu_2 + \nu_3$	6240.105	1.603	$1.838 \cdot 10^{-23}$	$235 \cdot 10^3$	461
$2\nu_1 + \nu_3$	5109.311	1.957	$4.003 \cdot 10^{-23}$	$107 \cdot 10^3$	210
$\nu_1 + 2\nu_2 + \nu_3$	4989.972	2.004	$1.332 \cdot 10^{-21}$	$3.1 \cdot 10^3$	6.1
$\nu_1 + \nu_3$	3597.963	2.779	$3.525 \cdot 10^{-20}$	110	0.22
ν_3	2361.466	4.235	$3.524 \cdot 10^{-18}$	2	0.003

Table 1 : TDLAS detection limits for CO_2 in the mid and near infrared.

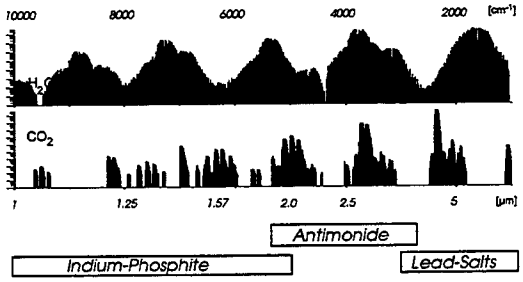

Figure 1 : Coverage of the spectral regions from near- and mid infrared region by different semiconductor materials.

The current great interest in carbon dioxide results from the observed rise of its atmospheric concentration and its importance for the greenhouse effect, due to its significant role in determing the heat balance of the atmosphere [2]. The actual average ambient concentration of CO_2 is about 350 ppm, compared to about 280 ppm before the industrialization era. An increase of the average temperature by 2 - 3 K is expected by doubling of the CO_2 concentration. Therefore, it is very important to quantify sources and sinks of carbon dioxide, especially the not well known influence of seas as sinks. To perform climatological studies the resolution of the ambient CO_2 level should be in the order of 10^{-4} or about 0.1 ppm with a time resolution of 0.1 s for flux measurements or about 10 s for long term measurements. In order to reach these requirements an instrument based on diode laser FM-spectroscopy has been built up. Some molecular absorptions that can be used to detect CO_2 using mid- and near-IR diode lasers is listed in Table 1, where the detection limit in terms of volume mixing ratio [ppt] is shown based upon an absorbance sensitivity of 10^{-6} @ $\Delta f = 1$ Hz and 25 m optical path-length. By averaging over periods longer than 1 sec or by using longer path-lengths the detection limits can be improved. While the predicted sensitivities are based on known line strengths and the performance of a typical FM-system, it is in the nature of field measurements that optimum performance is not always achieved. However, the 2 μm spectral region seems to be the best choice for a fieldable instrument. In Fig. 1, where the absorption bands of CO_2 are displayed in the spectral range from 1 to 10 μm together with water vapor, which might interfere for atmospheric measurements. For many field applications the use of liquid nitrogen must be avoided, only temperature stabilization by thermo-

electrical elements is acceptable. Therefore, in a recently developed fast CO_2 sensor we implemented InP-DFB-lasers with single-mode emission at $\lambda \leq 2$ µm together with InGaAs-detectors. The selection of the absorption lines suitable for precise CO_2 measurements is determined by interferences to other gases, mainly H_2O, and the availability of laser sources. As displayed in the top of Fig.1, stronger absorption bands exist around 1.44, 1.57, 1.6 and around 2 µm, but then the influence of H_2O has to be taken into account. The strongest CO_2 absorption lines in the near-infrared region can be found around 2 µm, but there also the influence of H_2O has to be considered.

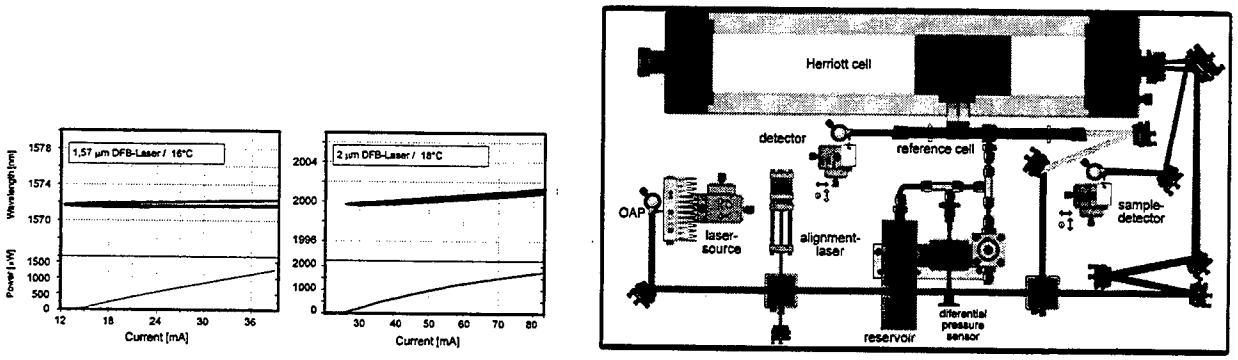

Figure 2 : Mode maps, tuning characteristics and laser power for two near-infrared diode-lasers at room temperature near 1.572 µm and 2.001 µm., which have been implemented in the near-infrared spectrometer.

Since 1997 also room-temperature DFB-lasers at 2 µm are commercially available (Sensors Unlimited), where at reduced pressure strong CO_2 lines unaffected by H_2O absorptions can be found [3-6]. Based on two lasers, emitting in vicinity of 1573 nm and at 2001 nm, a CO_2 sensor has been developed and the optical layout of the instrument is shown in Fig. 2. The DFB-laser is held inside a Peltier-cooled mount which is fixed on a xyz-stage. The laser beam is collimated by an off-axis parabola (OAP) with 10 mm diameter and 12 mm focal length. The beam is focused by a spherical mirror (f = 1 m) to the center of the Herriott-type measurement cell. After 181 reflections, corresponding to 100 m, the beam exits the cell and is focused onto a temperature-stabilized 'extended InGaAs' detector by another OAP. About 8% of the laser beam is coupled off by a beamsplitter and directed through the 28 cm reference cell onto another InGaAs detector. The reference cell is filled with a high concentration CO_2 mixture and connected to the measurement cell by a temperature bridge and a differential pressure sensor. With adjusted laser power and the right concentration in the reference cell the signals from both detectors have identical shape and amplitude and after system calibration using certificated gas mixtures the reference signal can be used as a secondary calibration standard. The signal processing schemes for single-tone and two-tone FM-spectroscopy can be found in a recent review of advances in semiconductor laser based gas monitors [1]. The NIR system has been applied for the detection of atmospheric CO_2. The DC-current of the temperature-stabilized DFB-laser is adjusted to the selected absorption line. The laser is scanned over this line by a 1 kHz-ramp and additionally modulated by high frequency. In order to optimize the signal-to-noise ratio (SNR) and the system stability [7] both FM-techniques (single-tone and two-tone [1]) have been implemented. Due to the limited detector bandwidth frequencies up to 300 MHz are applied, corresponding to the linewidth of CO_2 at a pressure of 100 mbar. Some FM-signals from a near infrared InP diode laser operating around 2 µm are shown in Fig. 3a when outdoor air has been pumped through the Herriott cell and the ambient CO_2 signal of 350 ppm was recorded at 2.004 µm. From the weaker absorption lines of CO_2 and H_2O under high amplification a precision of up to 10^{-4} has been estimated for 256 averages in less than 1 sec. At 2 µm the line-strength is still weaker than in the fundamental band, but room temperature operation of diode lasers is still possible for cw applications. In order to compare spectral regions and the system performance, first the 1.57 µm laser has been mounted in the CO_2 spectrometer. Since the wavelength range at a fixed temperature is very limited, the line identification in the 1.57 µm region has been done comparing the direct absorption signals of a gas mixture (3.38% CO_2 in synthetic air) with the calculated values from the HITRAN database: At 120 mbar and 100 m path length an absorption of 40% is expected for the strongest line at 1.5723 µm, with the next-strongest neighbouring CO_2-lines weaker by a few percent. With this procedure the lines could be unequivocally identified, although a small difference in the relative intensities could be found compared to the values reported in the HITRAN database. This might be due to temperature changes during the measurement. The absorption by ambient water vapour is so small inside this wavelength interval (below 0.04%) that lines have been detected only when working with frequency modulation, but then the absolute absorption level was not available. The relative positions and amplitudes of the detected water lines confirmed the CO_2 line identification. From measurements of the SNR of several strong lines, as well as from relative amplitude ratios to weak neighbouring lines and from stability tests, a 2σ-reproducibility of about 2 ppm CO_2 could be determined at a measurement time of 1s within an effective electronic bandwidth of 6 Hz.With improved signal processing a better performance is expected. Working at 90 reflections in the cell could further enhance the signal amplitude by a factor of about 2 (half absorption, but 4.5 times more power), whereas the noise on the signal would be about 20% higher, since the measurement is still dominated by the thermal noise of the detector-preamplifier combination. Therefore, a detection limit of 0.3 ppm CO_2 is feasible (1 s, 50 m, 120 mbar) corresponding to an optical density of 10^{-6} @ 1Hz. Line identification at 2 µm is much easier than

at 1.57 µm, since within the full current range at fixed temperature up to 4 strong and many weak CO_2 absorption lines together with water vapour lines can be found. Switching between N_2, CO_2 calibration gas and ambient air in the cell allows the identification of CO_2 lines. From these measurements a SNR better than 10000 can be estimated, when only the noise between absorption lines is considered. Further tests have been made to determine the stability of the instrument by Allan variance analysis [7] using a faster data acquisition and 12 bit resolution. From the Allan-plot in Fig. 3b it can be found that at an integration time of 0.1 s a standard deviation of 0.87 ppm is obtained; this corresponds to a change in optical density of $7 \cdot 10^{-4}$, or $1 \cdot 10^{-4}$ normalized to 1Hz bandwidth. Due to the white noise behaviour further averaging improves the measurement reproducibility, e.g. at 10 s integration time a factor of 10 can be obtained in noise reduction. At longer measurement times drift effects dominate. At 1 s averaging time the signal is very smooth and practically no noise can be identified at 12 bit resolution. But the reproducibility is only 0.3 ppm, which is worse by one order of magnitude compared to the value expected by noise considerations above. It can be assumed that temperature changes during the measurement have been below 1 K; therefore, changes in the line strength are below 0.1. For a measurement application it implies that a concentration level of 0.1 ppm CO_2 can be detected more precise than a 0.1 ppm concentration change on a 350 ppm signal.

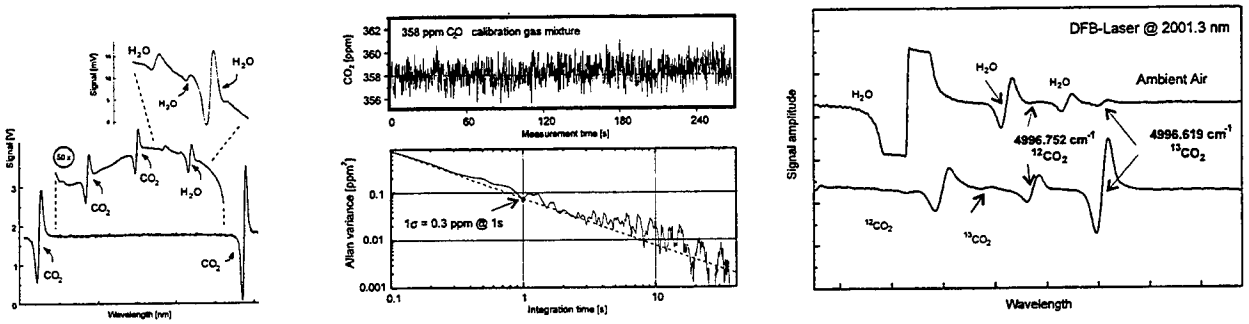

Figure 3 : a) $^2CO_2$ in ambient air b) Allan variance analysis of the system performance c) Identification of $^{12}CO_2$ and $^{13}CO_2$ absorption lines

Besides ambient measurements another possible application are isotopic ratio measurements for medical diagnosis e.g. breath test. In the wavelength range accessible for the 1.57 µm laser no suitable $^{13}CO_2$ lines could be identified, the absorption strengths are too weak. Therefore, $^{13}CO_2/^{12}CO_2$ line pairs within the operation range of the tested 2 µm laser have been analysed. Lines in the vicinity of 2000.8 nm and 2001.3 nm have been identified. The latter line pair is partly influenced by water vapour as displayed in Fig. 3c, but one has to consider that the CO_2 absorptions in expiration air are by a factor of 20-30 higher than the displayed ones. For medical applications the measuring instrument should be able to determine the ratio of $^{13}CO_2$ and $^{12}CO_2$ with a resolution of at least 1% [8], while the absolute CO_2 concentration in human expiration air is 3-5%, with 100% relative humidity at body temperature. A breath test sample is typically about 1 L. The natural ratio $^{13}CO_2$: $^{12}CO_2$ is 1.095 ± 0.003%. Therefore, the instrument must be able to detect both isotopes with a resolution of $<10^{-3}$ unaffected by H_2O. The measurement of the $^{13}CO_2$ content in expiration air using the lines at 2000.8 and 2001.3 nm produces about the same signal as $^{12}CO_2$ in ambient atmospheric air masses at 2004 nm. For a precise determination of the $^{13}C/^{12}C$ ratio, the neighbouring $^{12}CO_2$ lines, which are weaker by a factor of 4, dominate the sensitivity, but even at absorption path lengths of less than 10 m clear signals are expected. The main problem of accuracy is connected with temperature: the ratio of the line strength must be kept constant, which means here that the temperature during the analysis including calibration must be stable within 0.01 K, because the involved line strengths show opposite temperature dependencies. A reliable measurement of the $^{13}CO_2$:$^{12}CO_2$ ratio using the 2000.8 and 2001.3 nm spectral region is not easy to perform, but feasible using a small multipass cell. Nevertheless, the utilization of line pairs with reduced sensitivity to temperature changes is recommended.

Acknowledgement. This research was carried out with support from the European Community under Contract ENV4-CT95-0033.

References

1. P. Werle: Spectrochimica Acta A **54** ,197 (1998).
2. F. D'Amato, A. Lancia, P. Werle: Proc. SPIE **2834**, 242 (1996).
3. R.U. Martinelli: Laser Focus World **3**, 77 (1996)
4. D.M. Sonnenfroh, M.G. Allen: Appl. Opt. **36**, 3298 (1997).
5. S. Chou, D.S. Baer, R.K. Hanson: Appl. Opt. **36**, 3288 (1997).
6. A. Stanton, C. Hovde: Laser Focus World **8**, 117 (1992).
7. P. Werle, R. Mücke, F. Slemr: Appl. Phys. B**57**, 131 (1993).
8. D. Cooper, R.U. Martinelli, C.B. Carlisle, H. Riris, D.B. Bour, R.J. Menna: Appl. Opt. **32**, 6727 (1993).

Detection of Naturally-Occurring Aerosol Particles Under Ambient Conditions Using Cavity Ring-down Spectroscopy

Dr. Andrew D. Sappey and Mr. E. Steven Hill
LaserWave Technologies, Inc.
2280 Juniper Ct.
Golden, CO 80401
and
Mr. Tom Settersten and Dr. Mark A. Linne
Engineering Department, Colorado School of Mines
Golden, CO 80401

Abstract

We have used cavity ring-down spectroscopy as a diagnostic for naturally occurring atmospheric particulate for the first time .

Summary

A non-resonant cavity ring-down diagnostic to measure light attenuation from atmospheric particulate at 532 nm is described. The presence of atmospheric particulate is clearly detectable using this technique, as demonstrated by experimental results.

Cavity ring-down spectroscopy (CRDS) is a relatively new technique that has recently attracted a great deal of attention. CRDS is an extremely sensitive means of performing absorption spectroscopy with pulsed lasers.[1,2,3,4,5,6] Previous work using CRDS has focused on studying the spectroscopy of weak transitions[1,3] or unusual molecules such as noble metal silicides.[4] In contrast, the work presented here takes advantage of the long path lengths characteristic of CRDS to detect Mie scattering from atmospheric aerosol under ambient conditions. The sensitivity results from the extremely long path lengths (path lengths over 100 km have been demonstrated in a 1.3 meter cell)[3] and the fact that the quantity measured, the cavity decay time constant, τ, is unaffected by fluctuations in the intensity of the laser source.

In a CRDS experiment, a pulsed laser is coupled into a non-resonant optical cavity typically formed from two mirrors in a near-confocal geometry. Coupling of pulses into the cavity is dependent on the length of the cavity, which can be thought of as a thick etalon relative to the spectral bandwidth of the laser. As long as the bandwidth of the laser is sufficiently broad to encompass one or more of the cavity longitudinal modes, a significant fraction of the pulse will be coupled into the cavity.[3] For a one meter cavity such as the one used here, the longitudinal modes are spaced by 0.01 cm^{-1}, and the bandwidth of the frequency doubled or tripled Nd:YAG laser is on the order of 1 cm^{-1} which is more than sufficient. The fraction of the pulse that is not reflected from the input mirror is trapped in the cavity resonating between the mirrors and gradually loosing energy due to the finite reflectivity of the mirrors and any absorbing or scattering species present in the cavity.

The decay is monitored by a detector placed at the opposite end of the cavity, sensing the small number of photons that escape on each pass. For an evacuated cavity, the decay time is completely governed by the mirror losses. For a cavity filled with an absorbing gas, particulate, and air, the decay time is given by:[1]

$$\tau = L/c[\ln R + \sigma_{Mie}N_{particles} + \sigma_{Rayleigh}N_{scattering\ molecules} + \sigma_{abs}N_{absorbers} + \ldots. +] \quad 1$$

Here, L is the cavity length (98 cm for the experiments described here), R is the mirror reflectivity, σ is the cross section for absorption or scattering, and N is the number density of molecules or particles absorbing or scattering the light. The Rayleigh cross section for air is readily calculated, and the Mie cross section can be calculated if the size and refractive index of the particles are known. In these experiments, there was nominally no absorbing gas present; so the last term of the equation is zero.

A near-confocal 532 nm cavity was formed by two mirrors with a radius of curvature of 1 meter, separated by 0.98 m. The 7.75 mm super-polished mirrors have a specified reflectivity of five nines (99.999%) at 532 nm, and they were aligned using standard techniques. The radiation from a 10 Hz, frequency-doubled Nd:YAG laser was directed to the input mirror of the cavity. The pulse width was on the order of 6 nsec, and the pulse energy was attenuated to approximately 100 μJ prior to coupling the beam into the cavity. Transverse mode matching was not performed for this initial work. Using this technique, we achieved an equivalent path length of 31 km at 532 nm. A 532 nm-interference-filtered mini-PMT served as the detector (Hamamatsu H5783). The signal transient from the PMT was directed to a 500 MHz bandwidth digital oscilloscope (50 Ω termination) that was used to average 100 transient decays.

To study scattering by atmospheric particulate, a hollow aluminum purge tube with a 1 inch square cross section was inserted between the cavity mirrors with approximately 5 mm of clearance on either end. The purge tube was equipped with a Gelman 47 mm stainless steel filter housing that contained either a 0.8 μm Teflon membrane filter or a 5.0 μm low ash PVC filter. A purge flow of ambient air at up to 30 l/min was forced through the filter housing to control the size distribution and number density of particles in the cavity.

Experimental decay curves were obtained, normalized by the maximum signal excursion, inverted and linearized by taking the natural logarithm of the data. The decays are initially heavily non-exponential most likely due to the fact that we did not complete transverse mode matching - any higher order cavity modes will tend to decay more quickly than the fundamental. After about 30 μsecs, the decays become relatively single exponential, and this region was fit using a linear least squares fit. The decay constants for a variety of purge conditions are given in Table 1.

Table 1: Experimental Decay Constants for a Variety of Purge Conditions

Purge Condition	Decay Constant, τ (μsec)
1. No tube, ambient conditions	91.7 ± 0.6
2. Tube in place but no purge flow	100.9 ± 0.7
3. 5 μm low ash PVC filter	106.0 ± 0.7
4. 0.8 μm membrane filter	107.2 ± 0.5

Several important pieces of information are apparent from the data. First, the tube (with no purge flow) has a substantial effect on the ring-down time presumably because charged particles are removed from the air through interactions with the walls. The net effect is to lower the number of particles in the probe volume and increase the ring-down time. Second, the ring-down technique is able to measure ambient aerosol with good sensitivity. This can be seen by comparing τ for ambient conditions and for flow through an 0.8 μm membrane filter that removes nearly all particles. Third, the ring-down technique is able to reproducibly measure the difference between the particle filtering capacity of the 5 μm and 0.8 μm filters. The significance of the latter two observations is explained below.

The 0.8 μm membrane filter removes nearly all particles larger than 3 nm, as confirmed with a TSI model 3025A condensation counter. Thus, the ring-down time under purge flow condition number 4 can be used to calculate the mirror reflectivity with knowledge of the Rayleigh scattering cross section for air at 532 nm (which is easily calculated). The mirror reflectivity calculated in this way is 99.9986%, very close to the value quoted by the manufacturer. The data of Table 1 have been used in conjunction with additional data presented elsewhere[7] to calculate the sensitivity of the ring-down technique for measuring particles. CRDS, for our experimental configuration, is capable of detecting as few as 200 particles per liter. This compares to 1 particle per liter for commercially available light scattering instruments.

References

1. A. O'Keefe and D. Deacon, Rev. Sci. Instrum. **59** 2544 (1988).
2. J.J Scherer, D. Voekel, D.J. Rakestraw, J.B. Paul, C.P. Collier, R.J. Saykally, and A. O'Keefe, Chem. Phys. Lett. **245** 273 (1995).
3. D. Romanini and K.K. Lehmann, J. Chem. Phys. 99 6287 (1993).
4. J.B. Paul, J.J. Scherer, C.P. Collier, and R.J. Saykally, J. Chem. Phys. **104** 2782 (1996).
5. P. Zalicki and R.N. Zare, J. Chem. Phys. **102** 2708 (1995).
6. R.T. Jongma, M.G.H. Boogaarts, I. Holleman, and G. Meijer, Rev. Sci. Instrum. 66 2821 (1995).
7. A.D. Sappey, E.S. Hill, T. Settersten, and M.A. Linne, submitted to Optics Letters February (1998).

Detection of Multiple Metals in Soil Using Laser-Induced Breakdown Spectroscopy

Dr. Andrew D. Sappey
Mr. Pat D. French
and
Mr. Frank Sagan
ADA Technologies
304 Inverness Way South, Suite 365
Englewood, CO
80112

Abstract

We have built and tested a laser-induced breakdown spectrometer for the detection of lead in paint and soil during a Phase I SBIR program.

Summary

We have built and tested a laser-induced breakdown (LIBS) spectrometer for the detection of lead in paint and soil during a Phase I SBIR program. This program was funded by the Army to develop a robust field instrument to detect lead contamination (and eventually other metals) in soil at Army facilities as well as lead in paint that still covers the walls of many Army buildings including facilities that house military families with small children. The design is essentially that of Cremers et al. at Los Alamos National Laboratory (LANL). The instrument is pictured in Figure 1. It consists of a Kigre model MK-365 pulsed Nd:YAG laser, a Scientific Measurement Systems Jarrel Ash 1/8 meter monochromator, and a SBIG ST6 CCD camera. The Kigre laser produces 3 nsec, 17 mJ pulses at a wavelength of 1064 nm with a pulse repetition frequency of 0.5 Hz. During Phase II, significant changes will be made in the design of the analyzer to allow the instrument to detect multiple metals in soil and to allow the elemental analysis of single particles. The changes will include the use of a proprietary spectrometer design to cover the spectral region from 200 nm - 900 nm with a single monochromator and single 2-dimensional CID detector or with a series of fiber-optically-coupled mini-spectrometers using linear-array detectors. The advantage of the former approach is the speed with

which the necessary CID pixels can be interrogated while the latter approach uses off-the-shelf technology.

The current LIBS system uses the Santa Barbara Instruments Group (SBIG) ST-6 charge coupled device (CCD) camera to obtain a spectrum. The timing sequence is as follows: the user fires the instrument by pushing a button on the front panel. After a 20 msec delay, the CCD camera integration cycle begins so that the camera is on when the laser fires. Meanwhile, the camera controller also sends a trigger pulse to initiate the flash-lamp pulse in the Kigre laser. The laser fires (on average) 700 μsec later with a jitter of ± 500 μsec. The enormous jitter is caused by the passive Q-switch system in the Kigre laser which causes its own set of problems but keeps the cost of the laser low. The camera integration cycle is one second in duration to ensure that the CCD is on when the laser fires. This value is set by the CCD manufacturer and is the result of the communications protocol used by the camera controller.

This timing sequence is problematic for a number of reasons. First, the CCD integrates the light from the flash-lamp pulse as well as the entire temporal history of the micro-plasma initiated by the laser. Both of these light sources produce a broad-band background that reduces the overall sensitivity of the instrument. In addition, the camera integration cycle is sufficiently long that the dark current integrated over one second can be significant when compared to the signal from the metal of interest excited by the plasma.

To maximize sensitivity, the camera should only be activated after the micro-plasma has cooled for several microseconds so that only elemental line emission is observed. In addition, the camera should only remain gated on for a few hundred microseconds after the initiation of the plasma rather than one second so that integration of dark current is minimized. Gating of the detector also minimizes the amount of flash-lamp light that the CCD sees.

To improve the sensitivity of the current LIBS instrument for up-coming field tests, we are significantly altering the functionality of the instrument. The updated design will alleviate all of the problems identified above. The updated instrument will utilize a Hamamatsu linear MOS photodiode array that can be gated quickly with a rise time of 200 nsec and a minimum integration time of 500 nsecs. Gating the detector will avoid many of the problems mentioned above. In addition, the gate will be triggered by light from the laser-produced plasma so that the gate can be precisely controlled relative to plasma initiation. This eliminates the problems caused by the jitter of the Kigre laser and the broadband emission from the plasma at early times. The MOS linear array has pixels that are 25 microns wide and 0.25 cm tall so that the active area of the detector in the vertical dimension is similar to the current CCD camera in which the vertical pixels are currently binned in the vertical dimension to produce a total signal at a particular wavelength. The current CCD camera has an active region that is 6.5 mm high in the vertical dimension. Thus, at most a factor of 2.5 loss of signal is expected from the change to the new detector, and the background signal is expected to be reduced by at least an order of magnitude. The overall signal-to-noise of the instrument is expected to improve significantly.

D'Amato, F. ■ PD1

French, Pat D. ■ PD3

Hill, E. Steven ■ PD2

Lancia, T. ■ PD1

Linne, Mark A. ■ PD2

Mücke, R. ■ PD1

Sagan, Frank ■ PD3

Sappey, Andrew D. ■ PD2, PD3

Settersten, Tom ■ PD2

Werle, P. ■ PD1

Laser Applications to Chemical and Environmental Analysis Technical Program Committee

Robert P. Lucht, *University of Illinois, General Chair*
Kay Niemax, *Institute of Spectrochemistry and Applied Spectroscopy, Germany, General Chair*
Mark G. Allen, *Physical Sciences Inc., Program Chair*
Robert W. Shaw, *Oak Ridge National Laboratory, Program Chair*
Volker Sick, *University of Michigan, Program Chair*
Dieter Brueggemann, *University of Stuttgart, Germany*
Ernest Cespedes, *U.S. Army Waterways Experiment Station*
Jay B. Jeffries, *SRI International Inc., OSA Technical Council Representative*
Kevin McNesby, *U.S. Army Research Laboratory*
David J. Rakestraw, *Sandia National Laboratories*
Markus Sauer, *University of Heidelberg, Germany*
Alan C. Stanton, *Southwest Sciences Inc.*
Nicholas Winograd, *Pennsylvania State University*
Edward S. Yeung, *Iowa State University*